

CALIBRATION OF STRAPDOWN SYSTEM ACCELEROMETER DYNAMIC ERRORS

by

Richard Lee Needham, Jr.

B.S., Aerospace Engineering, United States Naval Academy
Annapolis, Maryland (1992)

Submitted to the Department of Aeronautics and Astronautics
in Partial Fulfillment of the Requirements for the Degree of

MASTER OF SCIENCE IN AERONAUTICS AND ASTRONAUTICS

at the

MASSACHUSETTS INSTITUTE OF TECHNOLOGY

June 1994

© Richard Lee Needham, Jr., 1994. All Rights Reserved

Signature of Author

Department of Aeronautics and Astronautics
13 May 1994

Certified by

Professor Wallace E. Vander Velde
Department of Aeronautics and Astronautics
Thesis Advisor

Certified by

Tom P. Thorvaldsen
Charles Stark Draper Laboratory, Inc.
Technical Supervisor

Accepted by

Professor Harold Y. Wachman
Chairman, Department Graduate Committee

MASSACHUSETTS INSTITUTE
OF TECHNOLOGY

JUL 11 1994
~~JUL 11 1994~~

1

LIBRARIES

Aero

CALIBRATION OF STRAPDOWN SYSTEM ACCELEROMETER DYNAMIC ERRORS

by

Richard Lee Needham, Jr.

Submitted to the
Department of Aeronautics and Astronautics
on May 13, 1994.

In Partial Fulfillment of the Requirements for the Degree of
Master of Science in Aeronautics and Astronautics

Abstract

The calibration of the error terms in strapdown system accelerometers due to angular motion is performed using a three-axis gimbale test table simulation. The sensitivities of the accelerometers to angular velocities and angular accelerations are reduced to accelerometer error coefficients so that a linear estimation can be performed. Linear covariance analysis, using a square root Kalman filter, is used to predict the error dynamics for the simulation.

Various test table gimbale trajectories are implemented to reduce the errors in the accelerometer coefficients. The effects of increasing either the sensitivities or the observabilities of the accelerometer coefficients are compared. The time the gimbals are held at their maximum rates and the initial gimbale angles are varied to observe their effects on the resulting errors in the accelerometer error coefficients. The effects of the displacements between the gimbale axes of the test table are also investigated and shown to be small. The performances of all the trajectories are compared to a previously existing trajectory, resulting in errors that are up to 87.8% lower. The best trajectory found in this research is one that is locally optimized over three trajectory characteristics.

Thesis Advisor: Professor Wallace E. Vander Velde
 Professor of Aeronautics and Astronautics

Technical Supervisor: Tom P. Thorvaldsen
 Principal Member Technical Staff
 The Charles Stark Draper Laboratory, Inc.

Acknowledgments

I would like to express my sincere appreciation to all those who helped me throughout my research effort. Primary thanks go to my technical supervisor, Tom P. Thorvaldsen, who provided the initial idea for this research. His tireless support and guidance were instrumental in developing and completing this thesis. He also managed to squeeze in a few late nights, providing invaluable help when I needed it most. I would also like to extend my deepest gratitude to Professor Wallace E. Vander Velde, who always kept me focused and provided new insights. His ability to describe complex ideas in a clear, concise manner helped me both in the classroom and in the most difficult parts of this research.

I would also like to express my thanks to the Charles Stark Draper Laboratory for making my studies at MIT possible. Thanks go to the technical staff of the Guidance and Navigation Analysis Division, including Tony Bogner, Darold Riegsecker, and Howie Musoff, for providing invaluable technical support and assistance. Although I learned much in the classroom, I learned just as much from my officemates and friends at the lab. Matt and Chris both helped me along the way and made my experience here not only a learning one, but an enjoyable one. Jeff was also always there, providing me with technical help, financial advice, and friendship.

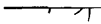

I would like to thank my parents, for without them I never would have made it this far. They have taught me that anything is possible, and that no matter what I decide to do, they will support me in every way. I cannot express how much I appreciate their constant love and support.

Finally, I would like to thank Deborah. She has made the past year and a half one of the happiest times in my life. Her thoughtfulness, patience, and love have meant more to me than she will ever know.

This thesis was researched and written at the Charles Stark Draper Laboratory under the Navy RIMU-S CONTINUATION Project, Contract N00030-93-G-0074-EK08.

Publication of this thesis does not constitute approval by the Charles Stark Draper Laboratory or the United States Navy of the findings or conclusions contained herein. It is published for the exchange and stimulation of ideas.

I hereby assign my copyright of this thesis to the Charles Stark Draper Laboratory, Inc., of Cambridge, Massachusetts.


Richard L. Needham, Jr. 
May 13, 1994

Permission is hereby granted by the Charles Stark Draper Laboratory, Inc. to the Massachusetts Institute of Technology to reproduce and to distribute copies of this thesis document in whole or in part.

Table of Contents

Description	Page
List of Figures	10
List of Tables	13
List of Symbols	14
Chapter 1: Introduction	17
1.1 Background and Motivation	17
1.2 Inertial Navigation Systems	18
1.2.1 Basic Inertial Navigation Systems	18
1.2.1.1 Gimbaled Systems vs. Strapdown Systems	20
1.2.2 Accelerometer Structure	20
1.2.3 Errors in Accelerometers	23
1.2.3.1 Static Errors	24
1.2.3.2 Angular Motion Errors	26
1.2.3.3 Testing Errors	27
1.2.4 Error Terms Calibrated in This Thesis	28
1.3 Previous Work	28
Chapter 2: Analytic Development	31
2.1 Accelerometer Error Model	31
2.1.1 Assumptions on Previously Calibrated Quantities	31
2.1.2 Angular Effects on Accelerometer Output	32
2.1.2.1 Angular Velocity Sensitivity	32
2.1.2.2 Angular Acceleration Sensitivity	35
2.1.2.3 Total Sensitivity to Angular Motion in Accelerometer Frame	37
2.1.3 Reduction of Parameters into Angular Dependent Coefficients	39
2.2 Simulation Model	42
2.2.1 Test Table	43
2.2.2 Navigator Position	44
2.2.2.1 Gimbal Axis Displacements	44
2.3 Measurements and the Kalman Filter	47
2.3.1 Covariance Analysis	48
2.3.2 States and Dynamics Equation	48

2.3.3 Modeling Noise	51
2.3.4 Measurements and Measurement Equation	52
2.3.4.1 Measurement Noise	53
2.3.5 Filter Propagation and Update Equations	54
2.3.5.1 Square Root Filter Implementation	55
2.3.5.2 Propagation of Covariance Matrix	56
Chapter 3: Implementation	59
3.1 Initial Assumptions	59
3.1.1 Initial Covariance	59
3.1.2 Test Table Setup	61
3.1.2.1 Type and Geometry of Table	61
3.1.2.2 Table Constraints	62
3.1.2.3 Table Accuracies	63
3.2 Initial Trajectories	64
3.2.1 Previous Trajectory	64
3.2.1.1 Testing Time Modifications	68
3.2.2 Heuristic Trajectories	69
3.3 Improved Trajectories	74
3.3.1 Objective of Improved Trajectories	74
3.3.2 Effects of Small Changes in Characteristics of Trajectory	75
3.3.2.1 Time at Maximum Rate	75
3.3.2.2 Initial Angles	76
3.3.3 Maximizing Body Frame Angular Rates and Angular Accelerations ...	77
3.3.3.1 Sensitivities to Body Angular Accelerations	78
3.3.3.2 Sensitivities to Squares of Body Angular Velocities	82
3.3.3.3 Sensitivities to Products of Body Angular Velocities	84
3.3.4 Use of Extended Trajectories	87
Chapter 4: Results	91
4.1 Initial Trajectories	92
4.1.1 Previous Trajectory	92
4.1.2 Initial Heuristic Trajectories	97
4.2 Trajectory Characteristic Effects	100
4.2.1 Time at Maximum Rate Effects	102
4.2.2 Initial Angle Effects	103

4.2.3 Summary of Trajectory Characteristic Effects	108
4.3 Extended Trajectories	109
4.3.1 Full Extended Trajectories	109
4.3.2 Extended Initial Trajectories	114
4.3.3 Summary of Extended Trajectories	116
4.4 Modeling Effects	116
4.4.1 Runge Kutta Integration Step Size Effects	117
4.4.2 Measurement Frequency Effects	117
4.4.3 Incorporation of Gimbal Axis Displacements	118
4.5 General Error Estimation Trends	121
4.5.1 Summary of Results	121
4.5.2 Position and Velocity Errors	124
4.5.3 Worst Coefficient Estimates	124
 Chapter 5: Conclusions	 127
5.1 Summary	127
5.2 Proposed Future Work	129
 Appendix A: Test Table Gimbal Trajectories	 131
Appendix B: Graphical Results	157
Appendix C: Gimbal to Body Transformations	175
Appendix D: Square Root Filter	181
 List of References	 185

List of Figures

Description	Page
Figure 1.1 : Pendulous Accelerometer Structure	21
Figure 1.2 : Simplified Pendulous Accelerometer Cross Section	23
Figure 1.3 : Null Offset Error Mechanism	25
Figure 2.1 : Angular Velocity Acting on Accelerometer	32
Figure 2.2 : Misalignment of Pendulum Axes About Case Axes	38
Figure 2.3 : Orientation of Individual Accelerometer Axes to Case Axes	40
Figure 2.4 : Three-Axis Gimbal Test Table	43
Figure 2.5 : Middle Gimbal Origin in Outer Gimbal Frame	45
Figure 2.6 : Inner Gimbal Origin in Middle Gimbal Frame	46
Figure 3.1 : GT0 Gimbal Trajectory	66
Figure 3.2 : GT0 Body Frame Sensitivities	67
Figure 3.3 : GT1 Gimbal Trajectory	71
Figure 3.4 : Representative GT1 Body Frame Sensitivities	73
Figure 4.1 : X Accelerometer Coefficient Errors for GT0	94
Figure 4.2 : Y Accelerometer Coefficient Errors for GT0	95
Figure 4.3 : Z Accelerometer Coefficient Errors for GT0	96
Figure 4.4 : Representative GT1 Body Frame Y-Axis Sensitivities	98
Figure 4.5 : Representative GT3 Body Frame Y-Axis Sensitivities	99
Figure 4.6 : Y Accelerometer Coefficient Errors for GT1	101
Figure 4.7 : Holding Period Effects on Final Cost	104
Figure 4.8 : Initial Middle Gimbal Angle Effects on Final Cost	106
Figure 4.9 : Initial Inner Gimbal Angle Effects on Final Cost	107
Figure 4.10 : Z Accelerometer Coefficient Errors for GT6	111
Figure 4.11 : Z Accelerometer Coefficient Errors for GT6b	112
Figure 4.12 : Z Accelerometer Coefficient Errors for GT6c	113
Figure 4.13 : Extra Cost Due to Gimbal Axis Displacements for GT0	119
Figure 4.14 : Extra Cost Due to Gimbal Axis Displacements for GT3	120
Figure A.1 : GT0 Gimbal Trajectory	132
Figure A.2 : GT1 Gimbal Trajectory	133
Figure A.3 : GT2 Gimbal Trajectory	134
Figure A.4 : GT3 Gimbal Trajectory	135
Figure A.5 : GT4 Gimbal Trajectory	136

Figure A.6 : GT5 Gimbal Trajectory	137
Figure A.7 : GTX1 Extended Gimbal Trajectory	138
Figure A.8 : GTX1b Extended Gimbal Trajectory	139
Figure A.9 : GTX2 Extended Gimbal Trajectory	140
Figure A.10 : GTX2b Extended Gimbal Trajectory	141
Figure A.11 : GTX3 Extended Gimbal Trajectory	142
Figure A.12 : GTX3b Extended Gimbal Trajectory	143
Figure A.13 : GTX4 Extended Gimbal Trajectory	144
Figure A.14 : GTX5 Extended Gimbal Trajectory	145
Figure A.15 : GTX6 Extended Gimbal Trajectory	146
Figure A.16 : GTX7 Extended Gimbal Trajectory	147
Figure A.17 : GTX7b Extended Gimbal Trajectory	148
Figure A.18 : GTX8b Extended Gimbal Trajectory	149
Figure A.19 : GTX9 Extended Gimbal Trajectory	150
Figure A.20 : GT6 Gimbal Trajectory	151
Figure A.21 : GT6b Gimbal Trajectory	152
Figure A.22 : GT6c Gimbal Trajectory	153
Figure A.23 : GT3opt Gimbal Trajectory	154
Figure A.24 : GT4x Gimbal Trajectory	155
Figure A.25 : GT7 Gimbal Trajectory	156
Figure B.1 : GT6 Body Frame X-Axis Sensitivities	158
Figure B.2 : GT6 Body Frame Y-Axis Sensitivities	159
Figure B.3 : GT6 Body Frame Z-Axis Sensitivities	160
Figure B.4 : GT6b Body Frame Sensitivities	161
Figure B.5 : Cost Function for GT0	162
Figure B.6 : Cost Function for Initial Heuristic Trajectories	163
Figure B.7 : Cost Function for GT4 and GT5 Trajectories	164
Figure B.8 : Holding Time Effects on Cost Function	165
Figure B.9 : Initial Middle Gimbal Angle Effects on Cost Function	166
Figure B.10 : Initial Inner Gimbal Angle Effects on Cost Function	167
Figure B.11 : Cost Function for Full Extended Trajectories	168
Figure B.12 : Cost Function for Extended Initial Trajectories	169
Figure B.13 : Runge Kutta Step Size Effects on Cost Function	170
Figure B.14 : Measurement Frequency Effects on Cost Function	171
Figure B.15 : Gimbal Axis Displacement Effects on Cost Function for GT3	172
Figure B.16 : Gimbal Axis Displacement Errors vs. Time for GT1	173

Figure B.17 : Position and Velocity Errors for GT1 vs. Time	174
Figure C.1 : Local Level Frame to Body Frame (3-2-1) Transformation	175

List of Tables

Description	Page
Table 2.1 : Accelerometer Axes to Accelerometer Case Axes Relations	40
Table 2.2a : X-Accelerometer Error Coefficients	41
Table 2.2b : Y-Accelerometer Error Coefficients	41
Table 2.2c : Z-Accelerometer Error Coefficients	42
Table 3.1 : Initial Standard Deviations	60
Table 3.2 : Initial Accelerometer Coefficient Standard Deviations (Inches)	61
Table 3.3 : Test Table Constraints	63
Table 3.4 : Test Table Performance Specifications	64
Table 3.5 : INS Orientation for GT0 Trajectory	65
Table 3.6 : Testing Time Modifications to Previous Trajectory	68
Table 3.7 : Extended Trajectory Gimbal Accelerations, Velocities, and Angles	88
Table 3.8 : Segment Orders for GT6b and GT6c	90
Table 4.1 : Effects of Successive One-Dimensional Optimizations on Final Cost	108
Table 4.2 : Final Costs for All Basic Trajectories	121
Table 4.3 : Final Costs for Variations in Holding Times in GT3 Trajectory	122
Table 4.4 : Final Costs for Variations in Initial Middle Gimbal Angle for GT3	122
Table 4.5 : Final Costs for Variations in Initial Inner Gimbal Angle for GT3	123

List of Symbols

Symbol	Description
a	distance along pendulous axis from accelerometer hinge to point P
a_{error}	acceleration error
$\mathbf{A}_p^{r_{OI}}$	matrix relating gimbal axis displacements to \mathbf{r}_{OI}
$\mathbf{A}_{g\omega}^{b\omega}$	matrix relating gimbal rates to angular velocities in the body frame
b	distance along input axis from accelerometer hinge to point P
c	distance along output axis from accelerometer hinge to point P
c1	X-accelerometer error coefficient vector
c2	Y-accelerometer error coefficient vector
c3	Z-accelerometer error coefficient vector
\mathbf{C}_a^b	transformation matrix from frame a to frame b
C_{ij}	jth coefficient (1-9) of the ith accelerometer (1-3)
\mathbf{f}_i	force vector acting on the ith mass element
F	dynamics matrix
G	sensitivity matrix of body frame acceleration errors to angular motion
h	measurement geometry vector
H	measurement geometry matrix
I_u	pendulum moment of inertia about the ith axis
I_{ij}	pendulum product of inertia with respect to the i and j axes
I	identity matrix
K	Kalman gain matrix
l_0	distance between pendulum hinge and the pendulum center of mass
m_i	ith mass element
M	total mass of the pendulum
OO	origin of the outer gimbal frame
OM	origin of the middle gimbal frame
OI	origin of the inner gimbal frame
P	pendulosity of the pendulum
P	covariance matrix
$\mathbf{Q}(t)$	power spectral density matrix of the process noise vector \mathbf{w}
\mathbf{Q}_k	discrete covariance matrix of process noise
r	position vector
R_{ij}	distance along the jth body axis from accelerometer hinge to point P
R	covariance matrix of measurement noise

t	time
T	characteristic time period for a gimbal to reach ω_{\max} accelerating at α_{\max}
\mathbf{u}	control vector of gimbal angular accelerations
\mathbf{v}	velocity vector
\mathbf{v}_k	measurement noise vector
$\mathbf{w}(t)$	process noise vector
\mathbf{w}_a	vector of process noise in accelerometers
\mathbf{w}_b^T	accelerometer coefficient sensitivity row vector
\mathbf{W}	square root of the covariance matrix
X_α	distance from the pendulum hinge to the center of angular acceleration
X_ω	distance from the pendulum hinge to the center of spin
\mathbf{z}	measurement vector
α_{\max}	maximum obtainable angular acceleration
$\underline{\alpha}$	angular acceleration vector
β_{ij}	misalignment of the i th accelerometer about the j th case axis
δa_{error}	change in acceleration error due to misalignments
δa_{total}	total acceleration error due to angular motion and misalignments
δa_i	total acceleration error for the i th accelerometer
Φ_{ww}	power spectral density matrix of \mathbf{w}_a
$\underline{\rho}$	vector of gimbal axis displacements
ρ_{MI2}	displacement of OI from OM along middle gimbal mg2 axis
ρ_{MI3}	displacement of OI from OM along middle gimbal mg3 axis
ρ_{OM1}	displacement of OM from OO along outer gimbal og1 axis
σ_i	standard deviation of i
σ_i^2	variance of i
ω_{\max}	maximum obtainable angular velocity
$\underline{\omega}$	angular velocity vector

Subscript

b	body frame
i	inner gimbal, input axis
m	middle gimbal
MI	middle gimbal origin to inner gimbal origin
o	outer gimbal, output axis
OI	outer gimbal origin to inner gimbal origin
OM	outer gimbal origin to middle gimbal origin

p pendulous axis

Superscript

b body frame

c accelerometer case frame

g gimbal

ig inner gimbal frame

mg middle gimbal frame

og outer gimbal frame

p pendulum frame

T transpose

$\hat{}$ estimate, unit vector

$+$ immediately after a measurement update

$-$ immediately before a measurement update

Operator

$c\theta$ cosine of θ

$E[]$ expected value operator

$s\theta$ sine of θ

$\mathbf{X}()$ cross product matrix operator

$\delta(t)$ delta function

Acronym

GPS Global Positioning System

INS Inertial Navigation System

Chapter 1

Introduction

1.1 Background and Motivation

Many platforms that navigate using inertial navigation systems (INS's) experience some sort of angular motion. This angular motion may consist of an aircraft rolling, a spacecraft tumbling or a missile spinning. If the instruments used to measure the inertial forces are rigidly attached to the vehicle, then angular rates and angular accelerations of the vehicle will produce linear accelerations in the accelerometers. The internal characteristics of these accelerometers, as well as their placement in the vehicle, will dictate to what extent the vehicular angular motion will affect their outputs.

Accurate navigation of ballistic missile reentry bodies is essential in determining the effect of deployment from the missile bus on the trajectory of the reentry body. For the case of ballistic missile reentry bodies, the angular motion effects on navigation are very important. When the reentry bodies are released from the missile bus they are spun up about their longitudinal axes at very high accelerations. When the reentry bodies move away from the missile bus they are spinning at very high angular rates. Deployment from the missile bus also results in forces on the reentry body that must be measured accurately in order to navigate properly. One of these forces is the impingement of the missile bus firing on the reentry body. Errors in both measured position and velocity will result if the angular motion effects on the navigation system are not compensated out. Therefore, an accurate model of the angular motion effects on the navigation system must be developed.

This thesis calibrates the error terms due to angular effects on strapdown inertial navigation system accelerometers. The INS can be mounted on a three-gimbal test table

and rotated about the three gimbal axes to measure the errors introduced through angular motion.

1.2 Inertial Navigation Systems

1.2.1 Basic Inertial Navigation Systems

An inertial navigation system (INS) is a set of instruments that allow position and velocity of a vehicle to be determined solely from internal measurements. While other navigation systems may make use of external measurements, such as radar ranging, Doppler shifts, or GPS pseudoranges, an INS merely measures the inertial angular rates and forces on the vehicle. For a properly initialized INS, these measurements can be processed to provide a continuous navigation solution. This allows the INS to navigate without any external sensors that either transmit or receive radiation (radars, lasers, radio waves, etc.).

In order for an INS to navigate, it must be capable of performing four distinct functions [1]:

- Instrument a reference frame
- Measure a specific force
- Have knowledge of the gravitational field
- Time integrate the specific force data to obtain velocity and position information

These functions are performed by the four basic components of any INS: three gyroscopes, three accelerometers, a gravity calculator, and an onboard digital computer used to integrate the equations of motion.

Gyroscopic instruments are used to accomplish the first function. The three gyroscopes (assumed to have a single-degree-of-freedom) can either be placed on a gimballed platform or rigidly attached to the vehicle. If they are placed on a gimballed platform, they define an inertially nonrotating cartesian frame. Angular motion of the vehicle about a gyros input axis will cause the gimbal supporting the spin axis to precess

about the output axis. Torques can then be applied to the gyro-supporting gimbals in order to keep the gyro spin axes pointing along the same inertial axes. This maintains an inertially stable platform in which the gyro spin axes maintain their orientation with respect to inertial space. The torques that are required to keep the gimbal supports from precessing are taken as the measurements and used to determine the orientation of the vehicle. If the gyros are rigidly attached to the vehicle, then they will no longer be nonrotating with respect to inertial space. Instead, they are used as sensing elements using a closed-loop servo system. The resulting torques applied to each gyro are then proportional to the particular gyro's inertially referenced angular velocity. The torques can be used to determine the orientation of the gyros with respect to their original orientation. Systems that use rigidly attached gyros instead of placing them on a gimbaled platform are called strapdown systems.

The second function of the INS is performed by devices called accelerometers. The accelerometers are an integral part of either gimbaled or strapdown INS's. The accelerometers are the instruments that actually measure the forces acting on the body. This is accomplished by using three orthogonal accelerometers. Each accelerometer has a proofmass that is constrained to move in one direction. When a force acts on the body, the body accelerates. If the force has a component along a particular accelerometer's input axis, then the proofmass of that accelerometer will deflect. By measuring the deflection of all the proofmasses, the acceleration magnitude and direction can be determined. Unfortunately, the accelerometer measurements also include the effects of the gravitational field. An accelerometer at rest with no external forces acting on it will read $1g$ down due to gravity. In order to determine the motion of the vehicle, the gravity accelerations must be removed from the accelerometer outputs. The third function of the INS is then required to accurately compensate the accelerometer outputs for the local gravity forces.

The final function of the INS, performed by an onboard navigating computer, is the integration of the measured forces. The data obtained from the accelerometers and gyros is processed, resulting in the accelerations in the inertial frame. These accelerations may then be integrated once to provide velocity information. The velocity information is then integrated once more to provide position information.

1.2.1.1 Gimbaled Systems vs. Strapdown Systems

Two forms of inertial navigation systems are the gimbaled system and the strapdown system. The difference between the two systems is the way in which the instruments are mounted on the vehicle. In gimbaled systems, the instruments maintain their orientation in an inertially nonrotating frame. In strapdown systems, the instruments are rigidly attached to the vehicle and experience the same angular motion as the vehicle.

Strapdown systems have both advantages and disadvantages over gimbaled systems. The greatest advantage of strapdown systems is their smaller size. Current systems are so small that their weight is almost negligible. Also, the power consumption for these small devices is significantly less than that of the gimbaled systems. With these advantages comes the disadvantage of a larger computational burden in computing a navigation solution. The gyro data must now be processed to determine the orientation of the vehicle with respect to an inertial frame. Also, since the instruments are rotating with the vehicle, there will be errors introduced due to angular motion. These angular motion errors are only present in strapdown systems.

1.2.2 Accelerometer Structure

There are many different ways to mechanize an accelerometer [2]. Popular designs include unbalanced cylinders, integrating unbalanced gyros, and pendulous accelerometers. One of the most common types is the pendulous accelerometer. This type of accelerometer is similar to a pendulum, consisting of a proofmass that is constrained to rotate about one axis. Accelerations experienced by the instrument are

determined by measuring the current necessary to produce a restoring torque when the pendulum deflects. The Bell XI-79 pendulous accelerometer will be used as the primary example of a strapdown system accelerometer throughout this thesis. However, all strapdown accelerometers, regardless of their design, will experience errors due to angular motion of the vehicle.

The structure of a pendulous accelerometer is shown in Figure 1.1. The ring-shaped proofmass is constrained to rotate only about the hinge (or output) axis. An acceleration along the input axis causes an angular deflection of the proofmass about the hinge axis. An electrical pickoff is used to sense the angular deflection. A current proportional to the angular deflection is produced and passed through a coil that is

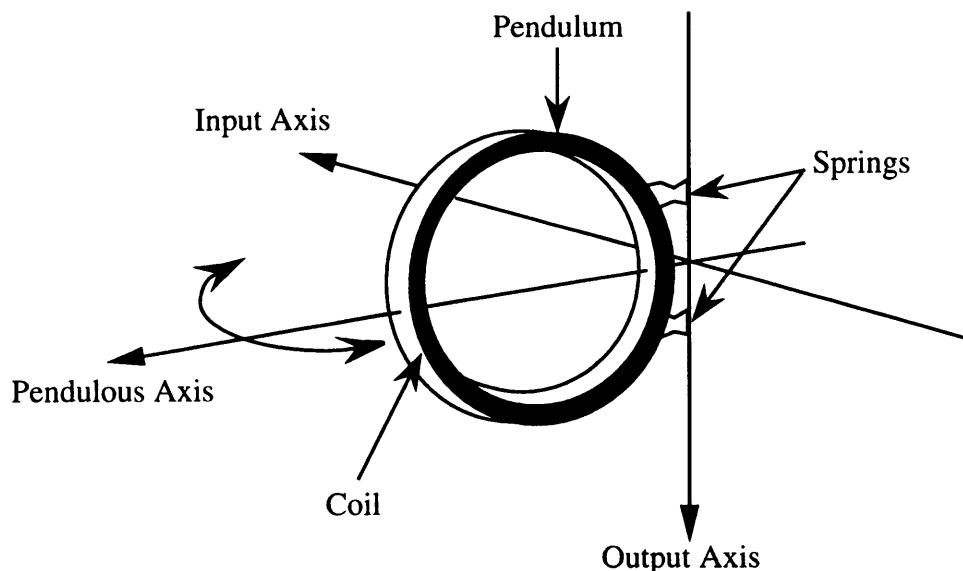


Figure 1.1: Pendulous Accelerometer Structure

wrapped around the proofmass. The coil is situated in a magnetic field, so a current passed through the coil produces a restoring force that drives the proofmass back to its null (undeflected) position. The acceleration is determined by measuring the current necessary to restore the proofmass to its null position.

Accelerometers are designed such that the relationship between the input acceleration and the output torquing current is as linear as possible [3]. This linear relationship means that the input acceleration may be measured accurately by simply measuring the current required to restore the proofmass to its null position. Many physical aspects of the accelerometer contribute to this linear relationship. For example, the pendulum is made of an alloy with a high modulus of elasticity. This prevents unwanted deflections that would change the input-output characteristics of the accelerometer.

The two thin cantilever springs used to attach the pendulum to the hinge axis also help maintain a linear input-output relation. By using two supports, the pendulum is prevented from rotating about the input or pendulous axes. These two springs may also be used to carry the torquing current to the coil wrapped around the outside of the pendulum [3]. The springs may be insulated from the pendulum structure with the epoxy used to attach them. By passing the current to the coil through the springs, the problems associated with flex leads are eliminated. These flex lead problems include errors due to flex lead deflections and fatigue of the leads over the lifetime of the accelerometer.

Another feature that keeps the accelerometer characteristics linear is a constant magnetic field through the center of the coil. Figure 1.2 shows how the pendulum structure is situated within the magnets, flux plates, and capacitive bridge pickoff. The magnetic field is generated using two axially-symmetric magnets separated by a pair of flux plates [3]. The flux plates are placed in the center of the coil carrying the torquing current. The flux plates maintain a constant, radial, high-density magnetic field through the coil by concentrating and redirecting the magnetic flux lines from the two magnets.

The deflection of the pendulum is measured through a capacitive bridge pickoff [3]. In its undeflected or null position, the pendulum lies centered between two plates of a capacitor. This effectively creates two equal capacitors. When the pendulum is deflected, the balance between the capacitors is disrupted and a phase shift results in the

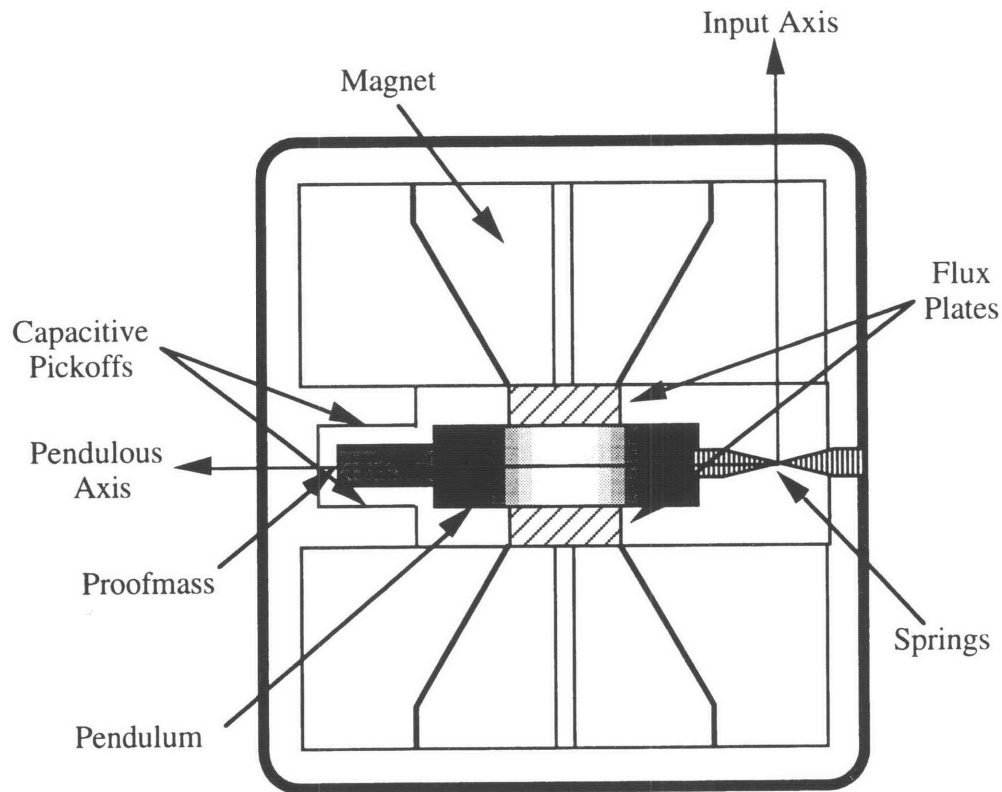


Figure 1.2: Simplified Pendulous Accelerometer Cross Section

a.c. signal passing through the bridge circuit. The shifted signal is then demodulated and used in the servo loop to generate the restoring current. The pendulum is forced back to its null position and the restoring current is measured.

1.2.3 Errors in Accelerometers

Although accelerometers are designed for linearity, there are many sources of error that prevent a simple linear relationship between the input acceleration and the restoring current. Some error sources appear in both strapdown systems and gimballed systems. These errors include biases, scale factors, g-squared terms, misalignments, and higher order terms. Other error sources are dynamic in nature and only appear in strapdown systems. These dynamic error sources include anisonertia terms, output axis coupling terms, and size effects. Still other error sources are introduced when testing or

calibrating the accelerometers. The two error sources due to testing are lever arms to the center of the table and non-incident gimbal axes.

1.2.3.1 Static Errors

Although the accelerometers are built very carefully, they are not perfect. Even if there are no forces acting on the body, the accelerometers may still show an output, called a bias. This output exists because the proofmass may actually have a null position that is offset from the assumed null position. If the bias is known it may be subtracted from the output to arrive at the true acceleration.

Another error source is the scale factor of the accelerometer. The scale factor is the proportionality constant between the measured acceleration and the actual acceleration. This proportionality constant may not be known precisely. Also, the scale factor for a positive acceleration may be different than the scale factor for a negative acceleration. The difference between the two scale factors arises from the torque rebalance loop in the accelerometer. Therefore, there are generally two separate scale factors for a given accelerometer.

G-squared terms are one more source of error for both strapdown and gimballed systems. "G-squared" means the terms depend on either the square of a single acceleration, or the product of two orthogonal accelerations. The squared acceleration terms are a result of nonlinearities in the accelerometer. These errors are usually observed when the acceleration along the input axis is very large. The large input accelerations will cause the pendulum to deflect significantly, producing nonlinear characteristics. G-cubed terms, which depend on the cube of the input acceleration, are also a result of nonlinearities in the accelerometer.

The g-squared error terms are also sensitive to two orthogonal accelerations. For example, suppose the body is being accelerated along the pendulous axis of one of the accelerometers. Since the acceleration is orthogonal to the input axis, there will be no output for that particular accelerometer. However, the pendulum itself will be slightly

stretched and the center of mass of the pendulum will move along the pendulous axis. The relationship between an acceleration along the input axis and the restoring current will now be different for this accelerometer, because the moment arm of the pendulum has changed.

Another contributing factor to the g-squared error is that the pendulum never actually makes it back to the null position. In order to measure an acceleration at all, the pendulum must deflect slightly. Ideally, the pendulum is restored to its null position. This would be true if there were an infinite loop gain. Since the gain is finite, there will always be a null offset that is a function of the input acceleration. This creates a moment arm upon which an acceleration along the pendulous axis may act, causing an error in the measurement. This error mechanism is shown in Figure 1.3. There are other g-squared terms as well. Some of these can be described from a mechanical standpoint, while others are measured experimentally.

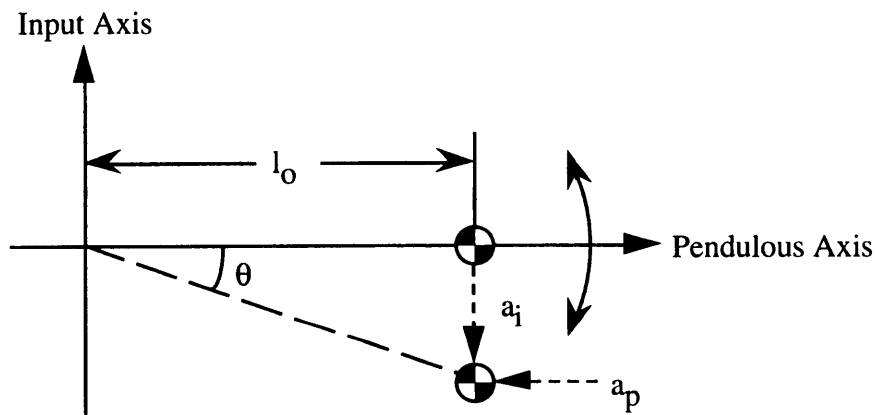


Figure 1.3: Null Offset Error Mechanism

Misalignments between the accelerometer axes and the body axes will also result in errors in both strapdown and gimballed systems. If the three accelerometers are perfectly aligned with the body axes, then the accelerometer outputs will represent the accelerations along each of the body axes. However, if the accelerometer input axes are

misaligned, then the accelerometer outputs will be combinations of the accelerations along the body axes. If these small misalignment angles are known, then the accelerations along the body axes may be computed from the accelerometer outputs.

1.2.3.2 Angular Motion Errors

Some of the error sources in accelerometers only appear in strapdown configurations. These errors are a result of body angular rates and angular accelerations. In strapdown systems, the accelerometers experience the same angular motion as the body because they are rigidly attached to the body. This angular motion produces errors in the indicated accelerations. The error terms due to this angular motion are anisonertia terms, output axis coupling terms, and size effect terms.

When the INS unit is spun about some axis with a constant angular velocity, there will be some indicated linear acceleration. This indicated acceleration will be due, in part, to the centripetal acceleration of the center of mass, which will typically have some component along the input axis of one or more of the accelerometers. For certain spin axes, the resultant acceleration output will be minimized. The point on the pendulous axis through which these minimum acceleration axes pass is called the center of spin. The distance from this point to the hinge depends on the difference between two of the moments of inertia of the pendulum. Hence, these error terms are called anisonertia terms.

Similarly, when the INS unit is subjected to an angular acceleration, there will be an output that depends on the location and the orientation of the axis of angular acceleration. Once again, there is a point along the pendulous axis through which any axis of angular acceleration will result in a minimum output acceleration. This point is defined as the center of angular acceleration. When the system experiences an angular acceleration about this point, the torque developed at the hinge enables the pendulum to keep up with the angular acceleration of the encasement. Hence, no error torques are developed and there will be no indicated acceleration. Since this error depends on the

acceleration about the output axis, the corresponding error terms are called output axis coupling terms.

Size effects are another error source for strapdown systems. These terms refer to the distances between the three accelerometers, their orientations to one another, and the small internal distances within the accelerometers. In a gimbale system, these distances are unimportant because the rotation of the body does not affect the output of the accelerometers. However, in a strapdown system the accelerometers are subjected to angular velocities and angular accelerations. These angular motions will translate into error torques and indicated accelerations that are functions of the size effect terms. Therefore, the distances between the accelerometers and both the spin and angular acceleration axes are significant error sources.

1.2.3.3 Testing Errors

A group of accelerometers may be calibrated by placing them on a three-axis test table and rotating the body about all three axes. Calibrating the accelerometers will accurately determine all the error terms. However, still more error terms are introduced by using a test table. The test table provides two major error sources: lever arms to the center of the table and non-incident gimbal axes.

The lever arm terms dictate how the table's angular rates and accelerations affect the output of the accelerometers. The errors due to the table's angular motion will be greater for accelerometers that are farther away from the center of the table. These distances must be determined accurately in order to calibrate the other error terms of the accelerometer.

Ideally, all three axes of the test table intersect at one point. This provides a center of rotation that is the same for all of the table axes. However, the gimbal axes do not intersect at one point. The nominal calibration test consists of mounting the INS on the inner gimbal such that the reference point in the INS is at the center of the test table. If the axes all intersected at one point, then the INS reference point would experience no

motion, and the position outputs of the navigator could be compared to a nominal zero position. However, if all the gimbals are being rotated, every point in the inner gimbal frame will experience some type of motion due to the displacements between the gimbal axes. Therefore, the navigator position must be compared to the estimated displacement of the navigation reference point.

1.2.4 Error Terms Calibrated in This Thesis

This thesis calibrates the dynamic error terms of a group of strapdown accelerometers. It is assumed that the accelerometer's static error terms are already calibrated. The static terms include the biases, scale factors, and the g-squared terms. These are the terms present in both gimballed and strapdown systems. Static error sources may be calibrated without using a dynamic test table. If the static error terms are already calibrated, then the navigator can compensate for these errors. The only remaining errors will be depend solely on angular motion.

In addition to calibrating the dynamic error terms, the thesis must also address the errors introduced during testing. These errors include the lever arms to the axes of rotation as well as the small displacements between the gimbal axes. The displacements between the gimbal axes must be measured accurately because the accelerometers will be used on a body that experiences very high angular rates and accelerations. Therefore, the test table will be spun at high rates with correspondingly high angular accelerations. These large angular rates and accelerations will produce noticeable errors even if the displacements between the gimbal axes are very small.

1.3 Previous Work

Calibration of inertial navigation systems has been a heavily studied area. Error models for both gyros and accelerometers are developed in many references [1,4,5]. The application of optimal estimation to the calibration problem, using Kalman filtering and optimal smoothing techniques, has been investigated [6,7,8]. Both in-flight calibration

and laboratory testing have been addressed [9]. However, most of these calibration studies focus on the effects of accelerometer biases and scale factors, while either ignoring the angular motion errors or lumping them into a general error term. It is true that the scale factors and biases are the dominant error terms in most applications. However, the errors induced by angular motion become significant when the vehicle experiences very large angular accelerations and velocities.

Some recent work has been done on calibrating the angular motion errors [10,11]. Test table trajectories were developed in order to observe some or all of these error terms. However, these trajectories were either not optimal or only designed to calibrate one of the error terms.

The goal of this thesis was to develop a trajectory that allowed calibration of all the error terms introduced due to angular motion. The trajectories developed in the thesis were designed to reduce the uncertainties in the error terms compared to a previous trajectory. The effects of changing various trajectory characteristics were also investigated. The tradeoff between observability and sensitivity of the error terms was performed by designing trajectories that emphasized either the observabilities or the sensitivities and analyzing the effects on the uncertainties of the error terms. The trajectories that produced the lowest uncertainties were identified. By applying the testing techniques described in these trajectories, the effects of angular motion on an INS may be compensated out with a greater degree of accuracy. The end result will be more accurate navigation in the presence of large angular rates and accelerations.

Chapter 2

Analytic Development

2.1 Accelerometer Error Model

An accurate error model must be derived in order to calibrate the set of accelerometers. This error model will be used in the simulation to relate the accelerometer error coefficients to the errors in navigation. Once the accelerometer error coefficients are accurately estimated, the effects of angular motion on the accelerometer outputs can be compensated out, providing the true linear accelerations experienced by the vehicle.

2.1.1 Assumptions on Previously Calibrated Quantities

Static calibration tests will already have been completed before the dynamic testing of the accelerometers is performed. Optimum test table positions for calibration of the static error terms are described in [12]. These tests calibrate the accelerometer error terms that are independent of angular motion. These error terms include the positive and negative scale factors, g -sensitive terms, g^2 -sensitive terms, and the accelerometer biases. These are the error terms that produce errors in the indicated accelerations due to linear accelerations of the vehicle. The uncertainties of these initially calibrated values are also given in [12].

Since the error terms associated with linear accelerations are assumed to be calibrated, the only errors in the navigator will be due to the accelerations developed as a result of angular motion.

2.1.2 Angular Effects on Accelerometer Output

The dynamic error terms relate angular motion of the vehicle to errors in the indicated accelerations. In order to determine the errors in the navigation solution, an equation that relates angular velocity and angular acceleration to errors in indicated acceleration must be developed. The following development of the error acceleration equations follows the derivation contained in [3].

2.1.2.1 Angular Velocity Sensitivity

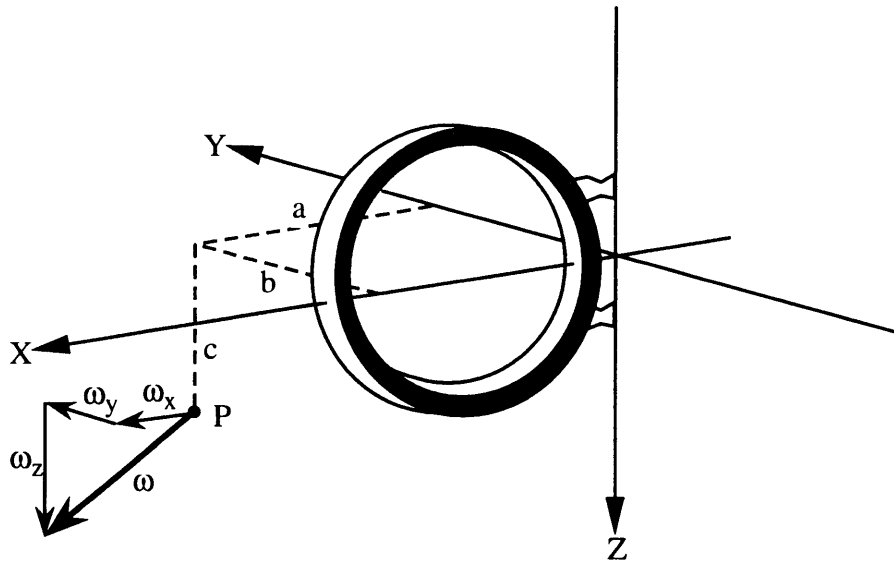


Figure 2.1: Angular Velocity Acting on Accelerometer

In this section we determine the effects of angular spin on the output of the accelerometers. Referring to Figure 2.1 we define a point P through which the spin axis passes. The direction of the spin axis given in terms of the pendulum coordinate frame is $\underline{\omega} = \omega_x \hat{i} + \omega_y \hat{j} + \omega_z \hat{k}$, where \hat{i} , \hat{j} , and \hat{k} are the unit vectors in the X, Y and Z directions, respectively. As shown in Figure 2.1, the X, Y, and Z axes represent the accelerometer's pendulous, input, and output axes, respectively.

We need an equation that relates angular velocity to the error torque developed about the accelerometer's output axis. This equation can be derived by summing the torques developed, due to angular rotation, of each mass element of the pendulum. Some preliminary definitions are needed:

$$\begin{aligned}\mathbf{r}_i &= X_i \hat{\mathbf{i}} + Y_i \hat{\mathbf{j}} + Z_i \hat{\mathbf{k}} \\ \mathbf{r}'_i &= (X_i - a) \hat{\mathbf{i}} + (Y_i - b) \hat{\mathbf{j}} + (Z_i - c) \hat{\mathbf{k}} \\ \underline{\omega} &= \omega_x \hat{\mathbf{i}} + \omega_y \hat{\mathbf{j}} + \omega_z \hat{\mathbf{k}}\end{aligned}$$

where

\mathbf{r}_i = position vector from the accelerometer frame origin to the i th mass element

\mathbf{r}'_i = position vector from point P to the i th mass element

$\underline{\omega}$ = angular velocity vector in the accelerometer frame

The force on the i th mass element due to the centripetal acceleration produced by the angular velocity vector $\underline{\omega}$ is:

$$\mathbf{f}_i = m_i \underline{\omega} \times (\underline{\omega} \times \mathbf{r}'_i)$$

where m_i is the mass of the i th element. This can also be written as:

$$\mathbf{f}_i = m_i [\underline{\omega}(\underline{\omega} \cdot \mathbf{r}'_i) - \mathbf{r}'_i(\underline{\omega} \cdot \underline{\omega})]$$

The torque about the origin of the accelerometer frame is then:

$$\boldsymbol{\tau}_i = \mathbf{r}_i \times \mathbf{f}_i = m_i [\mathbf{r}_i \times \underline{\omega}(\underline{\omega} \cdot \mathbf{r}'_i) - \mathbf{r}_i \times \mathbf{r}'_i(\underline{\omega} \cdot \underline{\omega})] \quad (2.1)$$

where we note that:

$$\begin{aligned}\underline{\omega} \cdot \underline{\omega} &= \omega^2 = \omega_x^2 + \omega_y^2 + \omega_z^2 \\ \underline{\omega} \cdot \mathbf{r}'_i &= (X_i - a)\omega_x + (Y_i - b)\omega_y + (Z_i - c)\omega_z\end{aligned}$$

$$\mathbf{r}_i \times \underline{\omega} = \begin{vmatrix} \hat{\mathbf{i}} & \hat{\mathbf{j}} & \hat{\mathbf{k}} \\ X_i & Y_i & Z_i \\ \omega_x & \omega_y & \omega_z \end{vmatrix} = (Y_i \omega_z - Z_i \omega_y) \hat{\mathbf{i}} - (X_i \omega_z - Z_i \omega_x) \hat{\mathbf{j}} + (X_i \omega_y - Y_i \omega_x) \hat{\mathbf{k}}$$

$$\mathbf{r}_i \times \mathbf{r}'_i = \begin{vmatrix} \hat{\mathbf{i}} & \hat{\mathbf{j}} & \hat{\mathbf{k}} \\ X_i & Y_i & Z_i \\ X_i - a & Y_i - b & Z_i - c \end{vmatrix} = \begin{matrix} +[Y_i(Z_i - c) - Z_i(Y_i - b)]\hat{\mathbf{i}} \\ -[X_i(Z_i - c) - Z_i(X_i - a)]\hat{\mathbf{j}} \\ +[X_i(Y_i - b) - Y_i(X_i - a)]\hat{\mathbf{k}} \end{matrix}$$

The error in indicated acceleration will be due to the torque developed about the output axis of the accelerometer as a result of the angular velocity. Therefore, we are only interested in the torque about the Z-axis. Substituting the above relations into equation (2.1), we have:

$$\tau_z = m_i \{ [(X_i - a)\omega_x + (Y_i - b)\omega_y + (Z_i - c)\omega_z](X_i\omega_y - Y_i\omega_x) - \omega^2(aY_i - bX_i) \} \quad (2.2)$$

We sum over all the mass elements to determine the total resultant torque. When summing over all the mass elements we note that:

$$\begin{aligned} \Sigma m_i(X_i^2 + Z_i^2) &= I_{yy} \\ \Sigma m_i(Y_i^2 + Z_i^2) &= I_{xx} \\ I_{xy} &= \Sigma m_i X_i Y_i, \quad I_{yz} = \Sigma m_i Y_i Z_i, \quad I_{zx} = \Sigma m_i Z_i X_i \\ Ml_0 &= \Sigma m_i X_i \end{aligned}$$

where

I_{xx}, I_{yy} = pendulum moments of inertia about the X and Y axes

I_{ij} = product of inertia with respect to the i and j axes

M = total mass of the pendulum

l_0 = distance along the X axis between the hinge and the center of mass of the pendulum

Performing the indicated substitutions, we arrive at the general formula for the torque about the Z-axis:

$$\begin{aligned} \tau_z &= (I_{yy} - I_{xx} - aMl_0 + b\Sigma m_i Y_i)\omega_x\omega_y + (I_{zz} - cMl_0)\omega_y\omega_z \\ &\quad + (c\Sigma m_i Y_i - I_{yz})\omega_x\omega_z + I_{xy}(\omega_y^2 - \omega_x^2) + a\omega_x^2\Sigma m_i Y_i \\ &\quad - b\omega_y^2 Ml_0 + b\omega^2 Ml_0 - a\omega^2\Sigma m_i Y_i \end{aligned} \quad (2.3)$$

The pendulum is designed to be symmetrical about the origin of the accelerometer frame along both the input and output axes. Therefore, the products of inertia and $\Sigma m_i Y_i$ are very small. Eliminating these terms we arrive at:

$$\tau_z = (I_{yy} - I_{xx} - aMl_0)\omega_x\omega_y - cMl_0\omega_y\omega_z - bMl_0\omega_y^2 + bMl_0\omega_z^2$$

or

$$\tau_z = (I_{yy} - I_{xx} - aMl_0)\omega_x\omega_y - cMl_0\omega_y\omega_z + bMl_0(\omega_x^2 + \omega_z^2)$$

Writing this equation in terms of the accelerometer's pendulous, input, and output axes we have:

$$\tau_o = (I_{ii} - I_{pp} - aMl_0)\omega_i\omega_p - cMl_0\omega_i\omega_o + bMl_0(\omega_p^2 + \omega_o^2) \quad (2.4)$$

This is the expression for the error torque developed about the pendulum's output axis due to the angular velocity vector $\underline{\omega}$. This equation is valid for all three accelerometers, as long as the orientation of the pendulous, input, and output axes are the same as those defined in Figure 2.1.

If the spin axis is defined to go through the pendulous axis (b=0, c=0), then the only term left in equation (2.4) will depend on the difference of two moments of inertia and the angular velocities about the input and pendulous axes. This error term is then referred to as an anisonertia term. In order to minimize the error torque, the value for a can be chosen so that,

$$a = \frac{I_{ii} - I_{pp}}{Ml_0} = X_\omega$$

This point is called the center of spin, because no error torques are developed if the spin axis passes through this point on the pendulous axis.

2.1.2.2 Angular Acceleration Sensitivity

The pendulum will also experience a torque about the output axis when an angular acceleration is applied. This angular acceleration can be represented in the accelerometer frame as:

$$\frac{d}{dt}\underline{\omega} = \underline{\alpha} = \alpha_x\hat{\mathbf{i}} + \alpha_y\hat{\mathbf{j}} + \alpha_z\hat{\mathbf{k}}$$

The force on the i th particle due to the angular acceleration will act in the tangential direction to the angular acceleration and is given by:

$$\mathbf{f}_i = m_i \underline{\alpha} \times \mathbf{r}'_i$$

Therefore, the torque about the origin is:

$$\boldsymbol{\tau}_i = \mathbf{r}_i \times \mathbf{f}_i = m_i \mathbf{r}_i \times (\underline{\alpha} \times \mathbf{r}'_i)$$

or

$$\boldsymbol{\tau}_i = m_i [\underline{\alpha} (\mathbf{r}_i \cdot \mathbf{r}'_i) - \mathbf{r}'_i (\underline{\alpha} \cdot \mathbf{r}_i)] \quad (2.5)$$

where

$$\mathbf{r}_i \cdot \mathbf{r}'_i = X_i(X_i - a) + Y_i(Y_i - b) + Z_i(Z_i - c)$$

$$\underline{\alpha} \cdot \mathbf{r}_i = \alpha_x X_i + \alpha_y Y_i + \alpha_z Z_i$$

Once again, we are only interested in the torque about the Z-axis. Therefore, we substitute the above expressions into equation (2.5) and get:

$$\tau_i = m_i [(X_i^2 - aX_i + Y_i^2 - bY_i + Z_i^2 - cZ_i)\alpha_z - (\alpha_x X_i + \alpha_y Y_i + \alpha_z Z_i)(Z_i - c)] \quad (2.6)$$

Summing over all the mass elements and using the previous definitions for the moments and products of inertia we obtain:

$$\tau_z = (I_{zz} - aMl_0 - b\Sigma m_i Y_i)\alpha_z - (I_{xz} - cMl_0)\alpha_x - (I_{yz} - c\Sigma m_i Y_i)\alpha_y$$

Eliminating the products of inertia and the $\Sigma m_i Y_i$ terms and expressing the result in terms of the accelerometer's pendulous, input, and output axes we have:

$$\tau_o = (I_{oo} - aMl_0)\alpha_o + cMl_0\alpha_p \quad (2.7)$$

This is the expression for the error torque about the pendulum's output axis that results from the angular acceleration vector $\underline{\alpha}$.

If the spin axis is defined to pass through the pendulous axis ($b=0, c=0$) in this case, then the error torque will depend only on the output axis moment of inertia and the angular acceleration about the output axis. This error term is referred to as an output axis coupling term. Once again, an appropriate value for a can be chosen to minimize the error torque. Specifically, for the case of angular acceleration, the minimizing value for a is

$$a = \frac{I_{oo}}{Ml_0} = X_\alpha$$

This point is referred to as the center of angular acceleration or the effective center of mass, because no error torques are experienced if the angular acceleration axis passes through this point on the pendulous axis.

2.1.2.3 Total Sensitivity to Angular Motion in Accelerometer Frame

Using the definitions for the centers of spin and angular acceleration, the total error torque developed due to angular motion in the accelerometer frame can be written as:

$$\tau_{o,total} = Ml_0[(X_\omega - a)\omega_i\omega_p - c\omega_i\omega_o + b(\omega_p^2 + \omega_o^2) + (X_\alpha - a)\alpha_o + c\alpha_p]$$

Since the error in indicated acceleration due to the error torque is given by:

$$a_{error} = \frac{\tau_{o,total}}{P}$$

where P is the pendulosity of the pendulum and is defined as Ml_0 , then the acceleration error is:

$$a_{error} = (X_\omega - a)\omega_i\omega_p - c\omega_i\omega_o + b(\omega_p^2 + \omega_o^2) + (X_\alpha - a)\alpha_o + c\alpha_p \quad (2.8)$$

This acceleration error was determined assuming that the pendulum frame was identical to the frame in which the spin axis was defined. However, the angular velocity will be known in the accelerometer case frame rather than the pendulum frame. Since the pendulum may not be aligned with the accelerometer case's pendulous axis, additional errors will be generated. These errors are due to the resultant torque components along the pendulum's output axis. The orientation of the pendulum's axes (p', i', o') to the accelerometer case axes (p, i, o) is shown in Figure 2.2, where β_p , β_i , and β_o are the small misalignment angles about the case pendulous, input, and output axes, respectively. The transformation of a vector from case coordinates (p, i, o) into pendulum coordinates (p', i', o') can be done using the small angle rotation matrix C_c^p [13]:

$$\begin{aligned} \mathbf{v}^p &= \mathbf{C}_c^p \mathbf{v}^c \\ &= [\mathbf{I} - \mathbf{X}(\underline{\beta}^c)] \mathbf{v}^c \\ &= \mathbf{v}^c - \underline{\beta}^c \times \mathbf{v}^c \end{aligned}$$

where $\mathbf{X}(\underline{\beta})$ is the cross product matrix of the misalignment angles. The additional error in indicated acceleration is a function of the resultant torque component about the pendulum's output axis [3,14]:

$$\begin{aligned} \delta a_{error} = & (\beta_i X_\alpha - \beta_p c) \alpha_p + [\beta_o c - \beta_p (X_\alpha - a)] \alpha_i - \beta_o b \alpha_o \\ & + (\beta_p c - \beta_o X_\omega) \omega_p^2 + [\beta_p c + \beta_o (X_\omega - a)] \omega_i^2 - \beta_o a \omega_o^2 \\ & + \beta_o b \omega_p \omega_i + [\beta_o c + \beta_p (X_\omega - a)] \omega_p \omega_o - (\beta_p b - \beta_i X_\omega) \omega_i \omega_o \end{aligned} \quad (2.9)$$

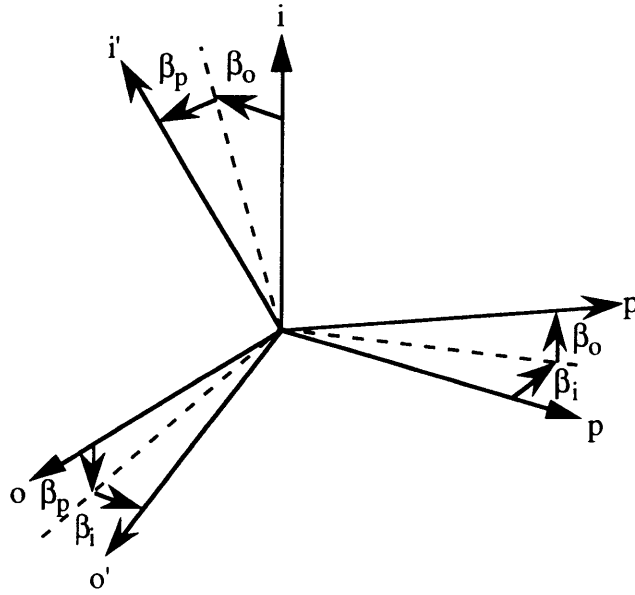


Figure 2.2: Misalignment of Pendulum Axes About Case Axes

Combining the errors in (2.8) and (2.9), an equation for the total acceleration error that takes angular velocity, angular acceleration, and misalignments into account can be written:

$$\begin{aligned} \delta a_{total} = & (c + \beta_i X_\alpha - \beta_p c) \alpha_p + [\beta_o c - \beta_p (X_\alpha - a)] \alpha_i + (X_\alpha - a - \beta_o b) \alpha_o \\ & + (b + \beta_p c - \beta_o X_\omega) \omega_p^2 + [\beta_p c + \beta_o (X_\omega - a)] \omega_i^2 + (b - \beta_o a) \omega_o^2 \\ & + (X_\omega - a + \beta_o b) \omega_p \omega_i + [\beta_o c + \beta_p (X_\omega - a)] \omega_p \omega_o - (c + \beta_p b - \beta_i X_\omega) \omega_i \omega_o \end{aligned} \quad (2.10)$$

2.1.3 Reduction of Parameters into Angular Dependent Coefficients

The dynamic error terms are represented in this thesis by nine coefficients for each of the three accelerometers. The nine error coefficients are combinations of error parameters arising from lever arm effects, size effects, anisonertia effects and output axis coupling effects. The general equation for acceleration error in a given accelerometer can be written as:

$$\begin{aligned} \delta a_i = & c_{i1}\alpha_x + c_{i2}\alpha_y + c_{i3}\alpha_z \\ & + c_{i4}\omega_x^2 + c_{i5}\omega_y^2 + c_{i6}\omega_z^2 \\ & + c_{i7}\omega_x\omega_y + c_{i8}\omega_x\omega_z + c_{i9}\omega_y\omega_z \end{aligned} \quad (2.11)$$

where

δa_i = acceleration error in the i th (X, Y, or Z) accelerometer

c_{ij} = j th error coefficient for the i th (X, Y, or Z) accelerometer

$\alpha_x, \alpha_y, \alpha_z$ = angular acceleration along the accelerometer case X, Y, and Z axes

$\omega_x, \omega_y, \omega_z$ = angular velocity along the accelerometer case X, Y, and Z axes

The error coefficients of (2.11) are obtained from (2.10) and the orientation of the accelerometers to the accelerometer case.

In order to write the acceleration error equations for all three accelerometers, the orientation of the accelerometers to the case must be defined. The orientation shown in Figure 2.3 [14] was used for the simulation, where p, i, and o denote the pendulous, input and output axes for each of the accelerometers. This orientation was based on the assumption that the maximum angular velocities and angular accelerations will be along the X-axis of the case. In order to minimize the effects of the output axis coupling terms, none of the output axes of the accelerometers were placed along the X-axis [15]. Table 2.1 summarizes the relations between the case axes and the axes for the X, Y, and Z accelerometers. The coefficients for each accelerometer, as represented in (2.11) were determined using equation (2.10) and Table 2.1. Table 2.2 lists the combinations of accelerometer parameters that make up the error coefficients. Note that the lever arm distances a, b, and c were replaced with R_{ij} terms, where the "i" subscript refers to the

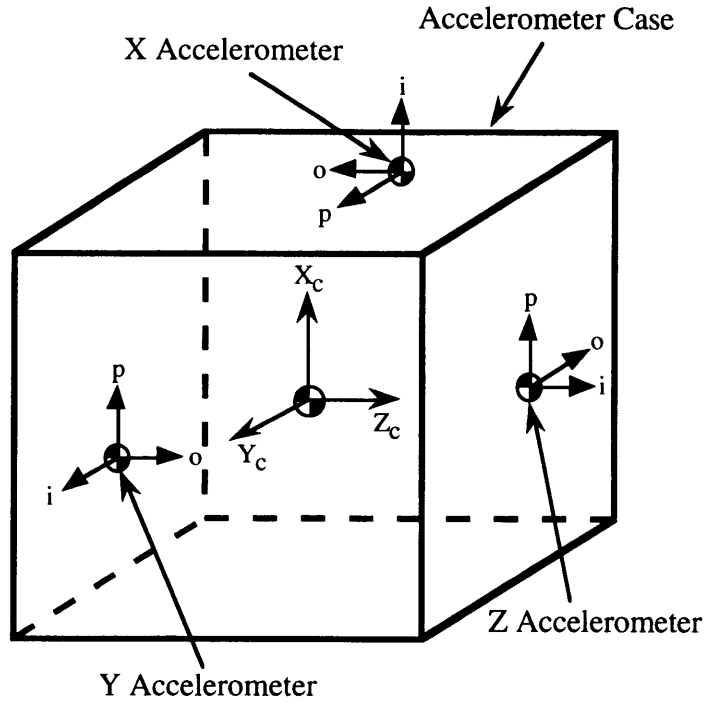


Figure 2.3: Orientation of Individual Accelerometer Axes to Case Axes

accelerometer (X, Y, Z) and the "j" subscript refers to the appropriate case axis (X, Y, Z).

The combination of accelerometer parameters into error coefficients was done for two reasons. First, many of the error terms are not separable. For example, referring to equation (2.10), an angular acceleration about the case's output axis (α_o) would produce an indicated acceleration because of an output axis coupling term ($X_{\alpha-a}$) and a

Table 2.1: Accelerometer Axes to Accelerometer Case Axes Relations

Accelerometer Axes	Individual Accelerometers		
	X	Y	Z
Pendulous	$+Y_c$	$+X_c$	$+X_c$
Input	$+X_c$	$+Y_c$	$+Z_c$
Output	$-Z_c$	$+Z_c$	$-Y_c$

Table 2.2a: X-Accelerometer Error Coefficients

c ₁₁	α_x	$\beta_{xz}R_{xz}-\beta_{xy}X_{\alpha x}+\beta_{xy}R_{xy}$
c ₁₂	α_y	$-R_{xz}+\beta_{xx}X_{\alpha x}+\beta_{xy}R_{xz}$
c ₁₃	α_z	$-X_{\alpha x}+R_{xy}-\beta_{xz}R_{xx}$
c ₁₄	ω_x^2	$-\beta_{xy}R_{xz}-\beta_{xz}X_{\omega x}+\beta_{xz}R_{xy}$
c ₁₅	ω_y^2	$R_{xx}-\beta_{xy}R_{xz}+\beta_{xz}X_{\omega x}$
c ₁₆	ω_z^2	$R_{xx}+\beta_{xz}R_{xy}$
c ₁₇	$\omega_x\omega_y$	$X_{\omega x}-R_{xy}-\beta_{xz}R_{xx}$
c ₁₈	$\omega_x\omega_z$	$-R_{xz}+\beta_{xy}R_{xx}-\beta_{xx}X_{\omega x}$
c ₁₉	$\omega_y\omega_z$	$-\beta_{xz}R_{xz}-\beta_{xy}X_{\omega x}+\beta_{xy}R_{xy}$

Table 2.2b: Y-Accelerometer Error Coefficients

c ₂₁	α_x	$R_{yz}+\beta_{yy}X_{\alpha y}-\beta_{yx}R_{yz}$
c ₂₂	α_y	$\beta_{yz}R_{yz}-\beta_{yx}X_{\alpha y}+\beta_{yx}R_{yx}$
c ₂₃	α_z	$X_{\alpha y}-R_{yx}-\beta_{yz}R_{yy}$
c ₂₄	ω_x^2	$R_{yy}+\beta_{yx}R_{yz}-\beta_{yz}X_{\omega y}$
c ₂₅	ω_y^2	$\beta_{yx}R_{yz}+\beta_{yz}X_{\omega y}-\beta_{yz}R_{yx}$
c ₂₆	ω_z^2	$R_{yy}-\beta_{yz}R_{yx}$
c ₂₇	$\omega_x\omega_y$	$X_{\omega y}-R_{yx}+\beta_{yz}R_{yy}$
c ₂₈	$\omega_x\omega_z$	$\beta_{yz}R_{yz}+\beta_{yx}X_{\omega y}-\beta_{yx}R_{yx}$
c ₂₉	$\omega_y\omega_z$	$-R_{yz}-\beta_{yx}R_{yy}+\beta_{yy}X_{\omega y}$

misalignment and lever arm term ($-\beta_0b$). The errors due to these two terms cannot be determined individually, but rather as a combination of their effects.

Table 2.2c: Z-Accelerometer Error Coefficients

c ₃₁	α_x	$-R_{zy} + \beta_{zz}X_{\alpha z} + \beta_{zx}R_{zy}$
c ₃₂	α_y	$-X_{\alpha z} + R_{zx} - \beta_{zy}R_{zz}$
c ₃₃	α_z	$\beta_{zy}R_{zy} - \beta_{zx}X_{\alpha z} + \beta_{zx}R_{zx}$
c ₃₄	ω_x^2	$R_{zz} - \beta_{zx}R_{zy} + \beta_{zy}X_{\omega z}$
c ₃₅	ω_y^2	$R_{zz} + \beta_{zy}R_{zx}$
c ₃₆	ω_z^2	$-\beta_{zx}R_{zy} - \beta_{zy}X_{\omega z} + \beta_{zy}R_{zx}$
c ₃₇	$\omega_x\omega_y$	$-\beta_{zy}R_{zy} + \beta_{zx}X_{\omega z} - \beta_{zx}R_{zx}$
c ₃₈	$\omega_x\omega_z$	$X_{\omega z} - R_{zx} - \beta_{zy}R_{zz}$
c ₃₉	$\omega_y\omega_z$	$-R_{zy} + \beta_{zx}R_{zz} - \beta_{zz}X_{\omega z}$

The second reason the accelerometer parameters were combined into error coefficients is that by grouping the parameters into nine coefficients, the estimation problem becomes a linear filtering problem. The coefficients are actually sensitivities of the acceleration error to the angular accelerations, angular velocities squared, and the products of the angular velocities in the accelerometer case frame. The final result of processing the error acceleration equations using the coefficients will be accurate estimates of the sensitivities of the acceleration error to angular motion. These sensitivities may then be used to compensate out acceleration errors due to vehicular angular motion.

2.2 Simulation Model

This section describes the tools used to perform the simulation. The testing method using a three-gimbal test table is outlined. The equations are presented for the covariance analysis using a Kalman filter. The unique characteristics of the Kalman filter are described in detail.

2.2.1 Test Table

The test table used in the simulation is a three-axis motion simulator. The three orthogonal axes allow control over the dynamic motion of the INS system, which is rigidly mounted inside the innermost gimbal of the table. Figure 2.4 is a picture of a typical three-axis gimbal test table.

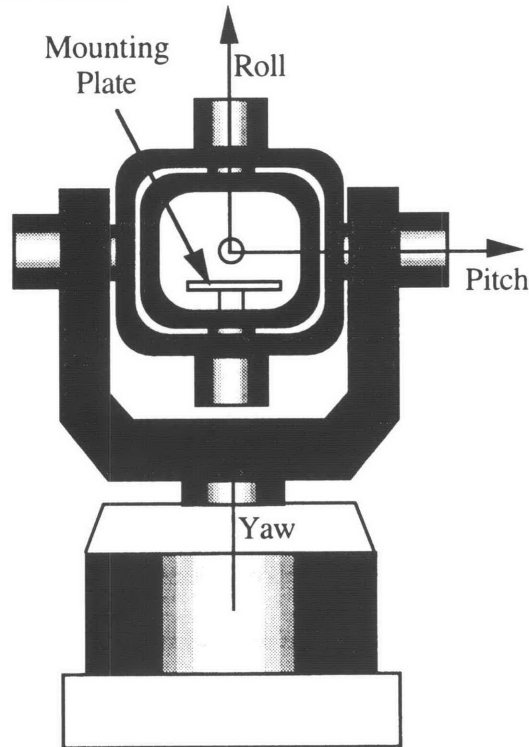


Figure 2.4: Three-Axis Gimbal Test Table

Figure 2.4 shows that the outer, middle, and inner gimbals control deflections about the yaw, pitch, and roll axes, respectively. For the configuration shown, the yaw and roll angles are zero and the pitch angle is 90 degrees.

The control inputs to the test table were individual gimbal angular accelerations. By controlling the gimbal angular accelerations, a wide range of angular motions for the system inside the test table were developed. The type and limitations of the specific table assumed for this thesis are detailed in Section 3.1.2.

2.2.2 Navigator Position

A static calibration of the INS will already have been performed. This calibration allows the INS to navigate in the absence of angular motion. Since the test table subjected the INS to angular motions, and no linear motions, the nominal navigator position output was zero. This assumed that the reference point in the INS was at the intersection of all three table gimbal axes. Also, it was assumed that the navigator compensated for the gravity vector effects. However, the angular motion of the INS would produce nonzero outputs in the accelerometers. These outputs would then be integrated in the navigator, yielding a nonzero position. Therefore, the outputs of the navigator were assumed to be the errors due solely to angular motion.

The navigation reference point must lie at the intersection of all three gimbal axes in order for the navigator to have a nominal position output of zero for all possible gimbal motion. However, as mentioned in Section 1.2.3, the gimbal axes of the test table do not intersect at a point. The table manufacturer specifies a small sphere, inside of which the table axes intersect. The gimbal axis displacements will result in motion of the navigation reference point, regardless of where it is placed inside the inner gimbal. To compensate for the effects of the gimbal axis displacements, the position vector from the origin of the local level frame to the origin of the inner gimbal frame must be estimated. The equations that give this position vector as a function of the displacements and the gimbal angles are derived below [16].

2.2.2.1 Gimbal Axis Displacements

The origin of the local level frame and the outer gimbal frame may be defined to be the same point, OO . This point was defined to be the intersection of the outer gimbal axis and the plane of the middle gimbal frame, as shown in Figure 2.5. The outer gimbal coordinate axis $og1$ was defined to be perpendicular to the middle gimbal spin axis, and pointing toward the middle gimbal spin axis in the plane of the middle gimbal frame.

Then, the position vector from the origin of the outer gimbal frame to the origin of the middle gimbal frame was constant in outer gimbal coordinates and was given by:

$$\mathbf{r}_{OM}^{og} = (\rho_{OM1}, 0, 0) \quad (2.12)$$

where ρ_{OM1} is the displacement between the outer and middle gimbal axes. The subscript "OM" denotes the position vector from the outer gimbal origin to the middle gimbal origin, and the superscript "og" denotes the vector is expressed in outer gimbal frame coordinates.

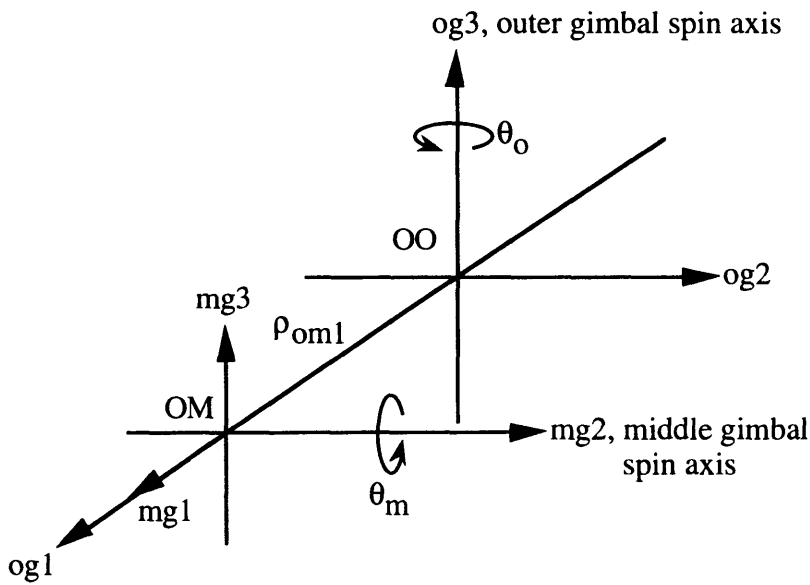


Figure 2.5: Middle Gimbal Origin in Outer Gimbal Frame

Similarly, the origin of the inner gimbal frame was displaced from the origin of the middle gimbal frame, as shown in Figure 2.6. The position vector from the middle gimbal origin to the inner gimbal origin was constant in middle gimbal coordinates and was given by:

$$\mathbf{r}_{MI}^{mg} = (0, \rho_{MI2}, \rho_{MI3}) \quad (2.13)$$

where ρ_{MI2} and ρ_{MI3} are the displacements of the inner gimbal origin from the middle

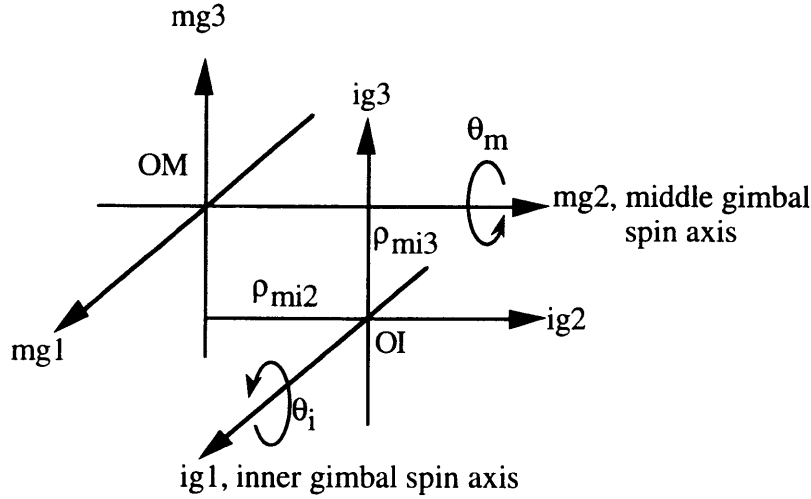


Figure 2.6: Inner Gimbal Origin in Middle Gimbal Frame

gimbal origin along the middle gimbal mg_2 and mg_3 axes, respectively. As before, the subscript "MI" means the vector is from the middle gimbal origin to the inner gimbal origin, and the superscript "mg" means the vector is expressed in middle gimbal frame coordinates.

The position vector from the origin of the local level frame to the origin of the inner gimbal frame was then expressed in the middle gimbal frame as:

$$\begin{aligned}
 \mathbf{r}_{OI}^{mg} &= \mathbf{r}_{OM}^{mg} + \mathbf{r}_{MI}^{mg} \\
 &= \mathbf{C}_{og}^{mg} \mathbf{r}_{OM}^{og} + \mathbf{r}_{MI}^{mg} \\
 &= \begin{bmatrix} \cos \theta_m & 0 & -\sin \theta_m \\ 0 & 1 & 0 \\ \sin \theta_m & 0 & \cos \theta_m \end{bmatrix} \begin{bmatrix} \rho_{OM1} \\ 0 \\ 0 \end{bmatrix} + \begin{bmatrix} 0 \\ \rho_{MI2} \\ \rho_{MI3} \end{bmatrix} \\
 &= \begin{bmatrix} \rho_{OM1} \cos \theta_m \\ \rho_{MI2} \\ \rho_{OM1} \sin \theta_m + \rho_{MI3} \end{bmatrix}
 \end{aligned} \tag{2.14}$$

This vector was expressed in inner gimbal coordinates by multiplying by the middle to inner gimbal frame transformation matrix, \mathbf{C}_{mg}^{ig} :

$$\begin{aligned}
\mathbf{r}_{oi}^{ig} &= \mathbf{C}_{mg}^{ig} \mathbf{r}_{oi}^{mg} \\
&= \begin{bmatrix} 1 & 0 & 0 \\ 0 & \cos \theta_i & \sin \theta_i \\ 0 & -\sin \theta_i & \cos \theta_i \end{bmatrix} \begin{bmatrix} \rho_{OM1} \cos \theta_m \\ \rho_{MI2} \\ \rho_{OM1} \sin \theta_m + \rho_{MI3} \end{bmatrix} \\
&= \begin{bmatrix} \rho_{OM1} \cos \theta_m \\ \rho_{MI2} \cos \theta_i + (\rho_{OM1} \sin \theta_m + \rho_{MI3}) \sin \theta_i \\ -\rho_{MI2} \sin \theta_i + (\rho_{OM1} \sin \theta_m + \rho_{MI3}) \cos \theta_i \end{bmatrix}
\end{aligned} \tag{2.15}$$

Therefore, the vector \mathbf{r}_{oi}^{ig} was a function of the gimbal axis displacements and the gimbal angles and was written as:

$$\mathbf{r}_{oi}^{ig} = \mathbf{A}_p^{roi} \underline{\rho} \tag{2.16}$$

where

$$\mathbf{A}_p^{roi} = \begin{bmatrix} \cos \theta_m & 0 & 0 \\ \sin \theta_m \sin \theta_i & \cos \theta_i & \sin \theta_i \\ \sin \theta_m \cos \theta_i & -\sin \theta_i & \cos \theta_i \end{bmatrix}$$

$$\underline{\rho} = \begin{bmatrix} \rho_{OM1} \\ \rho_{MI2} \\ \rho_{MI3} \end{bmatrix}$$

The position of the inner gimbal origin as a function of time was estimated using equation (2.16), where $\underline{\rho}$ was added to the original state vector. This position was then used to more accurately model the measurements incorporated in the filter. The state vector and measurements are described in Section 2.2.3.

2.3 Measurements and the Kalman Filter

The primary tool for analysis of the uncertainties of the accelerometer error coefficients was linear covariance analysis using a continuous Kalman filter incorporating discrete time measurements. The instruments in the INS take measurements that provide information about the position and velocity of the system. The Kalman filter weighs these measurements, according to their accuracy, and uses them to estimate the states in

an optimal way [17,18]. If the measurements contain enough information about the states, then the state uncertainties may be systematically decreased to the level of accuracy of the measurements. However, the errors in some of the states due to the dynamics of the system may outweigh the effects of the measurements. These dynamic effects may cause the state uncertainties to remain unchanged or even increase with time.

For the case of calibrating the accelerometers, the position and velocity states were affected by the dynamics of the system, but the error coefficients were not. Therefore, if no measurements were taken, the uncertainties in the position and velocity states would increase while the uncertainties of the error coefficients would remain unchanged. The error coefficients were unaffected by the dynamics of the system because they were defined as constants, based on parameters of the accelerometers.

2.3.1 Covariance Analysis

A covariance matrix is a statistical representation of the errors in the state estimates and the correlations between them. The terms along the diagonal of the covariance matrix represent the variances of the corresponding states, while the off diagonal terms represent the cross correlations between states. The cross correlations are symmetric about the main diagonal. The covariance matrix is defined as

$$\mathbf{P} = E[(\mathbf{x} - \hat{\mathbf{x}})(\mathbf{x} - \hat{\mathbf{x}})^T]$$

where \mathbf{x} is the true state, $\hat{\mathbf{x}}$ is the state estimate, and $E[\cdot]$ is the expected value function.

By taking appropriate measurements, the state uncertainties will decrease. It is the goal of this thesis to determine what trajectory of the gimbals will result in the smallest state uncertainties at the end of the simulation.

2.3.2 States and the Dynamics Equation

The states estimated in the baseline simulation include the position and velocity errors in the local level frame, and the nine error coefficients for each accelerometer:

$$\mathbf{x} = \begin{bmatrix} \mathbf{r} \\ \mathbf{v} \\ \mathbf{c}_1 \\ \mathbf{c}_2 \\ \mathbf{c}_3 \end{bmatrix} \quad (2.17)$$

where

\mathbf{x} = system state vector (33x1)

\mathbf{r} = position error vector in the local level frame (3x1)

\mathbf{v} = velocity error vector in the local level frame (3x1)

\mathbf{c}_1 = X-accelerometer error coefficient vector (9x1)

\mathbf{c}_2 = Y-accelerometer error coefficient vector (9x1)

\mathbf{c}_3 = Z-accelerometer error coefficient vector (9x1)

The accelerometer error coefficients are defined in terms of the accelerometer parameters in Table 2.2.

When the gimbal axis displacements were included for determining the nominal navigator position, the state vector was augmented with $\boldsymbol{\rho}$, the vector of axis displacements defined in equation (2.16). This added three more states to the end of \mathbf{x} .

The system dynamic equation relates the change in the states to the states themselves and is given by:

$$\dot{\mathbf{x}}(t) = \mathbf{F}(\mathbf{u}(t);t)\mathbf{x}(t) + \mathbf{w}(t) \quad (2.18)$$

where

$\mathbf{F}(\mathbf{u}(t);t)$ = dynamics matrix

$\mathbf{u}(t)$ = control vector consisting of three gimbal angle accelerations

$\mathbf{w}(t)$ = modeling noise vector

As indicated, the dynamics matrix depends on time and the control inputs. Since the accelerometer error coefficients were constants, a large portion of \mathbf{F} consisted of zeros:

$$\mathbf{F}(\mathbf{u}(t);t) = \left[\begin{array}{c|c|c} \mathbf{0}_{3 \times 3} & \mathbf{I}_{3 \times 3} & \mathbf{0}_{3 \times 27} \\ \hline \mathbf{0}_{3 \times 3} & \mathbf{0}_{3 \times 3} & \mathbf{C}_b''(\mathbf{u}(t);t)\mathbf{G}(\mathbf{u}(t);t)_{3 \times 27} \\ \hline \mathbf{0}_{27 \times 3} & \mathbf{0}_{27 \times 3} & \mathbf{0}_{27 \times 27} \end{array} \right] \quad (2.19)$$

where

$\mathbf{I}_{3 \times 3}$ = identity matrix (3x3)

$\mathbf{C}_b''(\mathbf{u}(t);t)$ = transformation matrix from the body frame (inner gimbal frame) to the local level frame

$\mathbf{G}(\mathbf{u}(t);t)$ = matrix used to calculate error acceleration in the body frame

For the case where \mathbf{x} was augmented with $\underline{\rho}$, the dynamics matrix was appended with three more columns and three more rows of zeros, because the gimbal axis displacements were constants.

The model assumed that the INS system compensated for all errors in the indicated accelerations except for angular motion effects. Therefore, the error acceleration in the body frame was defined by equation (2.11). The matrix \mathbf{G} was then specified as:

$$\mathbf{G}(\mathbf{u}(t);t) = \left[\begin{array}{ccc} \mathbf{w}_b^T(\mathbf{u}(t);t)_{1 \times 9} & \mathbf{0}_{1 \times 9} & \mathbf{0}_{1 \times 9} \\ \mathbf{0}_{1 \times 9} & \mathbf{w}_b^T(\mathbf{u}(t);t)_{1 \times 9} & \mathbf{0}_{1 \times 9} \\ \mathbf{0}_{1 \times 9} & \mathbf{0}_{1 \times 9} & \mathbf{w}_b^T(\mathbf{u}(t);t)_{1 \times 9} \end{array} \right] \quad (2.20)$$

and by multiplying by \mathbf{C}_b'' the acceleration errors were determined in the local level frame. The vector \mathbf{w}_b^T depended on the angular velocities and angular accelerations in the body frame and was defined as:

$$\mathbf{w}_b^T(\mathbf{u}(t);t) = [\alpha_x \quad \alpha_y \quad \alpha_z \quad \omega_x^2 \quad \omega_y^2 \quad \omega_z^2 \quad \omega_x \omega_y \quad \omega_x \omega_z \quad \omega_y \omega_z] \quad (2.21)$$

The angular accelerations and angular velocities in the body frame are functions of the gimbal angles, angular velocities, and angular accelerations. These transformation functions were written as:

$$\underline{\alpha}^b = \mathbf{f}(\underline{\theta}^g, \underline{\omega}^g, \underline{\alpha}^g; t) \quad (2.22)$$

$$\underline{\omega}^b = \mathbf{A}_{g\omega}^{b\omega} \underline{\omega}^g \quad (2.23)$$

where

$\underline{\alpha}^b, \underline{\omega}^b$ = body frame angular acceleration and angular velocity vectors

$\underline{\alpha}^g, \underline{\omega}^g, \underline{\theta}^g$ = gimbal angular acceleration, angular velocity, and angle vectors

$\mathbf{A}_{g\omega}^{b\omega}$ = transformation matrix from gimbal angular velocities to body frame

angular velocities

The transformations indicated in equations (2.22) and (2.23) are derived in Appendix C. Note that the gimbal angular accelerations were the control inputs to the test table. The gimbal angular velocities were obtained by simply integrating the gimbal angular accelerations. Similarly, the gimbal angles were the integrals of the gimbal angular velocities. For this simulation, all the gimbal state vectors were ordered outer gimbal, middle gimbal, and inner gimbal. For example, the gimbal angular acceleration vector was defined as:

$$\underline{\alpha}^g = \begin{bmatrix} \alpha_o \\ \alpha_m \\ \alpha_i \end{bmatrix}$$

The dynamics matrix \mathbf{F} was then computed at a given time using equations (2.19) - (2.23). The gimbal controls, $\underline{\alpha}^g$, had to be specified as functions of time. These controls were then integrated to solve for $\underline{\omega}^g$ and $\underline{\theta}^g$ as functions of time.

2.3.3 Modeling Noise

The modeling noise vector, \mathbf{w} , accounts for modeling effects that are not contained in the filter equations. For this simulation, \mathbf{w} was assumed to be a zero mean, Gaussian white noise process in the accelerations in the local level frame. This modeling noise produced a random walk in velocity in the navigator. Therefore, \mathbf{w} was written as

$$\mathbf{w}(t) = \begin{bmatrix} \mathbf{0}_{3 \times 1} \\ \mathbf{w}_a(t)_{3 \times 1} \\ \mathbf{0}_{27 \times 1} \end{bmatrix} \quad (2.24)$$

with a covariance matrix given by

$$E[\mathbf{w}(t)\mathbf{w}(\tau)^T] = \mathbf{Q}(t)\delta(t - \tau)$$

$$\mathbf{Q}(t) = \begin{bmatrix} \mathbf{0}_{3 \times 3} & \mathbf{0}_{3 \times 3} & \mathbf{0}_{3 \times 27} \\ \mathbf{0}_{3 \times 3} & \Phi_{ww} \text{ } 3 \times 3 & \mathbf{0}_{3 \times 27} \\ \mathbf{0}_{27 \times 3} & \mathbf{0}_{27 \times 3} & \mathbf{0}_{27 \times 27} \end{bmatrix} \quad (2.25)$$

where $\mathbf{Q}(t)$ was the power spectral density matrix of \mathbf{w} and $\delta(t-\tau)$ is the Dirac delta function with units of 1/time. For small time steps, the discrete covariance matrix is given by the approximation [17,18]

$$\mathbf{Q}_k = \mathbf{Q}(t)\Delta t \quad (2.26)$$

The matrix \mathbf{Q}_k represents the increase in state uncertainties after propagating the covariance matrix forward in time by Δt . Since the process noises in acceleration included in $\mathbf{Q}(t)$ were assumed to be uncorrelated, Φ_{ww} was a diagonal matrix whose elements had units of (ft/s²)²/Hz. For the baseline simulation, the elements of Φ_{ww} were all assumed equal to 0.01 (ft/s²)²/Hz. These values resulted in a random walk in velocity with a standard deviation growth of 0.10 ft/s per $\sqrt{\text{sec}}$.

2.3.4 Measurements and the Measurement Equation

The position outputs of the INS navigator were used as measurements in the simulation. As mentioned previously, the ideal position outputs would be zero if the reference point of the INS were placed at the center of the test table. The lever arms from the center of the test table to the reference point in the INS were assumed to have been previously calibrated in the static calibration. Therefore, even if the reference point of the INS is offset from the center of the table, the position outputs should remain zero. The measurement equation was:

$$\mathbf{z}_k = \mathbf{H}\mathbf{x}_k + \mathbf{v}_k \quad (2.27)$$

where

\mathbf{z}_k = measurement vector (3x1)

\mathbf{H} = measurement geometry matrix (3x33)

\mathbf{v}_k = measurement noise vector (3x1)

Since the measurements were position in the local level frame, \mathbf{H} was simply written as:

$$\mathbf{H} = [\mathbf{I}_{3 \times 3} \mid \mathbf{0}_{3 \times 30}] \quad (2.28)$$

When the gimbal axis displacements were included the \mathbf{H} matrix had to be extended. The nominal navigator position was corrected for the gimbal axis displacements by subtracting out \mathbf{r}_{oi}^{ig} , the vector from the origin of the local level frame to the origin of the inner gimbal frame presented in equation (2.16). Before \mathbf{r}_{oi}^{ig} could be subtracted out, it had to be expressed in local level coordinates. When the state vector was augmented by adding ρ , the \mathbf{H} matrix became:

$$\mathbf{H} = [\mathbf{I}_{3 \times 3} \mid \mathbf{0}_{3 \times 30} \mid -\mathbf{C}_b^H \mathbf{A}_\rho^{r_{oi}}] \quad (2.29)$$

The gimbal axis displacement effects could have been included in the dynamics matrix and omitted from the \mathbf{H} matrix. This would account for the acceleration errors produced by the small displacements, with the navigator position error still referenced to the nominal zero position. By including the effects of the displacements in the \mathbf{H} matrix rather than the \mathbf{F} matrix, the filter avoids having to integrate the effects of the acceleration errors due to the displacements. This integration should yield a position error equivalent to the displacement of the inner gimbal origin from the outer gimbal origin. This position vector is the one subtracted out in the \mathbf{H} matrix of equation (2.29). Therefore, rather than integrating the acceleration errors due to the displacements, the equivalent error position was subtracted out from the measurements.

2.3.4.1 Measurement Noise

The measurement noise was assumed to be a white sequence with known covariance structure. It was also assumed that there was no cross correlation between the measurement noise and the modeling noise[17,18]:

$$E[\mathbf{v}_k \mathbf{v}_i^T] = \begin{cases} \mathbf{R}_k, & i = k \\ 0, & i \neq k \end{cases} \quad (2.30)$$

$$E[\mathbf{w}(t) \mathbf{v}_k^T] = 0, \quad \text{for all } t \text{ and } k$$

The diagonal elements of \mathbf{R} were the variances of the individual position measurement errors. The off diagonal terms of \mathbf{R} were assumed to be zero, indicating no cross correlation between the measurement errors. The variances of the measurement errors were assumed to be the same, and therefore, \mathbf{R} was written as:

$$\mathbf{R} = \begin{bmatrix} \sigma_v^2 & 0 & 0 \\ 0 & \sigma_v^2 & 0 \\ 0 & 0 & \sigma_v^2 \end{bmatrix} \quad (2.31)$$

The subscript was dropped on \mathbf{R} , because the measurement errors were considered to be independent of time. For this simulation, the standard deviations in the position measurement errors were assumed to be 0.01 ft.

2.3.5 Filter Propagation and Update Equations

The covariance matrix tends to grow over time when no measurements are taken. The propagation of the covariance matrix \mathbf{P} for the continuous filter case is described by the matrix Riccati equation [17,18]:

$$\dot{\mathbf{P}} = \mathbf{F}\mathbf{P} + \mathbf{P}\mathbf{F}^T + \mathbf{Q} \quad (2.32)$$

This equation can be used to determine the changes in the covariance matrix between measurement times.

When a measurement is taken, the Kalman filter incorporates it into the state estimation process in a way that minimizes the variances. The error covariance update equation for a discrete measurement is given as [17,18]:

$$\mathbf{P}_k^+ = [\mathbf{I} - \mathbf{K}_k \mathbf{H}_k] \mathbf{P}_k^- \quad (2.33)$$

where the "+" indicates immediately after the measurement and the "-" indicates just before the measurement. The matrix \mathbf{K}_k is called the Kalman gain matrix and represents

the optimal weighting of the measurement information to obtain the smallest variances. The Kalman gain matrix is given as [17,18]:

$$\mathbf{K}_k = \mathbf{P}_k^- \mathbf{H}_k^T [\mathbf{H}_k \mathbf{P}_k^- \mathbf{H}_k^T + \mathbf{R}_k]^{-1} \quad (2.34)$$

Equations (2.33) and (2.34) show how the Kalman filter weighs the measurements based on the relative accuracy of the measurements and the previous state estimates. If the measurements are poor (\mathbf{R}_k large) then \mathbf{K} will be comparatively small and the measurements will not significantly alter the previous state estimates. On the other hand, if the measurements are very accurate (\mathbf{R}_k small) then \mathbf{K} will be large, weighing the measurements more heavily.

2.3.5.1 Square Root Filter Implementation

The measurement incorporation equation (2.33) contains a matrix subtraction. For an ill-conditioned calculation, this can result in a nonpositive covariance matrix. For the simulation in this thesis, the errors were expected to be numerically very small. The standard deviation in the measurements was 0.01 ft, which resulted in a variance of 0.0001 ft². The numerically small measurement uncertainties combined with the initially coarse state estimates produced filter equations that were ill conditioned. In ill conditioned problems, the roundoff errors in the computer may cause the filter to produce incorrect results. As expected, a nonpositive covariance matrix was produced when the filter was run in this simulation using the standard Kalman filter equations. Therefore, another form of the Kalman filter equations was required to perform the covariance analysis.

Square root methods of formulation were developed to eliminate the problem of a nonpositive covariance matrix [19,20,21]. These methods use the square root of the covariance matrix in computations, assuring that the covariance matrix remains positive definite. In [21] Carlson introduced a square root method that maintained the square root of \mathbf{P} in triangular form. This resulted in computation times that were much faster than previous square root formulations. This thesis used the measurement incorporation

algorithm of Carlson's square root method to update the covariance matrix with a measurement. The propagation of the square root of the covariance matrix was performed using an algorithm due to Andrews [20]. These equations are summarized below where \mathbf{W} represents the square root of \mathbf{P} :

$$\text{Covariance Matrix Square Root: } \mathbf{P} = \mathbf{W}\mathbf{W}^T \quad (2.35)$$

$$\text{Measurement Incorporation: } \mathbf{f} = \mathbf{W}^T \mathbf{h} \quad (2.36)$$

$$\alpha = r + \mathbf{f}^T \mathbf{f} \quad (2.37)$$

$$\mathbf{W}^+ = \mathbf{W}[\mathbf{I} - \mathbf{f}\mathbf{f}^T / \alpha]^{1/2} \quad (2.38)$$

$$\text{Propagation: } \dot{\mathbf{W}} = \mathbf{F}\mathbf{W} + \frac{1}{2}\mathbf{Q}(\mathbf{W}^T)^{-1} \quad (2.39)$$

Equations (2.36) through (2.38) replaced equation (2.33) while equation (2.39) replaced equation (2.32). Note that in equations (2.36) through (2.38) the measurements are processed one at a time. This method of processing the measurements was equivalent to vector measurement processing, because the measurement noise matrix \mathbf{R}_k was diagonal. To begin the filter, the initial square root of the covariance matrix was determined using a Cholesky square root decomposition method. The filter equations and the Cholesky decomposition are presented in Appendix D in more detail.

2.3.5.2 Propagation of the Covariance Matrix

Propagation of the covariance matrix was done by numerically integrating equation (2.39). A classic fourth order Runge Kutta integrator was used for the numerical integration. The dynamics matrix \mathbf{F} varied significantly with time, because it depended on gimbal angular accelerations, angular rates, and angles. Therefore, very small step sizes were used for the integration. In most cases, twenty Runge Kutta integrations were used to propagate between every two measurements. Since the measurements were taken every 0.05 seconds, the Runge Kutta step size was 0.0025 seconds. The simulation was also run using other Runge Kutta step sizes in order to

verify that the numerical integrator was accurate. The effect of the number of Runge Kutta integrations per measurement on the filter is described in section 4.4.1.

Chapter 3

Implementation

3.1 Initial Assumptions

Some initial assumptions were made for the simulation in this thesis. The system being tested underwent no net linear accelerations on the test table, because it was subjected to angular motion only. Also, the scale factor, bias, and misalignments were assumed to be perfectly compensated from the static calibration tests. Therefore, the position errors in the navigator were assumed to be completely due to the effects of gimbal angular motion on the accelerometers. Since the INS was traversing a wide range of orientations while being tested, the compensation of the force due to gravity was also important. The gravity vector in the local level frame was assumed to be constant over all the table orientations. The gimbal angles, angular velocities, and angular accelerations were assumed known from the test table output. Therefore, the transformation between the inner gimbal frame and the local level frame was known. This allowed the navigator to compensate for the gravity vector in the accelerometer outputs. With the gravity force compensated, the errors in acceleration were due solely to angular motion of the gimbals.

3.1.1 Initial Covariance

In order to start the simulation at a realistic point, it was necessary to initialize the covariance matrix properly. Since the accelerometer error coefficients were combinations of the accelerometer parameters, the statistics of the initial coefficient errors were calculated from the statistics of the initial parameter errors. The assumed initial accelerometer parameter errors are given in Table 3.1. Note that the standard deviations for each group of parameters were assumed to be the same among all three

accelerometers. The initial position and velocity errors are also included in Table 3.1 and were based on the initial position fix of the INS navigator.

As shown in Table 2.2, the accelerometer coefficients were combinations of accelerometer parameters and products of the parameters. All the accelerometer parameter errors were assumed to be independent, zero mean, Gaussian random variables with the standard deviations given in Table 3.1. Since the parameter errors were all independent and zero mean, the coefficient errors were also zero mean. Therefore, the initial variances of the coefficients were determined by taking the expected value of the square of the coefficients:

$$\sigma_{c_y}^2 = E[c_y^2]$$

The initial coefficient variances were therefore functions of the mean square errors in the parameters. A summary of the initial standard deviations in the accelerometer error coefficients is provided in Table 3.2, where all the coefficient standard deviations are in units of inches.

Table 3.1: Initial Standard Deviations

State/Accelerometer Parameter	Standard Deviation (σ)
Position (r_{ij})	0.01 ft
Velocity (v_{ij})	0.01 ft/s
Lever Arm (R_{ij})	.25 in
Misalignment (β_{ij})	600 arcsec
Size Effect ($X_{\alpha i}, X_{\omega i}$)	.125 in

There were significant correlations among the coefficients because the same combinations of parameters appeared in more than one coefficient. Therefore, the initial covariance matrix was assumed to have a number of non-zero off-diagonal terms. These

covariances were determined by taking the expected value of the products of the coefficients. Similar to the variances, the covariances were merely functions of the mean square errors of the parameters.

Table 3.2: Initial Accelerometer Coefficient Standard Deviations (Inches)

Accelerometer Coefficient	X Accelerometer	Y Accelerometer	Z Accelerometer
c ₁	0.0011	0.250	0.250
c ₂	0.250	0.0011	0.280
c ₃	0.280	0.280	0.0011
c ₄	0.0011	0.250	0.250
c ₅	0.250	0.0011	0.250
c ₆	0.250	0.250	0.0011
c ₇	0.280	0.280	0.0011
c ₈	0.250	0.0011	0.280
c ₉	0.0011	0.250	0.250

The smaller standard deviations of .0011 inches were due to the misalignment angles of the accelerometers. The standard deviation for the misalignment angles was assumed to be 600 arc sec, or 2.90 mrad, as shown in Table 3.1. All the standard deviations of 0.0011 inches in Table 3.2 were due to products of the misalignment angle errors and either the size effect errors or the lever arm errors. This multiplication resulted in coefficient errors that were significantly smaller than those that weren't dominated by misalignment error products.

3.1.2 Test Table Setup

3.1.2.1 Type and Geometry of Table

The specifications of the test table state that the gimbal axes intersect within a sphere of a specified radius. The test table assumed for this simulation was a Contraves Model 53M-3C Three-Axis Motion Simulator. The manufacturer specification for gimbal axis intersection was a sphere of radius 0.01 inches. Acceptance testing showed that the gimbal axes actually intersected within a 0.0085 inch radius sphere [22]. Figure 2.4 is a

diagram of the test table. The middle gimbal was assumed to be initially deflected positive 90 degrees from its position in Figure 2.4. This provided an initially orthogonal set of gimbal axes. Figure C.1 in Appendix C shows that the outer, middle, and inner gimbal rotations resulted in a 3-2-1 transformation from the local level frame to the body, or inner gimbal, frame.

3.1.2.2 Table Constraints

The test table had inherent limitations in the gimbal angular accelerations and angular velocities achievable. These constraints limited the maximum angular velocities and angular accelerations experienced in the body frame. Limitations in the body angular velocities and angular accelerations resulted in limitations of the error accelerations due to angular motion. Therefore, the test table constraints dictated limits on the sensitivities of the accelerometer error coefficients defined in equation (2.11). The constraints for the Contraves 53M-3C are given in Table 3.3 [23].

Table 3.3: Test Table Constraints

Gimbal Axis	ω_{\max} (deg/sec)	α_{\max} (deg/sec ²)
Inner	± 1000	± 1600
Middle	± 750	± 400
Outer	± 750	± 10
	± 700	± 120
	± 600	± 340
	± 500	± 540

The outer gimbal had different angular velocity constraints for different angular accelerations. It was possible to combine these constraints in a single trajectory. For example, the outer gimbal could be accelerated at $+540 \text{ deg/sec}^2$ up to an angular velocity of $+500 \text{ deg/sec}$. From that point, the gimbal could be further accelerated at $+340 \text{ deg/sec}^2$ up to $+600 \text{ deg/sec}$, and so on. The angular velocity constraint used for most of

the trajectories in this thesis was the ± 600 deg/sec constraint, using a maximum angular acceleration of ± 340 deg/sec². It was felt that this combination allowed for a high maximum angular velocity, while assuring that the gimbal could reach that velocity in a relatively short amount of time. The higher acceleration of ± 540 deg/sec² possible up to 500 deg/sec was only used for trajectories that required high outer gimbal acceleration, but did not require high outer gimbal rates. The higher acceleration was not used for most of the trajectories, because it involved twice the number of commanded acceleration switches. Furthermore, the higher acceleration only saved 0.54 seconds in reaching ± 600 deg/sec. Finally, the outer gimbal acceleration did not have to be high for the trajectories that required a high outer gimbal rate, because for these trajectories the outer gimbal acceleration was not a driving factor in the sensitivities of the accelerometer coefficients.

The Contraves test table also had an input bandwidth limitation of 200 Hz [23]. This meant that the controls could be changed up to 200 times per second. Smooth gimbal angular accelerations could be achieved with this bandwidth. The 200 Hz bandwidth was more than adequate for this simulation, because the fastest changes in commanded angular accelerations were on the order of one second.

3.1.2.3 Table Accuracies

In addition to the gimbal axis displacement specification, the test table also had specifications for axes orthogonality, position accuracy, position resolution, rate stability, and rate resolution. These specifications for the Contraves table are given in Table 3.4.

For this simulation, the gimbal angular accelerations, angular rates, and angles were all assumed to be known. From Table 3.4, it can be seen that these assumptions are valid when operating the table in the precision rate mode. The position errors given in Table 3.4 were significantly less than the initial errors assumed for the simulation. Also, since the rates were near their maximums for most of the simulation, the rate resolution

Table 3.4: Test Table Performance Specifications

Performance Specification		Accuracy
Axes Orthogonality		0.01 mrad
Position Accuracy		0.005 mrad RSS
Position Resolution		0.002 mrad
Rate Stability	Precision Rate Mode	$\pm 0.001\%$ over 360 deg
	Tach Rate Mode	$\pm 0.1\%$ over 360 deg
Rate Resolution in Precision Rate Mode	to 200 deg/sec	0.0001 deg/sec
	above 200 deg/sec	0.001 deg/sec

was certainly adequate. The angular rates of the gimbals were assumed to be stable based on the high accuracy of the rate stability specification.

3.2 Initial Trajectories

Initial heuristic gimbal trajectories were determined for comparison with later trajectories. The first trajectory implemented in the simulation was the trajectory outlined in [10]. The next initial trajectories were combinations of individual gimbal trajectories that maximized the gimbal angular velocities and angular accelerations. Plots for some of the trajectories described in this chapter are included in the text. All the trajectories described in this thesis are shown graphically in Appendix A. While this chapter presents the basic trajectories used and their characteristics, the results obtained by implementing the trajectories are described in Chapter 4.

3.2.1 Previous Trajectory

The dynamic calibration segment of the trajectory described by Riegsecker in [10] involved nine distinct segments. Each of these nine segments was designed to produce a specific angular velocity or angular acceleration profile in the body frame. The INS was reoriented at the beginning of each segment, after which the outer gimbal was accelerated to a high angular rate. The INS was left spinning at the high angular rate and was

eventually decelerated to the same angular rate, but in the negative direction. Once again, the outer gimbal was left spinning, then finally accelerated to a zero angular velocity. The gimbal angular accelerations, angular velocities, and angles for this trajectory are given in Figure 3.1. These plots also appear in Figure A.1. This trajectory is referred to as "GT0" throughout this thesis.

The reorientation of the INS for each segment can be seen in the plot of the gimbal angles in Figure 3.1. Note that the plot for the gimbal angles is in radians, so the reorientations appear small compared to the deflection of the outer gimbal. The middle and inner gimbal angles were set to specific values so that a desired accelerometer error coefficient was excited by angular motion in the body frame. The middle and inner gimbal angles for each of the nine segments are given in Table 3.5.

Table 3.5: INS Orientation For GT0 Trajectory

Segment Number	Middle Gimbal Angle (deg)	Inner Gimbal Angle(deg)
1	0	-90
2	180	-90
3	180	180
4	0	0
5	90	0
6	-90	180
7	0	-45
8	90	-45
9	45	0

These test table orientations, combined with the outer gimbal angular motion developed angular accelerations and angular velocities in the body frame. These body frame angular rates and accelerations were determined using equations (2.22) and (2.23) and are shown graphically in Figure 3.2.

GT0 GIMBAL TRAJECTORY

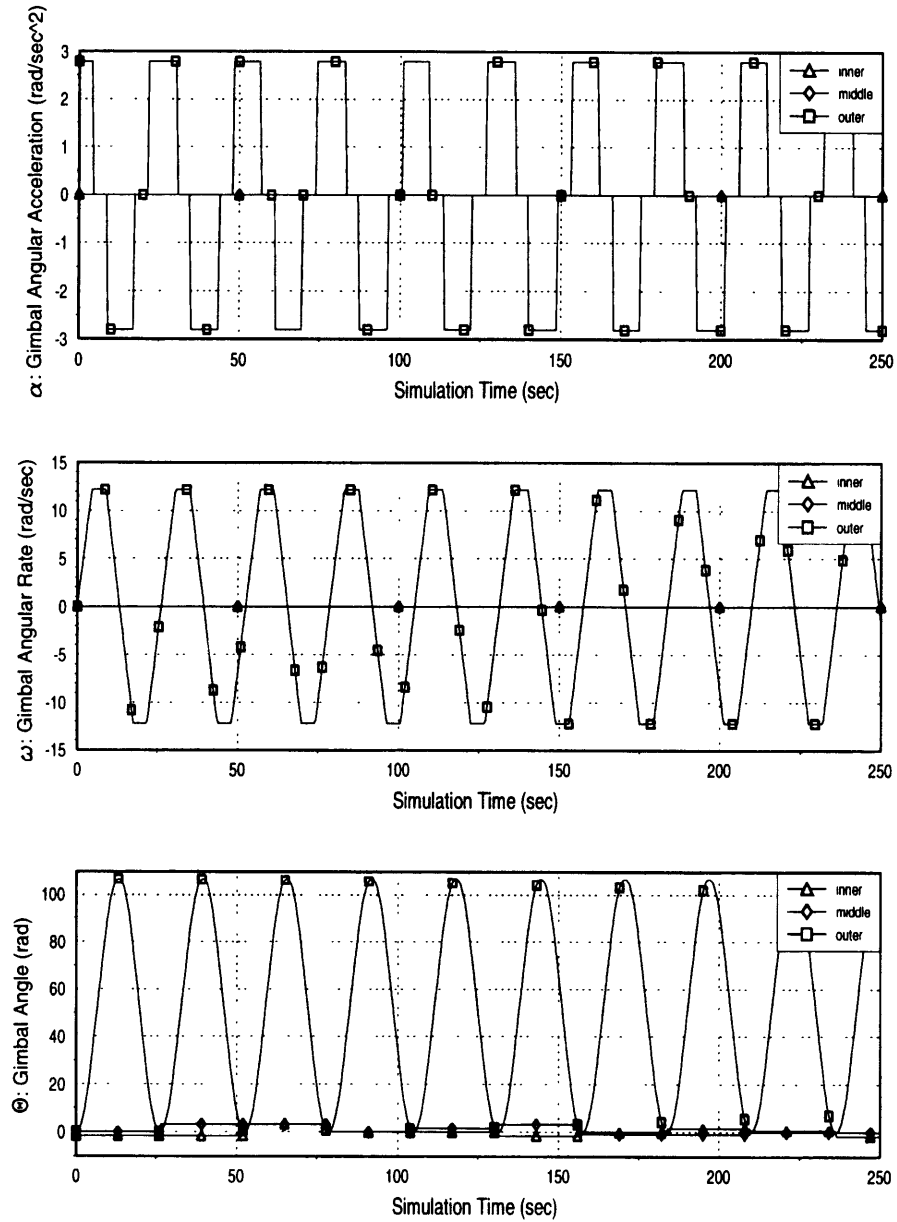


Figure 3.1: GT0 Gimbal Trajectory

GT0 BODY FRAME SENSITIVITIES

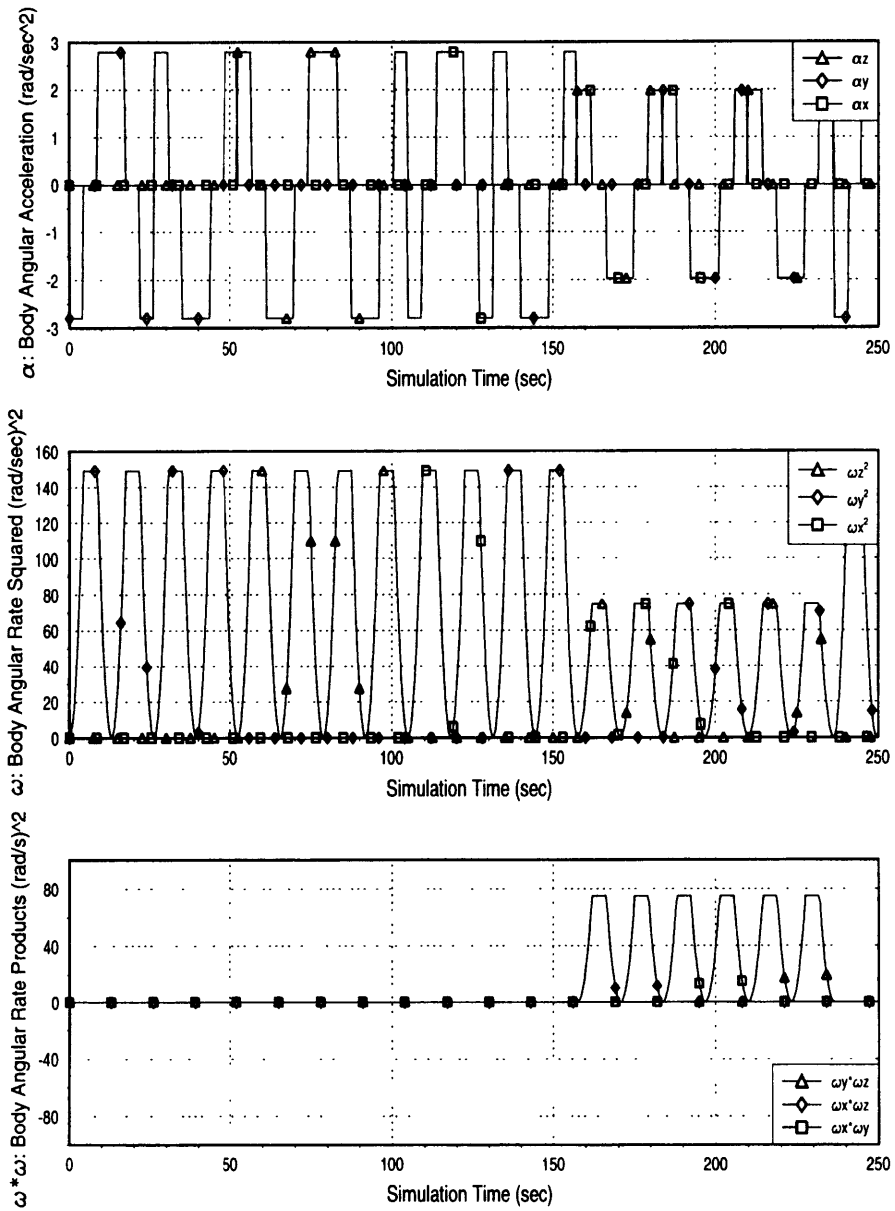


Figure 3.2: GT0 Body Frame Sensitivities

3.2.1.1 Testing Time Modifications

The time period for each segment in Figures 3.1 and 3.2 was 26.25 seconds, whereas each segment in the original trajectory described in [10] lasted for approximately 200 seconds. The segments were modified to last a total of 26.25 seconds each for comparison purposes. This reduction in testing time was done by changing two characteristics of the original testing segments. First, the two 30 second static holding periods before and after the dynamic motion were eliminated. Second, the period of time for which the outer gimbal was held at its maximum angular velocity was reduced from 60 seconds to 4.375 seconds. These changes are outlined in Table 3.6. Note that Figures 3.1 and 3.2 show the gimbal trajectory and the body frame angular dynamics up to 250 seconds. This time was chosen so that all nine of the 26.25 segments in GT0 could be displayed in each figure.

Table 3.6: Testing Time Modifications to Previous Trajectory

Segment Portion Description	Original Testing Time (sec)	Modified Testing Time (sec)
Hold INS stationary	30.000	-
Accelerate outer gimbal at +160 deg/s ² to gimbal rate of +700 deg/s	4.375	4.375
Rotate outer gimbal at +700 deg/s	60.000	4.375
Accelerate outer gimbal at -160 deg/s ² to gimbal rate of -700 deg/s	8.750	8.750
Rotate outer gimbal at -700 deg/s	60.000	4.375
Accelerate outer gimbal at +160 deg/s ² to gimbal rate of zero	4.375	4.375
Hold INS stationary	30.000	-
TOTAL SEGMENT TEST TIME	197.50	26.25

The testing time reduction was expected to reduce the errors in the accelerometer coefficients more quickly than the original GT0 trajectory. While the original trajectory

put the gimbals through each segment once, the reduced-time trajectory actually went through each segment a number of times. As shown in Figure 3.1, once the ninth segment was completed, the first segment was entered again. Each segment tended to produce a large initial decrease in the uncertainties of the specific coefficients it was designed to observe. Thereafter, the uncertainties continued to decrease, but at a much lower rate. Therefore, by shortening the trajectories, the initial drop in uncertainties was still present, but the long periods where the uncertainties slowly decreased were eliminated. The smaller decreases in uncertainties would be made when the segments were cycled through again, later in the simulation.

The GT0 trajectory used an angular acceleration of $\pm 160 \text{ deg/sec}^2$ and an angular velocity of $\pm 700 \text{ deg/sec}$ for the outer gimbal. According to the table specifications in Table 3.3, an angular velocity of $\pm 700 \text{ deg/sec}$ can only be achieved with a maximum angular acceleration of $\pm 120 \text{ deg/sec}^2$. Since the outer gimbal could actually accelerate to $\pm 700 \text{ deg/sec}$ in just over two seconds by using the multiple constraints in Table 3.3, it was assumed that $\pm 160 \text{ deg/sec}^2$ was a feasible "average" angular acceleration that remained within the table constraints.

3.2.2 Heuristic Trajectories

From equation (2.11) it can be seen that in order to maximize the observability of the accelerometer error coefficients, the angular velocities and accelerations experienced by the body must be large. High angular rates and accelerations caused the errors due to the dynamic accelerometer error coefficients to be more pronounced, and hence more sensitive to these coefficients. Therefore, it was assumed that trajectories designed for maximum sensitivity to the error coefficients involved the highest possible gimbal angular velocities and accelerations. Instead of accelerating only the outer gimbal, all gimbals were accelerated in the initial trajectories described below. By accelerating the other gimbals, the trajectory took advantage of the higher angular accelerations and angular velocities achievable with the inner and middle gimbals.

The first trajectory (GT1) was similar in form to the trajectory described in Section 3.2.1 (GT0), and is shown in Figure 3.3. The GT1 trajectory is also shown in Figure A.2. Only the first 25 seconds of GT1 were shown in Figure 3.3, because they represent the pattern of gimbal motion for the entire simulation. For the GT1 trajectory, each gimbal was subjected to a trajectory similar to the individual segments of GT0, using the individual gimbal velocity and acceleration constraints. All the gimbals were accelerated at their maximum angular accelerations to their maximum angular velocities. The amount of time it took for each gimbal to reach its maximum angular velocity by accelerating at its maximum acceleration was defined as the characteristic time for the gimbal, T :

$$\begin{aligned}
 T_o &= \frac{\omega_{o,\max}}{\alpha_{o,\max}} = \frac{600 \text{ deg / sec}}{340 \text{ deg / sec}^2} = 1.765 \text{ sec} \\
 T_m &= \frac{\omega_{m,\max}}{\alpha_{m,\max}} = \frac{750 \text{ deg / sec}}{400 \text{ deg / sec}^2} = 1.875 \text{ sec} \\
 T_i &= \frac{\omega_{i,\max}}{\alpha_{i,\max}} = \frac{1000 \text{ deg / sec}}{1600 \text{ deg / sec}^2} = 0.625 \text{ sec}
 \end{aligned} \tag{3.1}$$

Each gimbal was then left spinning at its maximum angular velocity for its characteristic time period. Next, the gimbals were decelerated to their maximum angular velocities in the negative direction, allowed to spin for their characteristic time periods, and finally accelerated to zero velocity. This sequence of accelerations and decelerations was repeated continuously for each gimbal.

The different characteristic time periods for the three gimbals resulted in a trajectory that covered many combinations of gimbal rates and accelerations. These varied combinations resulted in excitation of all the accelerometer error coefficients, by producing large body angular velocities and angular accelerations. These body frame

GT1 GIMBAL TRAJECTORY

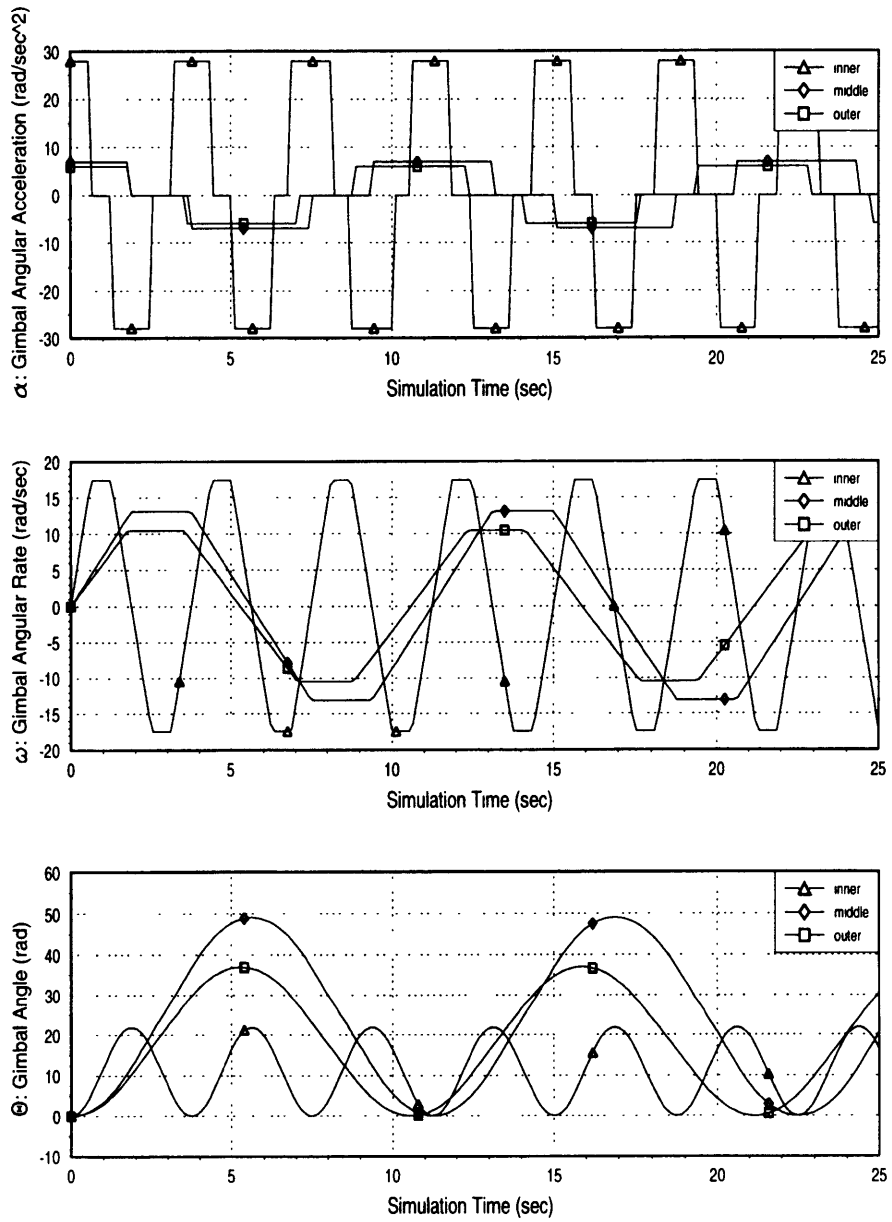


Figure 3.3: GT1 Gimbal Trajectory

angular accelerations and angular velocities were determined as before from equations (2.22) and (2.23) and are shown graphically in Figure 3.4. Only the first 4 seconds of simulation time were plotted, because they are representative of the body angular rates and accelerations over the entire simulation. Note that although the time scale for these plots only goes to 4 seconds, the body angular rates and accelerations change repeatedly in that time span. This high frequency oscillation was a result of the gimbal angles changing very rapidly, forcing the transformation from the gimbal angular accelerations and rates to body angular accelerations and rates to also shift rapidly.

In general, the maximum acceleration error sensitivities to the accelerometer coefficients occurred when the gimbal rates were at their maximum magnitudes. This can be seen in the interval between 2.0 and 3.6 seconds in Figure 3.4. In this interval, the body frame angular accelerations approached 350 rad/sec^2 , the squares of the angular velocities reached near 800 (rad/sec)^2 , and the products of the angular velocities were near 400 (rad/sec)^2 . From the gimbal trajectory plots in Figure 3.3, it is seen that the gimbals are all near their maximum angular velocities for this same interval.

Although the GT1 trajectory held the gimbals at their maximum angular rates, it only held the inner gimbal for 0.625 seconds before accelerating or decelerating back to zero. For the second heuristic trajectory (GT2), the inner gimbal was left spinning at its maximum rate for 1.250 seconds (twice its characteristic time period, T_i). This was done so the effects of the inner gimbal rate could be observed. The middle and outer gimbals were accelerated and decelerated just as in GT1. The GT2 trajectory is shown in Figure A.3.

The final initial trajectory (GT3) did not leave the gimbals spinning at their maximum rates. All the gimbals were simply accelerated to their maximum angular velocities, then immediately decelerated to their maximum negative velocities, and so on. This trajectory was used to see what the effects were of pure angular acceleration on the

GT1 BODY FRAME SENSITIVITIES

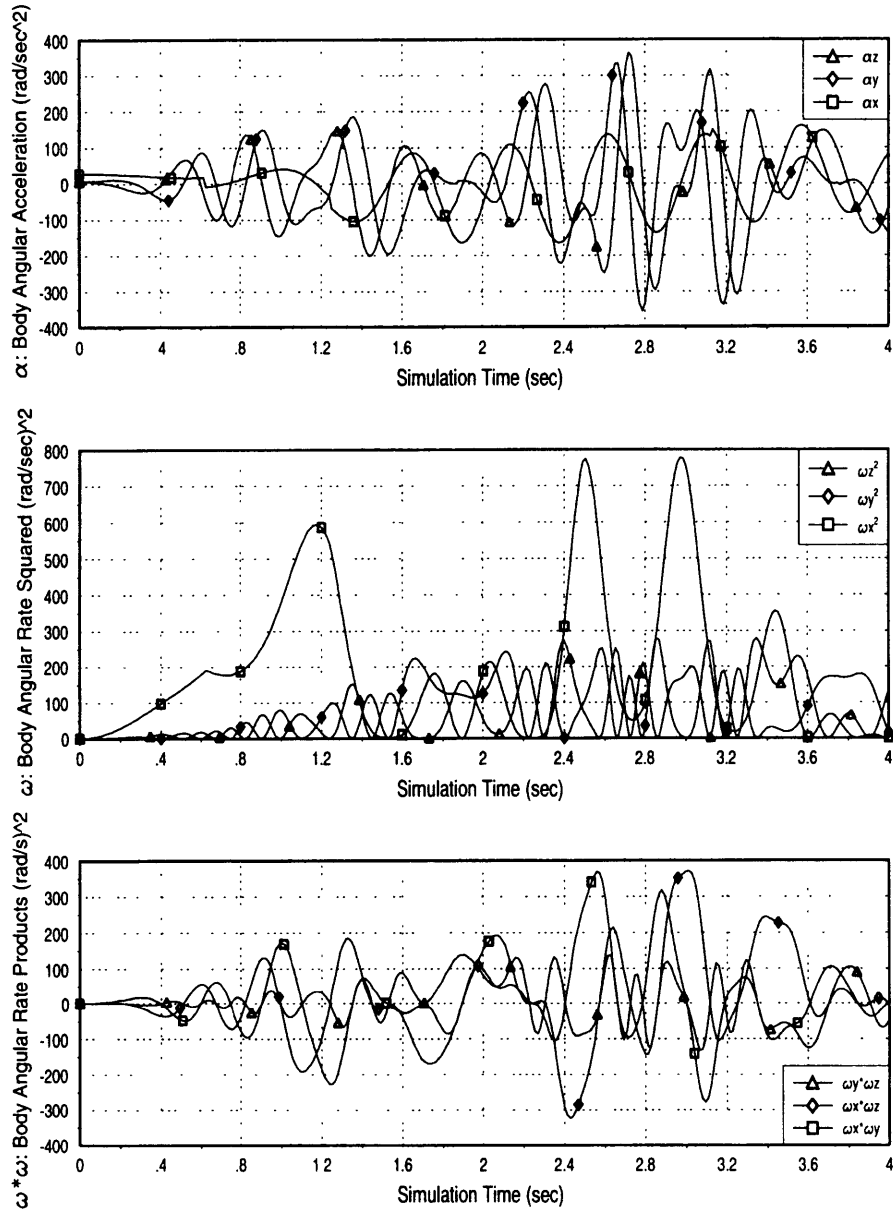


Figure 3.4: Representative GT1 Body Frame Sensitivities

gimbals and to use as a comparison for the other initial trajectories. The GT3 trajectory is shown in Figure A.4.

3.3 Improved Trajectories

3.3.1 Objective of Improved Trajectories

The goal of the simulation was to estimate the accelerometer error coefficients as accurately as possible for a given amount of testing time. Another way of stating this goal was to minimize a cost function based on the errors in the accelerometer error coefficients. One possible cost function was written as:

$$J = \text{trace}(\mathbf{P}_c) \quad (3.2)$$

where \mathbf{P}_c is the portion of the covariance matrix that contains the errors in the accelerometer error coefficients. Since the diagonal elements of \mathbf{P}_c were the variances of the accelerometer error coefficients, minimizing the cost function of equation (3.2) was equivalent to minimizing the sum of all the accelerometer coefficient variances. The minimization of the cost function was to be performed over all possible trajectories. The gimbal trajectories were also required to satisfy the table constraints where the constraints in this case were given by:

$$\begin{aligned} |\alpha| &\leq \alpha_{\max} \\ |\omega| &\leq \omega_{\max} \end{aligned} \quad (3.3)$$

The gimbal angular velocities and gimbal angles were integral functions determined from the commanded gimbal accelerations:

$$\begin{aligned} \omega(t) &= \int_0^t \alpha(t) dt \\ \theta(t) &= \int_0^t \omega(t) dt \end{aligned} \quad (3.4)$$

The inequality constraints given in equation (3.3) had to be satisfied for each gimbal at all times throughout the simulation.

Ideally, a gimbal trajectory could be found that would minimize the cost function over all control histories while satisfying all the constraints. However, optimizing the cost function of equation (3.2) over all possible trajectories was a highly nonlinear problem. The change in the covariance matrix over time was governed by equation (2.32), or equation (2.39) for the square root filter case. Both of these equations show that the dynamics matrix F and the process noise matrix Q determine how much P changes over time. The process noise matrix was independent of the controls, while the dynamics matrix was a nonlinear function of the controls. The transformation matrices and the vector w_b^T were all nonlinear functions of either the commanded gimbal angular accelerations, or the gimbal angular velocities and gimbal angles resulting from the integrations in equation (3.4). Therefore, in order to reduce the cost function, small changes were made in the gimbal trajectories. These small changes in the initial trajectories were the basis for the improved trajectories described in this section. It was assumed that the initial heuristic trajectories described in the previous section resulted in cost functions that were reasonably close to the minimum, since all the initial trajectories involved maximum gimbal angular rates and accelerations.

3.3.2 Effects of Small Changes in Characteristics of Trajectory

3.3.2.1 Time at Maximum Rate

The first way in which the trajectories were modified was by varying the amount of time that the gimbals were held at their maximum angular velocities. As mentioned in Section 3.2.2, this was the only difference among the initial trajectories, with the exception of GT0. The tradeoff involved with these trajectory perturbations was how the gimbal angular accelerations differed from the gimbal angular velocities in affecting the uncertainties. There was assumed to be a point at which decelerating some of the gimbals, rather than leaving them at their maximum angular velocities, would result in a more significant decrease in the uncertainties .

The GT3 trajectory represented one end of the spectrum, where the gimbals were always either being accelerated or decelerated at their maximum positive or negative angular accelerations. The GT1 trajectory held the gimbals at their maximum rates for their characteristic time periods, amounts of time that depended on the constraints of each of the gimbals and given in equation (3.1). This meant that the inner gimbal was accelerating or decelerating about three times as often as the middle and outer gimbals. GT2 increased the time at maximum rate for the inner gimbal to twice its characteristic time. The GT4 trajectory was similar to the GT2 trajectory, except the middle and outer gimbals were also held at their maximum rates for twice their characteristic time periods. The GT4 trajectory is shown in Figure A.5.

The GT5 trajectory was designed to represent the other end of the spectrum from GT3. In GT5 all the gimbals were accelerated to their maximum angular velocities and left there for the entire simulation. Therefore, the gimbal angular accelerations only affected the sensitivities in the first two seconds of the simulation. Thereafter, the sensitivities were driven by the gimbal rates and angles. The GT5 trajectory is given in Figure A.6.

3.3.2.2 *Initial Angles*

Another perturbation made to the initial trajectories was a change in the initial gimbal angles. These initial gimbal angles produced corresponding changes in the body frame angular dynamics, because the transformations between the gimbal motion and the body frame dynamics were altered. These effects were expected to be small over an extended period of time, because although the body frame dynamics were altered, they had basically the same characteristics.

The initial outer gimbal angle was not varied, because the body frame angular dynamics were unaffected by the outer gimbal angle. This can be seen from equations (2.22) and (2.23), which have no dependence on θ_o . Therefore, the INS would experience the same angular motions, regardless of what the initial outer gimbal angle

was. Hence, the only initial angle perturbations were of the inner and middle gimbal angles.

3.3.3 Maximizing Body Frame Angular Rates and Angular Accelerations

In order to better observe the navigation errors due to the accelerometer error coefficients, the angular velocities and angular accelerations in the body frame were increased. Equation (2.11) shows that increasing these angular rates and accelerations in the body frame results in larger errors in acceleration, and therefore larger position errors in the navigator.

Although maximizing the sensitivities of the accelerometer error coefficients was a priority, the loss of observability among the coefficients also had to be considered. Those trajectories that were able to force the body frame angular rates and accelerations to their maximums, and thus drive the accelerometer coefficient sensitivities higher, used combinations of high gimbal rates and accelerations. By using these combinations of gimbal motion, all the coefficients were excited with similar oscillatory characteristics. This made it more difficult for the filter to separate the effects of one coefficient from another. This tradeoff between maximizing the coefficient sensitivities and loss of observability had to be addressed in each of the trajectories described below. For most cases, two trajectories were developed. One provided for maximum sensitivities, while the other provided maximum observability at the cost of a significantly reduced sensitivity.

The equations relating the gimbal angular accelerations and angular velocities to the body frame angular accelerations and velocities are equations (2.22) and (2.23), respectively. Expressions for the sensitivities of the accelerometer error coefficients to the gimbal angle accelerations and rates were obtained from these two equations. These sensitivities were then examined in order to determine what gimbal trajectory would provide an increased sensitivity for each group of coefficients. The trajectories developed to increase the accelerometer coefficient sensitivities were called extended trajectories and

were named GTX1 through GTX9, based on which coefficient sensitivity they were designed to "maximize". For example, GTX1 was designed to increase the sensitivity of the first coefficient of each accelerometer. The sensitivities of the first coefficients were the same for all the accelerometers and are shown in equation (2.11) to be α_x , the angular acceleration along the body frame X-axis. Therefore, the goal of GTX1 was to develop large angular accelerations about the body frame X-axis.

Secondary extended trajectories were also developed to maximize the observability, rather than the sensitivity, of specific coefficients. These trajectories were similarly named GTX1b, GTX2b, and so on. The criteria used for maximum observability was that the trajectory produced a minimum number of non-zero sensitivities. For example, the GTX1b trajectory was designed to produce large accelerations along the body frame X-axis. Of course, accelerations along this axis resulted in angular velocities along the same axis, so the coefficient whose sensitivity depended on ω_x (C14) was also excited. However, the GTX1b trajectory assured that no other coefficients beside C11 and C14 were excited.

All the extended trajectories were designed to begin and end with all the gimbal rates and gimbal accelerations set to zero. However, they were able to begin at any set of initial angles. This was done so that the extended trajectories could be combined together in sequence or added to an already existing trajectory.

3.3.3.1 Sensitivities to Body Angular Accelerations

The sensitivity term for the first coefficient of each of the accelerometers was the angular acceleration along the body frame's X direction, α_x . The expression for α_x , obtained from equation (2.22), was:

$$\alpha_x = -\omega_o \omega_m c \theta_m - \alpha_o s \theta_m + \alpha_t \quad (3.5)$$

Maximizing this function of the gimbals angles, gimbals rates, and gimbals accelerations over all trajectories proved to be difficult, because both the gimbals rates and accelerations had inequality constraints imposed on them. Therefore, a trajectory that provided a comparatively large sensitivity was determined by examining equation (3.5) and making appropriate choices for the gimbals accelerations and rates. These gimbals accelerations and rates then determined the gimbals velocities and gimbals angles through the integrations of (3.4).

The products of the gimbals angular velocities are the dominant terms in equation (3.5). If these angular velocities are set to their maximums, then the gimbals angles will be changing rapidly and α_x will oscillate at a high frequency with a magnitude of $\omega_o\omega_m$. It can also be seen from the last term of equation (3.5) that α_x depends directly on the inner gimbals angular acceleration. Since the maximum angular acceleration for the inner gimbals was large, the inner gimbals could be accelerated back and forth between its maximum and minimum rates to increase α_x . Also, the additive effect of the inner gimbals angular acceleration was not affected by the orientation of the INS, whereas the products of the gimbals rates oscillated between their positive and negative maximums.

The gimbals trajectory that are used to produce a large α_x sensitivity consisted of setting the outer and middle gimbals to their maximum angular velocities. Since α_i affected the α_x sensitivity whereas ω_i did not, the inner gimbals was commanded to follow the same trajectory it had in GT3. This meant that the inner gimbals was accelerated and decelerated at its maximum angular acceleration, but it was not left spinning at its maximum angular rate, because α_x was unaffected by ω_i . This trajectory, called GTX1, is shown in Figure A.7 in Appendix A. Note that the first coefficient sensitivity α_x oscillated back and forth between values that were close to the maximums obtained in the GT1 trajectory. This implied that the GTX1 trajectory did manage to force α_x to near its maximum since the GT1 trajectory covered almost all possible gimbals configurations and was assumed to reach the maximum sensitivities at some point in the trajectory.

Although the trajectory GTX1 described above forced α_x to high values, similar oscillations were produced in the sensitivities of all the other coefficients. This resulted in a loss of observability among the coefficients. Therefore, another trajectory was designed to maximize the observability of the first coefficient. The goal of this trajectory, called GTX1b, was to produce the highest α_x while minimizing any other coefficient sensitivities. This trajectory involved setting the middle gimbal angle to -90 degrees, which aligned the outer and inner gimbal axes. The inner gimbal was then commanded to follow the GT3 trajectory, where it was accelerated and decelerated without any time spent at its maximum rate. The outer gimbal was also accelerated and decelerated at its highest maximum acceleration of 540 deg/sec² along with the inner gimbal, switching from acceleration to deceleration when the inner gimbal switched. The highest maximum angular acceleration was used to provide the largest α_x sensitivity. Since this acceleration acted for only $T_1=0.625$ seconds, the outer gimbal rate reached 337.5 deg/sec, which was well below 500 deg/sec, the angular rate constraint at an acceleration of 540 deg/sec². The GTX1b trajectory is shown in Figure A.8. Although only the α_x and ω_x^2 sensitivities were produced, the maximum α_x went from on the order of 130 rad/sec² to only 37 rad/sec².

The sensitivity terms for the second and third error coefficients of the accelerometers were the angular accelerations along the body Y-axis and Z-axis (α_y and α_z), respectively. The expressions for these terms were obtained from equation (2.22) and were given as:

$$\alpha_y = \omega_o \omega_i c \theta_i c \theta_m - \omega_o \omega_m s \theta_i s \theta_m - \omega_m \omega_i s \theta_i + \alpha_o s \theta_i c \theta_m + \alpha_m c \theta_i \quad (3.6)$$

$$\alpha_z = -\omega_o \omega_i s \theta_i c \theta_m - \omega_o \omega_m c \theta_i s \theta_m - \omega_m \omega_i c \theta_i + \alpha_o c \theta_i c \theta_m - \alpha_m s \theta_i \quad (3.7)$$

As with α_x , these body angular accelerations are dominated by the products of the gimbal angular velocities. However, the gimbal angular accelerations do not enter these

equations in a purely additive manner as the inner gimbal angular acceleration entered equation (3.5). Therefore, the trajectory used to increase these sensitivities set all the gimbals to their maximum rates for the entire trajectory. This trajectory was called GTX2 and is shown in Figure A.9.

Although the GTX2 trajectory produced large sensitivities for α_y and α_z , it also produced large sensitivities to all the other coefficients. This trajectory excited all the coefficients by producing large angular accelerations and rates in the body frame. This led to a loss of observability among the coefficients, because the body angular rates and angular accelerations were subjected to similar oscillations. The maximizing effects of this trajectory on the sensitivities had to be weighed against the loss of observability among the coefficients. The GT5 trajectory described in Section 3.3.2 was actually a GTX2 trajectory that was never brought back to zero gimbal rates. GT5 was used to investigate how the loss of observability affected the cost function over time.

The GTX2b trajectory was designed to produce the maximum sensitivity to the second accelerometer coefficient while keeping all the other sensitivities to a minimum. This trajectory was similar to the GTX1b trajectory, where the INS was oriented such that the applied gimbal angle accelerations produced a body frame angular acceleration along only the body frame X-axis. In this case, the INS was reoriented with the inner and middle gimbal angles set to 90 degrees and zero, respectively. Angular accelerations and decelerations were then applied to the outer gimbal axis, resulting in corresponding accelerations along the body Y-axis. The highest maximum angular acceleration of 540 rad/sec² was used, because the sensitivity was a function of the outer gimbal acceleration and not the outer gimbal rate. This angular acceleration could only be applied for 0.926 seconds, because the outer gimbal rate constraint using the 540 rad/sec² acceleration was 500 rad/sec. The GTX2b trajectory is shown in Figure A.10. While only the α_y and ω_y^2 sensitivities were produced, the magnitude of the maximum α_y dropped from just over 300 rad/sec² to only 9.4 rad/sec².

The third extended trajectory, GTX3, was designed merely for comparative purposes to the first two extended trajectories. GTX3 was similar to GTX1, except the outer gimbal was subjected to accelerations and decelerations while the inner gimbal was left at its maximum angular rate. This was done to observe the effects of the outer gimbal accelerations. The GTX3 trajectory is plotted in Figure A.11.

The GTX3b trajectory was developed in the same way as GTX1b and GTX2b. The INS was oriented and gimbal angular accelerations were applied to isolate α_z . The inner and middle gimbal angles were set to zero so that the outer gimbal could be used to apply the acceleration. Once again, the outer gimbal acceleration of 540 deg/sec^2 was used to provide the highest sensitivity. The GTX3b trajectory is shown in Figure A.12. The effects on the sensitivities was similar to the effects of GTX1b and GTX2b. Only the α_z and ω_z^2 sensitivities were non-zero, but the magnitude of α_z decreased from 350 rad/sec^2 to 9.4 rad/sec^2 .

All the body angular acceleration sensitivities were expressions involving gimbal angles, rates, and accelerations that were difficult to maximize due to the inequality constraints on all the gimbals. By setting the gimbals to their maximum rates, these sensitivities oscillated between values that were close to their maximums. However, since the gimbals produced a highly dynamic environment for the INS, all the other error coefficients were excited as well. These large gimbal dynamics reduced the observability of the individual coefficients, yet also provided information on all of them rather than just one or two. The tradeoff between observability and maximizing the sensitivities was investigated by observing the effects of the two separate trajectories for each sensitivity on the cost function of equation (3.2).

3.3.3.2 Sensitivities to Squares of Body Angular Velocities

The sensitivity of the fourth coefficient for each accelerometer was the square of the angular velocity along the body X-axis, ω_x^2 . The expression for ω_x , from equation (2.23) was:

$$\omega_x = -\omega_o \sin \theta_m + \omega_i \quad (3.8)$$

The magnitude of this term was easily maximized by setting the middle gimbal angle to -90 degrees and setting the outer and inner gimbals to their maximum rates. This trajectory (GTX4) developed an ω_x^2 of 1600^2 (deg/s)² or 780 (rad/sec)². This was equivalent to the maximum ω_x^2 produced by GT1, as shown in Figure 3.4. The plot for the GTX4 gimbal trajectory is given in Figure A.13.

The sensitivities of the fifth and sixth coefficients for each accelerometer were the squares of the body frame angular velocities along the Y and Z axes, respectively. These body frame angular velocities, computed from equation (2.23), were:

$$\omega_y = \omega_o \sin \theta_i \cos \theta_m + \omega_m \cos \theta_i \quad (3.9)$$

$$\omega_z = \omega_o \cos \theta_i \cos \theta_m - \omega_m \sin \theta_i \quad (3.10)$$

These equations show that to maximize ω_y and ω_z , the outer and middle gimbals will probably have to be set to their maximum angular rates. For both equation (3.9) and (3.10) a time history for θ_i as a function of θ_m was determined such that the two terms in each equation were additive, producing the largest possible angular velocity in the body frame. Unfortunately, the gimbal angular acceleration required to implement either time history was proportional to the square of the maximum middle gimbal angular velocity. This required an inner gimbal angular acceleration that was well outside the inner gimbal constraint of 1600 deg/sec².

As shown in Figure 3.4, the maximum squares of the Y and Z body frame angular velocities produced by GT1 were near 225 (rad/sec)², corresponding to a maximum body frame angular velocity of 15 rad/sec. This was close to the middle gimbal maximum rate of 750 deg/sec or 13.1 rad/sec. Therefore, to develop large squares of the Y and Z body angular velocities, the middle gimbal was set to its maximum

rate and the inner gimbal angle was set to align either the Y or Z body axis with the middle gimbal axis. The outer gimbal angle did not affect the sensitivity and was therefore left unchanged. The GTX5 trajectory used an inner gimbal angle of zero so that an angular velocity along the body Y-axis was developed. The GTX6 trajectory used an inner gimbal angle of -90 degrees so that the angular velocity was along the body Z-axis. The GTX5 and GTX6 trajectories are plotted in Figures A.14 and A.15, respectively.

3.3.3.3 Sensitivities to Products of Body Angular Velocities

The last three coefficients for each accelerometer were sensitive to products of the body frame angular velocities. These products were obtained using equations (3.8)-(3.10). Multiplying these equations and performing some simplification led to the following expressions for the body angular velocity products:

$$\omega_x \omega_y = \omega_o \sin \theta_i (\omega_i \sin \theta_m - \frac{1}{2} \omega_o \sin 2\theta_m) + \omega_m \cos \theta_i (\omega_i - \omega_o \sin \theta_m) \quad (3.11)$$

$$\omega_x \omega_z = \omega_m \sin \theta_i (\omega_o \sin \theta_m - \omega_i) + \omega_o \cos \theta_i (\omega_i \cos \theta_m - \frac{1}{2} \omega_o \sin 2\theta_m) \quad (3.12)$$

$$\omega_y \omega_z = \frac{1}{2} \sin 2\theta_i (\omega_o^2 \cos^2 \theta_m - \omega_m^2) + \omega_o \omega_m \cos 2\theta_i \cos \theta_m \quad (3.13)$$

Once again, maximizing these equations was difficult due to the inequality constraints. The products of the body frame angular velocities were similar to the body frame angular accelerations in that the products of the gimbal rates were the driving terms. These gimbal rate products were modulated by the gimbal angles, again producing high frequency oscillations in the body frame angular velocity products. Each equation (3.11) through (3.13) was examined individually to find a trajectory that would produce large body angular rate products.

The trajectory that produced maximum values for all three equations involved setting all the gimbals to their maximum rates. This was the same as the trajectory called GTX2 described above. As mentioned above, this trajectory led to poor observability

among the coefficients. Therefore, three trajectories that had better observability characteristics were developed.

The GTX7 trajectory was designed to excite the seventh coefficient, whose sensitivity was the body frame angular velocity product $\omega_x\omega_y$. In order to reduce the other coefficient sensitivities, one of the gimbal rates was set to zero. Since the inner gimbal had the highest possible rate, and thus contributed the most to the magnitude of $\omega_x\omega_y$, it was kept at its maximum rate. For the same reason, it was assumed that a larger sensitivity would be developed if the middle gimbal was left at its maximum rate and the outer gimbal rate was set to zero rather than the other way around. Equation (3.11) shows that when the outer gimbal rate is set to zero, the sensitivity oscillates between the product of the inner and middle gimbal rates. On the other hand, when the middle gimbal rate was set to zero and the outer gimbal rate was set to its maximum, the sensitivity became:

$$\omega_x\omega_y = \omega_o \sin \theta_i (\omega_i \sin \theta_m - \frac{1}{2} \omega_o \sin 2\theta_m) \quad (3.14)$$

An optimum middle gimbal angle was chosen to maximize equation (3.14), which led to an oscillation in $\omega_x\omega_y$. However, this oscillation was smaller in magnitude than the oscillation obtained from setting the middle gimbal to its maximum rate and the outer gimbal rate to zero. Therefore, GTX7 was the trajectory obtained by setting the middle and inner gimbal rates to their maximums and the outer gimbal rate to zero. This trajectory was plotted in Figure A.16.

The GTX7 trajectory was designed to exhibit somewhat better observability than the GTX2 trajectory, because it produced a zero sensitivity for the first coefficient (α_x was zero) and the resulting ω_x^2 sensitivity was constant over nearly the entire trajectory. The maximum magnitude of the $\omega_x\omega_y$ sensitivity was reduced from above 300 (rad/sec)² to about 230 (rad/sec)². Even though GTX7 had better observability of the seventh

coefficient effects, other coefficients were still being excited in similar oscillations. Therefore, a secondary trajectory was developed, GTX7b, that produced the highest observability of the seventh coefficients.

To produce the highest observability by isolating the $\omega_x\omega_y$ sensitivity, the outer gimbal was set to its maximum rate while the inner and middle gimbal angles were set to +90 and -45 degrees, respectively. This provided equal components of angular velocity along both the body X and Y axes. The resulting $\omega_x\omega_y$ sensitivity was constant at $\frac{1}{2}\omega_o^2$ or 55 (rad/sec)². The GTX7b trajectory is shown in Figure A.17.

The extended trajectories GTX8 and GTX9 followed the same development as GTX7. In the case of GTX8, the objective was to maximize the $\omega_x\omega_z$ sensitivity, while maintaining better observability than GTX2. Following the procedure that was used to find GTX7, it was determined that the best trajectory for the eighth coefficient sensitivity resulted when the inner and middle gimbal rates were set to their maximums and the outer gimbal rate was set to zero. Therefore, GTX7 and GTX8 were identical trajectories. This demonstrates that although the observability was better than GTX2 and the sensitivities were still rather high, there was some room for improvement in the observability of both the seventh and the eighth coefficients.

The secondary trajectory GTX8b was designed to produce the best observability of the $\omega_x\omega_z$ sensitivity. This was done by keeping the outer gimbal at its maximum rate and setting the middle gimbal angle to -45 degrees. This trajectory was similar to GTX7b, except equal angular velocities were produced along the body X and Z axes rather than the X and Y axes. This produced a sensitivity of 55 (rad/sec)², the same sensitivity magnitude as GTX7b. The plot of the GTX8b trajectory is shown in Figure A.18.

Equation (3.13) shows that the ninth coefficient sensitivity, $\omega_y\omega_z$, did not depend on the inner gimbal rate. As a result, when the middle gimbal rate was set to zero and the outer gimbal rate was set to its maximum, the resulting maximum sensitivity was $\frac{1}{2}\omega_o^2$.

When the outer gimbal rate was set to zero and the middle gimbal rate was set to its maximum rate, the resulting maximum sensitivity was $\frac{1}{2}\omega_m^2$. The second set of conditions was used for GTX9, because the maximum middle gimbal rate was larger than the maximum outer gimbal rate. To provide the maximum sensitivity, the inner gimbal angle was set to +45 degrees, which produced an $\omega_y\omega_z$ of $-\frac{1}{2}\omega_m^2$ or -86 (rad/sec)². The GTX9 trajectory is shown in Figure A.19. The GTX9 trajectory only excited the ω_y , ω_z , and $\omega_y\omega_z$ sensitivities. Hence, this trajectory generated the best observability for the ninth coefficient and a secondary trajectory was not necessary.

The gimbal characteristics for each of the extended trajectories are summarized in Table 3.7. Note that a "***" entry indicates the specific quantity varied and could be computed by integrating either the angular acceleration or the angular velocity. A "-" entry in the outer gimbal angle column indicates that this gimbal angle was not specified by the particular trajectory, and that it could take on any value. The outer gimbal angle was not important for any of the trajectories, because it did not affect the body angular rates or accelerations.

3.3.4 Use of Extended Trajectories

The extended trajectories described in the previous section were developed in order to produce better estimates of specific accelerometer error coefficients. GTX1 and GTX1b were designed to reduce the errors in the first coefficient for each accelerometer, GTX2 and GTX2b were designed to reduce the errors in the second coefficient for each accelerometer, and so on. These extended trajectories were used in two ways.

One way to utilize the extended trajectories was to piece them together sequentially. Each of the extended trajectory segments could be run for a specified amount of time, resulting in a reduction in a specific coefficient error. By piecing all nine extended trajectories together, the errors in all the accelerometer coefficients could be

Table 3.7: Extended Trajectory Gimbal Accelerations, Velocities, and Angles

Extended Trajectory Name	Angular Acceleration (deg/sec ²)			Angular Velocity (deg/sec)			Gimbal Angle (deg)		
	α_o	α_m	α_j	ω_o	ω_m	ω_j	θ_o	θ_m	θ_j
GTX1	0	0	± 1600	600	750	**	**	**	**
GTX1b	± 540	0	± 1600	**	0	**	**	-90	**
GTX2	0	0	0	600	750	1000	**	**	**
GTX2b	± 540	0	0	**	0	0	**	0	+90
GTX3	± 340	0	0	**	750	1000	**	**	**
GTX3b	± 540	0	0	**	0	0	**	0	0
GTX4	0	0	0	600	0	1000	**	-90	**
GTX5	0	0	0	0	750	0	-	**	0
GTX6	0	0	0	0	750	0	-	**	-90
GTX7	0	0	0	0	750	1000	-	**	**
GTX7b	0	0	0	600	0	0	**	-45	+90
GTX8	0	0	0	0	750	1000	-	**	**
GTX8b	0	0	0	600	0	0	**	-45	0
GTX9	0	0	0	0	750	0	-	**	+45

reduced, one at a time. This was the approach used in GT0. However, the extended trajectories described in the previous section produced larger sensitivities than the segments in GT0. The trajectory that pieced together all the extended trajectories GTX1 through GTX9 was GT6. For GT6, the time for each segment was set to 10 seconds. The GT6 trajectory continued to cycle through the nine extended trajectories for the entire simulation. Therefore, after the GTX9 segment was finished, it began again at GTX1. The GT6 gimbal trajectory is given in Figure A.20, and is seen to be merely a sequential combination of extended trajectories GTX1 through GTX9. The resulting body sensitivities, shown in Figures B.1 through B.3, were also a sequential combination of the sensitivities derived from the individual extended trajectories.

Figures B.1 through B.3 show that sensitivities were excited with similar oscillatory characteristics for some of the segments of the GT6 trajectory. The secondary trajectories (GTX1b, GTX2b, etc.) were designed to eliminate the problem of exciting multiple coefficients in the same way. The GT6b trajectory was similar to the GT6 trajectory, except it used the secondary extended trajectories. This trajectory was plotted in Figure A.21, and the body frame sensitivities are shown in Figure B.4. Note that some of the sensitivities are the same as those for the GT6 trajectory. This was because some of the segments in the GT6b trajectory were identical to those of the GT6 trajectory.

A third trajectory, called GT6c, was also developed and is shown in Figure A.22. This trajectory was the same as GT6b, except the order of the extended trajectory segments was changed. Since specific segments of GT6b require specific gimbal angles, the test table had to be reoriented between each segment. This reorientation was modeled in the simulation by accelerating and decelerating the required gimbals for two seconds in order to bring the gimbals to the desired positions. Table 3.7 shows that the GTX1b and the GTX4 segments both require a middle gimbal angle of -90 degrees. Therefore, these two segments were placed adjacent to each other. This meant that the table did not have to reorient between these two segments. Similarly, the GTX3b and the GTX5 segments both require an inner gimbal angle of zero. Since the GTX3b segment also requires a middle gimbal angle of zero, the GTX5 segment was placed directly after the GTX3b segment. These were the only two differences between the GT6b and the GT6c trajectories. The difference in segment orders is shown in Table 3.8.

Another way of using the extended trajectories was to append them to an already existing trajectory. If a trajectory significantly reduced the cost function in a short period of time, but then didn't improve it much further, it was assumed to be a perfect candidate for appending an extended trajectory. The initial trajectory could be run out to where the cost function ceased to be improving. Then, the individual accelerometer coefficient

Table 3.8: Segment Orders for GT6b and GT6c

Segment Order	GT6b	GT6c
	GTX1b	GTX1b
	GTX2b	GTX4
	GTX3b	GTX2b
	GTX4	GTX3b
	GTX5	GTX5
	GTX6	GTX6
	GTX7b	GTX7b
	GTX8b	GTX8b
	GTX9	GTX9

errors could be examined to determine which of them was known with the least amount of accuracy. An extended trajectory could then be applied that was designed to reduce the errors in that specific accelerometer coefficient. If there wasn't one specific coefficient error that was the worst, then many extended trajectory segments could be appended to the initial trajectory to minimize all the coefficient errors that remained high. The first appended trajectory was called GT4x, because it was identical to trajectory GT4 up to 120 seconds and then switched to the GT6 trajectory thereafter. By adding the GT6 trajectory, all the extended trajectories GTX1 through GTX9 were added. The gimbal trajectory for GT4x is shown in Figure A.24. The time scale is around 120 seconds, so that the switch from GT4 to GT6 can be seen.

Chapter 4

Results

The following sections present the results for all the trajectories used in the simulation. These trajectories include those developed in Chapter 3, as well as some new trajectories introduced in this chapter. These new trajectories were developed after analyzing the results and determining what factors affected the cost function most.

All of the gimballed trajectory profiles are presented graphically in Appendix A. These profiles include all full length gimballed profiles (such as GT1 and GT2) as well as the extended trajectory segment profiles (such as GTX1 and GTX2b). For the full length trajectories, a representative portion of the trajectory is shown. These full length trajectories continue to follow the pattern shown in the representative portion.

All of the extended trajectory segments are shown starting from zero initial conditions and spanning a period of 60 seconds, where the period of each segment was taken to be 20 seconds. Therefore, each extended trajectory plot shows three of the same segments. In some cases, the first segment appears different from the other two. This was due to the required angles for some of the extended trajectories. If the required gimballed angles for a particular extended trajectory were different than the initial angles, then the first two seconds of the segment were used to reorient the system. This reorientation is discussed further in Section 4.3.

Plots of the cost functions for each trajectory are given in Appendix B. These provide a basis of comparison between the various trajectories and were used to determine which trajectories were best for reducing the errors in the accelerometer coefficients. Some plots of specific coefficient errors are included in this chapter to show the effects of the trajectories on these individual coefficient errors. Finally, some body

frame sensitivity plots are included in the text to show the sensitivities developed by certain trajectories.

4.1 Initial Trajectories

This section discusses the results obtained from the previously implemented trajectory GT0, as well as the initial heuristic trajectories that were developed in Section 3.2. These initial trajectories included GT1, GT2, and GT3.

4.1.1 Previous Trajectory

As discussed in Section 3.2.1, the GT0 trajectory was designed to excite individual accelerometer coefficients in each segment. The GT0 trajectory is plotted in Figure A.1. Note that the body frame sensitivities developed in the GT0 trajectory were plotted in Figure 3.2. The cost function for this trajectory is shown in Figure B.5.

Although a sensitivity for each coefficient was produced in at least one segment of the trajectory, there was some redundancy among the segments. For example, the only difference between the first two segments was a 180 degree shift in the middle gimbal angle. This resulted in body frame sensitivities that were identical, except that the α_y sensitivity started out negative in the first segment and positive in the second segment. Figure 3.2 also shows that there was no difference between the sensitivities of the third and fourth segments. The same was true for the second and sixth segments, which developed identical sensitivities.

The effects of the segment redundancy can be seen in Figure B.5. Notice that during the second segment, the cost function does not decrease significantly. Since the sensitivities were essentially the same as the first segment, the same coefficient errors were being reduced. Although the second segment further reduced the coefficient errors reduced in the first segment, other coefficient errors remained at their initial values. This was why the cost function made no noticeable change during the second segment. The

cost function did actually decrease, but the magnitude of the unimproved errors overshadowed the small improvements made by the second segment.

The effects on the X-accelerometer coefficient errors are shown in Figure 4.1. The reduction of specific errors in Figure 4.1 was compared to the body frame sensitivities shown in Figure 3.2. As expected, the first and second segments reduced the errors of the second (C12) and the fifth coefficients (C15), whose sensitivities were α_y and ω_y^2 , respectively. These coefficient errors were reduced because the trajectory resulted in angular accelerations and angular velocities along the body frame Y-axis.

The third and fourth segments of GT0 (between simulation times of 52.5 and 105 seconds) produced angular accelerations and angular velocities along the body frame Z-axis. This resulted primarily in the reduction of the errors in the third (C13) coefficient. The errors in the sixth (C16) coefficient were also reduced, but only very slightly. The errors in the sixth coefficient were already very low, because the fifth and sixth coefficients of the X-accelerometer were highly correlated. Recall that the coefficients were composite functions of the accelerometer parameters, as shown in Table 2.2. Some of the coefficients had common expressions of the parameters in their definitions, and were therefore highly correlated. The initial covariances were computed and included in the initial covariance matrix. Since the errors in the fifth coefficient were reduced by the first two segments, the errors in the sixth coefficient were also reduced. As shown in Figures 4.1 through 4.3, many of the errors were reduced in pairs. This was due to similar correlations among these coefficients. Further reduction in specific coefficient errors were a result of the corresponding sensitivities being developed during the GT0 trajectory.

The coefficient errors for both the Y-accelerometer and the Z-accelerometer were reduced in the same manner as the X-accelerometer coefficients. The plots for these accelerometer coefficient errors are given in Figures 4.2 and 4.3. The major difference

X Accelerometer Coefficient Errors for GT0

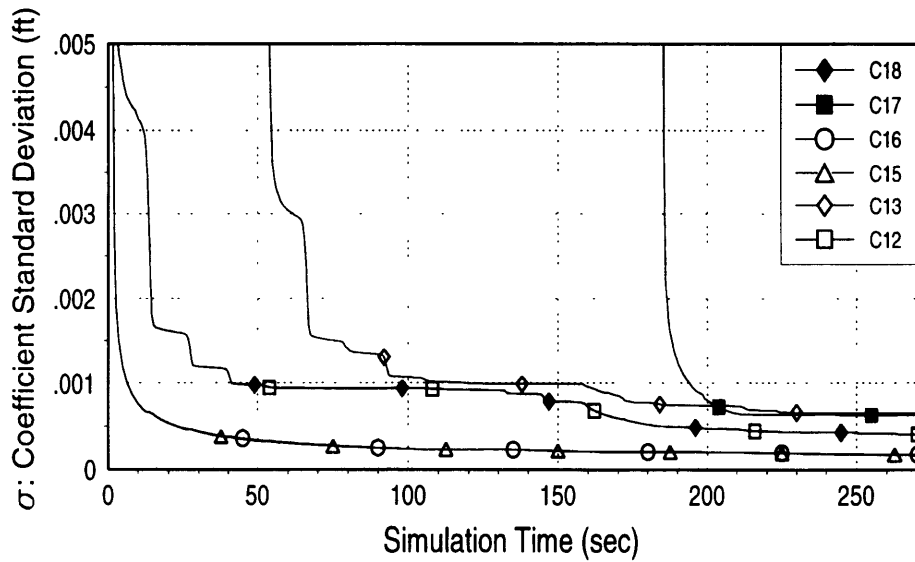
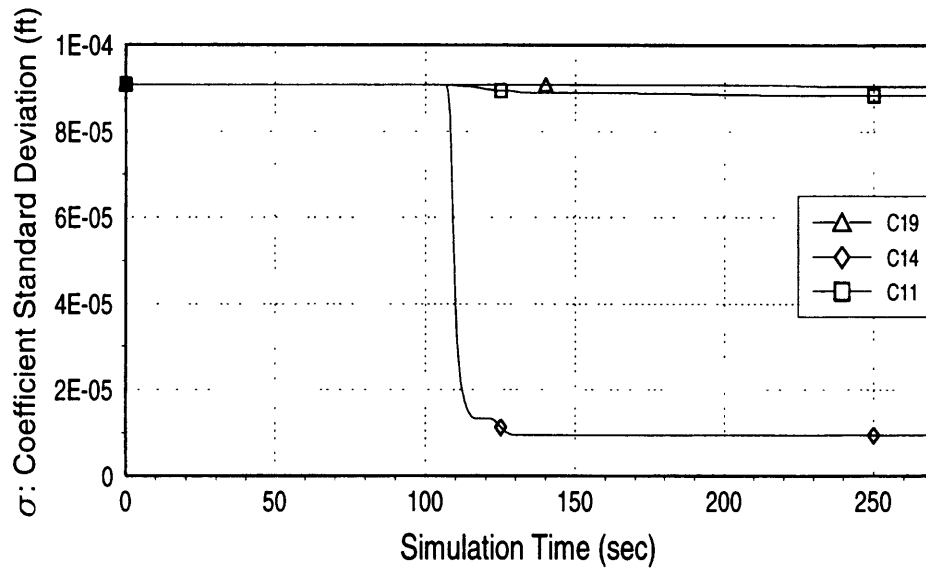


Figure 4.1: X Accelerometer Coefficient Errors for GT0

Y Accelerometer Coefficient Errors for GT0

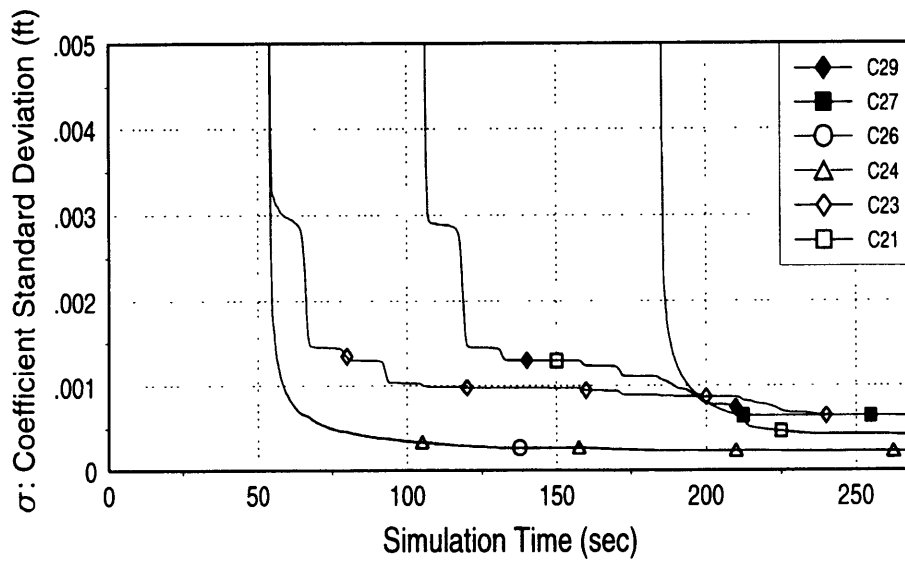
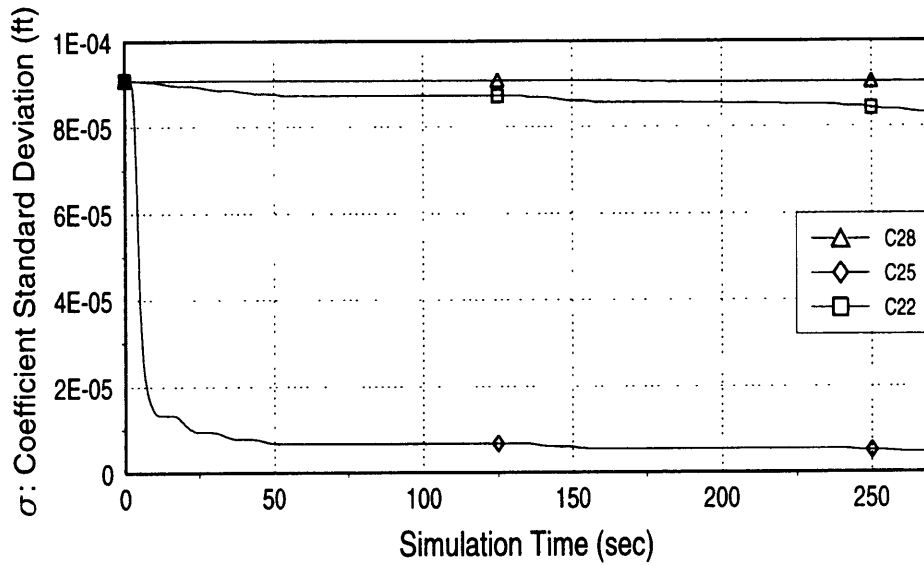


Figure 4.2: Y Accelerometer Coefficient Errors for GT0

Z Accelerometer Coefficient Errors for GT0

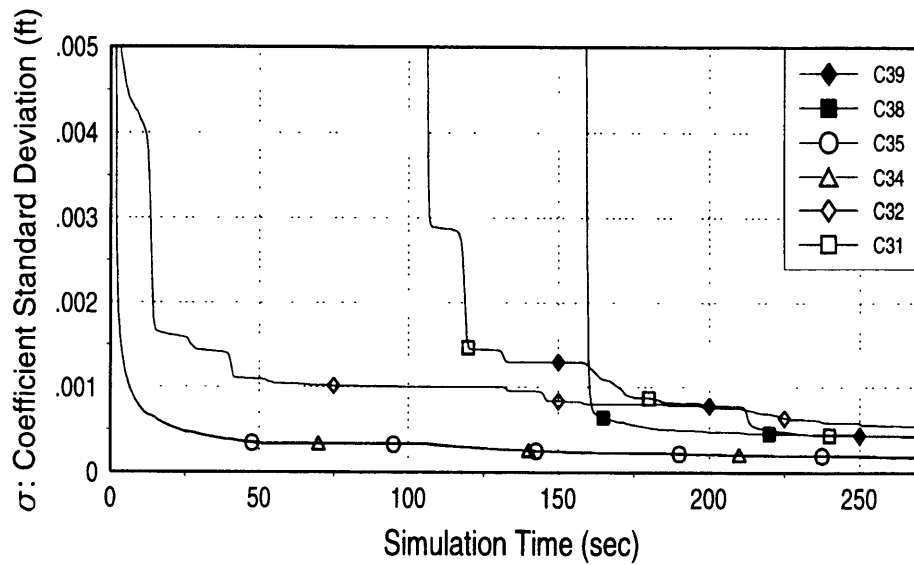
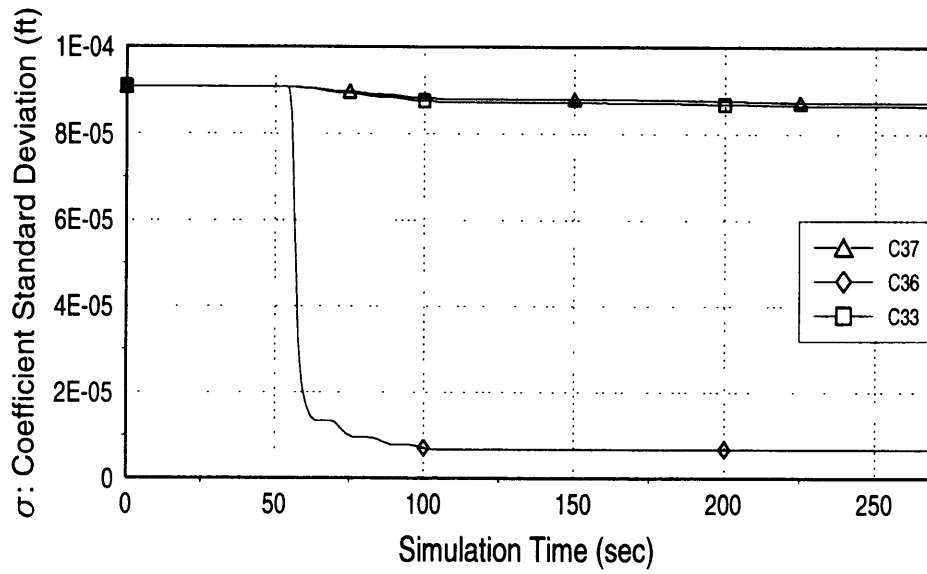


Figure 4.3: Z Accelerometer Coefficient Errors for GT0

among the three accelerometers were the coefficients that were correlated, and the coefficient errors that started out small. These differences were due to the different orientations of the three accelerometers defined in Table 2.1. Note that the errors that started out small for each accelerometer were errors in the coefficients that depended solely on the products of misalignments and distance terms. Since the initial misalignment errors were very small, these coefficient errors also started out small. For example, from Table 2.2 it can be seen that the Y-accelerometer coefficients that were functions of products of misalignments and distance terms were C22, C25, and C28. Therefore, the errors in these coefficients started out at .0011 inches, as shown in Table 3.2.

4.1.2 Initial Heuristic Trajectories

The initial trajectories presented in Section 3.2.2 were GT1, GT2, and GT3. The cost functions for all three of these trajectories are shown in Figure B.6. The cost functions are plotted over the whole simulation time interval of 270 seconds, but the cost axis was scaled so that only the results from 50 seconds on can be seen. This scale was used because the cost function decreased rapidly in the first 50 seconds for all three trajectories. If the first 50 seconds were plotted, the scaling would have made comparison of the trajectories at the final time difficult.

Figure B.6 shows that there was very little difference in the cost function between the GT1 and the GT2 trajectories. Recall that the difference between the two trajectories was in the amount of time that the inner gimbal was held at its maximum rate. GT1 held the inner gimbal at its maximum rate for 0.625 seconds, whereas GT2 held it for 1.25 seconds.

Figure B.6 also shows that the cost function was higher for the GT3 trajectory than it was for the GT1 and GT2 trajectories. This result was expected, because the sensitivities that were developed in GT3 were generally smaller than those developed by GT1 and GT2. Figures 4.4 and 4.5 show the sensitivities developed along the body Y-

Body Frame Y-Axis Sensitivities for GT1

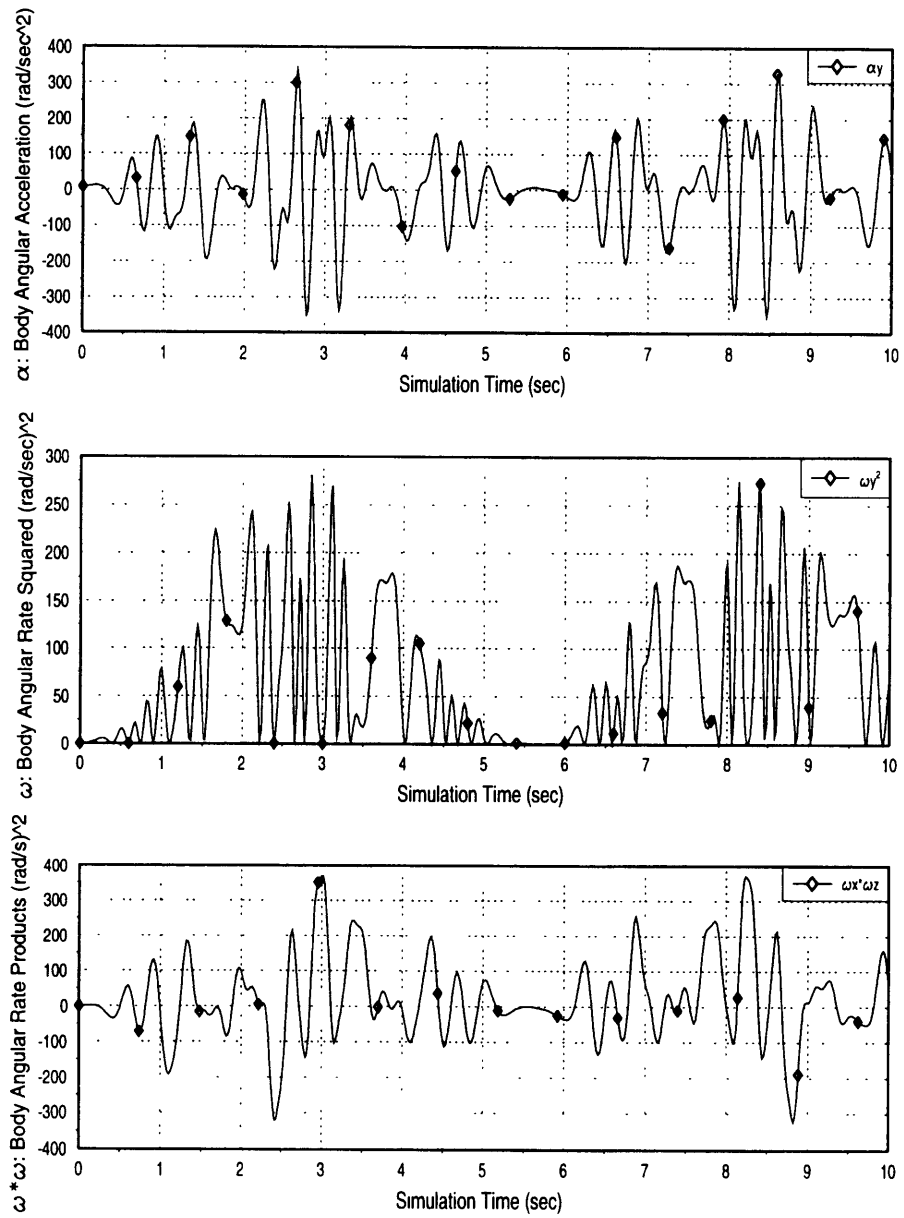


Figure 4.4: Representative GT1 Body Frame Y-Axis Sensitivities

Body Frame Y-Axis Sensitivities for GT3

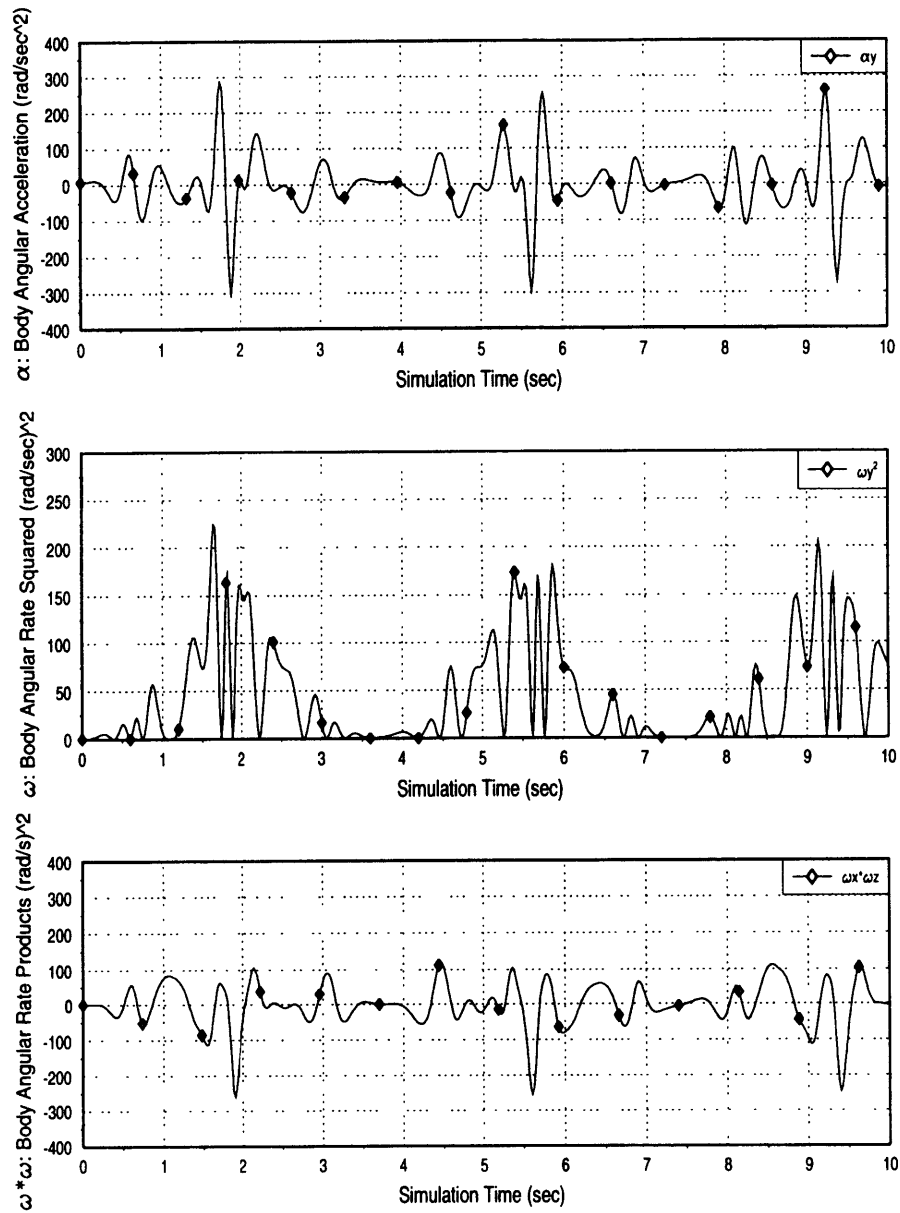


Figure 4.5: Representative GT3 Body Frame Y-Axis Sensitivities

axis for the GT1 and the GT3 trajectories. These sensitivities were representative of the sensitivities produced along the body X and Z axes, as well. Figures 4.4 and 4.5 demonstrate that all the sensitivities were greater for the GT1 trajectory. As shown in Section 3.3.3, the angular accelerations and products of angular velocities in the body frame were dominated by products of the gimbal rates. Since the GT3 trajectory did not hold the gimbals at their maximum rates, these sensitivities were generally less than those developed in the GT1 and GT2 trajectories. As a result, the cost function was noticeably higher for GT3 throughout the simulation.

An example of how the accelerometer coefficient errors were reduced in GT1 is given in Figure 4.6. This is a plot of the coefficient errors in the Y-accelerometer, but it was representative of all three of the accelerometers. The reduction of the coefficient errors was much smoother than it was for GT0 (as shown in Figures 4.1 through 4.3). This was because specific coefficients were not individually excited. Instead, the highly dynamic trajectory of GT1 produced angular accelerations and angular velocities in the body frame that excited all the coefficients. Since the periods of the gimbal motion were different, the sensitivities of the coefficients were modulated in different ways throughout the trajectory. For example, there were points where all the gimbals were spinning at their maximum rates, as well as points where only one or two of the gimbals were spinning at their maximum rates. These separate points in the trajectory excited separate coefficients. By following the GT1 trajectory, the gimbals apparently excited all of the coefficients in such a way that all the errors were steadily diminished.

4.2 Trajectory Characteristic Effects

This section describes the effects of two types of trajectory characteristic perturbations on the cost function. The first type of perturbation made to the trajectories was a change in the time that the gimbals were set to stay at their maximum spin rates. The second type of perturbation was a change in the initial gimbal angles. First, a "holding period" at the maximum rate was determined that provided a locally minimum

Y Accelerometer Coefficient Errors for GT1

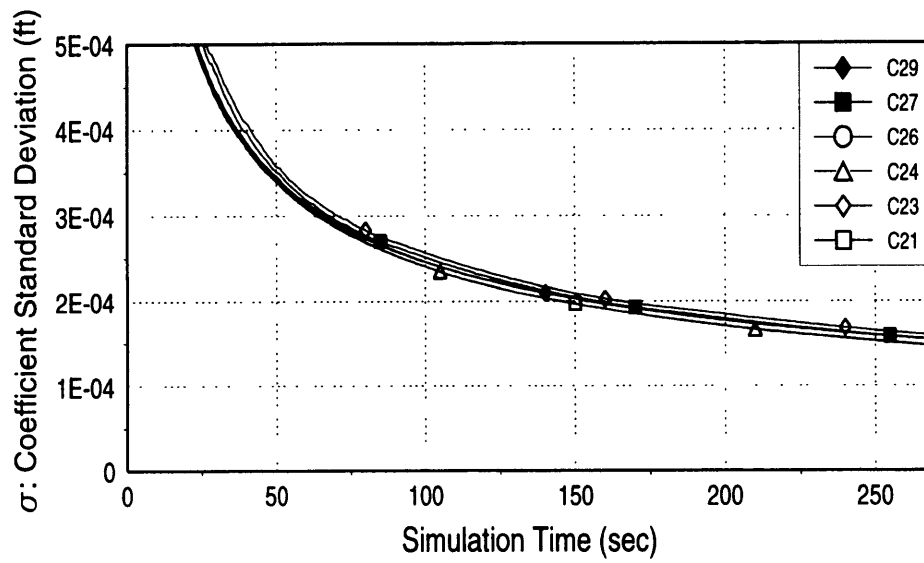
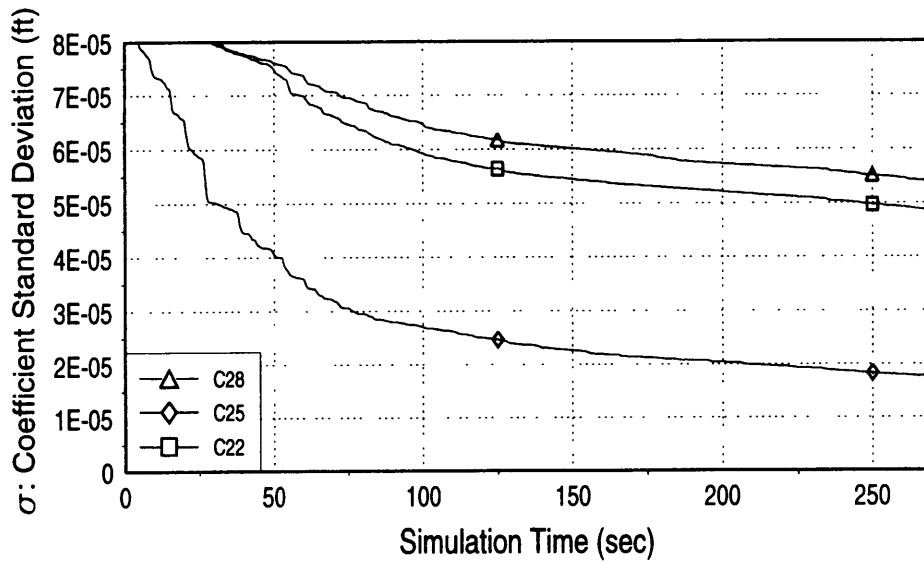


Figure 4.6: Y Accelerometer Coefficient Errors for GT1

final cost. Using this holding period, the initial middle gimbal was varied until another locally minimum final cost was found. Finally, using the holding period and initial middle gimbal angle from above, the initial inner gimbal angle was varied to produce another minimum in the final cost.

The effects of varying the trajectory characteristics were observed using the GT3 trajectory as the baseline. The GT3 trajectory was used as the baseline, because it did not hold the gimbals at their maximum rates, but continuously accelerated or decelerated them. The GT3 trajectory was also started at zero initial angles, so the effects of variations in the initial angles could be observed.

4.2.1 Time at Maximum Rate Effects

The initial trajectories GT1 through GT3 all accelerated and decelerated the gimbals at their maximum angular accelerations to their maximum angular velocities. The difference between these trajectories was the amount of time that the gimbals were set to stay at their maximum rates before they were accelerated or decelerated again. The GT4 and GT5 trajectories were designed to increase these holding periods for all of the gimbals. The cost functions for these two trajectories were plotted in Figure B.7. The cost function of GT5 shows that keeping the gimbals at their maximum rates for the whole trajectory did not produce the best results.

In order to investigate the effects of the holding period, variations were made to the GT3 trajectory so that the gimbals would be held for a specified amount of time at their maximum rates. The results of the different holding periods are shown in Figure B.8. The legend on each plot indicates the holding time in seconds for each simulation run. Note the scale for the second plot was reduced to magnify the differences between the various runs. Recall that GT3 had no holding period and that GT5 held the gimbals at their maximum rates for the entire simulation. These trajectories were then used as the two extremes for comparison to the holding period variations. The holding periods tested ranged from 0.05 seconds to 6.0 seconds.

From Figure B.8, it can be seen that as the holding period increased from 0 to 2.0 seconds, the cost function decreased. However, when the holding period was increased beyond 2.0 seconds, the cost function became larger. Simulation runs were performed at various holding times and the final costs were plotted versus these holding times in Figure 4.7. The final costs were defined to be the value of the cost function at a simulation time of 270 seconds. Note that the relation between the final costs and the holding times was not smooth, especially near the 2.0 second holding period interval. A third degree polynomial was fitted to the lower portions of the curve in Figure 4.7 in order to determine which holding period would produce a local minimum. This holding period was then used in the simulation to generate another data point, and the cycle was repeated. A locally minimum final cost of $4.2200 \times 10^{-7} \text{ (ft)}^2$ at a holding period of 2.02 seconds was found using this iterative process. Hence, the locally optimum holding time for the GT3 type of trajectory was determined to be 2.02 seconds.

4.2.2 Initial Angle Effects

All the initial gimbal angles were varied using the locally optimized trajectory determined in the previous section as the baseline. The initial variations were in increments of 45 degrees, starting at zero initial conditions and going up to 315 degrees. The final costs for each trajectory were plotted together to compare the effects of the initial angles on the cost function at the end of the simulation. Note that the variations of a given initial gimbal angle were done while holding the other two initial angles at zero.

The first angle that was varied was the outer gimbal angle. As mentioned in Chapter 3, the initial outer gimbal angle was not expected to affect the cost function, because the body frame sensitivities did not depend on the outer gimbal angle. When the initial outer gimbal angle was varied, the simulation produced cost functions that were identical over all the angle variations. These results validated the assumption that the initial outer gimbal angle did not affect the cost function.

Final Cost vs Gimbal Maximum Rate Holding Period

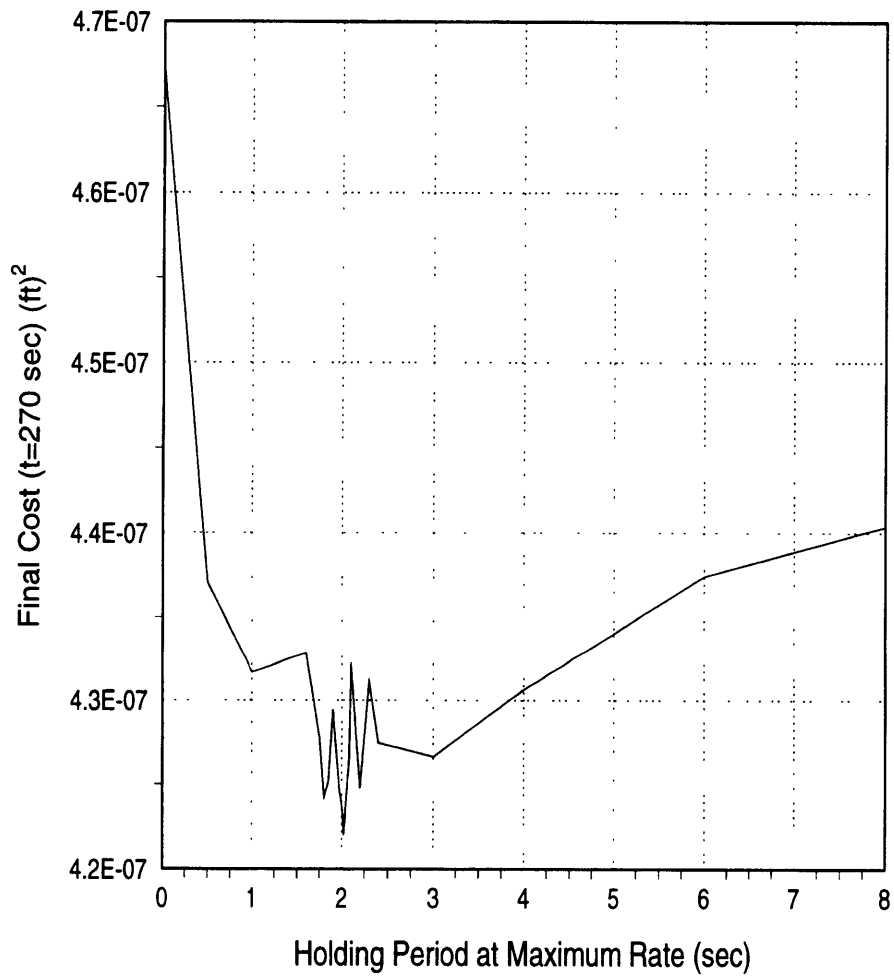


Figure 4.7: Holding Period Effects on Final Cost

When the initial inner gimbal angle was varied, there was very little effect on the final cost function. These results seemed non-intuitive, because the body frame sensitivities were very dependent on the initial inner gimbal angle. The results for these angle variations were not shown, because the effects on the final cost function were negligible.

When the initial middle gimbal angle was varied, there were corresponding variations in the cost function. These results are shown in Figure B.9, where the legend indicates the initial middle gimbal angle in degrees for each run. Note that the effects on the cost function were very small, and therefore the scale for the plot in Figure B.9 was adjusted to display the differences more clearly. Variations in the middle gimbal angle produced some cost function values that were better and some that were worse than the cost function for zero initial conditions. A plot of the final cost versus the initial middle gimbal angles is given in Figure 4.8. Recall that the baseline started at zero initial angles and had a holding period of 2.02 seconds.

The 45 degree variations in initial middle gimbal angle showed that lower final costs could be obtained by changing the initial conditions. Once again, polynomials were fitted to the lower portions of the curve in Figure 4.8. The initial angles that produced minimums in the polynomials were then used to perform more simulation runs. These extra data points were also included in Figure 4.8. The results of this local optimization showed that an initial middle gimbal angle of 159.5 degrees produced a minimum final cost of 4.2070×10^{-7} (ft)².

Using the initial middle gimbal angle of 159.5 degrees and the holding period of 2.02 seconds, the initial inner gimbal angle was varied once again to determine if it affected the final cost. In this case, the initial angle did affect the final cost. The effect of the initial inner gimbal angle on the cost function is shown in Figure B.10, where the legend indicates the initial inner gimbal angles in degrees for each run. The final cost is plotted versus the initial inner gimbal angle in Figure 4.9. The same procedure as above

Final Cost vs Initial Middle Gimbal Angle

Holding Period = 2.02 sec

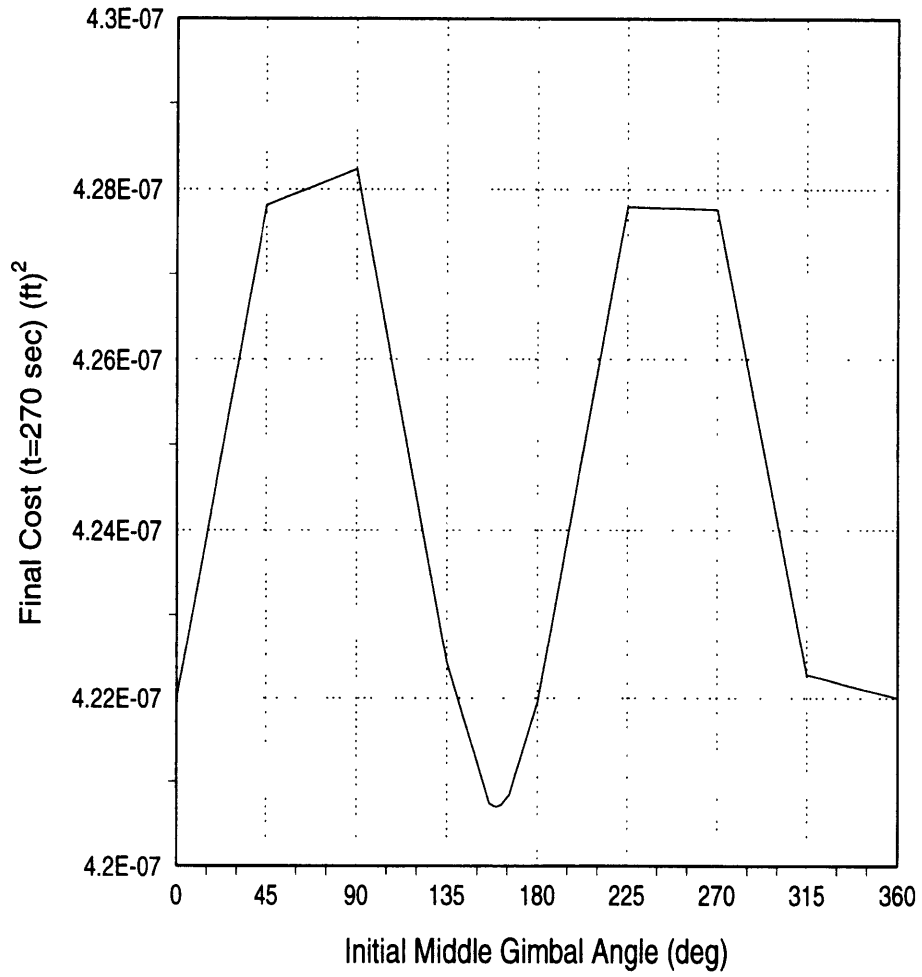


Figure 4.8: Initial Middle Gimbal Angle Effects on Final Cost

Final Cost vs Initial Inner Gimbal Angle

Initial Middle Gimbal Angle = 159.5 deg

Holding Period = 2.02 sec

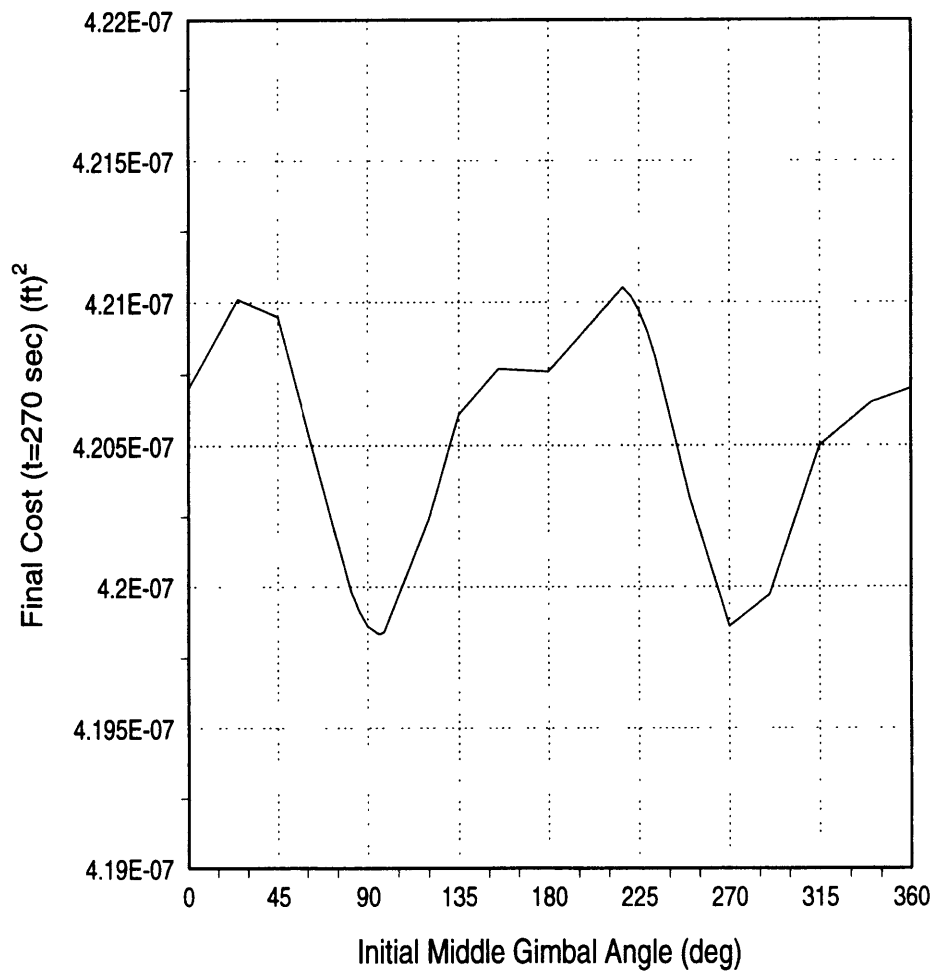


Figure 4.9: Initial Inner Gimbal Angle Effects on Final Cost

was used to find what initial inner gimbal angle resulted in the lowest final cost. The data points produced by the extra simulation runs were also used in Figure 4.9. The variations of initial inner gimbal angle showed that the final cost could be further reduced if an angle of 96.0 degrees was used. This initial inner gimbal angle resulted in a final cost function of $4.1983 \times 10^{-7} \text{ (ft)}^2$.

4.2.3 Summary of Trajectory Characteristic Effects

A locally optimal trajectory was found by varying the holding times at the maximum rate and the initial gimbal angles of GT3. First, a holding time was determined that resulted in the lowest final cost. Then, the initial middle gimbal angle was varied until another minimum in the final cost was found. Finally, the final cost was minimized over all initial inner gimbal angles. This trajectory was called GT3opt and is shown in Figure A.23. A summary of the effects on the final cost function is given in Table 4.1.

Table 4.1: Effects of Successive One-Dimensional Optimizations on Final Cost

Characteristics of GT3 Trajectory			Final Cost (ft) ²
Holding Time (sec)	Initial Middle Gimbal Angle (deg)	Initial Inner Gimbal Angle (deg)	
0	0	0	4.6738×10^{-7}
2.02	0	0	4.2200×10^{-7}
2.02	159.5	0	4.2070×10^{-7}
2.02	159.5	96.0	4.1983×10^{-7}

Table 4.1 shows that the final cost for the GT3 trajectory was reduced over ten percent by performing local optimizations over the holding time and the initial gimbal angles. Note that each of these local optimizations was one dimensional in nature because only one parameter was varied at a time. An optimization performed over all three of

these parameters would require an extensive number of simulation runs. Since each simulation run took approximately one and a half hours, an optimization over all three parameters was impractical. Therefore, the results of Table 4.1 indicate only one possible minimum for the final cost over all holding times and initial angles.

4.3 Extended Trajectories

This section discusses the results obtained from using the extended trajectory segments introduced in Section 3.3.3. Recall that the segments were used in two ways. First, they were used to develop an entire trajectory that excited individual coefficients. Second, they were appended on to other trajectories.

4.3.1 Full Extended Trajectories

The trajectories that used only the extended trajectory segments were GT6, GT6b, and GT6c. The purpose of these trajectories was similar to that of GT0. They were designed to decrease the uncertainties in a specific coefficient by producing a large sensitivity for that coefficient while minimizing the sensitivities of the other coefficients. The cost function for all three of these trajectories are plotted in Figure B.11. Note that three different scales were used for the cost function so that the results of the three trajectories could be compared over the entire interval.

Figure B.11 shows clearly that the GT6 trajectory results in a smaller final cost than both the GT6b and the GT6c trajectories. The GT6 trajectory reduced the cost function to under $4 \times 10^{-6} \text{ (ft)}^2$ in 30 seconds. The GT6b trajectory required 150 seconds and GT6c required 125 seconds to produce the same decrement in the cost. The major difference between the GT6 trajectory and the GT6b and GT6c trajectories was the emphasis placed on maximizing either the sensitivities or the observabilities of the coefficients. GT6 produced larger sensitivities, but also excited other coefficients. Apparently, the larger sensitivities rather than the higher observabilities were more beneficial to the filter in reducing the uncertainties in the coefficients .

The effects of each trajectory on the errors in the Z-accelerometer coefficients are shown in Figures 4.10 through 4.12. The Z-accelerometer was representative of all three accelerometers. Note that the errors were reduced relatively smoothly for the GT6 trajectory, whereas the GT6b and GT6c trajectories resulted in step-wise reductions. This difference was due to the segments of GT6 that excited more than one coefficient. The plot for GT6 also shows a step-wise reduction in errors between simulation times of 30 and 60 seconds. Recall that this portion of GT6 consisted of the three segments designed to increase the body frame angular rates (GTX4, GTX5, GTX6). These same segments were used in the GT6b and GT6c trajectories, because they did not excite any extra coefficients and therefore provided the best observabilities.

The step-wise reductions in the coefficient errors for GT6b and GT6c indicate that each segment was exciting a minimum number of coefficients, making them very observable. It can be seen from Figures 4.11 and 4.12 that the extended trajectory segments were indeed decreasing the errors in the coefficients they were designed to excite. For example, the 30 to 40 second interval of GT6b consisted of the GTX4 extended trajectory segment. This segment was designed to reduce the errors in the fourth coefficient. As shown in Figure 4.11, the errors for the fourth coefficient do indeed drop in this interval. The errors in the fifth coefficient also drop, because the fourth and fifth coefficients were highly correlated for the Z-accelerometer. Similarly, the 80 to 90 second interval of GT6c consisted of the GTX9 extended trajectory segment. The GTX9 segment was designed to reduce the errors in the ninth coefficient, and Figure 4.12 shows that this is exactly what happened.

The difference in results between the GT6b and the GT6c trajectories could be attributed to the order of the segments. The order of the segments dictated how many reorientations needed to be performed throughout the trajectory. The GT6c trajectory was designed to have fewer reorientations. For the first 60 seconds of the simulation the cost for the GT6b trajectory was less than that for the GT6c trajectory. This can be attributed

Z Accelerometer Coefficient Errors for GT6

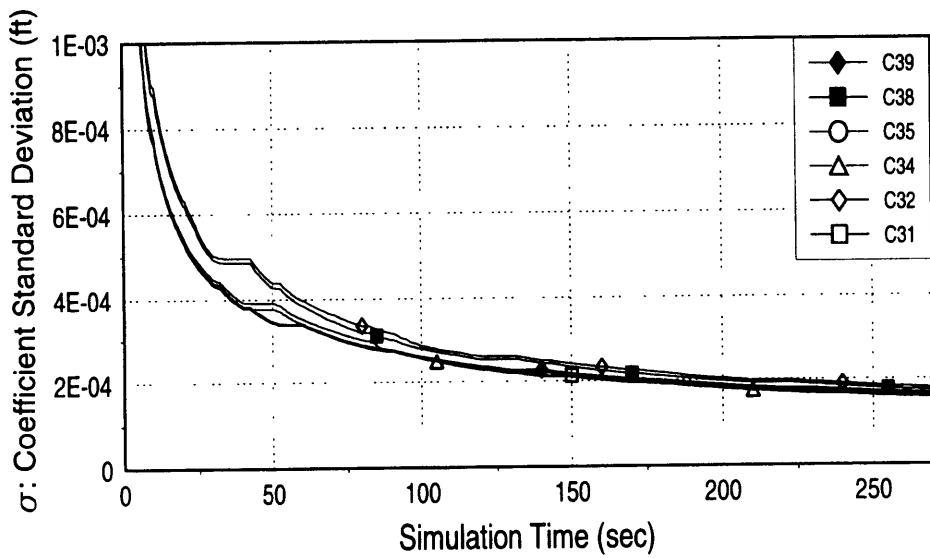
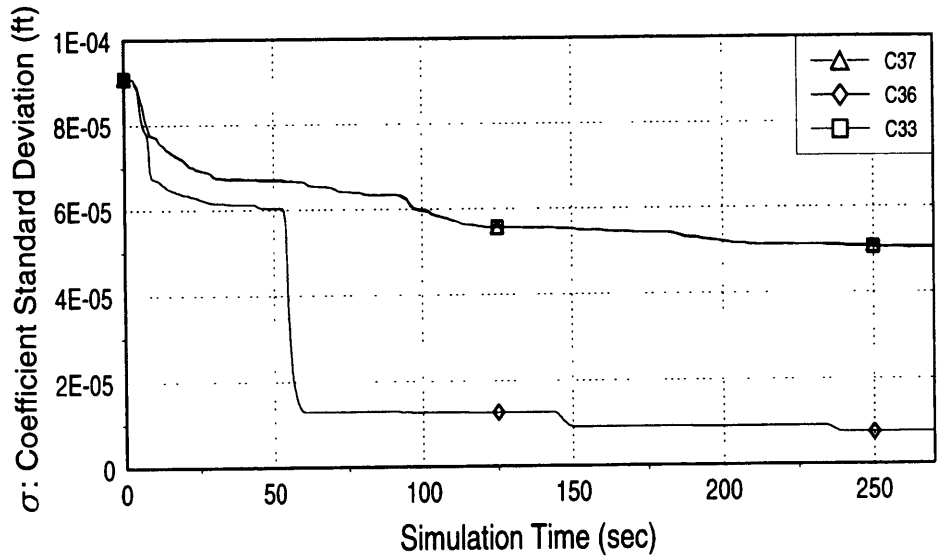


Figure 4.10: Z Accelerometer Coefficient Errors for GT6

Z Accelerometer Coefficient Errors for GT6c

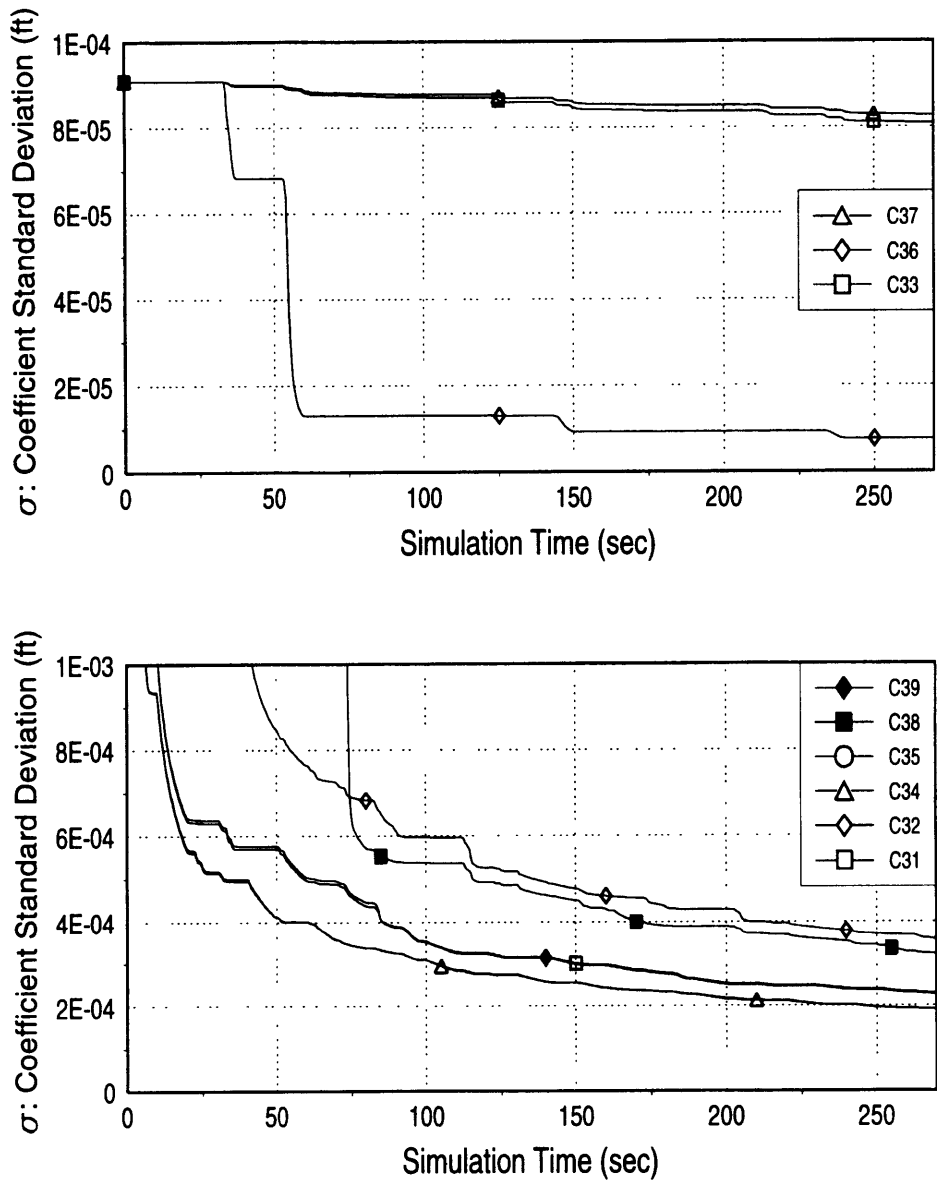


Figure 4.12: Z Accelerometer Coefficient Errors for GT6c

to the same type of redundancy noted in the GT0 trajectory. In this case, the GTX1b and GTX4 trajectories were placed adjacent to each other. Since the GTX1b segment was designed to produce an angular acceleration along the body frame X-axis and the GTX4 trajectory was designed to produce an angular velocity along the same axis, both segments developed similar sensitivities. The final costs indicated that the GT6c trajectory was better over the whole simulation in reducing the cost. This was a result of the GT6c trajectory spending less time reorienting the test table and more time actually within the extended trajectory segments.

All three of the full extended trajectories produced results that were considerably worse than the results of GT1. The lowest final cost was $5.1996 \times 10^{-7} \text{ (ft)}^2$ for the GT6 trajectory. This was twenty percent higher than the final cost for the GT1 trajectory, which was $4.3415 \times 10^{-7} \text{ (ft)}^2$. Therefore, the highly dynamic trajectories in which all the gimbals were moving were considered better candidates for calibrating the accelerometers than the full extended trajectories.

4.3.2 Extended Initial Trajectories

Another way in which the extended trajectories were used was to append them onto the initial trajectories. The extended trajectory segments were appended to the GT4 trajectory, since GT4 produced the best results out of the first five trajectories. For GT4, all the gimbal angular rates were near zero at a simulation time of 120 seconds. Therefore, this time was chosen to be the point at which the extended trajectories were appended, since the gimbal rates and accelerations could be started at zero.

The extended trajectories were originally designed to target specific coefficients that the filter had difficulty in estimating. However, the results of the GT4 trajectory at 120 seconds showed that none of the coefficient errors were significantly greater than any of the others. For this reason, two trajectories were developed that consisted of appending the extended segments onto GT4. The first trajectory appended all of the

segments in sequential order onto GT4, while the second trajectory appended the GTX1 trajectory onto GT4 and repeated this segment until the end of the simulation.

The first trajectory, called GT4x, started at 120 seconds with GTX1 and then went through each 10 second segment in the same order as GT6. This trajectory is shown in Figure A.24. Note that the time frame shown goes from 100 to 160 seconds of simulation time. This was done so the transition between the original GT4 trajectory and the extended trajectory segments could be observed.

The second extended initial trajectory that was developed was called GT7 and is shown in Figure A.25. This trajectory was the same as GT4 up to 120 seconds, then it ran the GTX1 extended segment over and over for the rest of the simulation. The GTX1 segments were repeated, because this segment seemed to reduce the cost function most in the GT6 trajectory. The GTX1 segment also excited all of the coefficients. If only one coefficient was targeted, the reduction of the errors in that specific coefficient would not reduce the cost by much. The cost would not be affected much since many of the coefficient errors were of the same magnitude at the end of 120 seconds in the GT4 trajectory.

The results of both GT4x and GT7 are plotted with the results of GT4 in Figure B.12. Two plots are shown in order to observe the initial effects of the extended segments on the cost functions. The second plot shows that for the first 30 seconds after the transition, both GT4x and GT7 result in lower cost functions. However, at 150 seconds, the cost function for the GT4x trajectory levels out. This was due to the segment that excited the angular velocity along the body frame X-axis. Similar flat portions of the cost function curves were observed in the GT6 trajectory. These level portions of the curve were due to the filter only getting information on two of the coefficients (one that depends on the angular velocity and one that depends on the angular acceleration, both along the body frame X-axis). The GT7 trajectory produced a very similar cost function reduction to that of GT4. This was expected, because the GTX1

trajectory segment was very similar to the gimbal motion in GT4. However, the final cost for the GT4 trajectory was $4.2981 \times 10^{-7} \text{ (ft)}^2$, which was slightly lower than the final cost for the GT7 trajectory ($4.3377 \times 10^{-7} \text{ (ft)}^2$).

4.3.3 Summary of Extended Trajectories

The extended trajectories discussed in this section were similar in design to the original trajectory GT0. Each segment was designed to excite one specific coefficient. In the case of the GT6 trajectory, other coefficients were also excited in some of the segments. The other coefficients were excited because these segments were designed to maximize the body frame sensitivities. In maximizing a particular sensitivity, some of the other coefficient sensitivities were also produced. The GT6b and GT6c trajectories were more similar to the GT0 trajectory in that maximum observability of a specific coefficient was achieved in each segment. However, the results from all the full extended trajectories indicate that producing more than one sensitivity at a time can provide better results.

A major difference between the full extended trajectories and the GT0 trajectory was the reorientation between segments. The GT0 trajectory does not explicitly include the time to reorient the test table between segments. Therefore, the actual testing time for the GT0 trajectory would be somewhat longer than indicated. The full extended trajectories defined in this thesis do incorporate short reorientations between segments. Measurements are still taken during the reorientation and are used in the filter. The difference between the GT6b and the GT6c trajectories indicate that these short reorientation periods play a significant role in the reduction of the estimate errors.

4.4 Modeling Effects

This section discusses the results of modifications made to the model or the filter used in the simulation. These modifications included changes in the step size used in the

Runge Kutta integration, changes in the frequency of measurements, and the addition of the three states used to characterize the gimbal axis displacements.

4.4.1 Runge Kutta Integration Step Size Effects

Since the dynamics matrix was changing rapidly for most of the simulation, small step sizes had to be used for the numerical integration. In order to verify the accuracy of the numerical integrator, the GT1 trajectory was run with variations in the number of Runge Kutta integrations per measurement. The measurements were assumed to be taken every 0.05 seconds. The resulting cost functions of these runs are shown in Figure B.13. This plot shows that there were significant differences among the trajectories that used less than twenty integrations between measurements. However, the results using twenty and forty integrations per measurement were identical. Therefore, the use of twenty integrations per measurement was validated. This resulted in a Runge Kutta step size of 0.0025 seconds.

4.4.2 Measurement Frequency Effects

The number of measurements taken in a given time period was varied in order to observe the effects of measurement frequency on the cost function. The GT1 trajectory with measurements taken every 0.05 seconds, a measurement frequency of 20 Hz, was used as the baseline. Only two variations were run, using measurement frequencies of 10 Hz and 100 Hz. The results of these variations are shown in Figure B.14, where the legend indicates the time between measurements in seconds for each run. The final cost for the 100 Hz measurement frequency was $1.1215 \times 10^{-7} \text{ (ft)}^2$ and the final cost for the 10 Hz measurement frequency was $8.3670 \times 10^{-7} \text{ (ft)}^2$. As expected, the higher measurement frequency produced much better results. This was due to more information being processed by the filter. Also, the process noise acted over a smaller interval of time before another measurement was made.

4.4.3 Incorporation of Gimbal Axis Displacements

Three more states were included in order to model the effects of the small gimbal axis displacements. The incorporation of the errors due to these states was performed by modifying the measurement matrix \mathbf{H} as shown in Section 2.2.2.1. The results of including these three extra states are shown in Figure B.15, where the GT3 trajectory was used as the baseline. Note that the scales on Figure B.15 are small in order to show the differences between the two runs. The results for the GT3 trajectory were representative of the results for all the high dynamic trajectories. It can be seen that the difference between the 33-state results and the 36-state results was quite small. For the GT3 trajectory, the final cost without incorporating the gimbal axis displacements was $4.6738 \times 10^{-7} \text{ (ft)}^2$ and the final cost with the displacements was $4.7065 \times 10^{-7} \text{ (ft)}^2$. The difference between the cost functions is more easily seen in Figures 4.13 and 4.14. These plots show the additional cost that resulted when the gimbal axis displacement states were used in the GT0 and GT3 trajectories, respectively. The additional cost was obtained by subtracting the cost of the 33-state simulation run from the cost of the 36-state simulation run at every time along the trajectory.

Both Figures 4.13 and 4.14 show that the additional cost was larger in the beginning of the simulation than at the end. This could be attributed to the filter gaining more information about the gimbal axis displacements as the simulation progressed. Note that the discrete jumps in the plot of Figure 4.13 occurred between the segments of the GT0 trajectory. The errors in the gimbal axis displacements versus the simulation time for the GT1 trajectory are plotted in Figure B.16. It can be seen that the filter was able to estimate the displacements between the middle and inner gimbal axes better than the displacement between the outer and middle gimbal axes. By reducing the errors in the gimbal axis displacements, the filter was better able to assign error accelerations to the effects of specific coefficients. Although the difference in coefficient errors between the 33 and the 36-state runs became smaller, the 36-state errors were still larger. This was

Extra Cost Due to Gimbal Axis Displacements vs Time

GT0 Trajectory

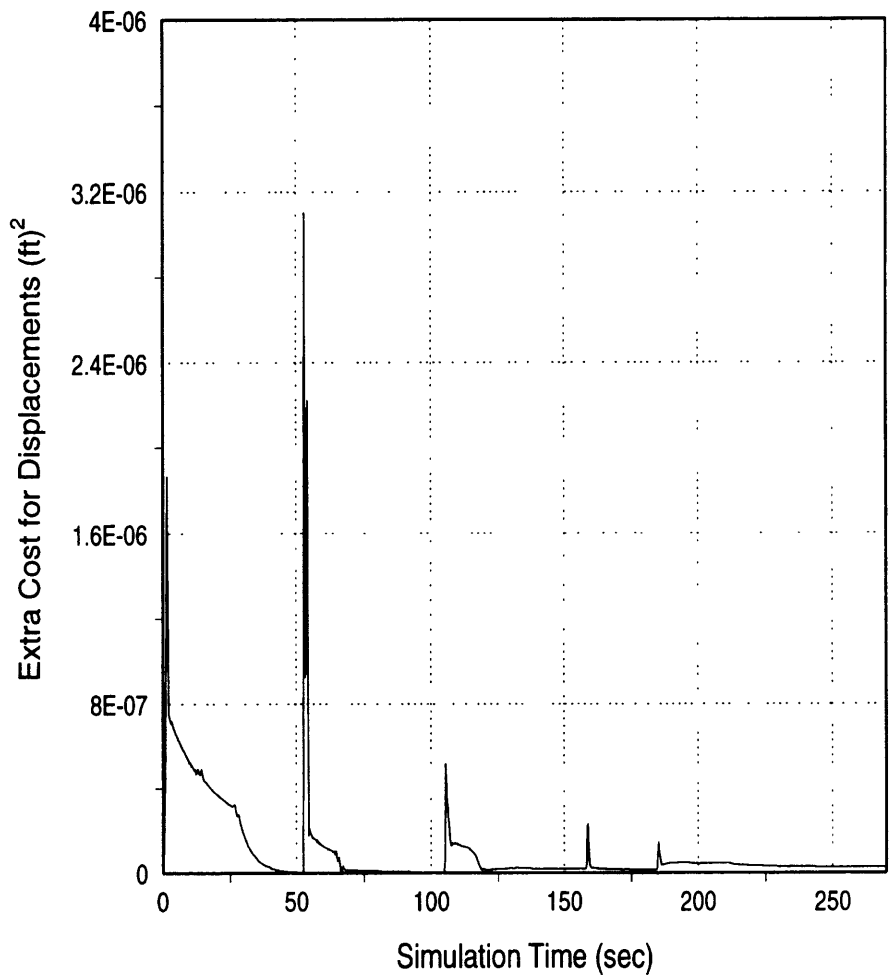


Figure 4.13: Extra Cost Due to Gimbal Axis Displacements for GT0

Extra Cost Due to Gimbal Axis Displacements vs Time

GT3 Trajectory

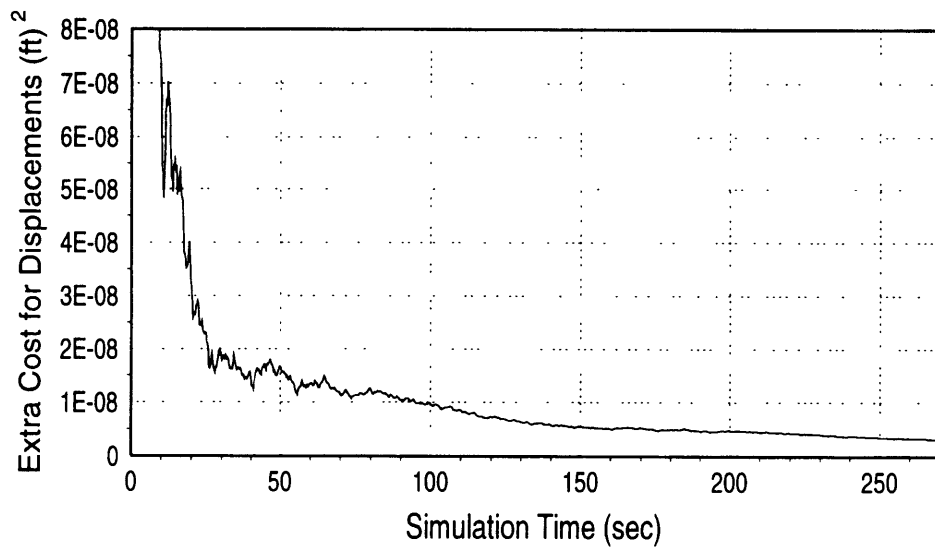
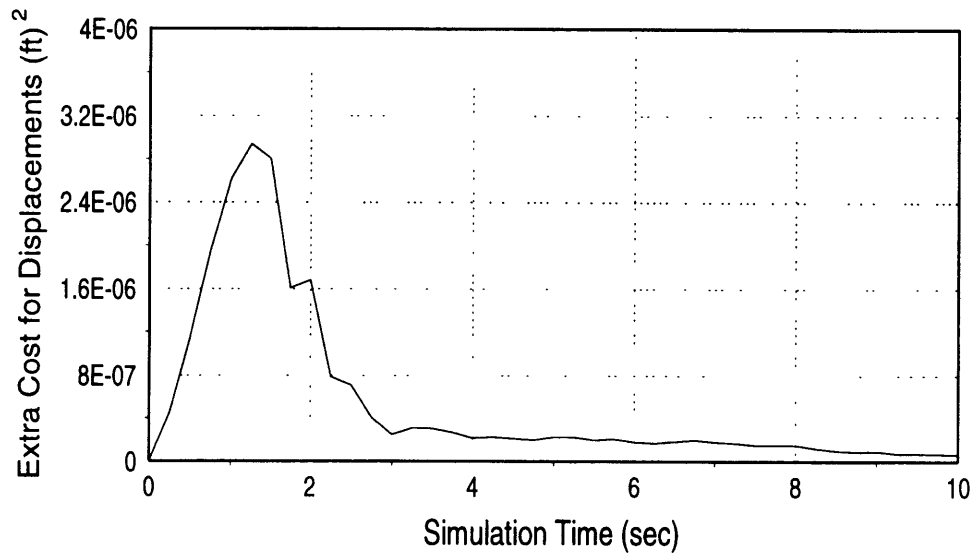


Figure 4.14: Extra Cost Due to Gimbal Axis Displacements for GT3

expected, since running the 33-state filter was analogous to running the 36-state filter with zero uncertainties in the gimbal axis displacement states.

4.5 General Error Estimation Trends

This section summarizes the results presented in the previous sections of this chapter. The costs at the final simulation time of 270 seconds are presented for each trajectory. Table 4.2 summarizes the results obtained from all the basic trajectories. The results obtained by performing the one-dimensional optimizations on the GT3 trajectory are shown in Tables 4.3 through 4.5. This section also describes general aspects of the results. These aspects include how the position and velocity errors changed during the simulation and which coefficients were the most difficult to estimate.

4.5.1 Summary of Results

Table 4.2: Final Costs for All Basic Trajectories

Trajectory Group	Trajectory Name	Final Cost (ft) ²
Previous Trajectory	GT0	3.4417×10^{-6}
Initial Heuristic Trajectories	GT1	4.3415×10^{-7}
	GT2	4.3201×10^{-7}
	GT3	4.6738×10^{-7}
Improved Trajectories	GT4	4.2981×10^{-7}
	GT5	8.2769×10^{-7}
Full Extended Trajectories	GT6	5.1996×10^{-7}
	GT6b	1.8697×10^{-6}
	GT6c	1.7193×10^{-6}
Extended Initial Trajectories	GT4x	4.6393×10^{-7}
	GT7	4.3377×10^{-7}
Trajectories Including Gimbal Axis Displacements	GT0_36	3.4678×10^{-6}
	GT1_36	4.3629×10^{-7}
	GT3_36	4.7065×10^{-7}
	GT6_36	5.2461×10^{-7}

Table 4.3: Final Costs for Variations in Holding Times on GT3 Trajectory

Holding Time (sec)	Final Cost (ft) ²
0.00	4.6738 x 10 ⁻⁷
0.50	4.3705 x 10 ⁻⁷
1.00	4.3169 x 10 ⁻⁷
1.60	4.3286 x 10 ⁻⁷
2.00	4.2369 x 10 ⁻⁷
2.02	4.2200 x 10 ⁻⁷
2.40	4.2748 x 10 ⁻⁷
3.00	4.2663 x 10 ⁻⁷
4.00	4.3065 x 10 ⁻⁷
6.00	4.3744 x 10 ⁻⁷

Table 4.4: Final Costs for Variations in Initial Middle Gimbal Angle for GT3

Initial Middle Gimbal Angle (deg)	Final Cost (ft) ²
0	4.2200 x 10 ⁻⁷
45	4.2781 x 10 ⁻⁷
90	4.2823 x 10 ⁻⁷
135	4.2243 x 10 ⁻⁷
159.5	4.2070 x 10 ⁻⁷
180	4.2195 x 10 ⁻⁷
225	4.2779 x 10 ⁻⁷
270	4.2776 x 10 ⁻⁷
315	4.2228 x 10 ⁻⁷
360	4.2200 x 10 ⁻⁷

Table 4.5: Final Costs for Variations in Initial Inner Gimbal Angle for GT3

Initial Middle Gimbal Angle (deg)	Final Cost (ft) ²
0	4.2070×10^{-7}
45	4.2095×10^{-7}
90	4.1986×10^{-7}
96.0	4.1983×10^{-7}
135	4.2061×10^{-7}
180	4.2076×10^{-7}
225	4.2097×10^{-7}
270	4.2097×10^{-7}
315	4.2050×10^{-7}
360	4.2070×10^{-7}

Table 4.2 shows that all the new trajectories provided significant improvements over the previous trajectory of GT0. Even the fully extended trajectories of GT6, GT6b, and GT6c resulted in costs that were approximately half that of the GT0 trajectory. Table 4.2 also shows that the high dynamic trajectories, where all the gimbal axes experienced motion simultaneously, produced lower costs than the fully extended trajectories, where typically only one or two gimbals at a time were subjected to motion. The best trajectory before any optimizations were done was the GT4 trajectory.

Tables 4.3 through 4.5 show that by performing a series of one-dimensional optimizations over the trajectory parameters, an even lower final cost can be obtained. The improvement over the GT3 trajectory was significant (10% reduction in final cost), but the improvement over the GT4 trajectory was small (2.3% reduction in final cost). Most of the improvement was realized by optimizing over the holding time, while the initial gimbal angles had a relatively small effect.

4.5.2 Position and Velocity Errors

The errors in the local level positions and velocities were also reduced throughout the simulation. The time history of the position and velocity errors for the GT1 trajectory are shown in Figure B.17. As shown in the plots, these errors oscillated with a decreasing amplitude and approached steady state values. The oscillations were due to the dynamics of the trajectory. At some points in the trajectory the gimbals were barely moving. This resulted in a nearly zero dynamics matrix, so the increase in the errors was due solely to the process noise matrix \mathbf{Q} . At other times, however, the gimbals produced a highly dynamic environment for the INS system, which resulted in a large growth in errors. The standard deviations of the position and velocity approached steady state values of 3.17×10^{-3} ft and 4.80×10^{-3} ft/s, respectively.

4.5.3 Worst Coefficient Estimates

In all the simulations run there were specific coefficients that were consistently more difficult for the filter to estimate. Looking at Figures 4.1 through 4.3 once again, we can see that for the GT0 trajectory, each accelerometer had a few coefficients whose standard deviations remained higher than all the others. For the X and Y-accelerometers, these were the third and seventh coefficients (C13, C17 and C23, C27). For the Z-accelerometer, the second and eighth coefficients (C32 and C38) both had high standard deviations relative to the other Z-accelerometer coefficients. Further investigation of the coefficient error plots in Figures 4.6, 4.10, 4.11, and 4.12 show that these specific coefficients remained the hardest to estimate. However, the difference between the errors in these coefficients and the other coefficients was not as noticeable for the high dynamic trajectories.

The significance of these particular coefficients is that they are the ones that contain the anisonertia and output axis coupling terms. Referring to the diagram in Figure 2.3, we see that the output axis for both the X and Y-accelerometers are parallel to the case frame Z-axis, while the output axis for the Z-accelerometer is parallel to the case Y-

Y-axis. Therefore, an angular acceleration along the body frame Z-axis (which is the same as the case Z-axis) will produce an error due to output axis coupling effects in the X and Y-accelerometers. Similarly, an angular acceleration about the body frame Y-axis will produce errors due to output axis coupling in the Z-accelerometer. The sensitivities to these effects are the C13, C23, and the C32 coefficients for the X, Y, and Z-accelerometers, respectively.

The anisonertia errors are due to the product of the angular velocities along the input and pendulous axes. For the X and Y-accelerometers, this becomes the product of the angular velocities along the body frame X and Y-axes. For the Z-accelerometer, this is the product of the angular velocities about the body frame X and Z-axes. The sensitivities to these angular velocity products are the C17, C27, and C38 coefficients for the X, Y, and Z-accelerometers, respectively.

The larger errors in these coefficient estimates were due to the higher initial errors in these terms. Table 3.2 shows that the initial standard deviations of these terms were the highest at 0.280 inches. This was due to the dependence of these coefficients on both a lever arm distance and a size effect distance. The other coefficients were mostly functions of products of misalignments and distance terms, with some of the coefficients also depending on a single lever arm distance.

The effects of isolating the anisonertia and output axis coupling coefficients can be seen in the cost function plot for the full extended trajectories (Figure B.11). Looking at the plot for the GT6b trajectory, we note that the C13 and C23 coefficients were targeted in the 110 to 120 second and the 200 to 210 second intervals. These portions of the cost plot show that very small decreases in the cost were realized in these intervals. The C17 and C27 coefficients were targeted in the 150 to 160 second and 240 to 250 second intervals. The results in these intervals show that a more significant reduction in the cost function was obtained. The intervals that targeted the C32 coefficient were 100 to 110 seconds and 190 to 200 seconds, while the intervals that targeted the C38 coefficient were

160 to 170 seconds and 250 to 260 seconds. The cost was reduced very slightly in the 100 to 110 interval, but was not noticeably affected in the other intervals.

The largest reduction in the cost function was realized when the $C17$ and $C27$ coefficients were targeted by applying the GTX7b trajectory. One possible reason for the better results obtained using the GTX7b trajectory was that both the X and Y-accelerometers were being targeted. This allowed for a reduction in the errors of two coefficients at the same time. On the other hand, targeting the Z-accelerometer anisonertia or output axis coupling coefficients only targeted one coefficient. Note, however, that the overall effects of targeting the anisonertia and output axis coupling coefficients were quite small.

Chapter 5

Conclusions

5.1 Summary

The goal of this thesis was to develop a trajectory that resulted in more accurate estimation of the error terms that related angular motion of a strapdown system to errors in the accelerometers. This was done by defining a cost function that was the sum of all the accelerometer error coefficient variances. Various trajectories were then implemented to measure their effects on the final cost. The results indicate that all the trajectories developed in this thesis provide a significant improvement over the previously existing trajectory. The best overall trajectory tested was the GT3opt trajectory, resulting in a final cost of $4.1983 \times 10^{-7} \text{ (ft)}^2$, which was an 87.8% decrease from the original GT0 trajectory results of $3.4417 \times 10^{-6} \text{ (ft)}^2$.

Another goal of the thesis was to investigate the effects of trajectory characteristics on the uncertainties of the error coefficients. One of the major tradeoffs between trajectories was whether to develop high sensitivities or to assure high levels of observability. The trajectories that produced the highest sensitivities did not have the best observability characteristics. The gimbal motion in these cases produced similar oscillations among many of the error coefficients. However, the trajectories that had the highest levels of observability produced sensitivities that were much smaller. The decrease in sensitivities resulted in smaller measurable acceleration errors, which made estimation of the accelerometer coefficients more difficult. The results indicate that the highly dynamic trajectories that produced large sensitivities were better than the segmented trajectories that assured the greatest observabilities.

Other trajectory parameters were varied to measure the effects they had on the uncertainties of the accelerometer error coefficients. The variations were done using one

of the high dynamic trajectories as a baseline. The two types of variations were the time the gimbals were commanded to stay at their maximum rates and the initial gimbal angles before the simulation was started. Variations in the holding times at maximum rate showed that a one-dimensional optimization could be performed that resulted in a final cost that was lower than that of the previously best trajectory by 1.8%. The improvement was so small because the trajectory that was optimized over all the holding times was very similar to the previously best trajectory (GT4). The holding time that resulted in the minimum final cost was 2.02 seconds. The variations in holding time were a measure of the tradeoff between the sensitivities developed by accelerating the gimbals and the sensitivities developed by leaving the gimbals at their maximum rates. Varying the holding times also changed the way in which the body frame sensitivities were modulated, producing variations in the observabilities of the error coefficients. This effect was more difficult to analyze, because a small change in the holding period produced body frame sensitivities that were significantly different as the simulation time increased.

Further improvements were made to the final cost by varying the initial gimbal angles. A locally optimum initial middle gimbal angle of 159.5 degrees was found such that the final cost was minimized. The initial middle gimbal angle variations were made to the trajectory that used the holding period of 2.02 seconds, obtained from the holding period optimization. After the initial middle gimbal angle was optimized, the initial inner gimbal angle was varied, keeping the holding time constant at 2.02 seconds and the initial middle gimbal angle at 159.5 degrees. This one-dimensional optimization resulted in a further reduction of the final cost when the initial inner gimbal angle was set to 96.0 degrees. The result of all three of these local, one-dimensional optimizations was the GT3opt trajectory, which produced the best results of all the trajectories.

The effect of modeling the small displacements between the test table gimbal axes was also investigated. There was very little difference between the results obtained when

the gimbal axis displacements were incorporated and when they were not. The small differences may be attributed to the magnitudes of the displacements. Since the displacements were known to be less than .0085 inches, the lever arm and size effect errors were expected to dominate any errors due to the gimbal axis displacements.

5.2 Proposed Future Work

One area of work that could be expanded further is the optimization of the dynamic trajectories. Since the best trajectory developed in this thesis was due to the optimizations, this method warrants further work. As mentioned, three one-dimensional optimizations were performed over three different parameters of the trajectory. This method provided one local minimum in the final cost. However, many such optimizations could be performed, resulting in a number of local minimums. A more global optimization, performed over all important characteristics of the trajectory could be implemented.

There were no specific requirements on the final accuracies to which the coefficients were determined. The best trajectory for reducing the cost function depended on what time the simulation was stopped. Some of the trajectories that did not provide the lowest cost at the final time of 270 seconds, actually provided superior results for shorter time intervals. Therefore, the best trajectory was a function of how long the simulation was run. The final time of 270 seconds was chosen as an arbitrary stopping point. A more realistic simulation would stop once the errors were reduced to an acceptable level. The time to reach that point would then be taken as the cost function to be minimized. Of course, the trajectories would have to be capable of calibrating the accelerometer coefficients to the desired accuracy.

Another area of further research could involve the separation of the test table errors from the accelerometer errors due to angular motion. This was partly accomplished by separating out the gimbal axis displacements, which did not appear in the accelerometer coefficients. However, the lever arms from the center of the test table

to the accelerometers were a part of the definition of every accelerometer coefficient. Ideally, the calibration would result in the distances between the accelerometers in the INS. If the lever arm from the axis of angular motion to the navigation reference point is known, the distances between the accelerometers could then be used to predict the accelerometer errors for any angular motion experienced by the INS. In laboratory tests, the lever arm from the center of the test table to the reference navigation point will be different for each mounting on any test table. Since the coefficients defined in this thesis are functions of these lever arms, then the calibration will produce different results for different mounts. To produce consistent calibrated quantities, the functional dependence of the coefficients on the lever arms must be removed. At the same time, the lever arms must also be calibrated separately, because they are still required to determine the acceleration errors.

Appendix A
Test Table Gimbal Trajectories

GT0 GIMBAL TRAJECTORY

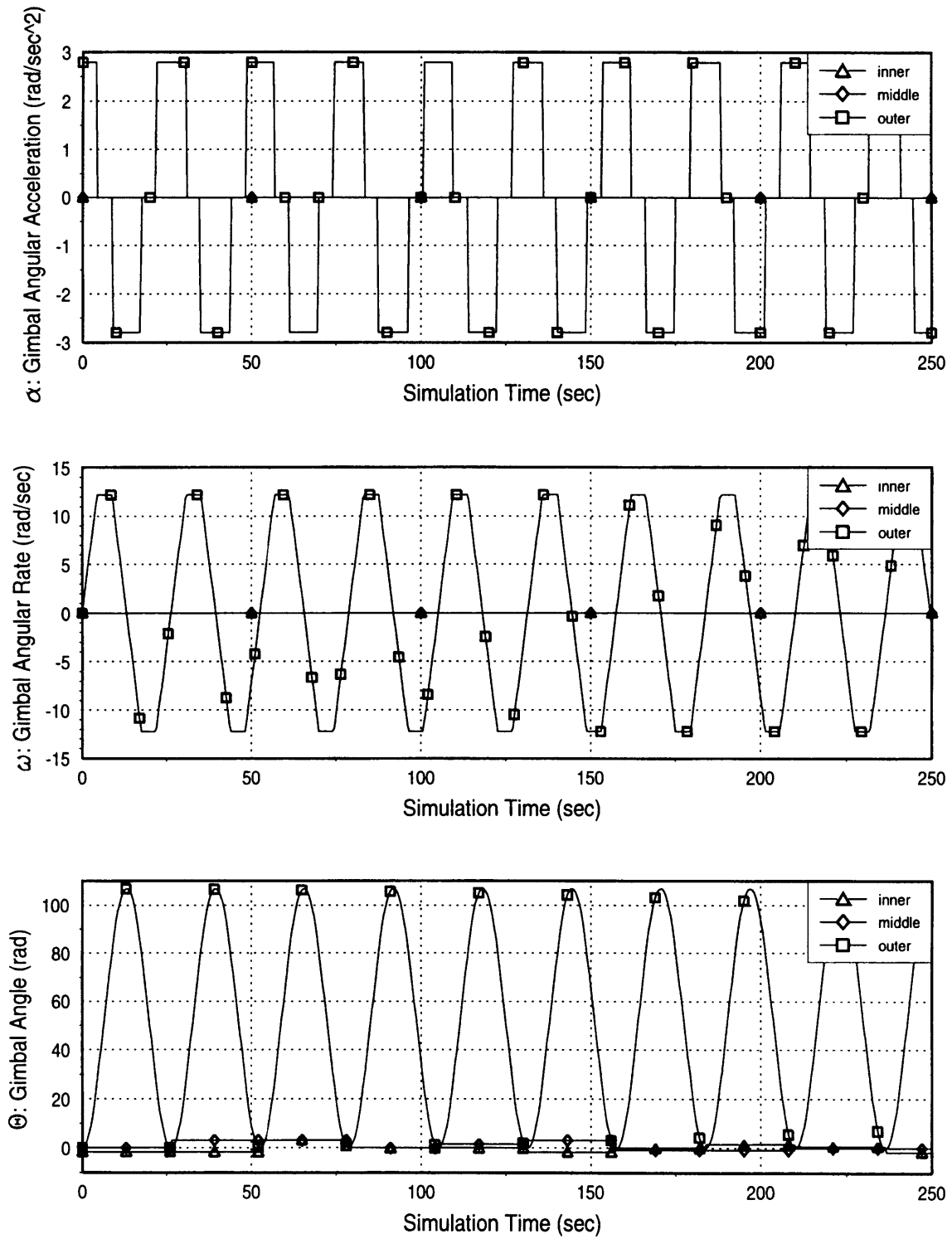


Figure A.1: GT0 Gimbal Trajectory

GT1 GIMBAL TRAJECTORY

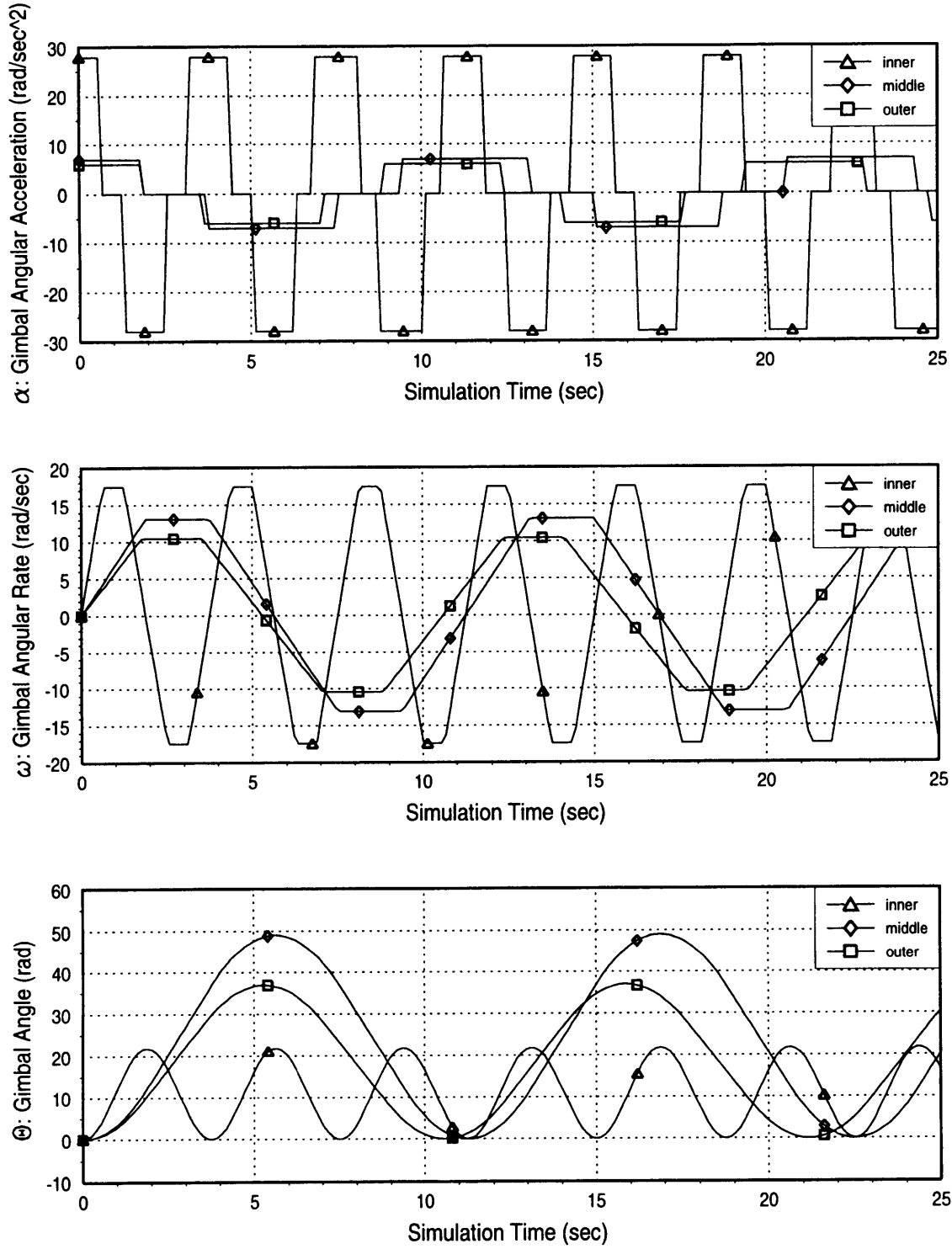


Figure A.2: GT1 Gimbal Trajectory

GT2 GIMBAL TRAJECTORY

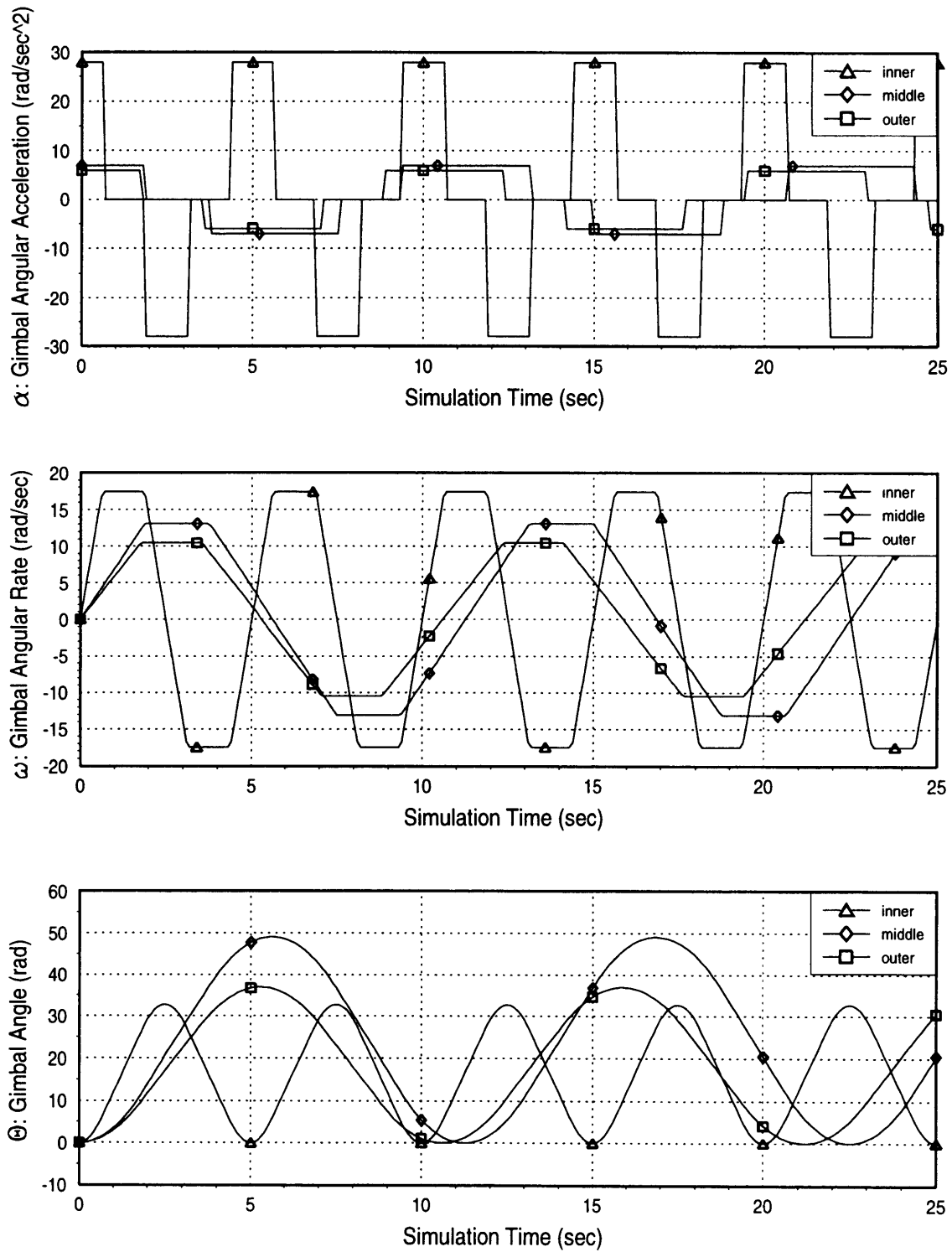


Figure A.3: GT2 Gimbal Trajectory

GT3 GIMBAL TRAJECTORY

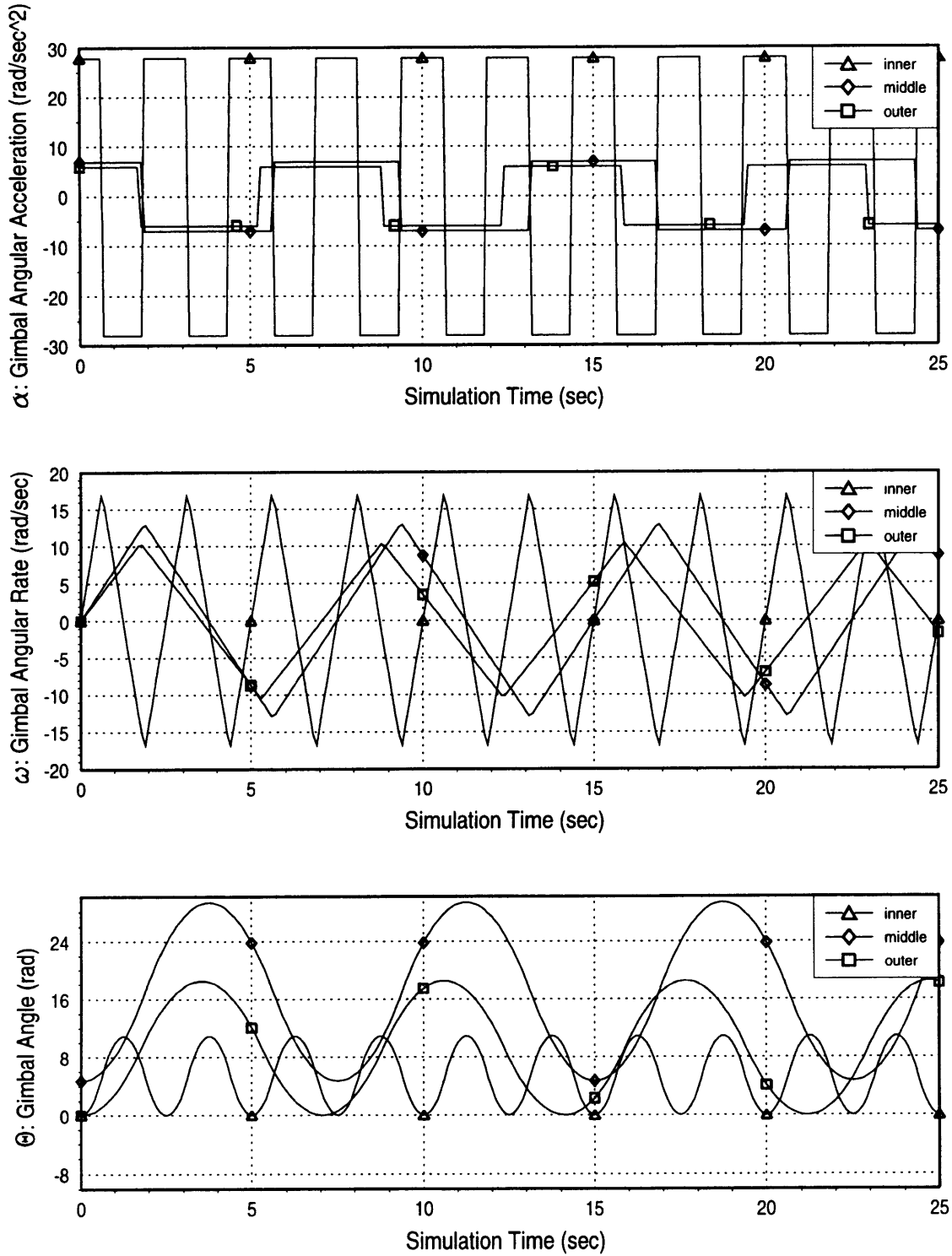


Figure A.4: GT3 Gimbal Trajectory

GT4 GIMBAL TRAJECTORY

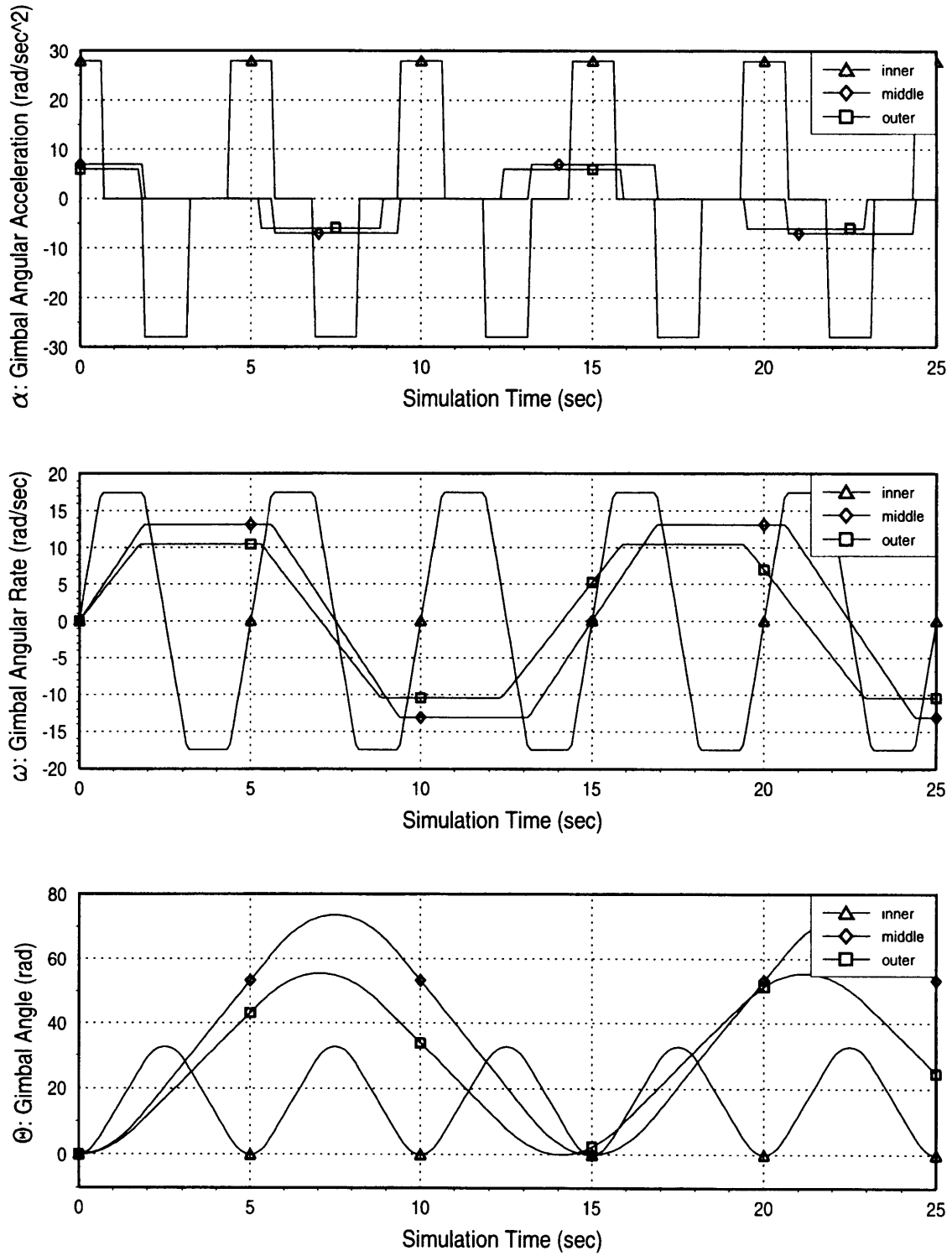


Figure A.5: GT4 Gimbal Trajectory

GT5 GIMBAL TRAJECTORY

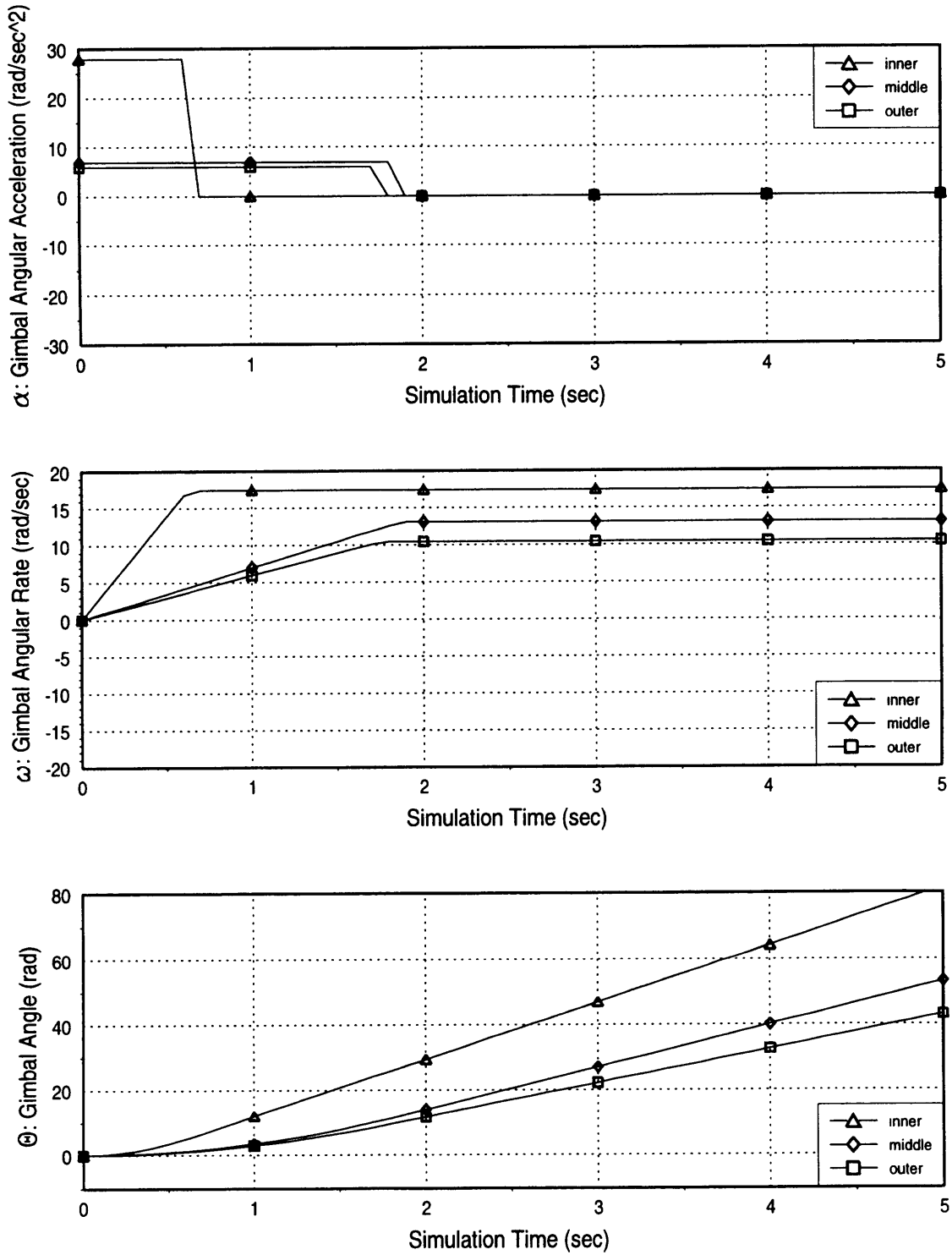


Figure A.6: GT5 Gimbal Trajectory

GTX1 EXTENDED GIMBAL TRAJECTORY

Time Period = 20 seconds

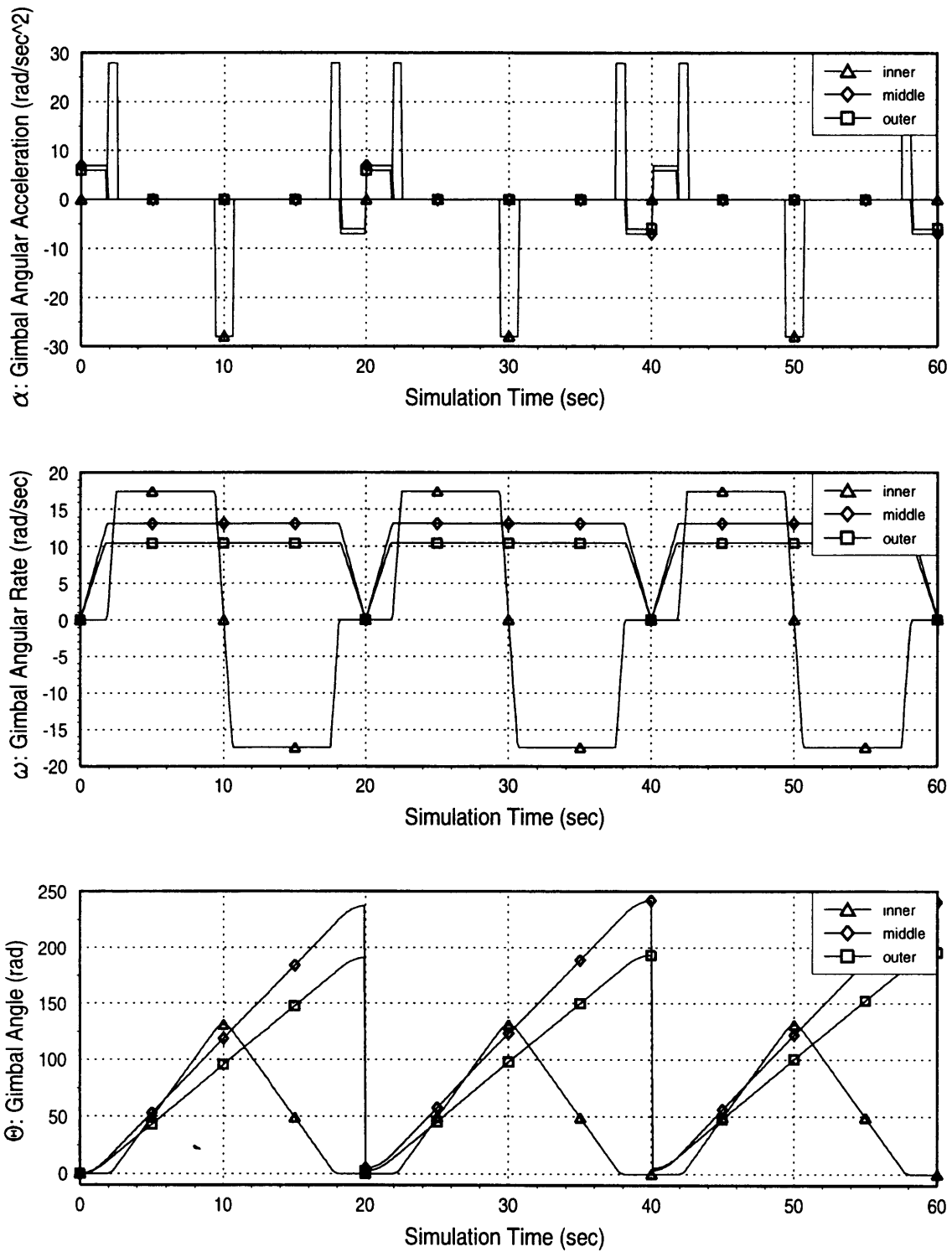


Figure A.7: GTX1 Extended Gimbal Trajectory

GTX1b EXTENDED GIMBAL TRAJECTORY

Time Period = 20 seconds

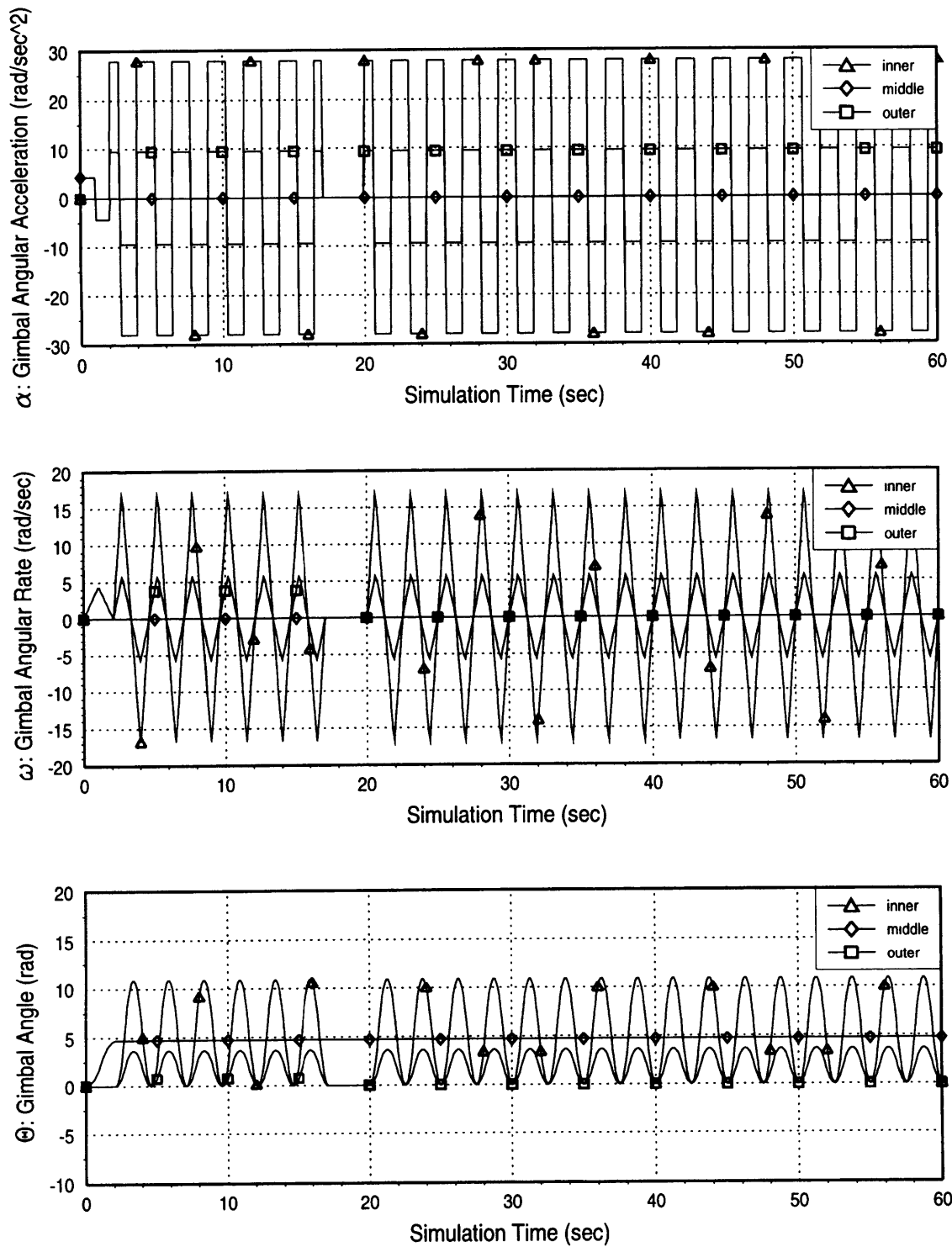


Figure A.8: GTX1b Extended Gimbal Trajectory

GTX2 EXTENDED GIMBAL TRAJECTORY

Time Period = 20 seconds

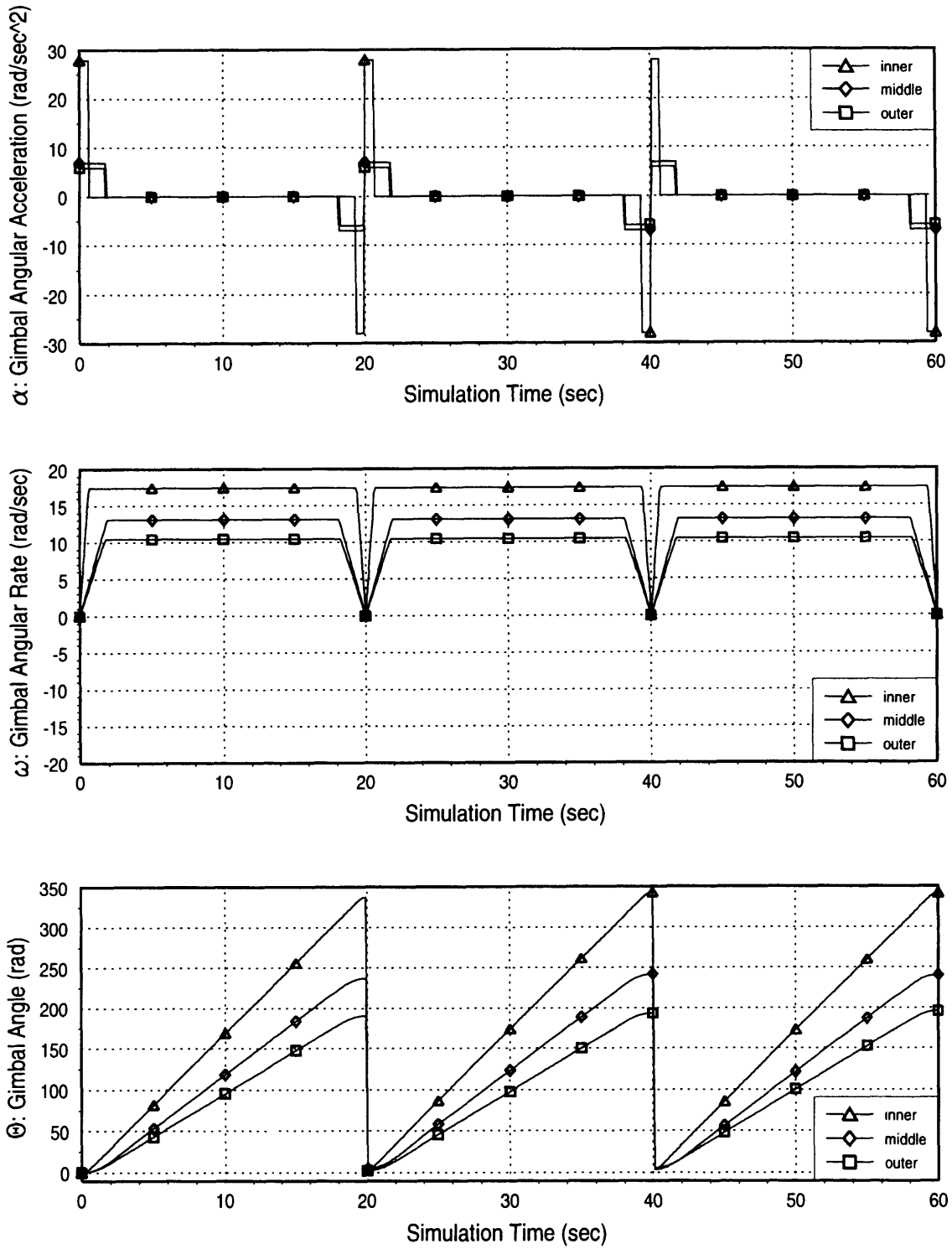


Figure A.9: GTX2 Extended Gimbal Trajectory

GTX2b EXTENDED GIMBAL TRAJECTORY

Time Period = 20 seconds

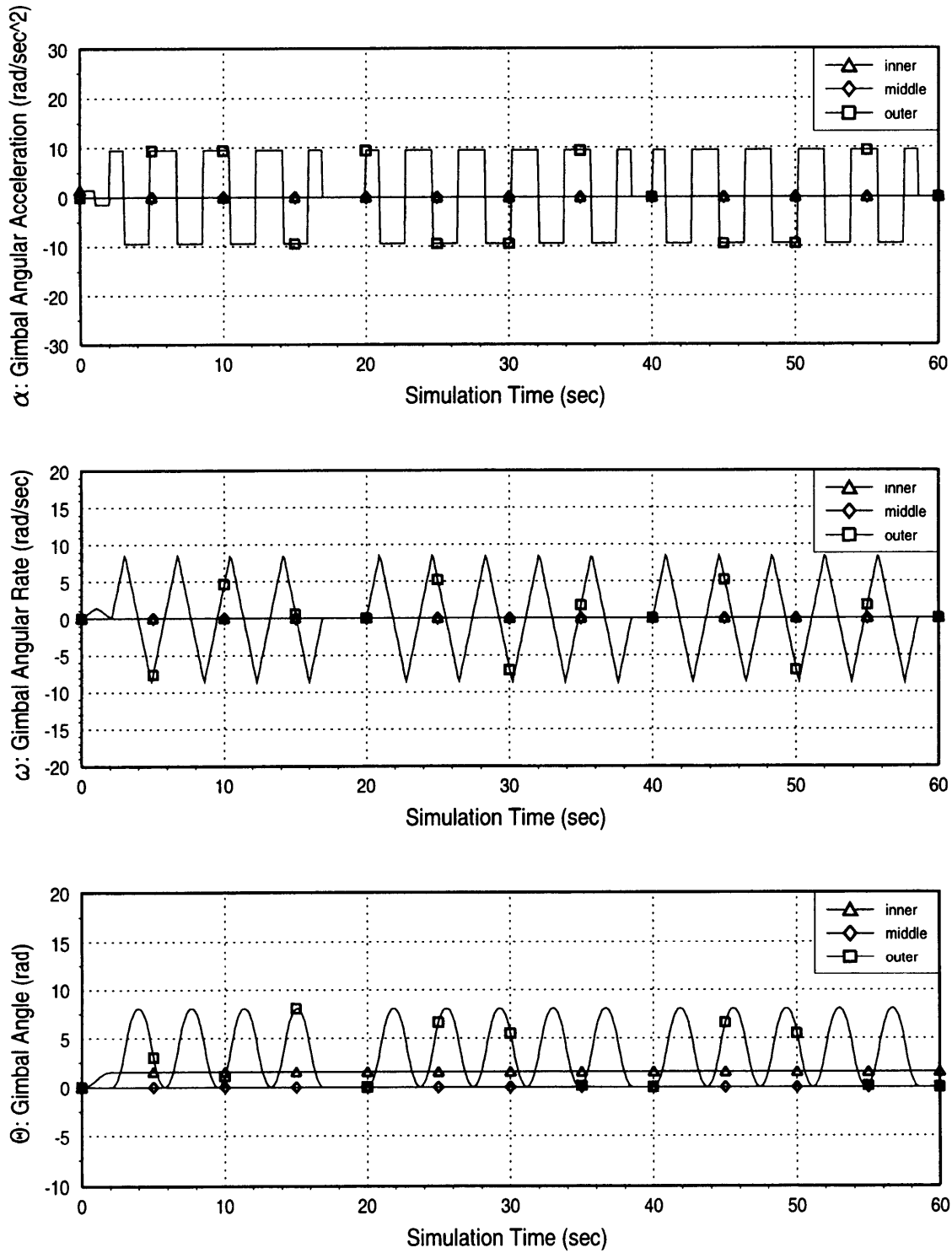


Figure A.10: GTX2b Extended Gimbal Trajectory

GTX3 EXTENDED GIMBAL TRAJECTORY

Time Period = 20 seconds

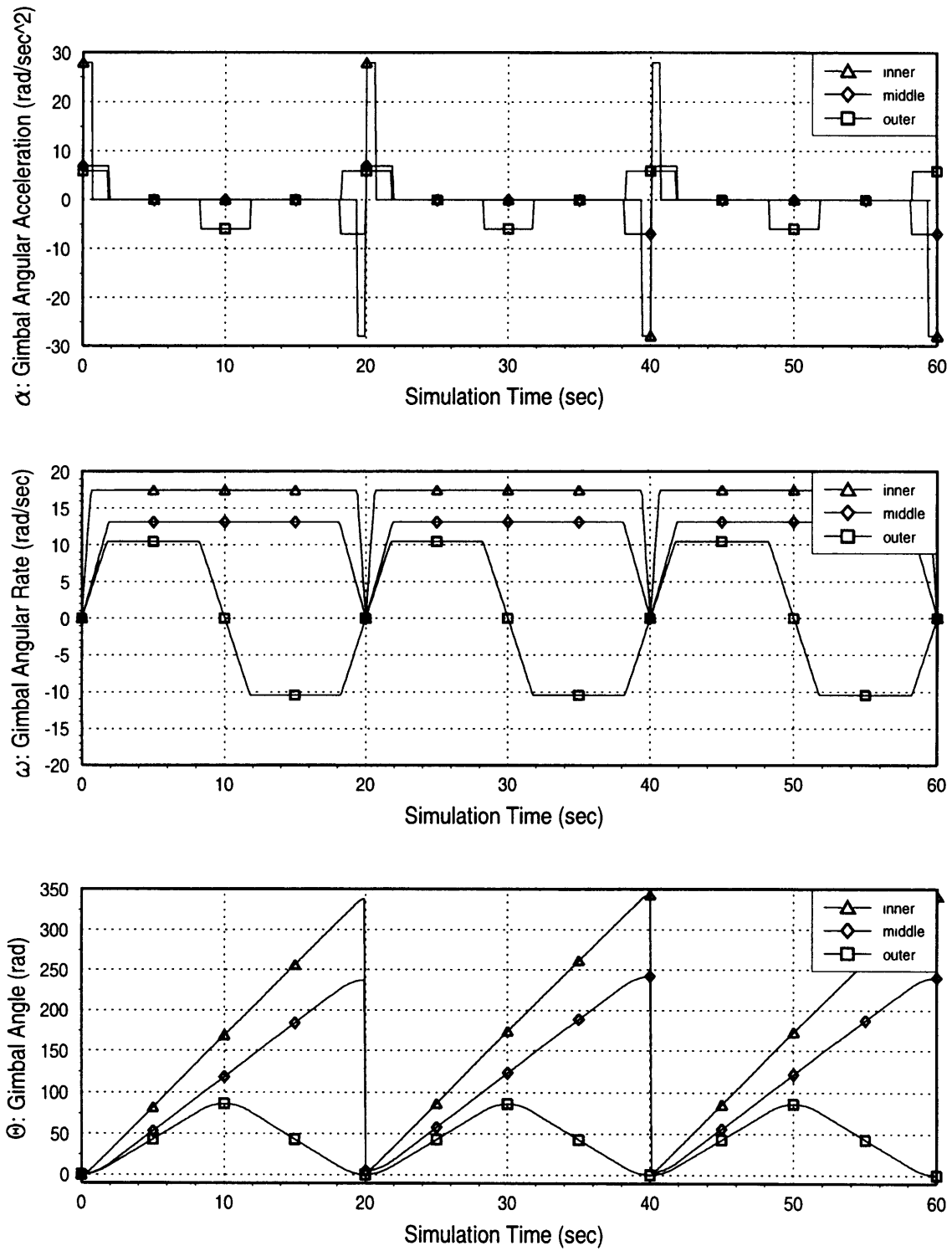


Figure A.11: GTX3 Extended Gimbal Trajectory

GTX3b EXTENDED GIMBAL TRAJECTORY

Time Period = 20 seconds

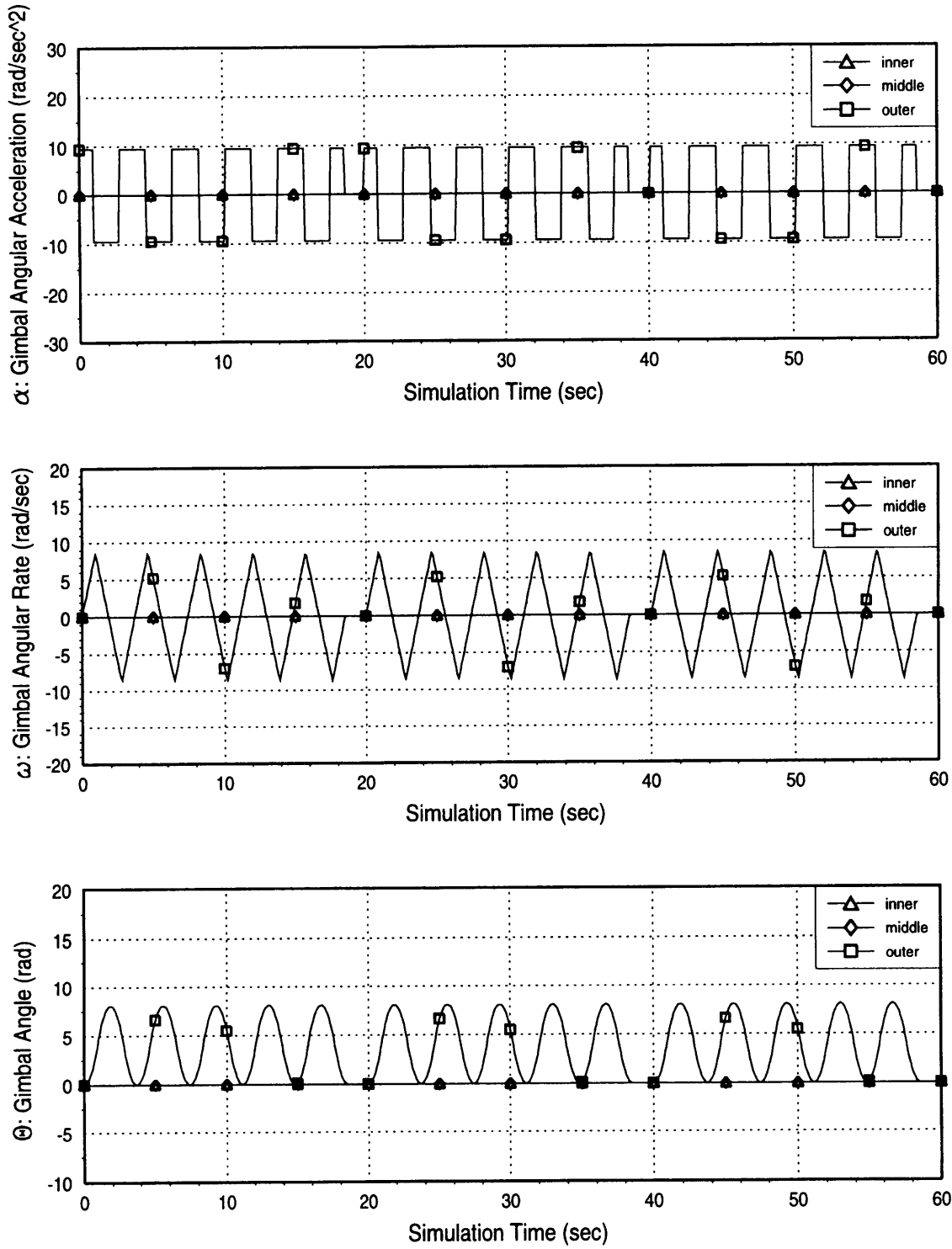


Figure A.12: GTX3b Extended Gimbal Trajectory

GTX4 EXTENDED GIMBAL TRAJECTORY

Time Period = 20 seconds

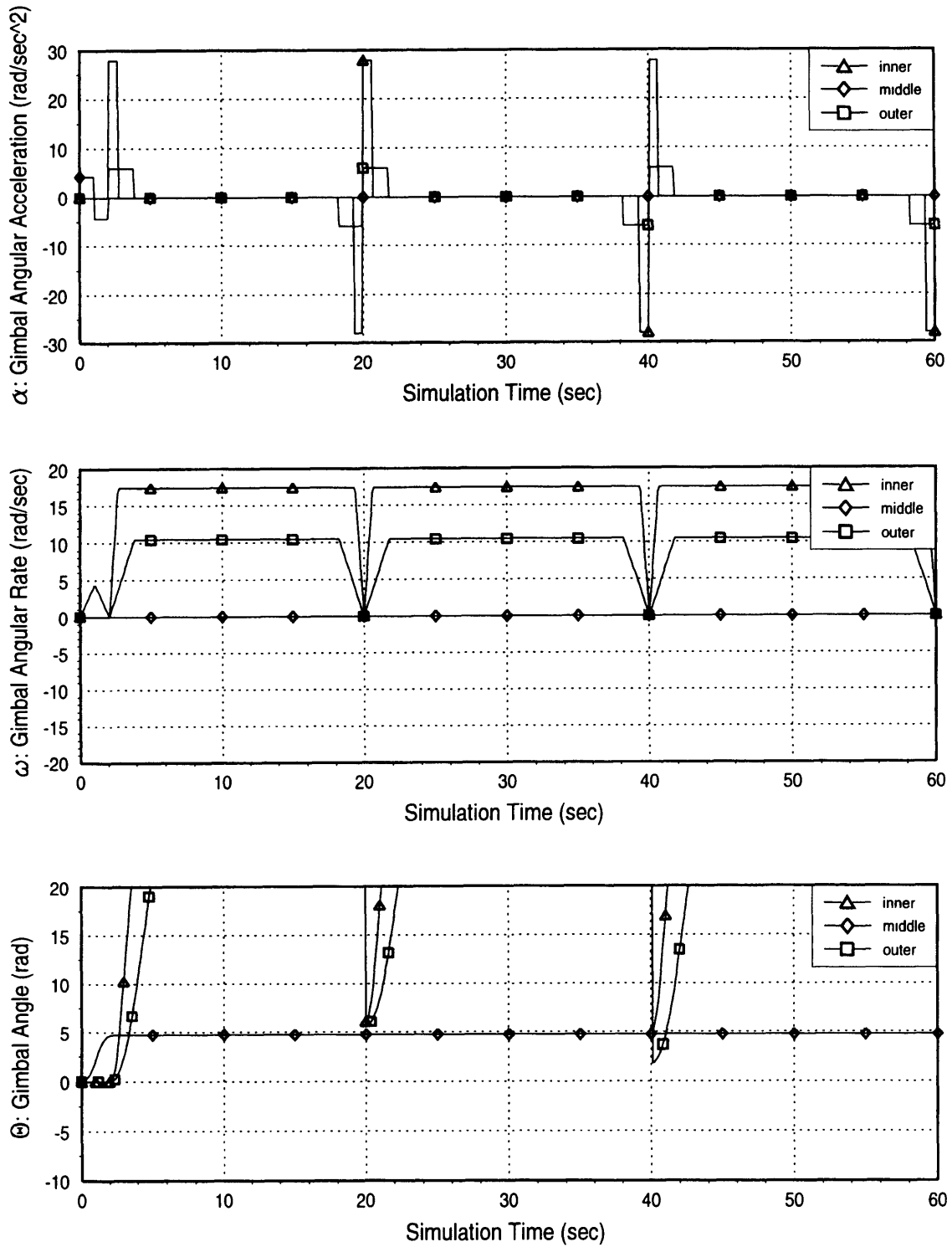


Figure A.13: GTX4 Extended Gimbal Trajectory

GTX5 EXTENDED GIMBAL TRAJECTORY

Time Period = 20 seconds

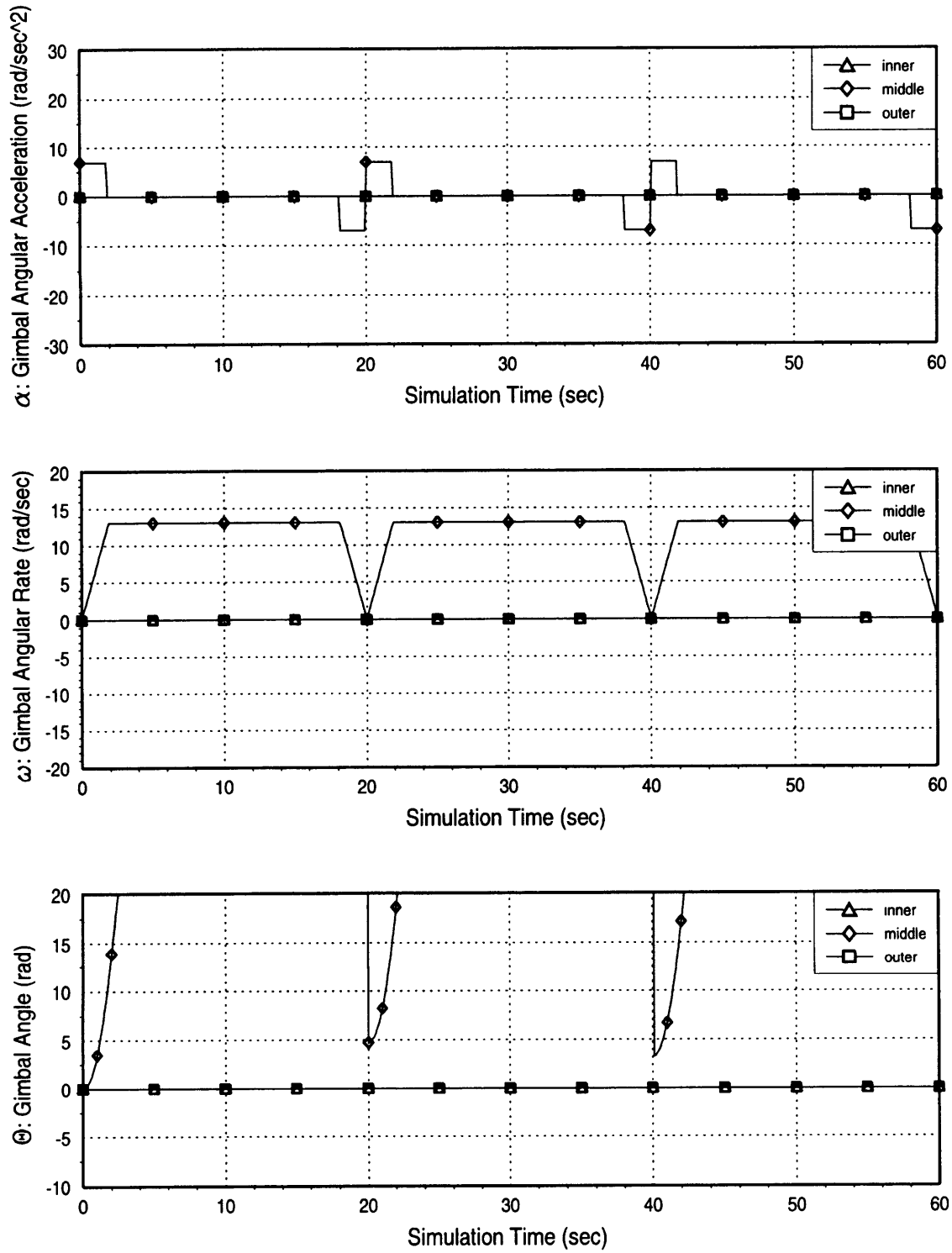


Figure A.14: GTX5 Extended Gimbal Trajectory

GTX6 EXTENDED GIMBAL TRAJECTORY

Time Period = 20 seconds

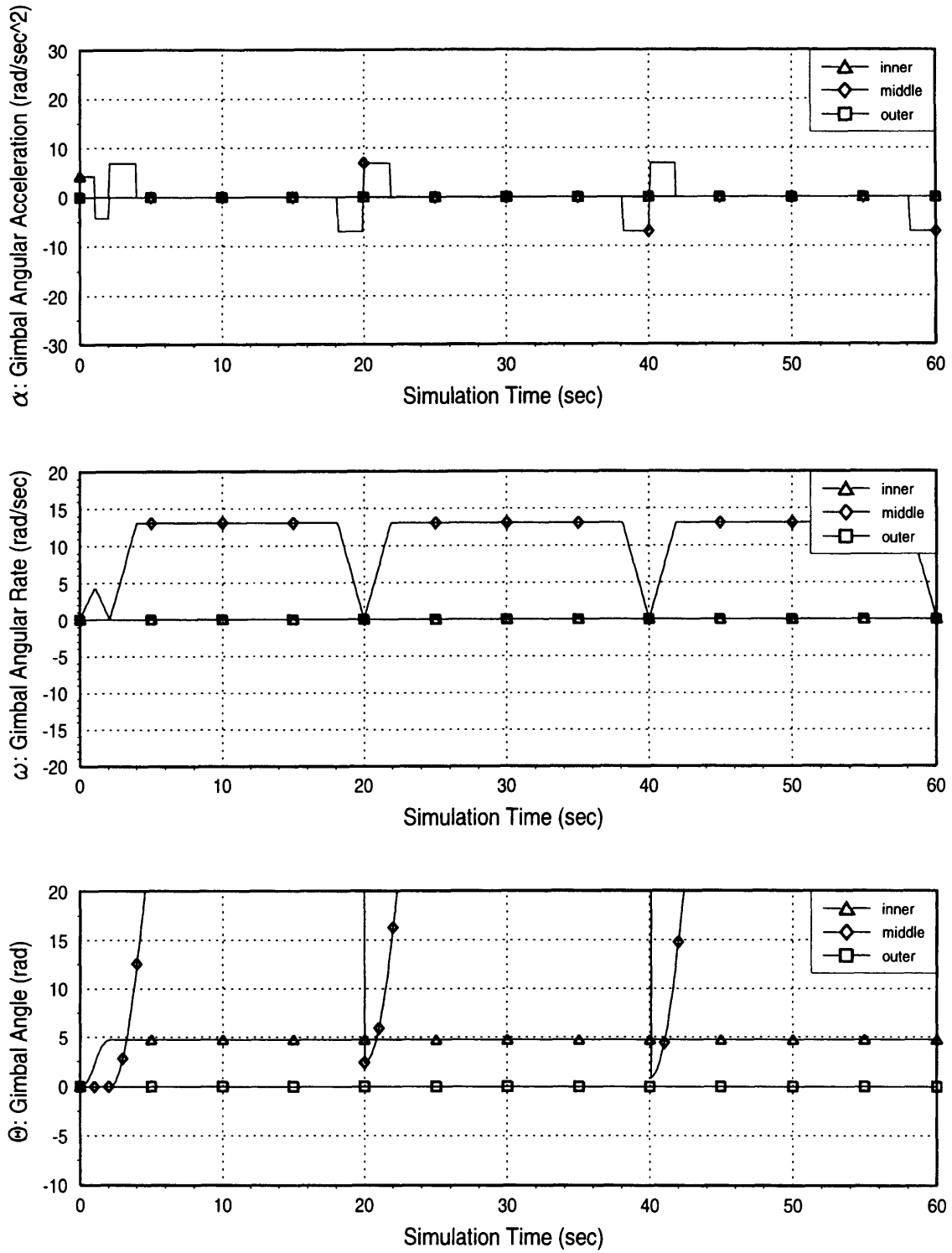


Figure A.15: GTX6 Extended Gimbal Trajectory

GTX7 EXTENDED GIMBAL TRAJECTORY

Time Period = 20 seconds

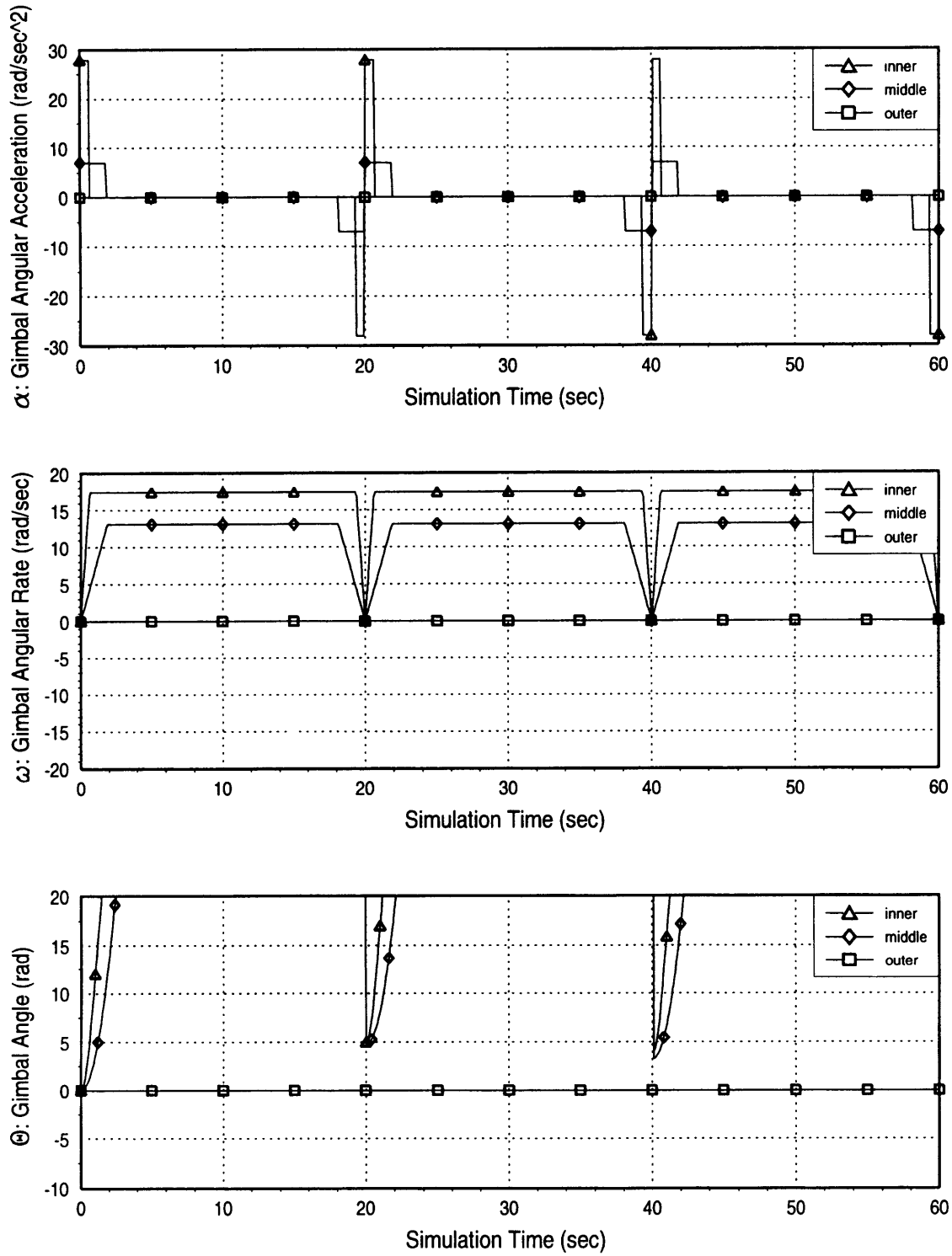


Figure A.16: GTX7 Extended Gimbal Trajectory

GTX7b EXTENDED GIMBAL TRAJECTORY

Time Period = 20 seconds

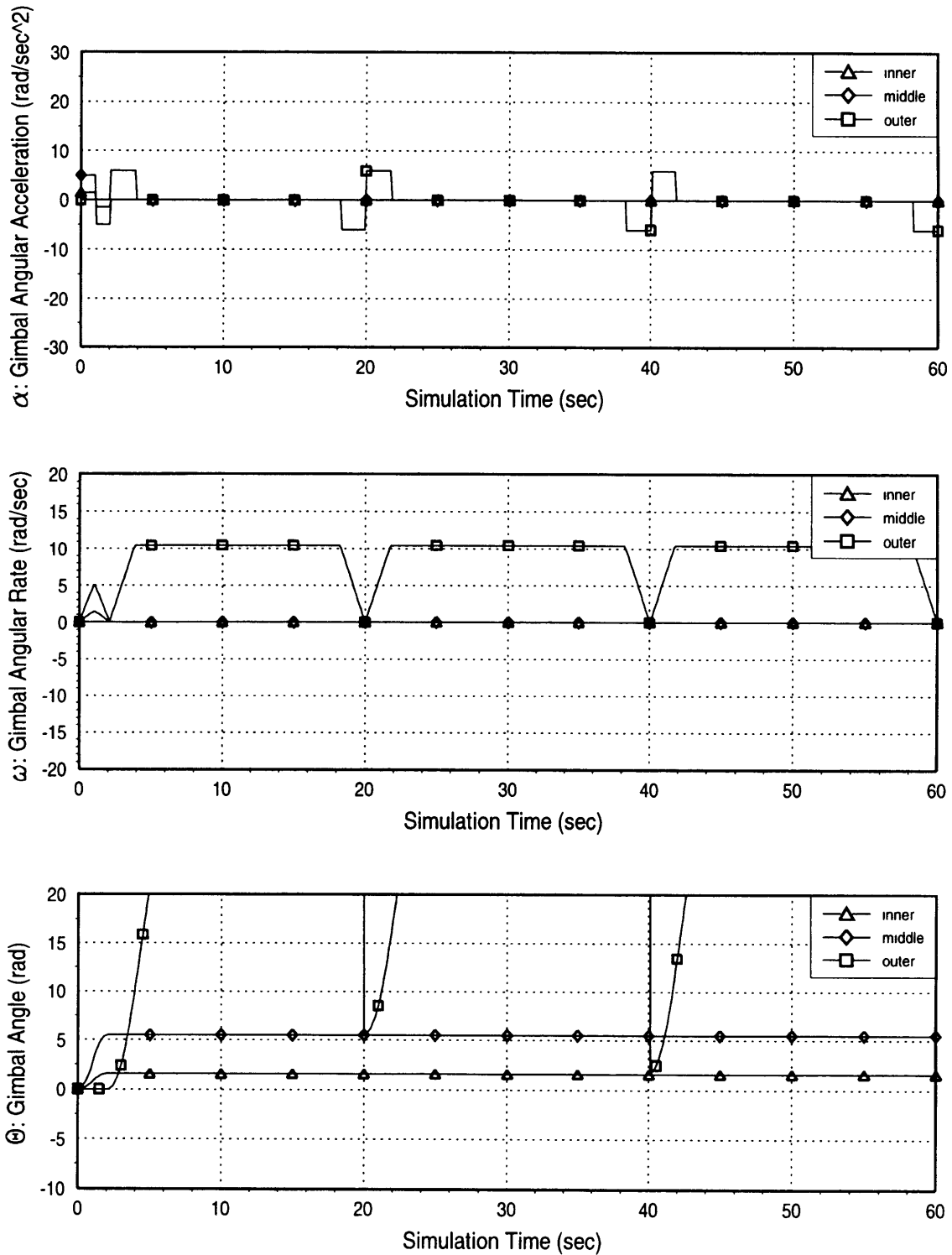


Figure A.17: GTX7b Extended Gimbal Trajectory

GTX8b EXTENDED GIMBAL TRAJECTORY

Time Period = 20 seconds

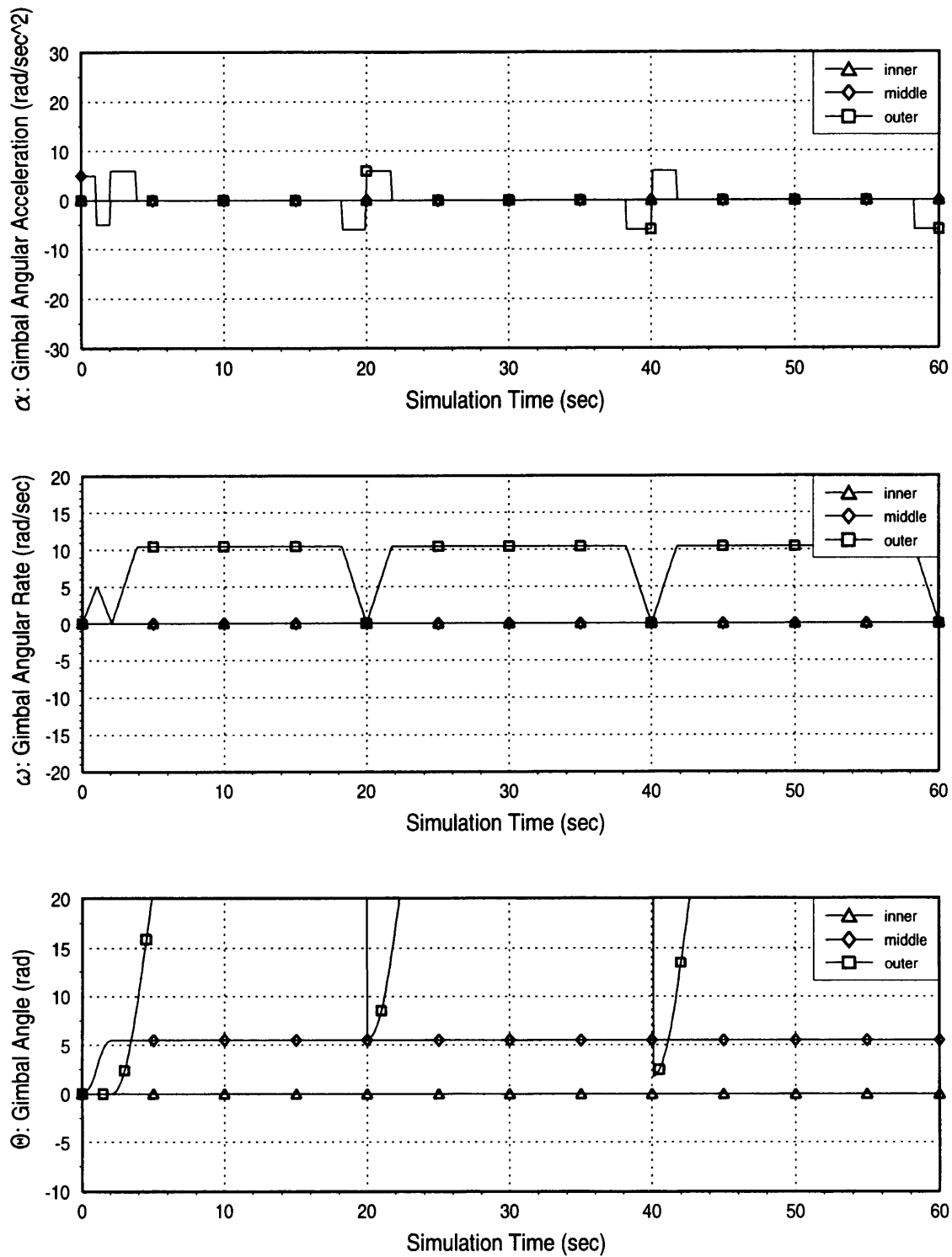


Figure A.18: GTX8b Extended Gimbal Trajectory

GTX9 EXTENDED GIMBAL TRAJECTORY

Time Period = 20 seconds

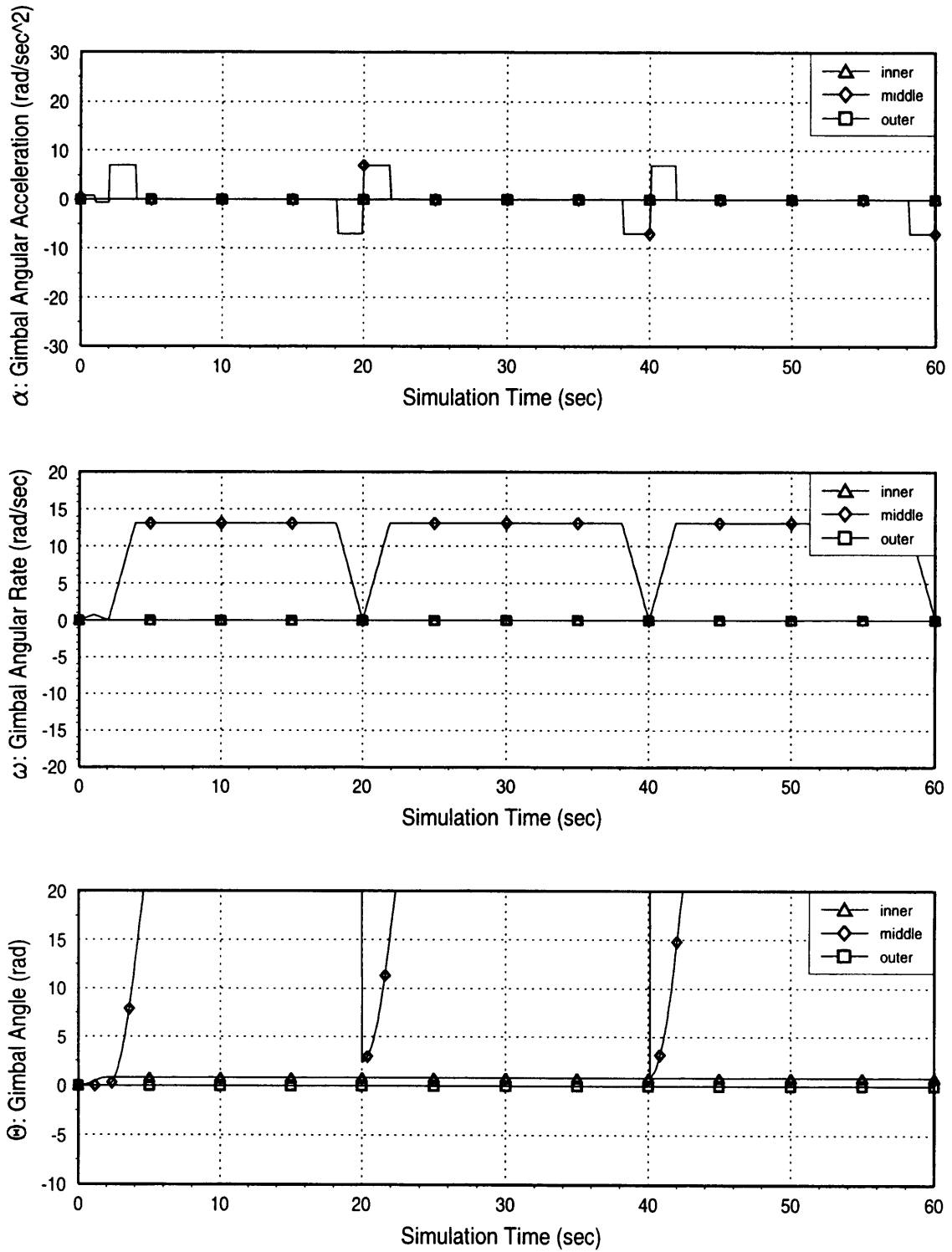


Figure A.19: GTX9 Extended Gimbal Trajectory

GT6 GIMBAL TRAJECTORY

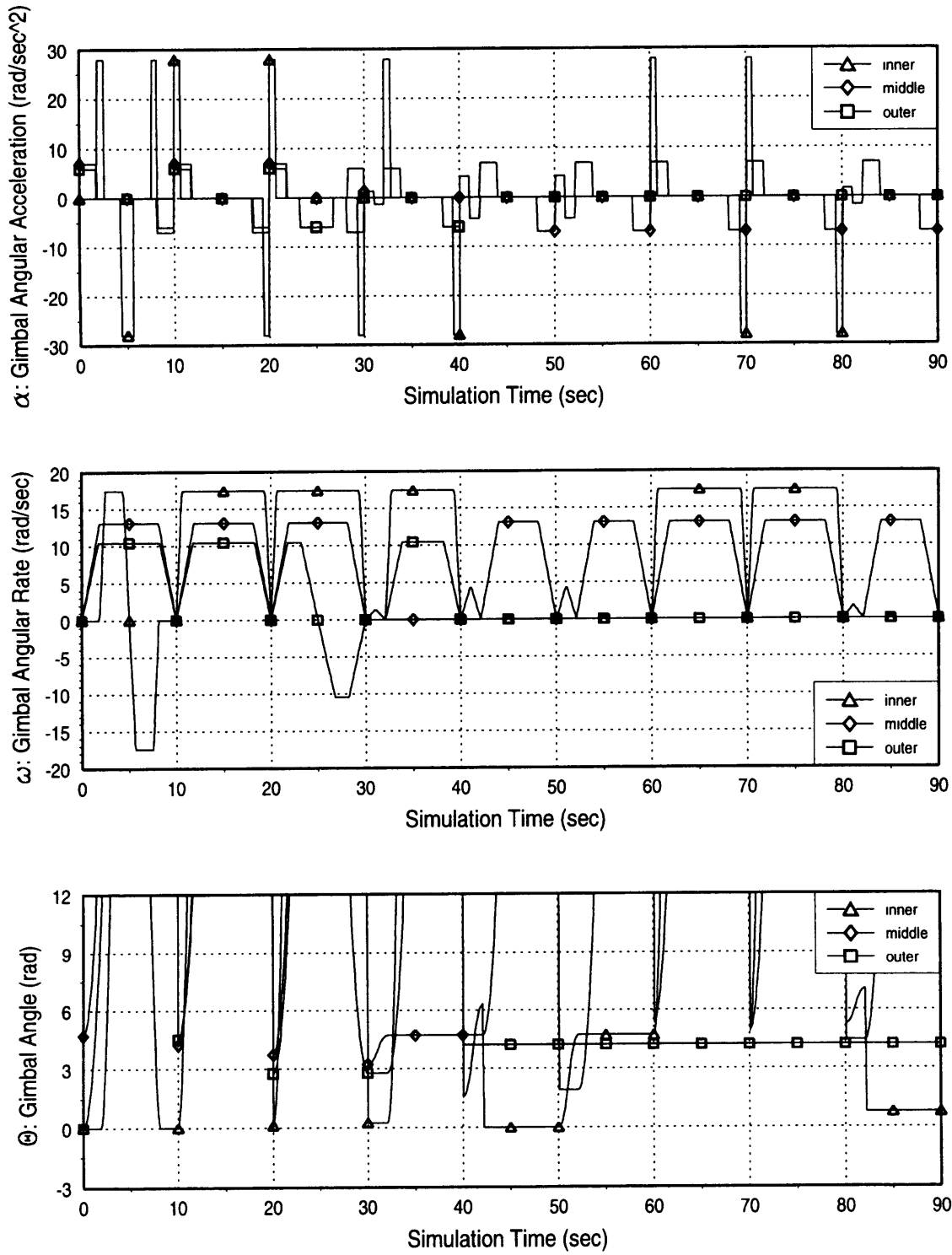


Figure A.20: GT6 Gimbal Trajectory

GT6b GIMBAL TRAJECTORY

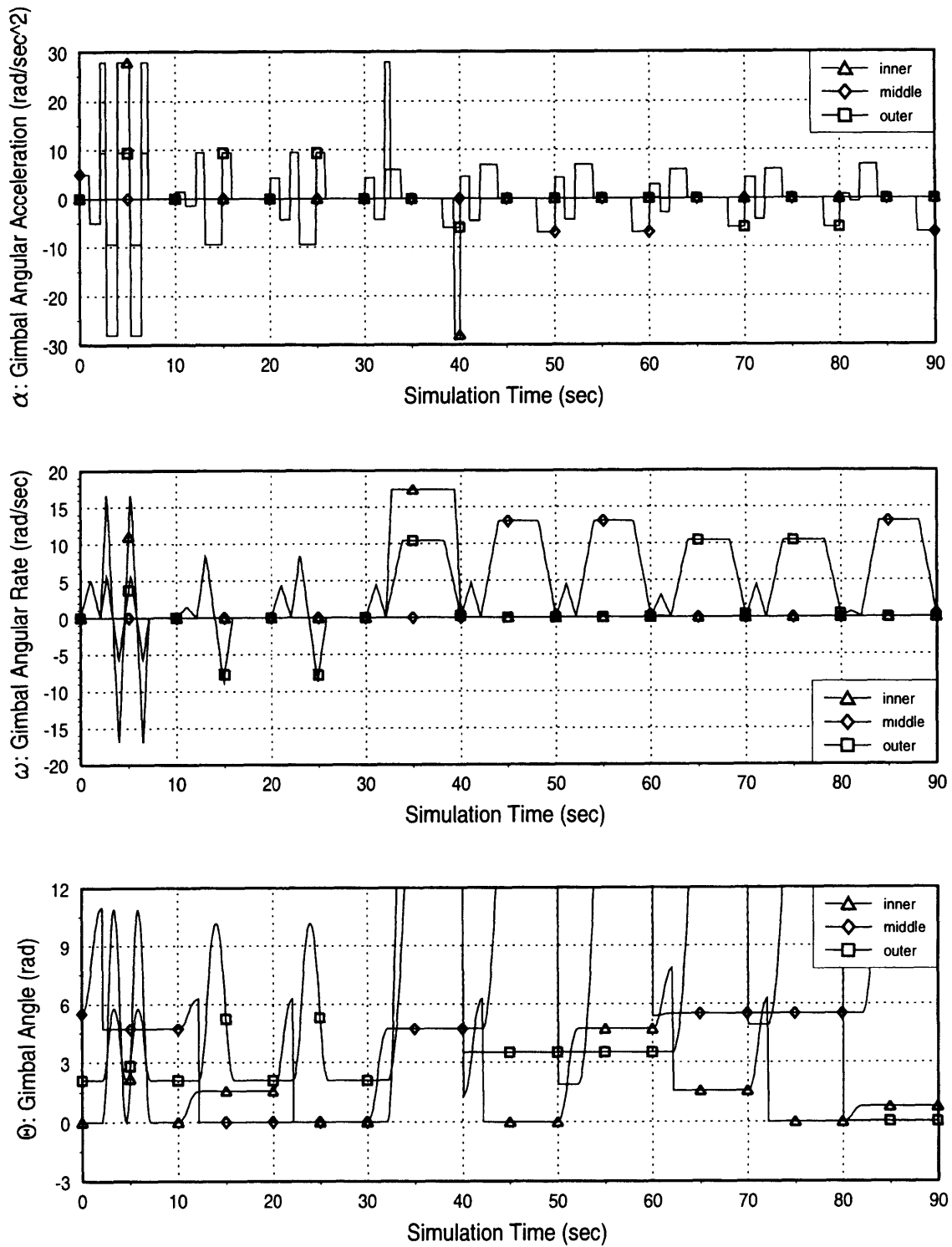


Figure A.21: GT6b Gimbal Trajectory

GT6c GIMBAL TRAJECTORY

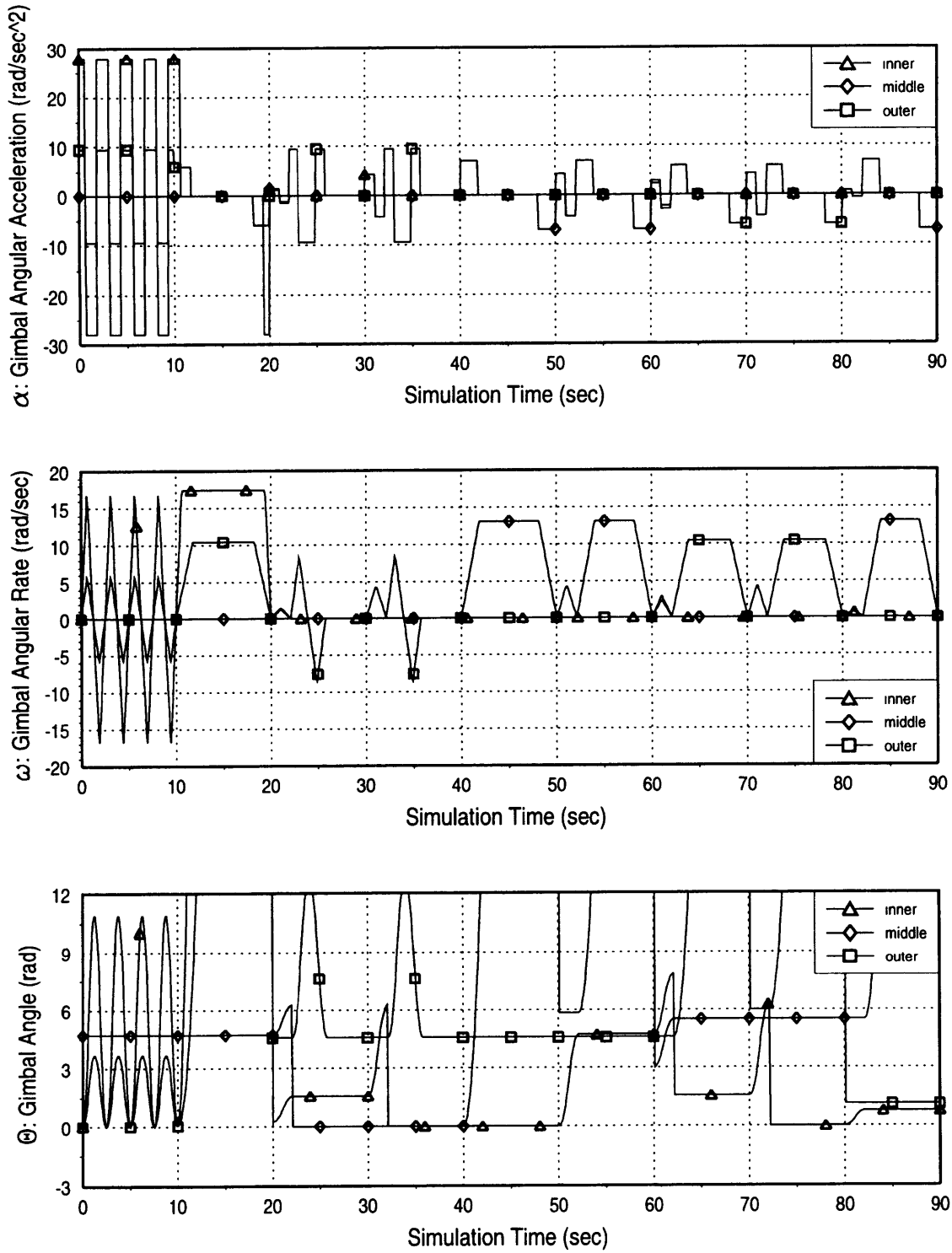


Figure A.22: GT6c Gimbal Trajectory

GT3opt GIMBAL TRAJECTORY

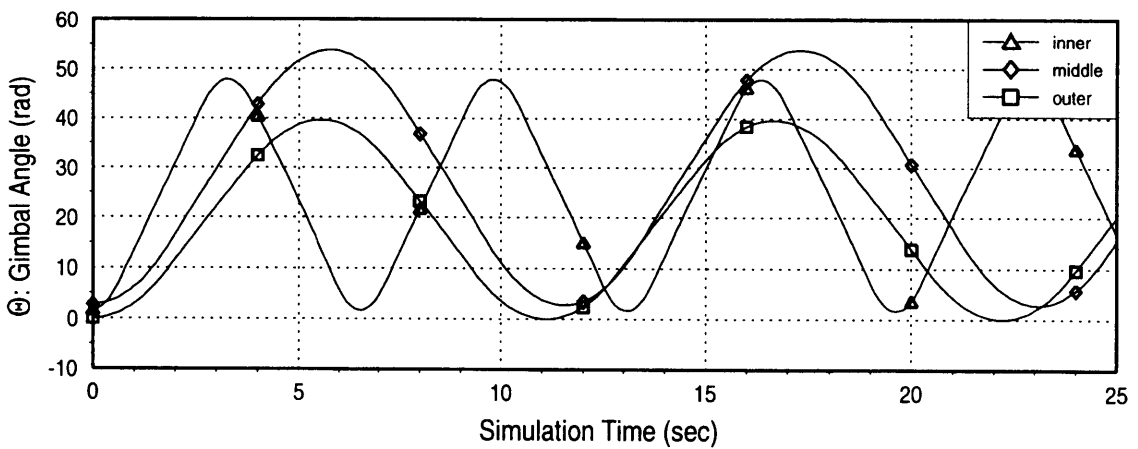
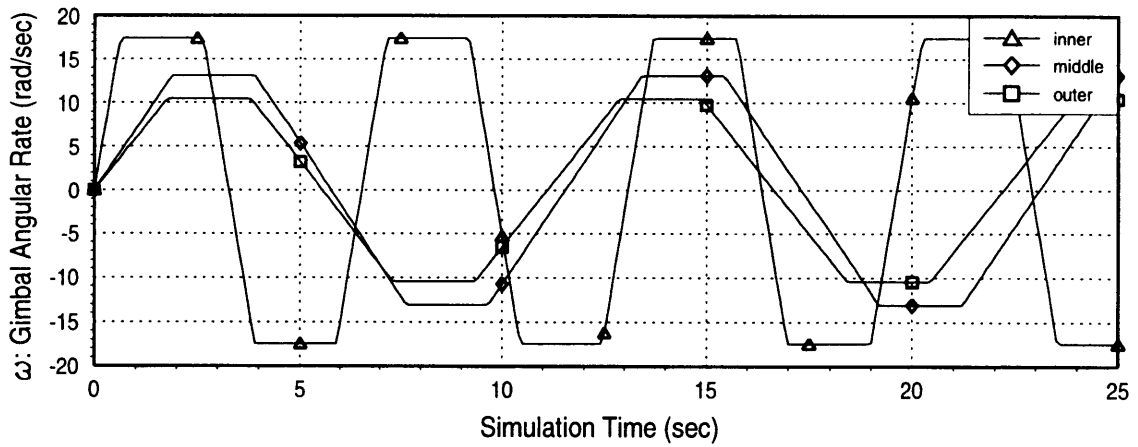
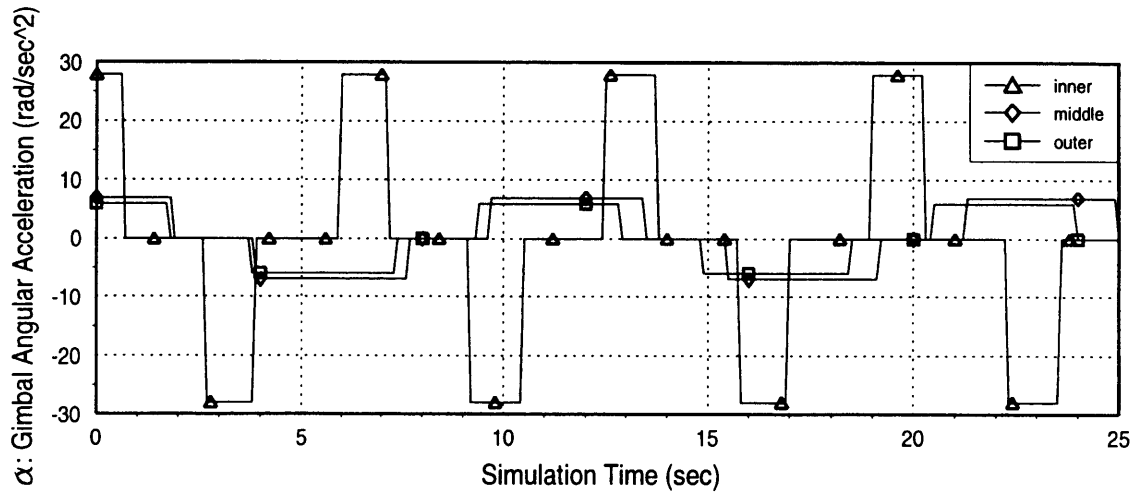


Figure A.23: GT3opt Gimbal Trajectory

GT4x GIMBAL TRAJECTORY

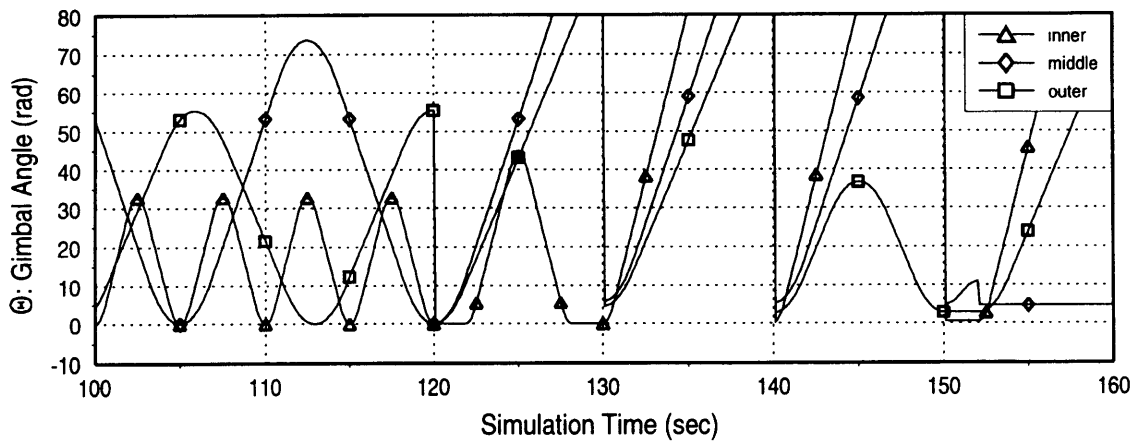
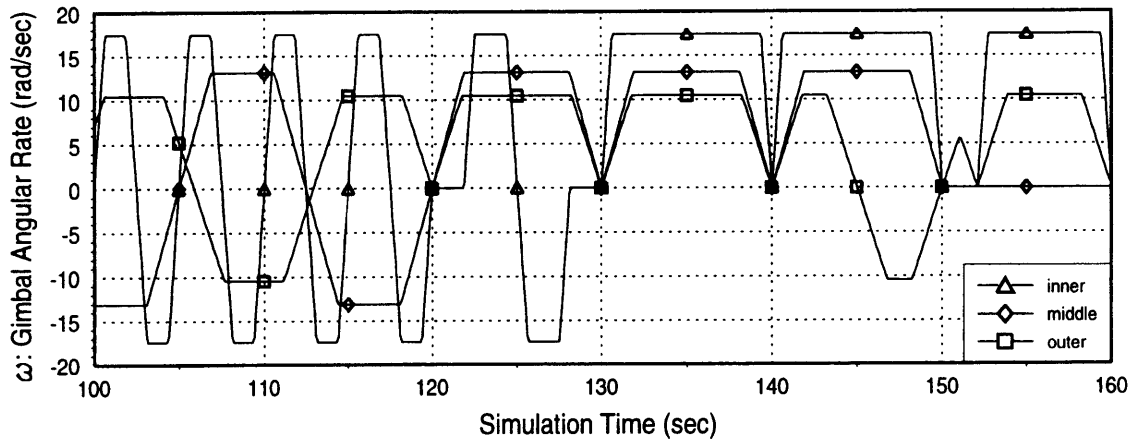
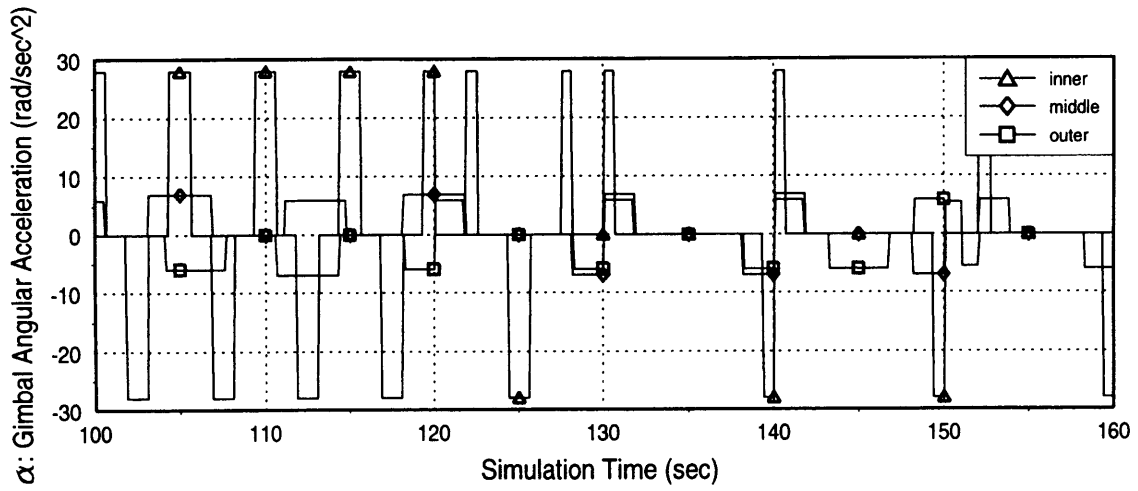


Figure A.24: GT4x Gimbal Trajectory

GT7 GIMBAL TRAJECTORY

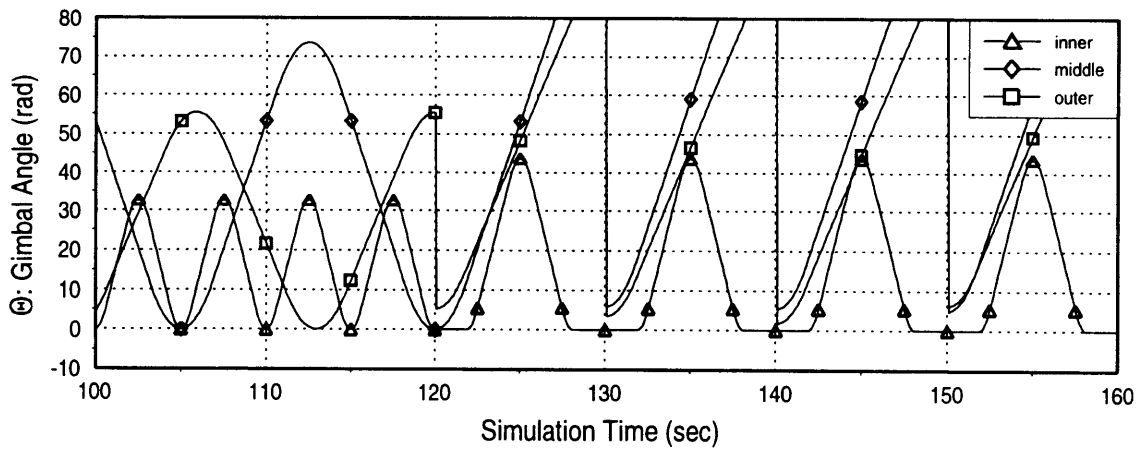
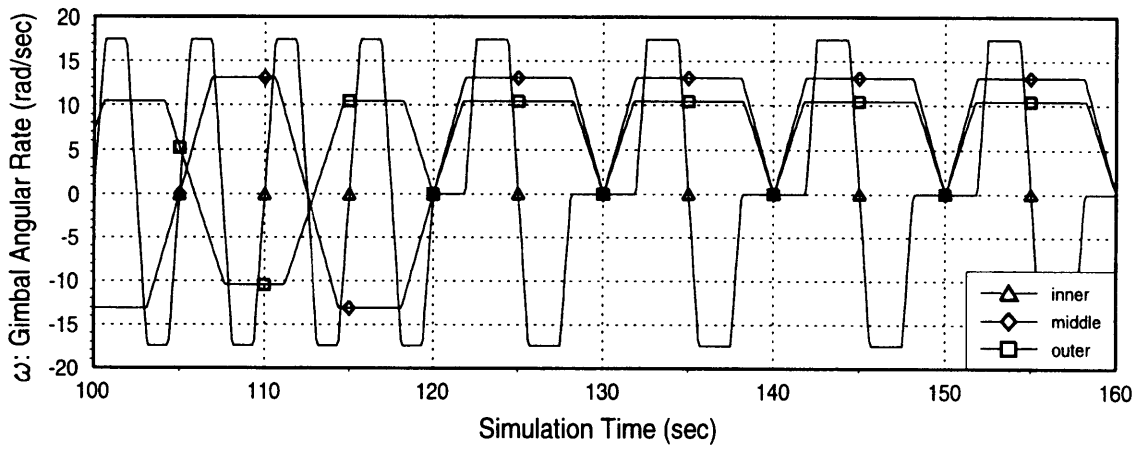
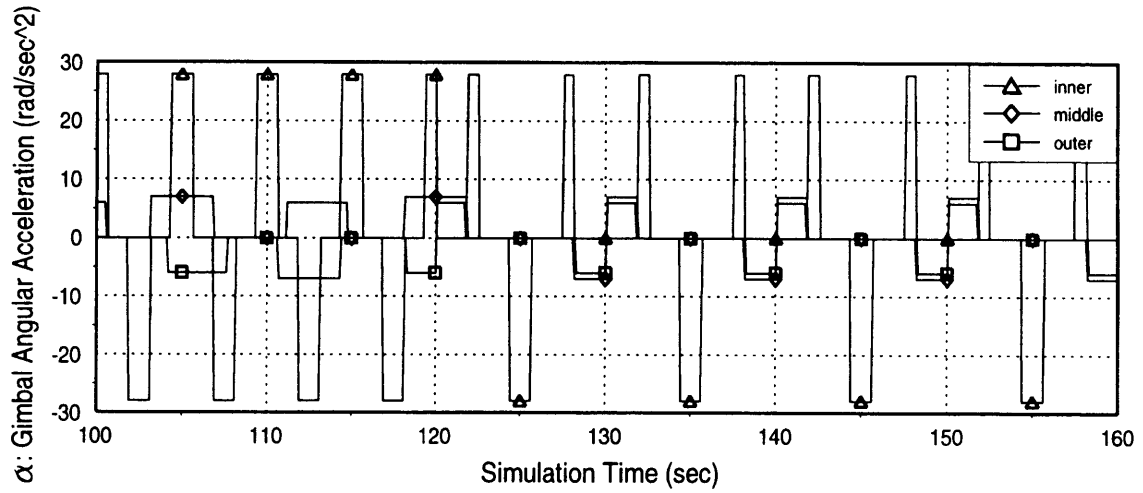


Figure A.25: GT7 Gimbal Trajectory

Appendix B

Graphical Results

Body Frame X-Axis Sensitivities for GT6

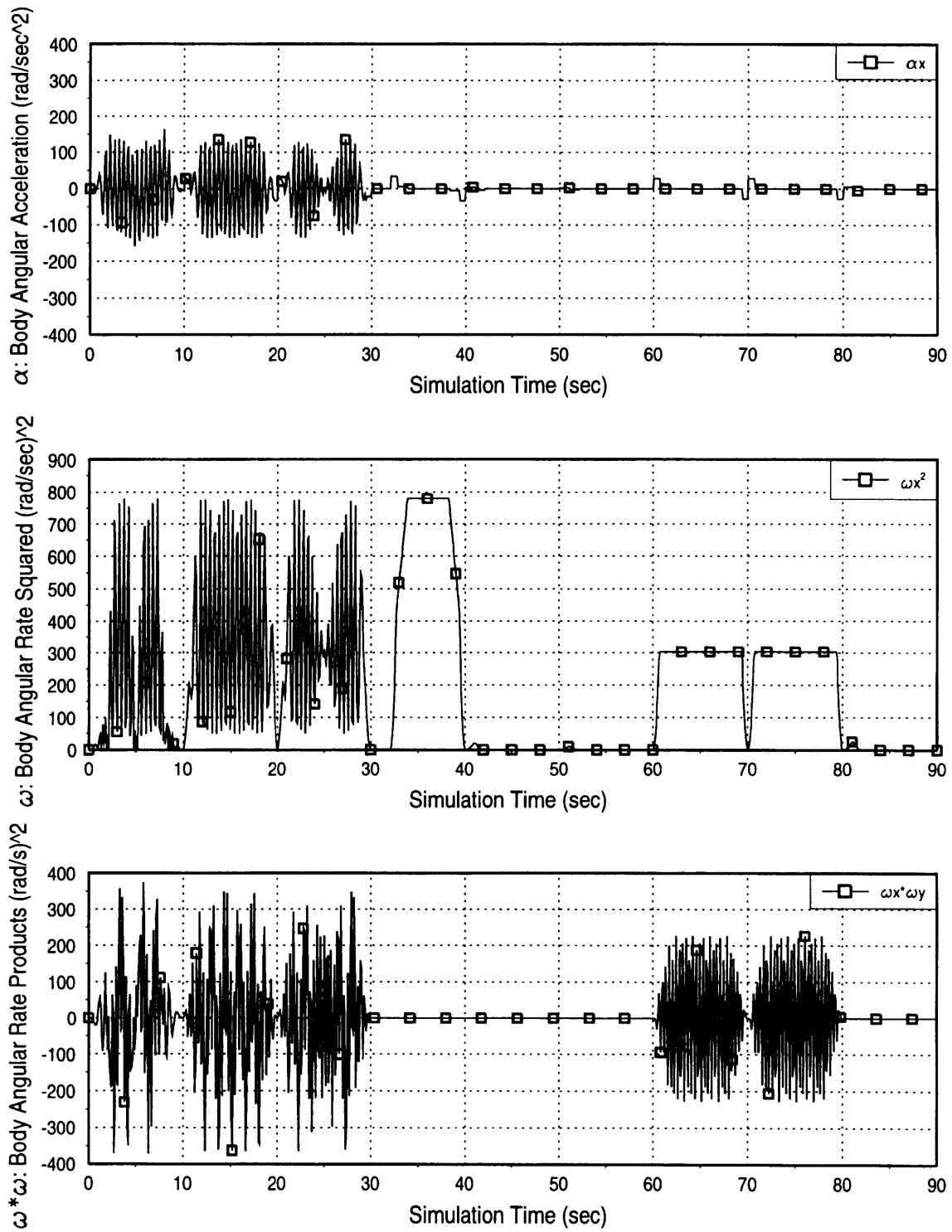


Figure B.1: GT6 Body Frame X-Axis Sensitivities

Body Frame Y-Axis Sensitivities for GT6

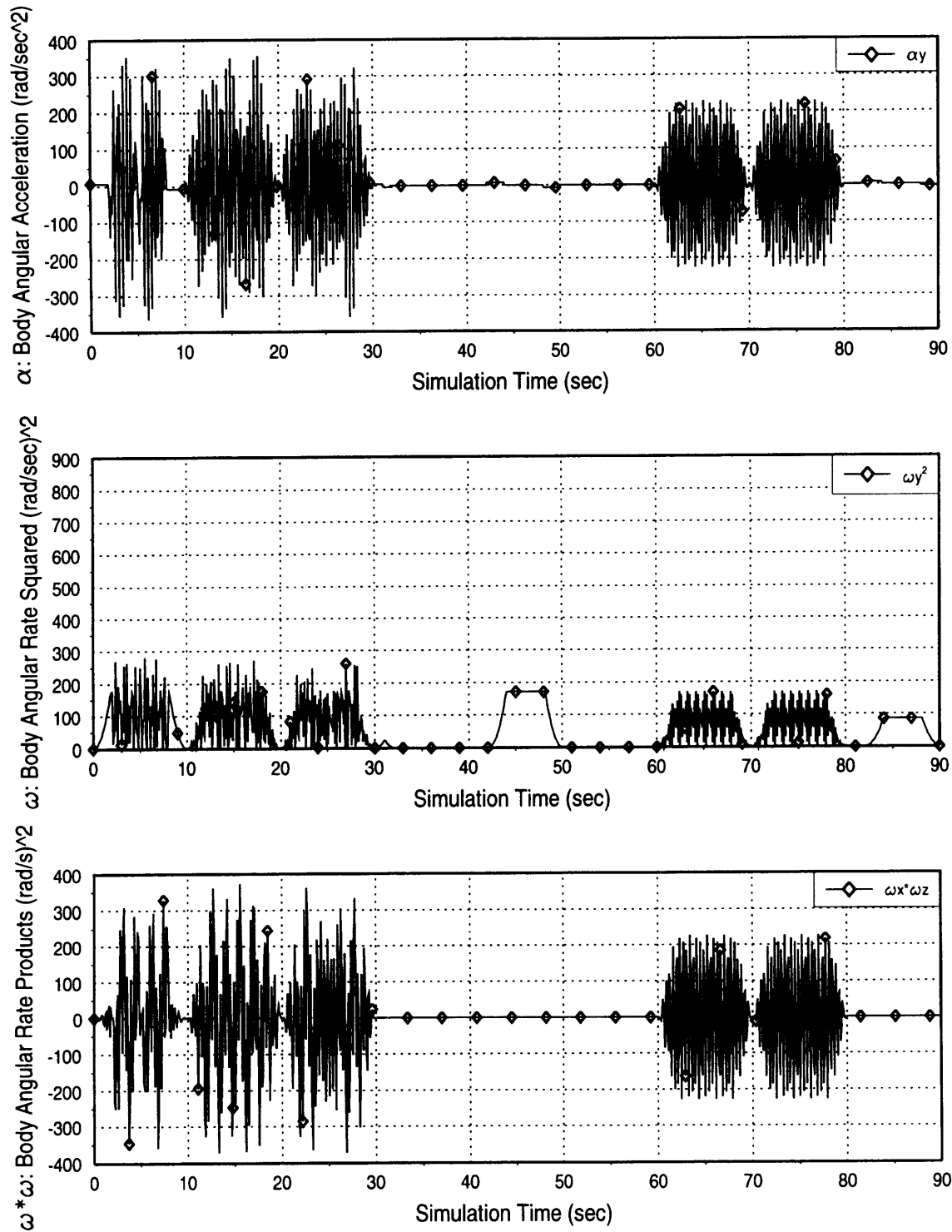


Figure B.2: GT6 Body Frame Y-Axis Sensitivities

Body Frame Z-Axis Sensitivities for GT6

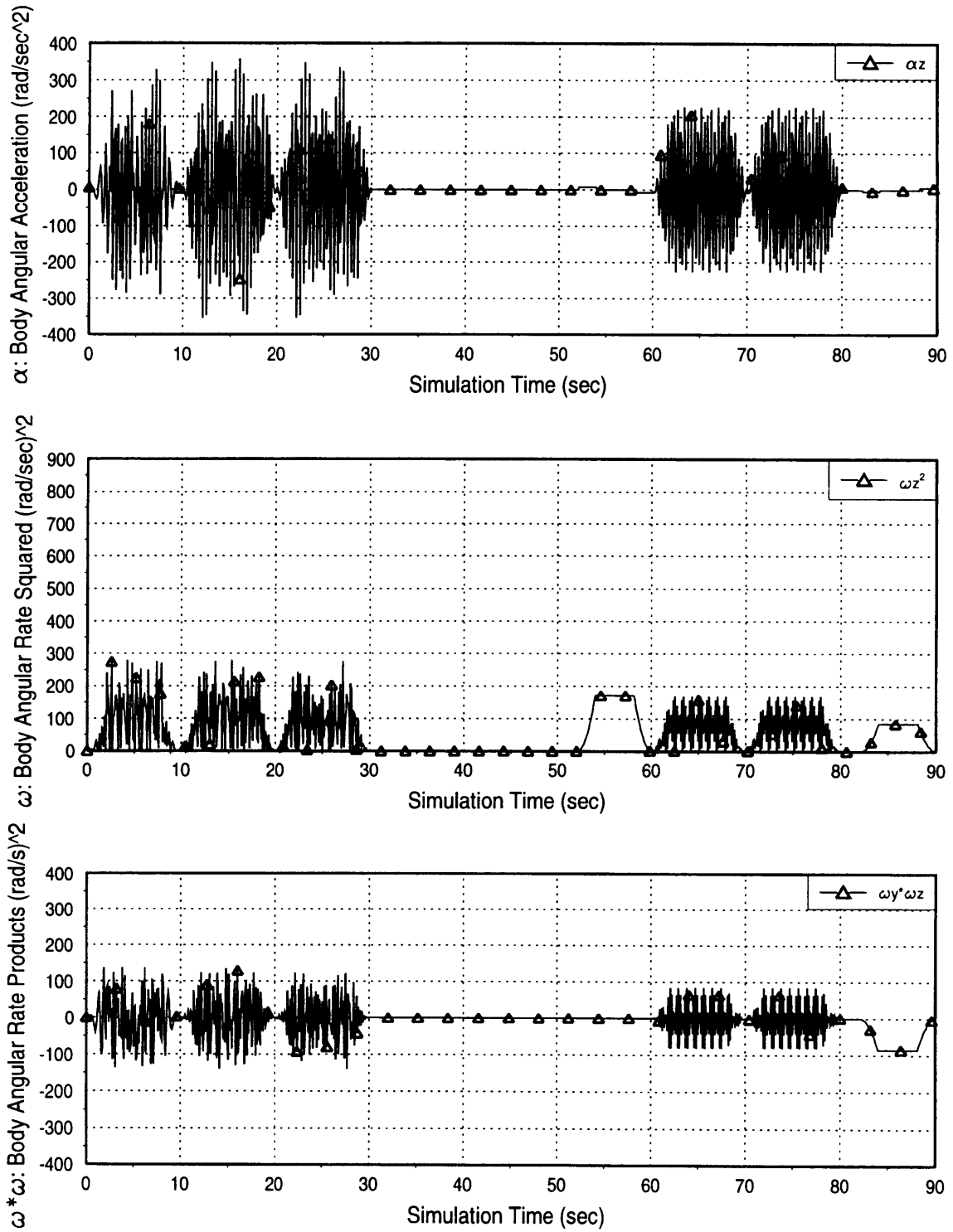


Figure B.3: GT6 Body Frame Z-Axis Sensitivities

Body Frame Sensitivities for GT6b

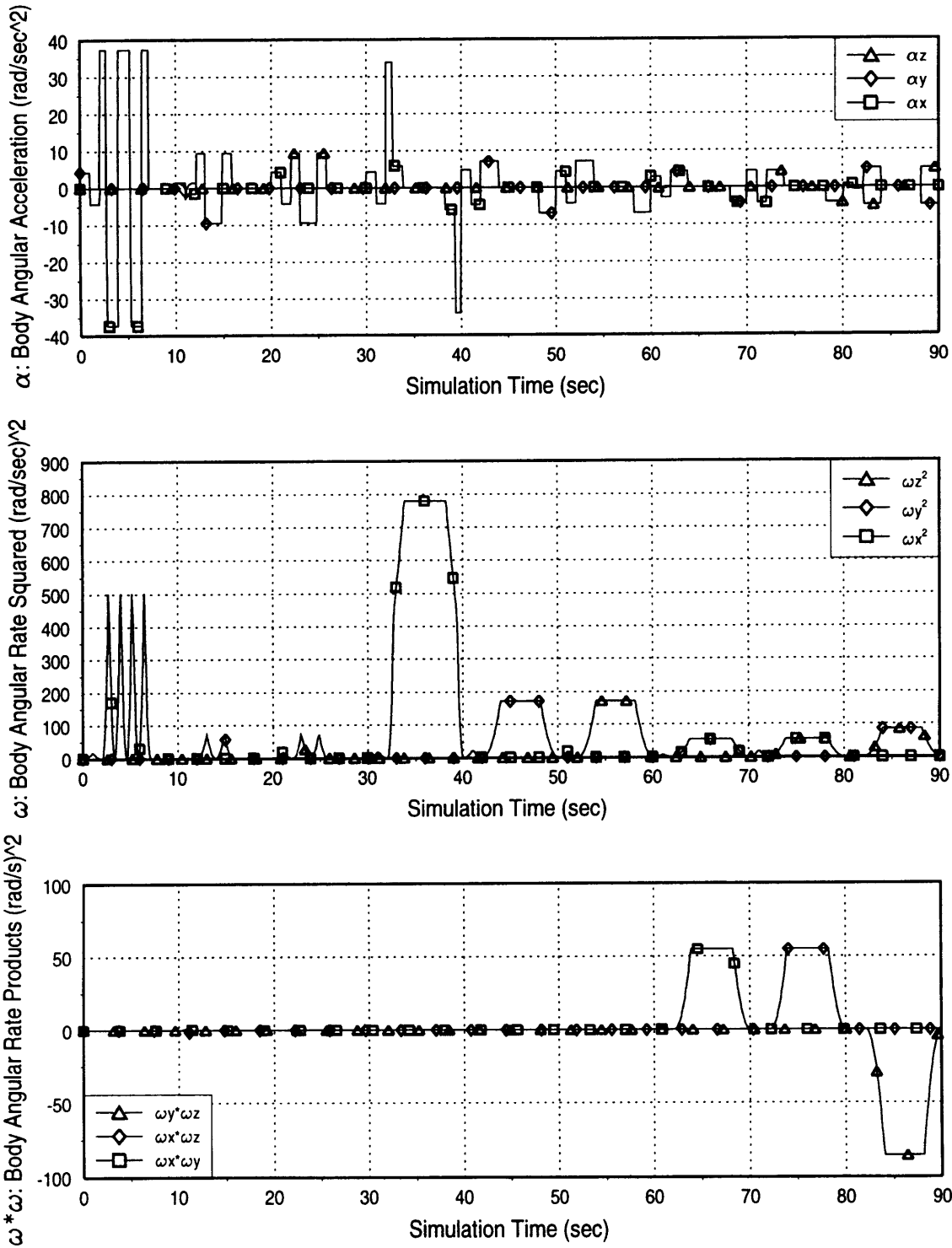


Figure B.4: GT6b Body Frame Sensitivities

Cost Function vs Time

GT0 Trajectory

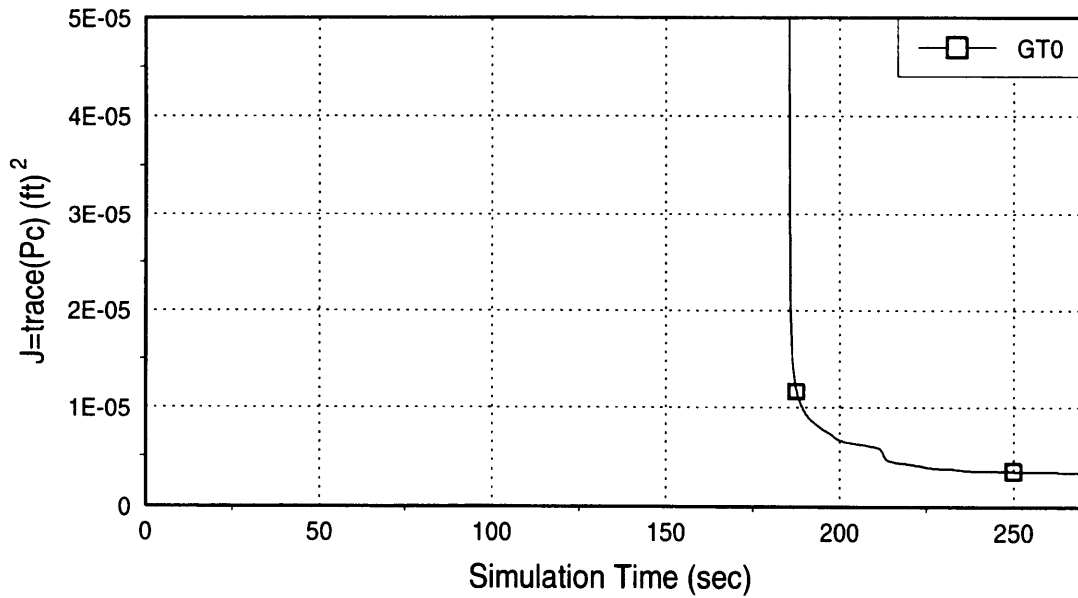
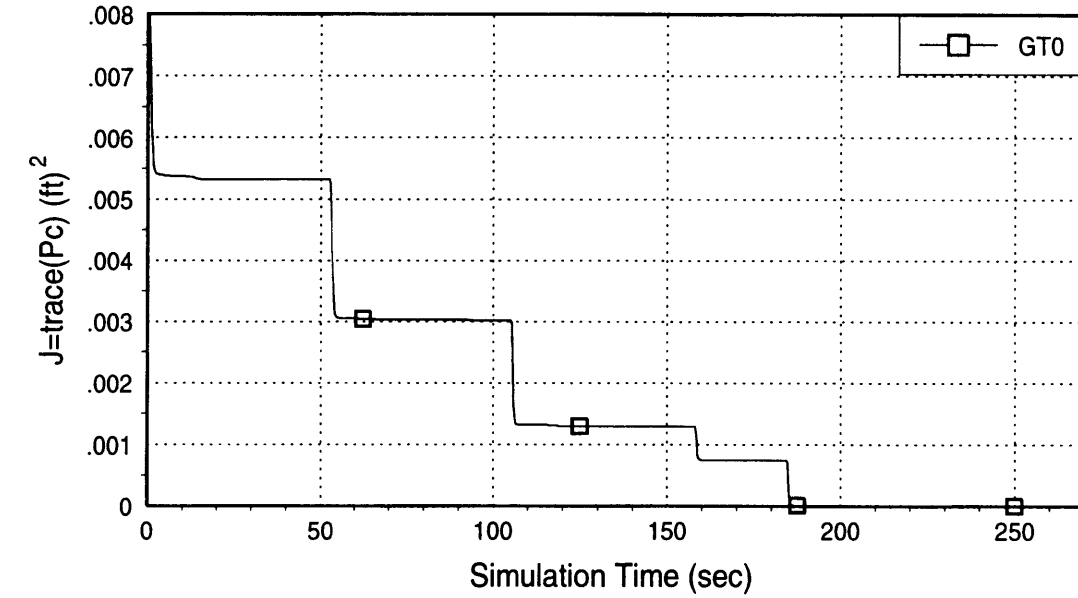


Figure B.5: Cost Function for GT0

Cost Function vs Time

Initial Heuristic Trajectories

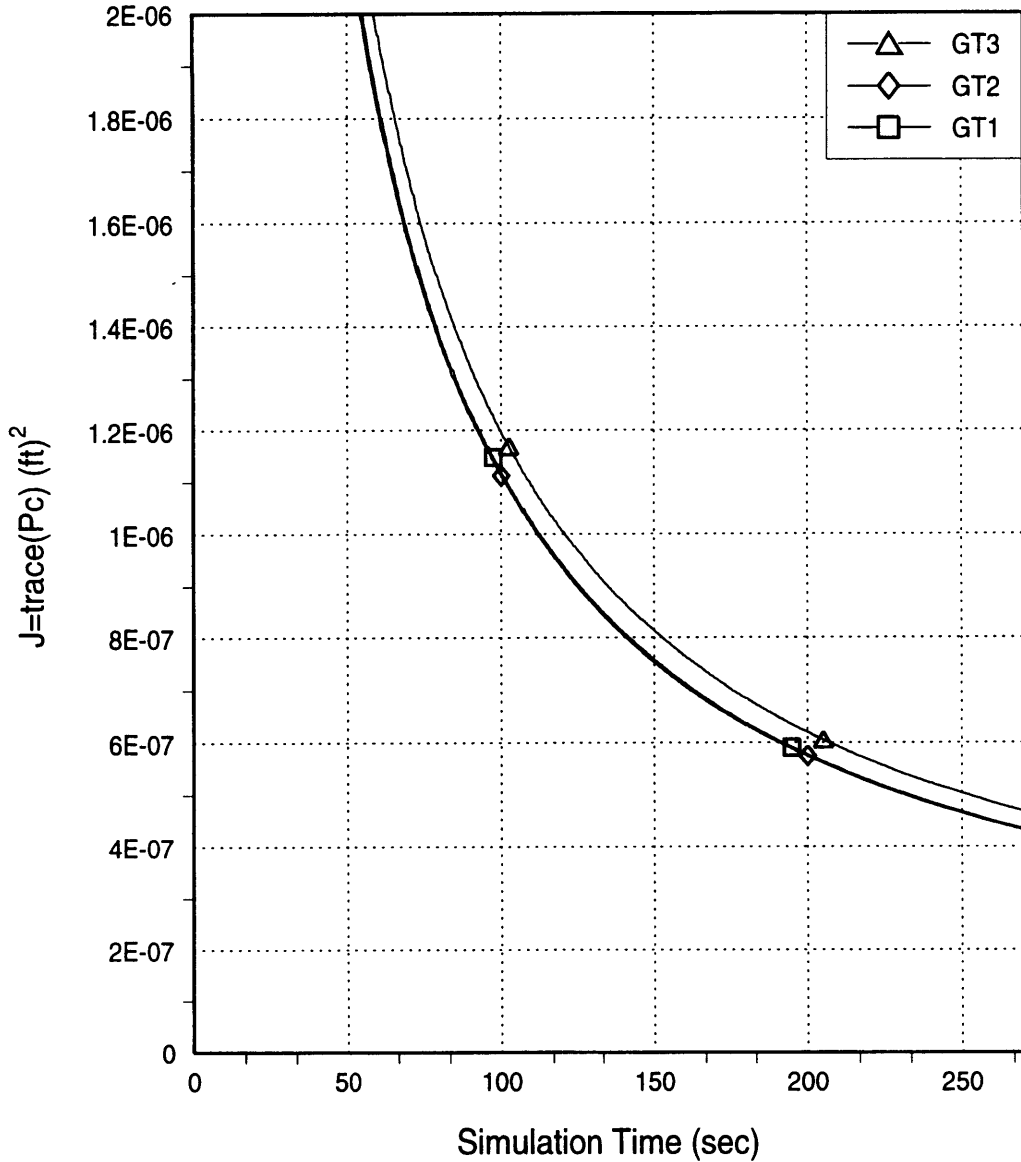


Figure B.6: Cost Function for Initial Heuristic Trajectories

Cost Function vs Time

GT4 and GT5 Trajectories

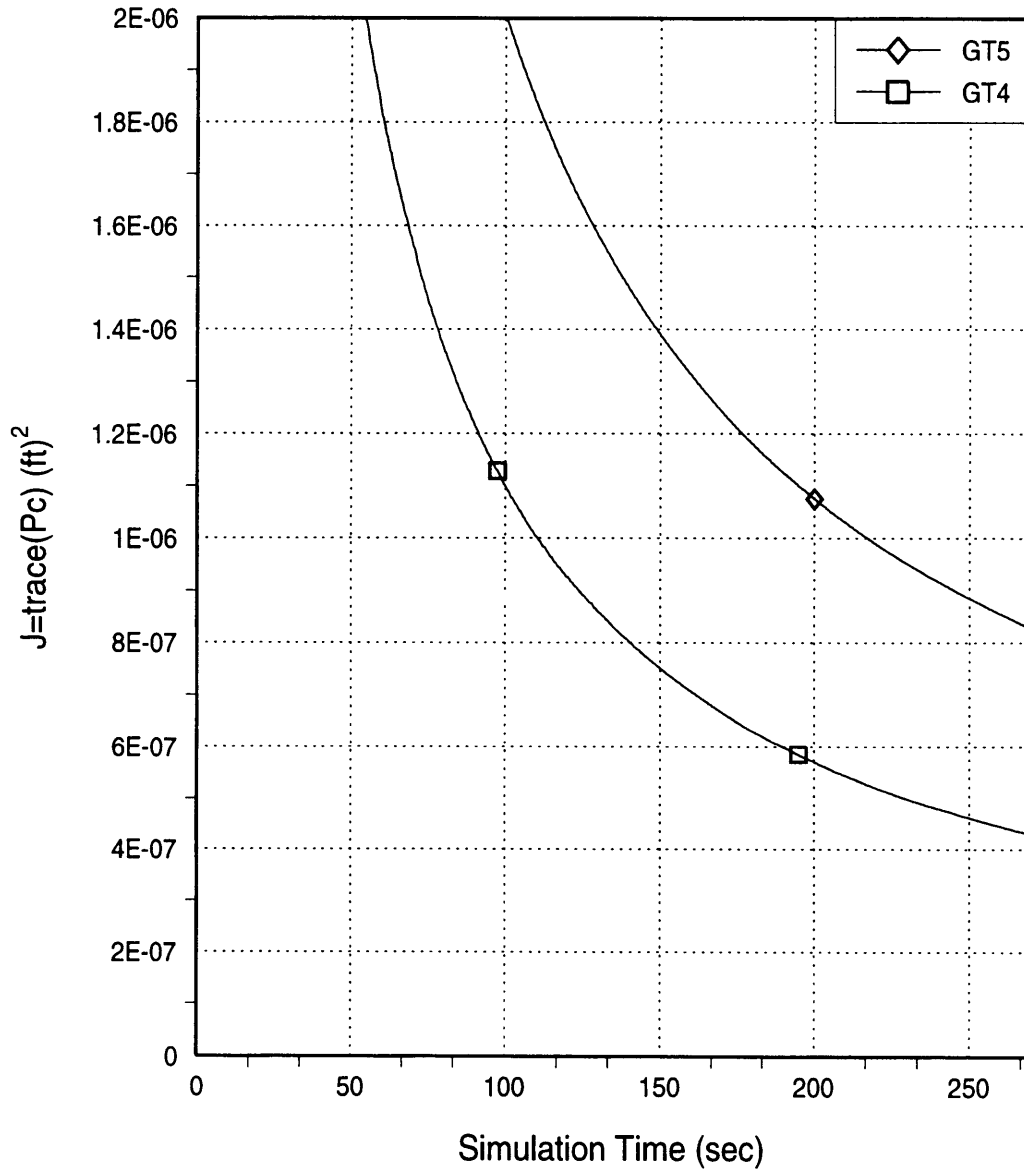


Figure B.7: Cost Function for GT4 and GT5 Trajectories

Cost Function vs Time

Holding Time Effects on Cost Function

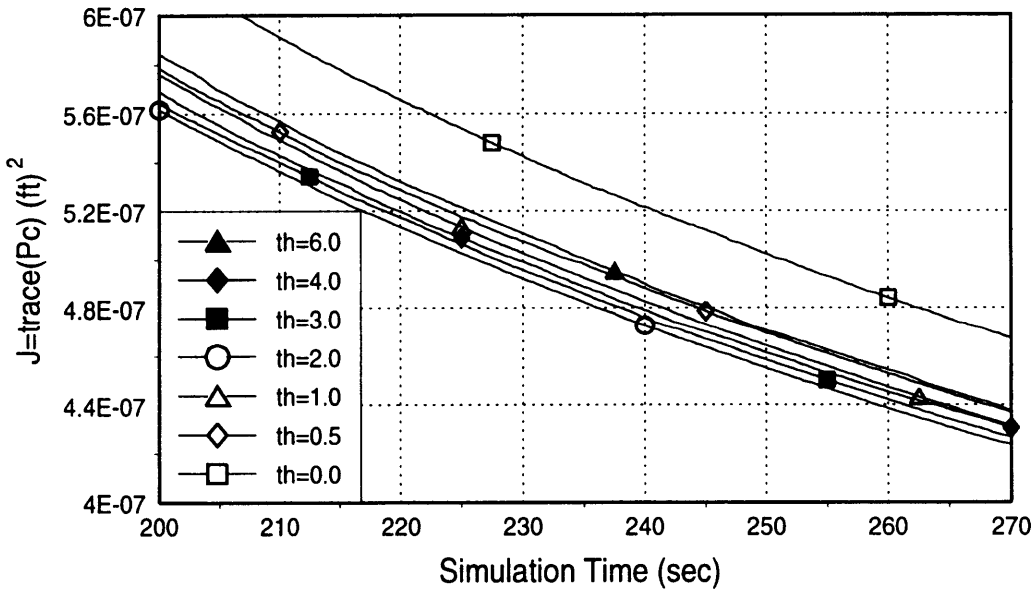
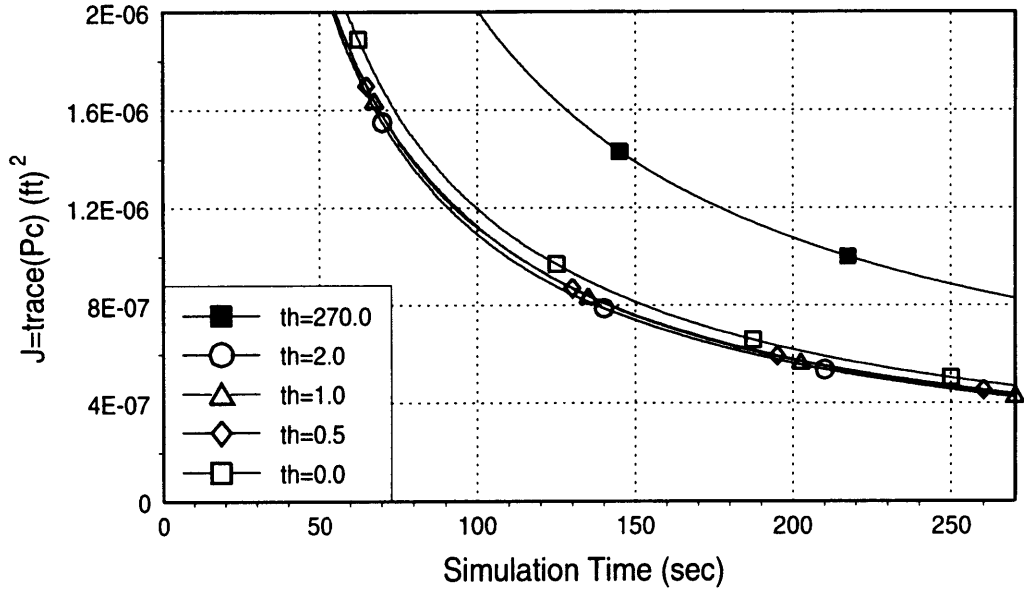


Figure B.8: Holding Time Effects on Cost Function

Cost Function vs Time

Initial Middle Gimbal Angle Effects on Cost Function

Holding Period = 2.02 sec

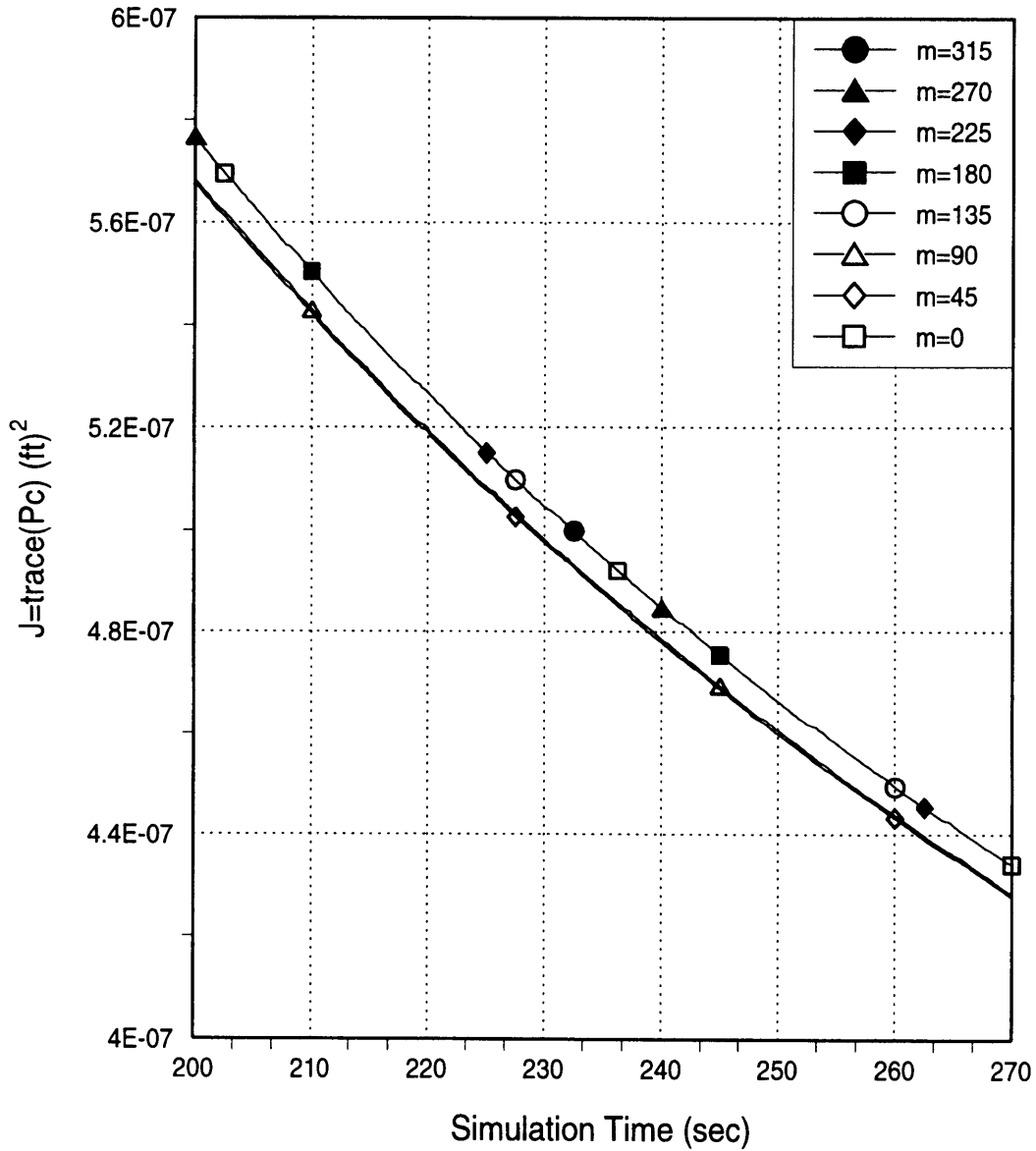


Figure B.9: Initial Middle Gimbal Angle Effects on Cost Function

Cost Function vs Time

Initial Inner Gimbal Angle Effects on Cost Function

Holding Period = 2.02 sec

Initial Middle Gimbal Angle = 159.5 deg

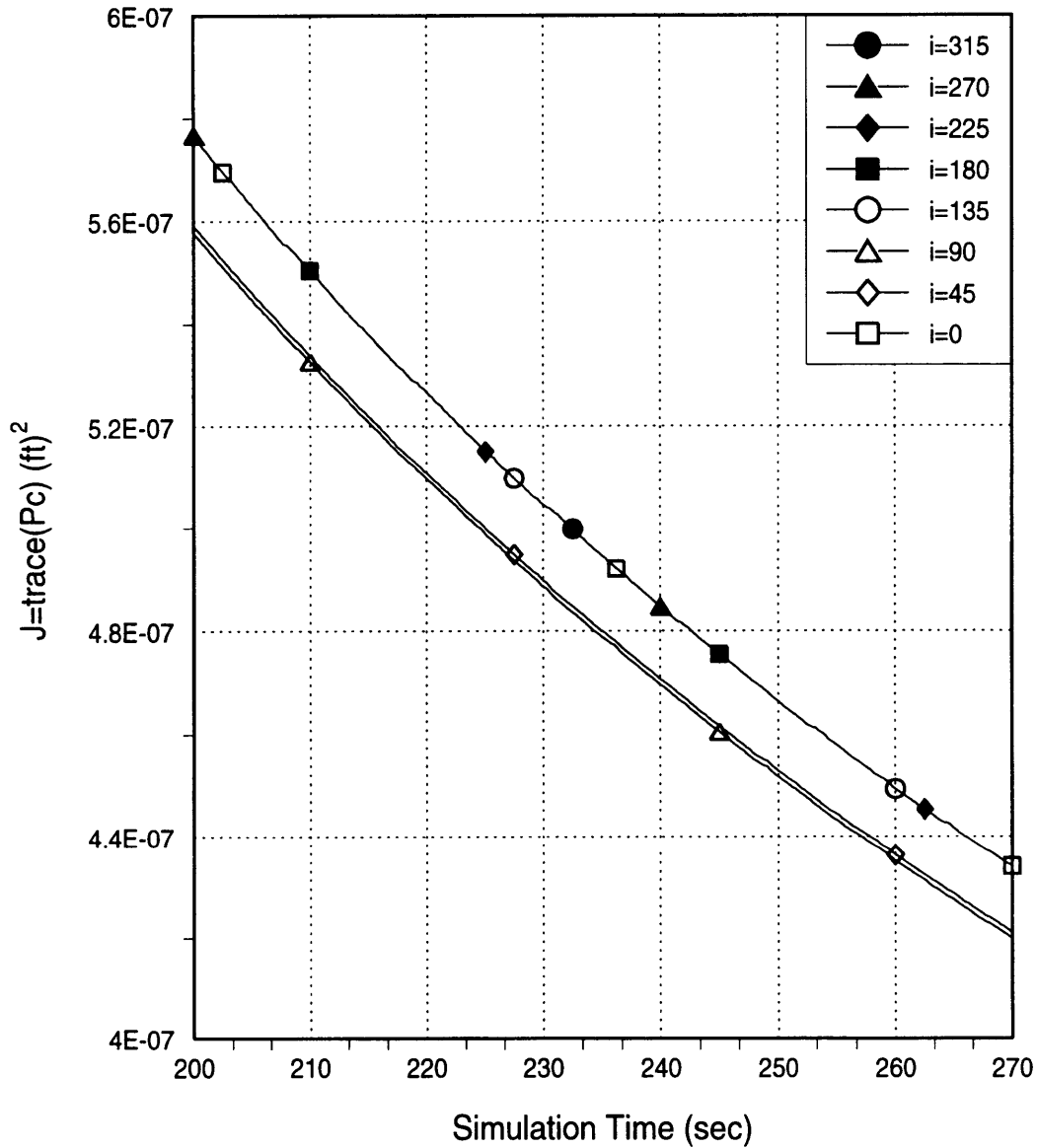


Figure B.10: Initial Inner Gimbal Angle Effects on Cost Function

Cost Function vs Time

Full Extended Trajectories

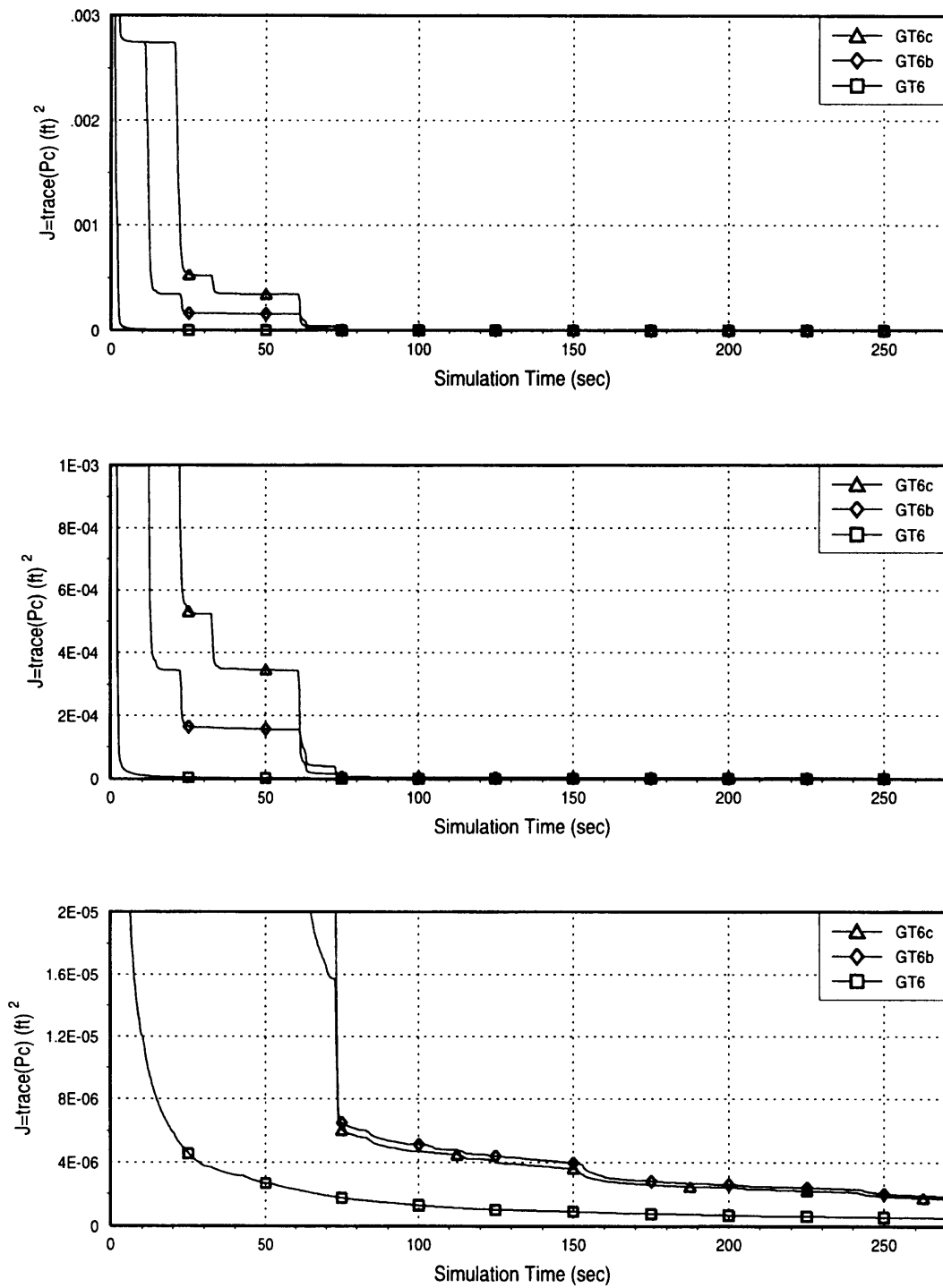


Figure B.11: Cost Function for Full Extended Trajectories

Cost Function vs Time

Extended Initial Trajectories

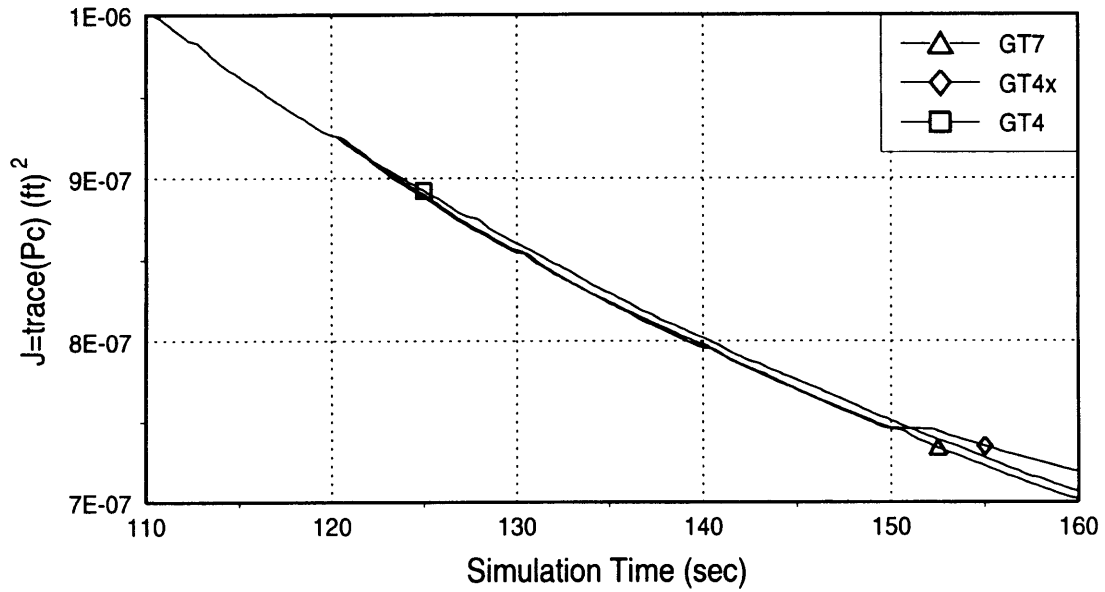
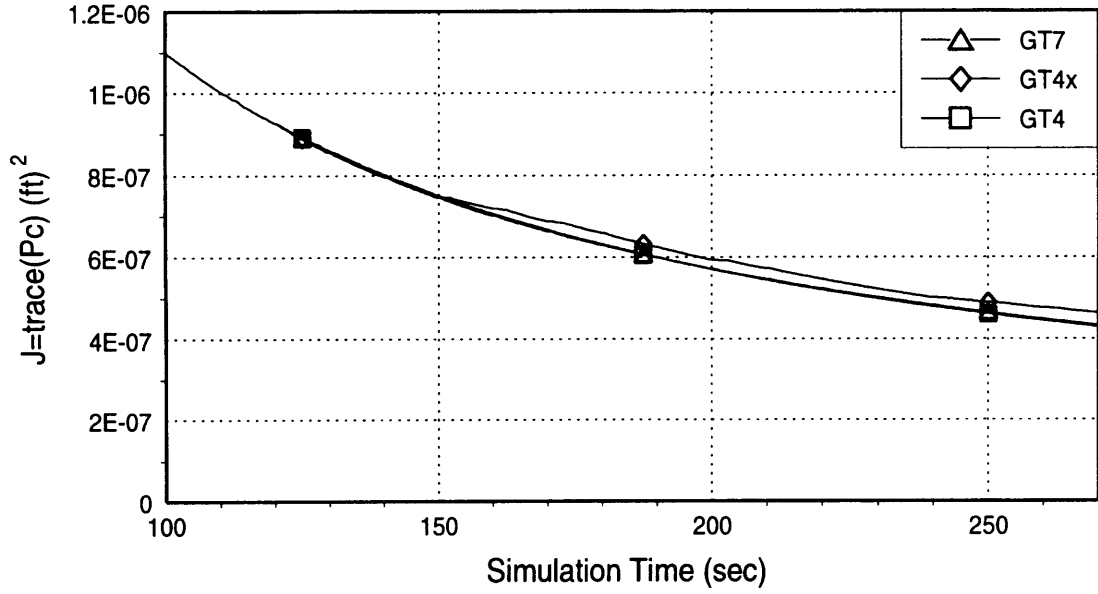


Figure B.12: Cost Function for Extended Initial Trajectories

Cost Function vs Time

Runge Kutta Step Size Effects

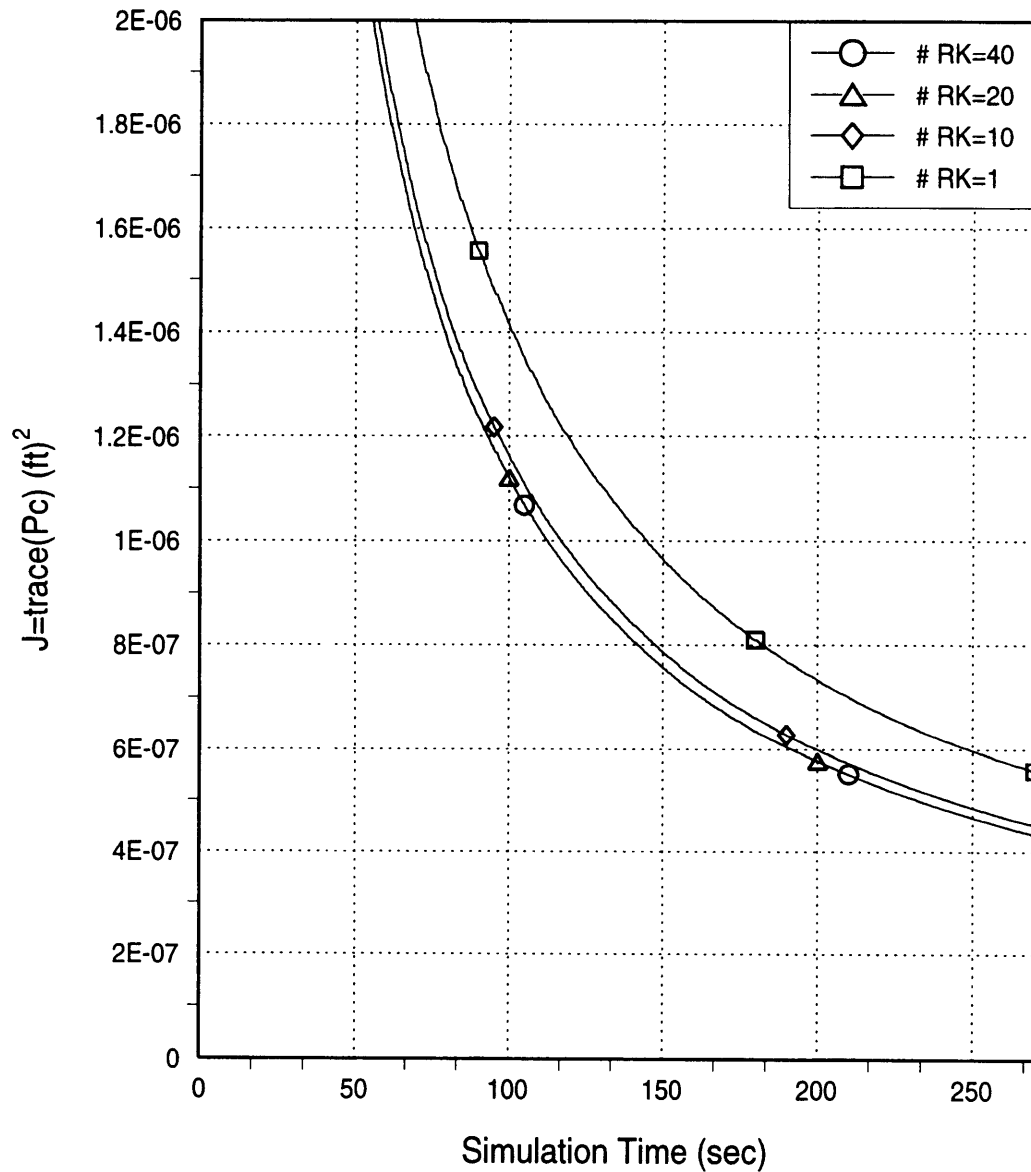


Figure B.13: Runge Kutta Step Size Effects on Cost Function

Cost Function vs Time

Measurement Frequency Effects

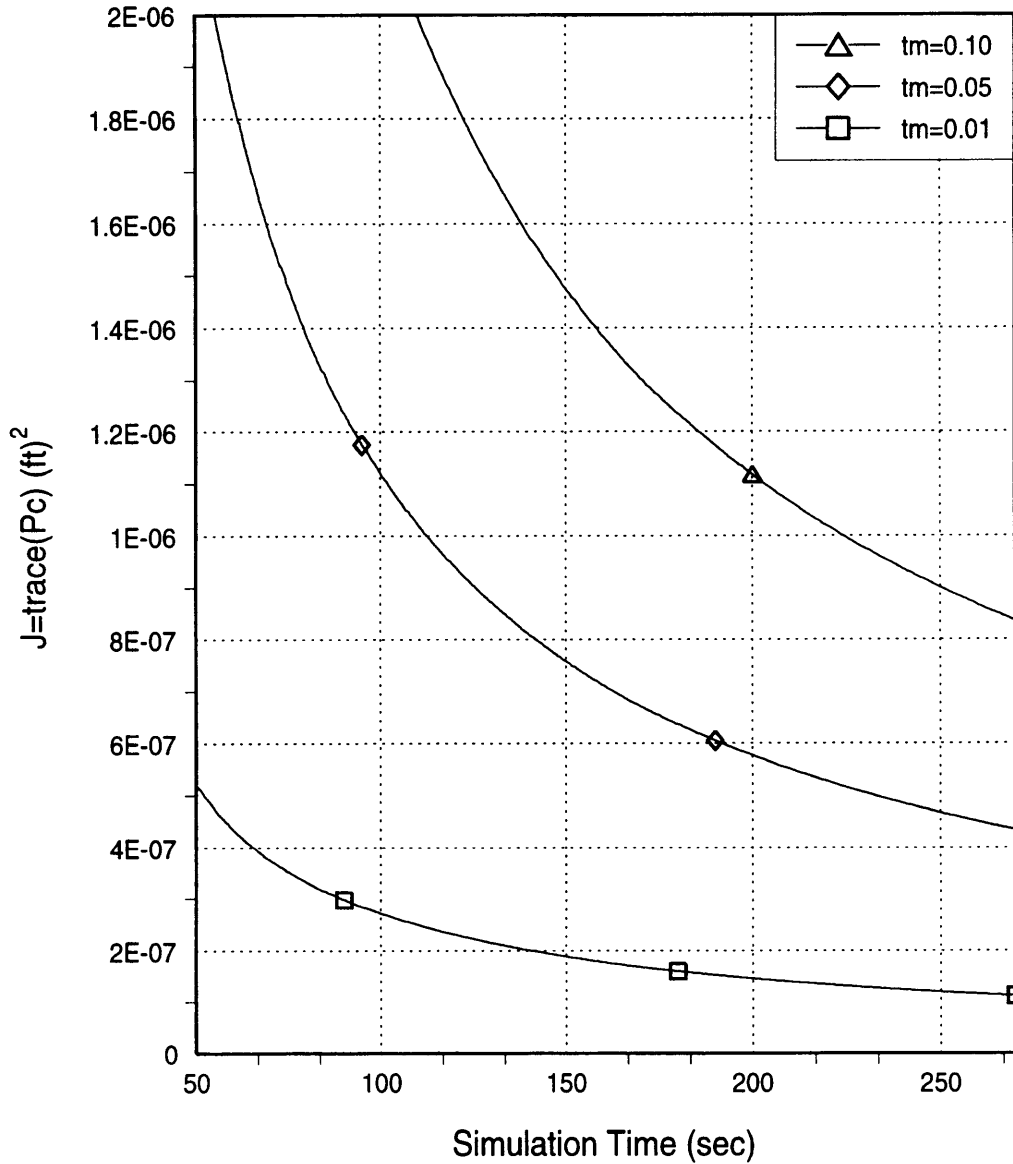


Figure B.14: Measurement Frequency Effects on Cost Function

Cost Function vs Time

Gimbal Axis Displacement Effects for GT3

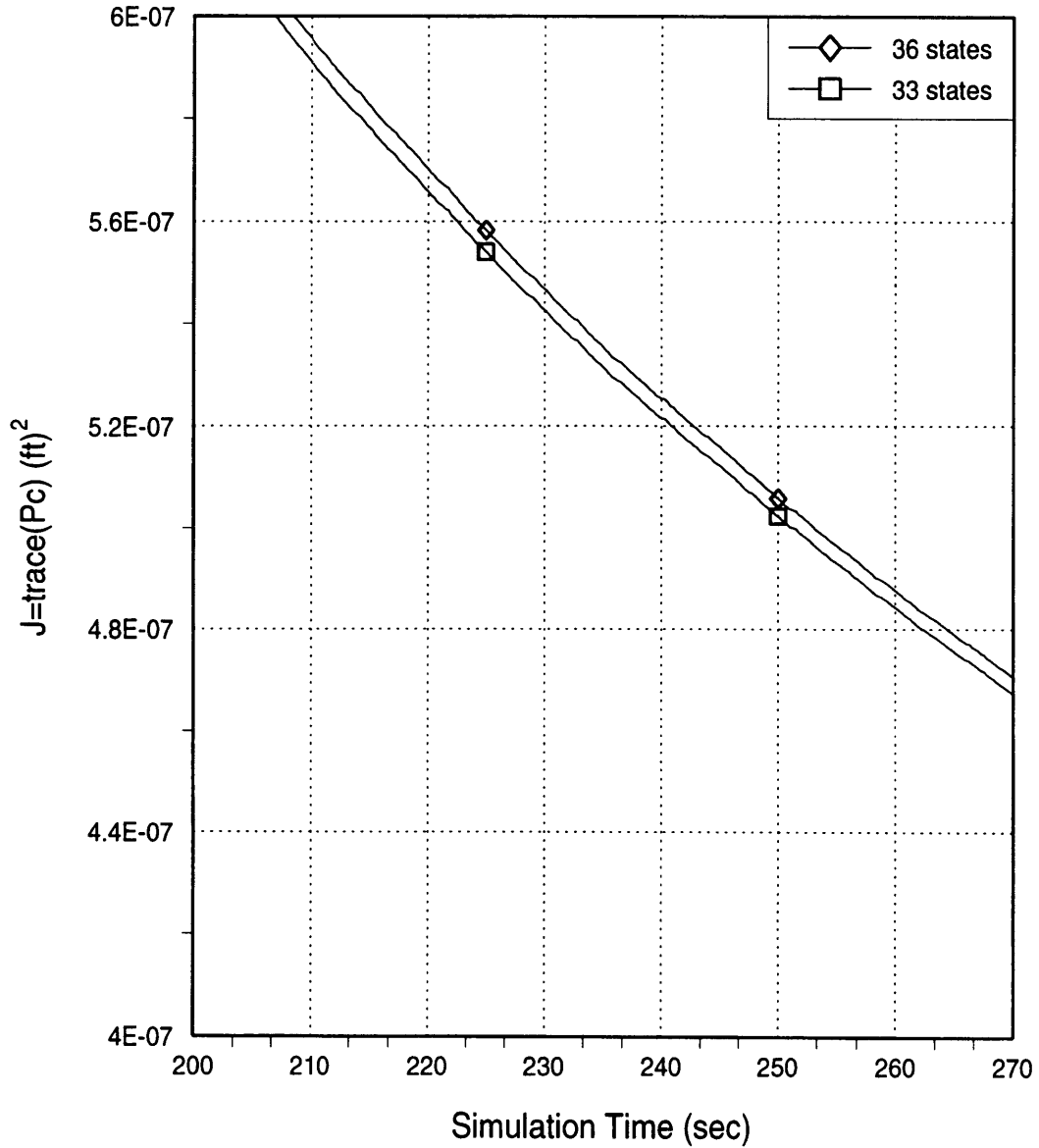


Figure B.15: Gimbal Axis Displacement Effects on Cost Function for GT3

Gimbal Axis Displacement Errors vs Time

GT1 Trajectory

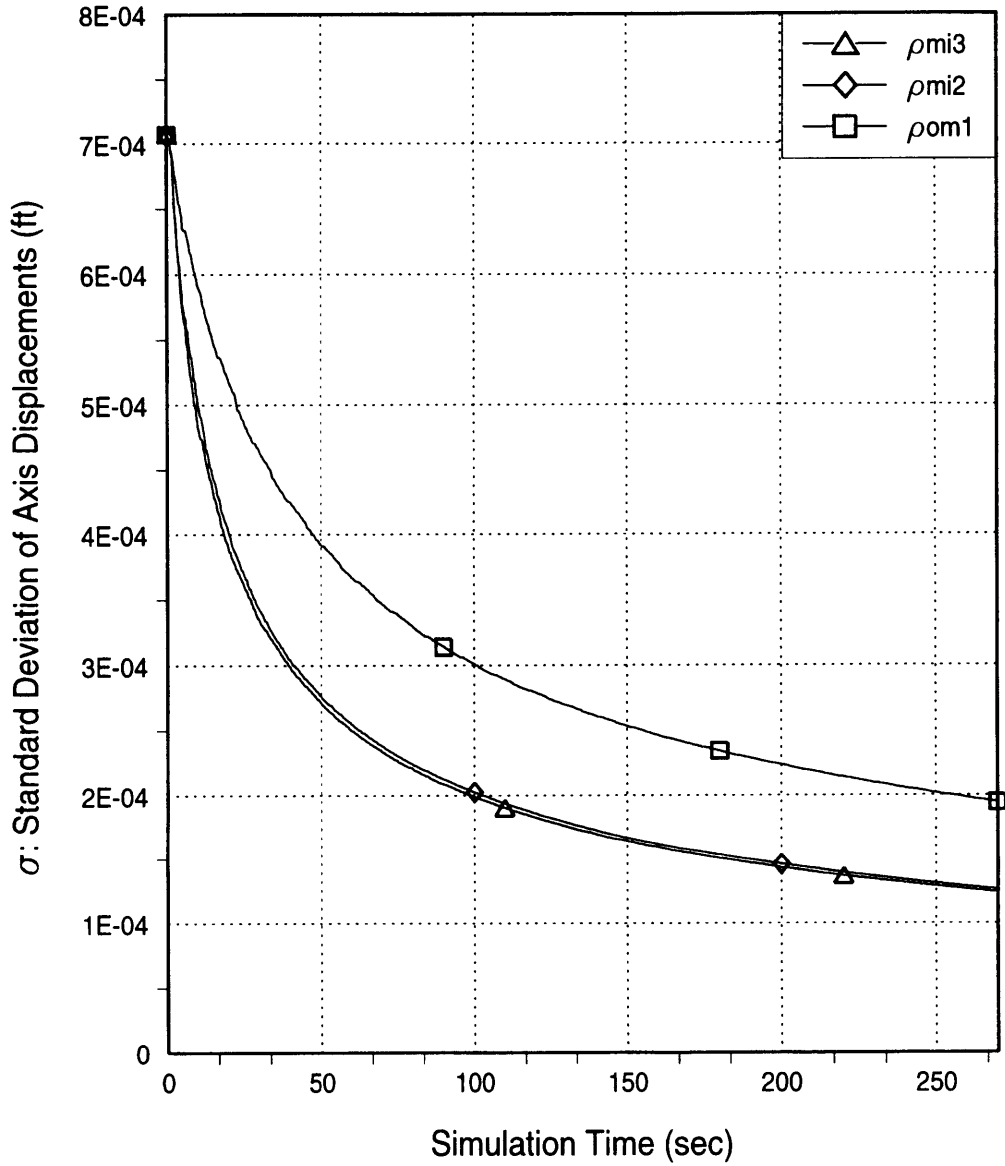


Figure B.16: Gimbal Axis Displacement Errors vs Time for GT1

Position and Velocity Errors vs Time

GT1 Trajectory

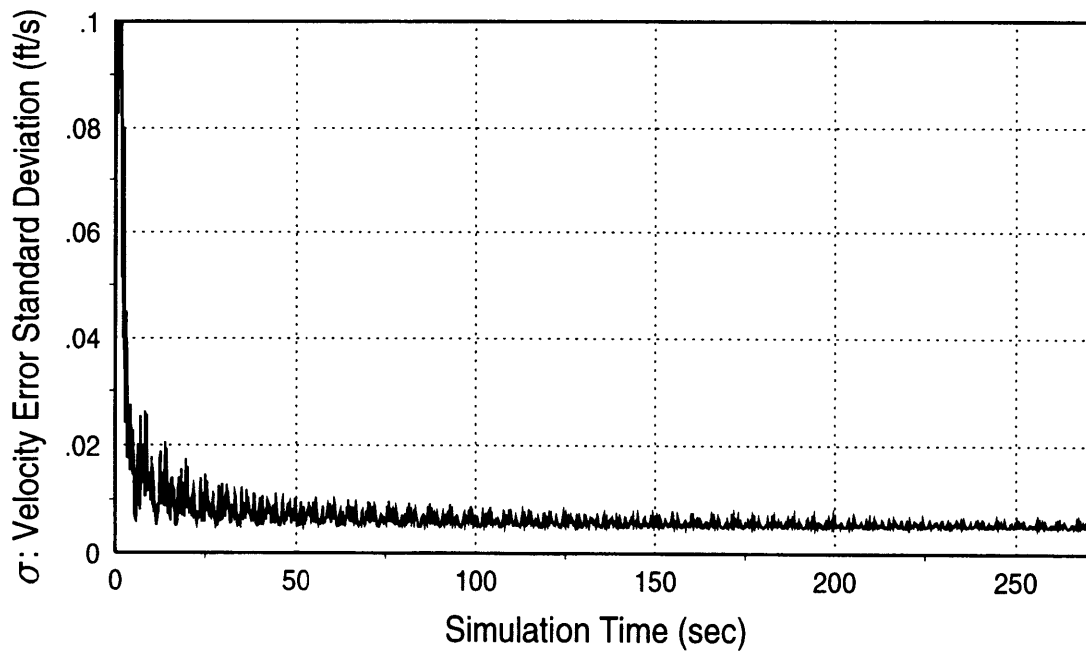
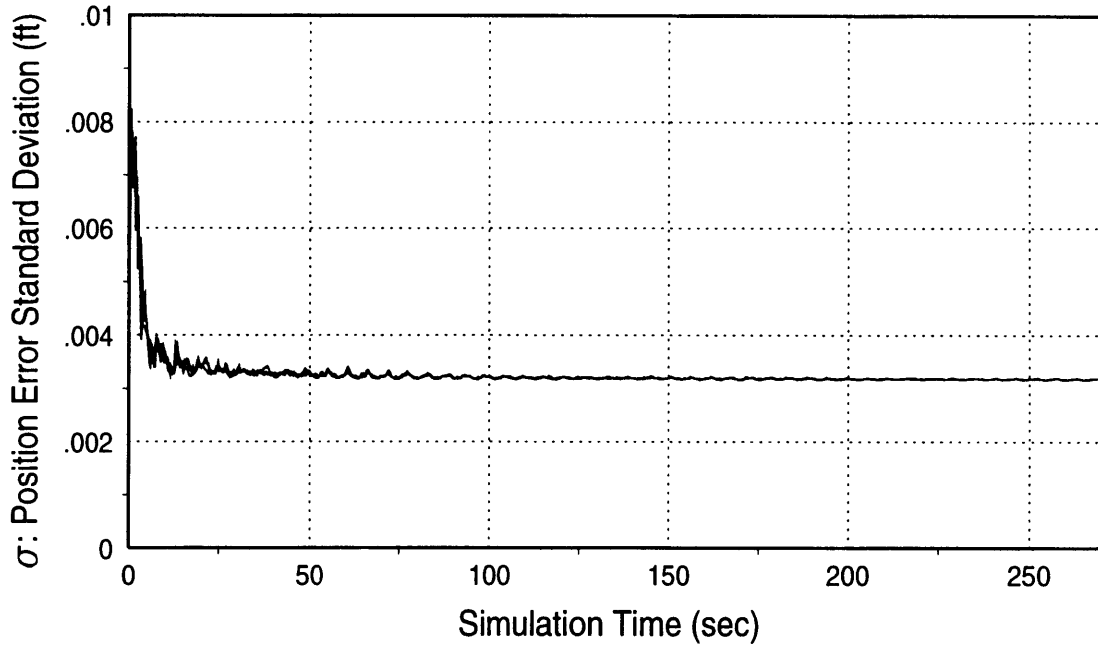


Figure B.17: Position and Velocity Errors for GT1 vs Time

Appendix C

Gimbal to Body Transformations

The transformations from the gimbal angular velocities and angular accelerations to the body frame angular velocities and angular accelerations are derived in this Appendix. The methodology described in [24] is used to derive the transformation from gimbal angular rates to body frame angular velocities. The transformations are given by equations (C.7) and (C.12), which are the same as equations (2.23) and (2.22) in the text.

Figure C.1 shows the transformation between the local level frame and the body frame. The body frame is fixed to the inner gimbal, and is therefore the same as the inner gimbal frame. Note that the transformation shown in Figure C.1 is a typical 3-2-1 Euler transformation through angles ϕ , θ , and ψ , respectively. For this transformation it was assumed that the middle gimbal of the test table, or the pitch axis, was initially deflected

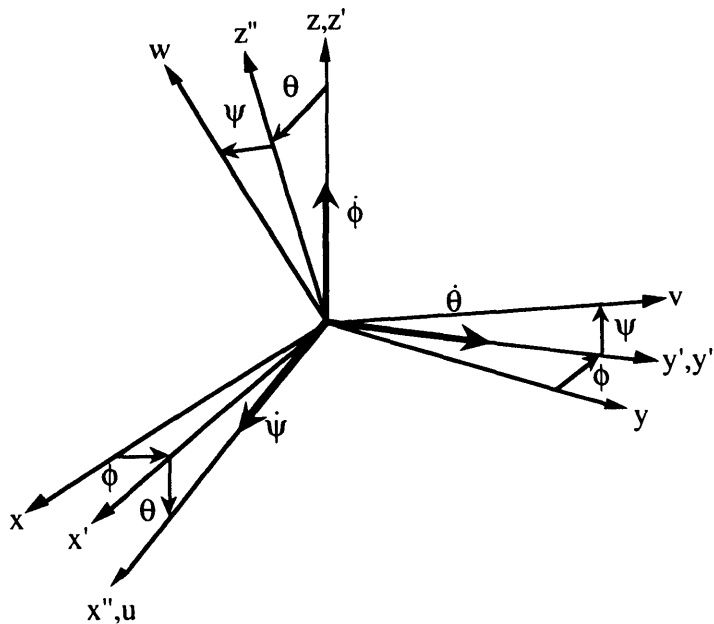


Figure C.1 Local Level Frame to Body Frame (3-2-1) Transformation

by positive 90 degrees. This deflection provided three gimbal axes that were initially orthogonal. The middle gimbal angles throughout the simulation are measured from this initially deflected position.

The transformation matrix \mathbf{C}_{xyz}^{uvw} , which transforms a vector from the local level frame (x,y,z) to the body frame (u,v,w) is given as a function of the Euler angles:

$$\mathbf{C}_{xyz}^{uvw} = \begin{bmatrix} c\theta c\phi & c\theta s\phi & -s\theta \\ -c\psi s\phi + s\psi s\theta c\phi & c\psi c\phi + s\psi s\theta s\phi & s\psi c\theta \\ s\psi s\phi + c\psi s\theta c\phi & -s\psi c\phi + c\psi s\theta s\phi & c\psi c\theta \end{bmatrix}$$

where $c()$ and $s()$ indicate the cosine and the sine of the appropriate angle. For the case of the test table used in this simulation, the angles ϕ , θ , and ψ were represented by the outer, middle, and inner gimbal angles (θ_o , θ_m , θ_i). Therefore, the transformation is written as:

$$\mathbf{C}_{xyz}^{uvw} = \begin{bmatrix} c\theta_m c\theta_o & c\theta_m s\theta_o & -s\theta_m \\ -c\theta_i s\theta_o + s\theta_i s\theta_m c\theta_o & c\theta_i c\theta_o + s\theta_i s\theta_m s\theta_o & s\theta_i c\theta_m \\ s\theta_i s\theta_o + c\theta_i s\theta_m c\theta_o & -s\theta_i c\theta_o + c\theta_i s\theta_m s\theta_o & c\theta_i c\theta_m \end{bmatrix} \quad (\text{C.1})$$

Angular Velocity Transformation

The Euler rates are given as the yaw rate, pitch rate, and roll rate. For the test table simulation these rates correspond to the outer gimbal rate, middle gimbal rate, and inner gimbal rate, respectively. From Figure C.1 the total angular rate is given by:

$$\underline{\omega} = \dot{\phi}\hat{z} + \dot{\theta}\hat{y}' + \dot{\psi}\hat{u} \quad (\text{C.2})$$

where \hat{z} , \hat{y}' , and \hat{u} are unit vectors along the indicated axes of Figure C.1 and

$\dot{\phi} = \omega_o$ = outer gimbal angular velocity

$\dot{\theta} = \omega_m$ = middle gimbal angular velocity

$\dot{\psi} = \omega_i$ = inner gimbal angular velocity

To find the angular velocity in the body frame, components of $\underline{\omega}$ are taken along the body axes:

$$\begin{aligned}
\omega_u &= \dot{\phi} \hat{z} \cdot \hat{u} + \dot{\theta} \hat{y}' \cdot \hat{u} + \dot{\psi} \\
\omega_v &= \dot{\phi} \hat{z} \cdot \hat{v} + \dot{\theta} \hat{y}' \cdot \hat{v} \\
\omega_w &= \dot{\phi} \hat{z} \cdot \hat{w} + \dot{\theta} \hat{y}' \cdot \hat{w}
\end{aligned} \tag{C.3}$$

Using the transformation matrix given in (C.1) we have

$$\begin{aligned}
\hat{z} \cdot \hat{u} &= C_{13} = -\sin \theta \\
\hat{z} \cdot \hat{v} &= C_{23} = \sin \psi \cos \theta \\
\hat{z} \cdot \hat{w} &= C_{33} = \cos \psi \cos \theta
\end{aligned} \tag{C.4}$$

The transformation from (x',y',z') coordinates to (u,v,w) coordinates is accomplished using C_{xyz}^{uvw} with ϕ set to zero. The rotation is now a simple 2-1 rotation through the angles θ and ψ and the following relations can be written:

$$\begin{aligned}
\hat{y}' \cdot \hat{u} &= C_{12}(\phi = 0) = 0 \\
\hat{y}' \cdot \hat{v} &= C_{22}(\phi = 0) = \cos \psi \\
\hat{y}' \cdot \hat{w} &= C_{32}(\phi = 0) = -\sin \psi
\end{aligned} \tag{C.5}$$

Substituting (C.4) and (C.5) into (C.3) we obtain:

$$\begin{aligned}
\omega_u &= -\dot{\phi} \sin \theta + \dot{\psi} \\
\omega_v &= \dot{\phi} \sin \psi \cos \theta + \dot{\theta} \cos \psi \\
\omega_w &= \dot{\phi} \cos \psi \cos \theta - \dot{\theta} \sin \psi
\end{aligned} \tag{C.6}$$

Substituting the table gimbal rates in for the Euler angle rates we obtain equation (2.23), the transformation from the gimbal rates to the body rates:

$$\underline{\omega}^b = \mathbf{A}_{g\omega}^{b\omega} \underline{\omega}^g \tag{C.7}$$

where

$$\underline{\omega}^b = \begin{bmatrix} \omega_u \\ \omega_v \\ \omega_w \end{bmatrix} = \text{angular velocity vector in the body frame (u,v,w)}$$

$$\underline{\omega}^g = \begin{bmatrix} \omega_o \\ \omega_m \\ \omega_t \end{bmatrix} = \text{gimbal angular velocities}$$

$$\mathbf{A}_{g\omega}^{h\omega} = \begin{bmatrix} -\sin \theta_m & 0 & 1 \\ \sin \theta_i \cos \theta_m & \cos \theta_i & 0 \\ \cos \theta_i \cos \theta_m & -\sin \theta_i & 0 \end{bmatrix}$$

Angular Acceleration Transformation

To derive the angular acceleration transformation, the derivative of equation (C.2) is taken:

$$\underline{\alpha} = \frac{d\underline{\omega}}{dt} = \ddot{\phi}\hat{z} + \dot{\phi}\dot{\hat{z}} + \ddot{\theta}\hat{y}' + \dot{\theta}\dot{y}' + \ddot{\psi}\hat{u} + \dot{\psi}\dot{\hat{u}} \quad (\text{C.8})$$

First, the three time derivatives of the unit vectors are analyzed. The time derivative of \hat{z} is zero, because \hat{z} is a local level axis that doesn't move with time. Since \hat{y}' is affected only by ϕ and not by θ or ψ , we can write:

$$\dot{\hat{y}}' = \frac{d\hat{y}'}{dt} = \frac{\partial \hat{y}'}{\partial \phi} \frac{\partial \phi}{\partial t} = \frac{\partial \hat{y}'}{\partial \phi} \dot{\phi}$$

where from Figure C.1 we have:

$$\hat{y}' = -\sin \phi \hat{x} + \cos \phi \hat{y}$$

Therefore,

$$\dot{\hat{y}}' = -(\cos \phi \hat{x} + \sin \phi \hat{y})\dot{\phi} \quad (\text{C.9})$$

Similarly, the body frame unit vector \hat{u} is affected by both ϕ and θ , so the time derivative is written as:

$$\dot{\hat{u}} = \frac{d\hat{u}}{dt} = \frac{\partial \hat{u}}{\partial \phi} \frac{\partial \phi}{\partial t} + \frac{\partial \hat{u}}{\partial \theta} \frac{\partial \theta}{\partial t} = \frac{\partial \hat{u}}{\partial \phi} \dot{\phi} + \frac{\partial \hat{u}}{\partial \theta} \dot{\theta}$$

From Figure C.1 we have:

$$\hat{u} = \cos \theta \hat{x}' - \sin \theta \hat{z}'$$

and

$$\begin{aligned}\hat{z}' &= \hat{z} \\ \hat{x}' &= \cos \phi \hat{x} + \sin \phi \hat{y}\end{aligned}$$

Therefore,

$$\begin{aligned}\hat{u} &= \cos \phi \cos \theta \hat{x} + \sin \phi \cos \theta \hat{y} - \sin \theta \hat{z} \\ \frac{\partial \hat{u}}{\partial \phi} &= -\sin \phi \cos \theta \hat{x} + \cos \phi \cos \theta \hat{y} \\ \frac{\partial \hat{u}}{\partial \theta} &= -\cos \phi \sin \theta \hat{x} - \sin \phi \sin \theta \hat{y} - \cos \theta \hat{z}\end{aligned}$$

The resulting $\dot{\hat{u}}$ is then

$$\dot{\hat{u}} = (-\sin \phi \hat{x} + \cos \phi \hat{y}) \cos \theta \dot{\phi} - [\sin \theta (\cos \phi \hat{x} + \sin \phi \hat{y}) + \cos \theta \hat{z}] \dot{\theta} \quad (\text{C.10})$$

Substituting (C.9) and (C.10) into (C.8), and taking components along the body axes we obtain the transformation from gimbal angular accelerations to body frame angular accelerations:

$$\underline{\alpha}^b = \mathbf{C}_{xyz}^{uvw} \mathbf{a1}(\underline{\theta}^s, \underline{\omega}^s, \underline{\alpha}^s) + \mathbf{a2}(\underline{\theta}^s, \underline{\alpha}^s) \quad (\text{C.11})$$

where \mathbf{C}_{xyz}^{uvw} is defined in (C.1) and $\mathbf{a1}$ and $\mathbf{a2}$ are vector functions of the gimbal angular accelerations, angular velocities, and angles. Substituting θ_o , θ_m , and θ_i for the Euler angles ϕ , θ , and ψ , and using $\omega = \dot{\theta}$ and $\alpha = \ddot{\theta}$, the expressions for $\mathbf{a1}$ and $\mathbf{a2}$ are:

$$\mathbf{a1} = \begin{bmatrix} -\omega_o \omega_m \cos \theta_o - \omega_o \omega_i \sin \theta_o \cos \theta_m - \omega_m \omega_i \sin \theta_m \cos \theta_o \\ -\omega_o \omega_m \sin \theta_o + \omega_o \omega_i \cos \theta_o \cos \theta_m - \omega_m \omega_i \sin \theta_m \sin \theta_o \\ \alpha_o - \omega_m \omega_i \cos \theta_m \end{bmatrix}$$

$$\mathbf{a2} = \begin{bmatrix} \alpha_i \\ \alpha_m \cos \theta_i \\ -\alpha_m \sin \theta_i \end{bmatrix}$$

The first term in equation (C.11) can be multiplied out and simplified into a vector function that depends on the gimbal angles, products of the gimbal angular rates, and the gimbal angular accelerations. Combining this vector function with the vector $\mathbf{a2}$ we arrive at the desired expression for the angular accelerations in the body frame:

$$\underline{\alpha}^b = \begin{bmatrix} -\omega_o \omega_m c \theta_m - \alpha_o s \theta_m + \alpha_i \\ \omega_o \omega_i c \theta_i c \theta_m - \omega_o \omega_m s \theta_i s \theta_m - \omega_m \omega_i s \theta_i + \alpha_o s \theta_i c \theta_m + \alpha_m c \theta_i \\ -\omega_o \omega_i s \theta_i c \theta_m - \omega_o \omega_m c \theta_i s \theta_m - \omega_m \omega_i c \theta_i + \alpha_o c \theta_i c \theta_m - \alpha_m s \theta_i \end{bmatrix} \quad (\text{C.12})$$

Equation (C.12) was used for equation (2.22) in the text.

Appendix D

Square Root Filter

The Cholesky decomposition algorithm and square root filter formulas presented in this appendix were taken from [21]. Also, the square root filter propagation equation of Andrews was taken from [20].

Cholesky Decomposition

Cholesky decomposition creates a triangular square root \mathbf{A} of a symmetric $n \times n$ positive semi-definite matrix \mathbf{B} such that $\mathbf{A}\mathbf{A}^T = \mathbf{B}$. \mathbf{A} is determined by equating the terms of $\mathbf{A}\mathbf{A}^T$ and \mathbf{B} . The columns of \mathbf{A} can be solved for sequentially, starting with the n th column. The following recursive algorithm produces an upper triangular square root matrix \mathbf{A} where $A_{ji} = 0$ for all $j > i$. For $i = n$ to 1 compute:

$$A_{ii} = \left[B_{ii} - \sum_{k=i+1}^n A_{ik}^2 \right]^{1/2} \quad (\text{D.1})$$

$$A_{ji} = \left[B_{ji} - \sum_{k=i+1}^n A_{jk}A_{ik} \right] / A_{ii} \quad j = i-1, 1 \quad (\text{D.2})$$

Square Root Filter Equations

For the square root formulation of the Kalman filter equations the measurements are incorporated one at a time as scalars. In this case, z , \mathbf{h}^T , and r replace \mathbf{z} , \mathbf{H} , and \mathbf{R} . The covariance measurement update equation (2.33) can be rewritten as:

$$\mathbf{W}^+\mathbf{W}^{+T} = \mathbf{W}^-[\mathbf{I} - \mathbf{f}\mathbf{f}^T/\alpha](\mathbf{W}^-)^T \quad (\text{D.3})$$

where \mathbf{W} is the square root of the covariance matrix \mathbf{P} defined by:

$$\mathbf{P} = \mathbf{W}\mathbf{W}^T$$

Carlson's optimal measurement incorporation equations in square root form are written as:

$$\mathbf{f} = (\mathbf{W}^-)^T \mathbf{h} \quad (\text{D.4})$$

$$\alpha = r + \mathbf{f}^T \mathbf{f} \quad (\text{D.5})$$

$$\mathbf{W}^+ = (\mathbf{W}^-) [\mathbf{I} - \mathbf{f} \mathbf{f}^T / \alpha]^{1/2} \quad (\text{D.6})$$

$$\hat{\mathbf{x}}^+ = \hat{\mathbf{x}}^- + (\mathbf{W}^-) \mathbf{f} \Delta z / \alpha \quad (\text{D.7})$$

where \mathbf{W}^- is assumed to be upper triangular. In order for equation (D.6) to yield a product in upper triangular form, an upper triangular square root of the matrix $[\mathbf{I} - \mathbf{f} \mathbf{f}^T / \alpha]$ must be used. This upper triangular square root matrix is determined through an analytic Cholesky decomposition described above, using equations (D.1) and (D.2). If \mathbf{A} is prescribed to satisfy the relation

$$\mathbf{A} \mathbf{A}^T = [\mathbf{I} - \mathbf{f} \mathbf{f}^T / \alpha] = \mathbf{B} \quad (\text{D.8})$$

then the elements of \mathbf{B} are given by

$$B_{ii} = 1 - f_i^2 / \alpha \quad (\text{D.9})$$

$$B_{ji} = -f_j f_i / \alpha \quad (\text{D.10})$$

The expressions for the elements of \mathbf{A} can be reduced to:

$$A_{ii} = (\alpha_{i-1} / \alpha_i)^{1/2} \quad (\text{D.11})$$

$$A_{ji} = -f_j f_i / (\alpha_{i-1} \alpha_i)^{1/2} \quad j=i-1, 1 \quad (\text{D.12})$$

where α_i represents a sequence of partial differences, which can also be expressed as a sequence of partial sums using equation (D.5):

$$\alpha_i \equiv \alpha - f_n^2 - \dots - f_{i+1}^2 \equiv r + f_1^2 + \dots + f_i^2 \quad (\text{D.13})$$

where $\alpha_n \equiv \alpha$. The values α_i were computed with no loss of precision due to subtraction using:

$$\begin{aligned} \alpha_0 &= r \\ \alpha_i &= \alpha_{i-1} + f_i^2 \quad i = 1, n \end{aligned} \quad (\text{D.14})$$

The extrapolation equation used to propagate the square root of the covariance matrix was given by Andrews as:

$$\dot{\mathbf{W}} = \mathbf{F}\mathbf{W} + \frac{1}{2}\mathbf{Q}(\mathbf{W}^T)^{-1} \quad (\text{D.15})$$

This equation can be verified by expanding the time derivative of the covariance matrix \mathbf{P} :

$$\begin{aligned} \dot{\mathbf{P}} &= \dot{\mathbf{W}}\mathbf{W}^T + \mathbf{W}\dot{\mathbf{W}}^T \\ &= [\mathbf{F}\mathbf{W} + \frac{1}{2}\mathbf{Q}(\mathbf{W}^T)^{-1}]\mathbf{W}^T + \mathbf{W}[\mathbf{W}^T\mathbf{F}^T + \frac{1}{2}\mathbf{W}^{-1}\mathbf{Q}] \\ &= \mathbf{F}(\mathbf{W}\mathbf{W}^T) + \frac{1}{2}\mathbf{Q} + (\mathbf{W}\mathbf{W}^T)\mathbf{F}^T + \frac{1}{2}\mathbf{Q} \\ &= \mathbf{F}\mathbf{P} + \mathbf{P}\mathbf{F}^T + \mathbf{Q} \end{aligned}$$

which is the matrix Riccati equation (2.32). Equation (D.15) is numerically integrated between measurement times to propagate \mathbf{W} forward in time.

List of References

1. Britting, K. R., *Inertial Navigation Systems Analysis*, John Wiley and Sons, New York, 1971.
2. Sabin, H. B., "Seventeen Ways to Measure Acceleration," *Control Engineering*, 8, No. 2: 106 (February 1961).
3. Johnson, Dan R., "Mechanical Evaluation of the Bell XI-79 Pendulous Accelerometer," TRW Report, September, 1981.
4. Widnall, W. S. and P. Grundy, "Inertial Navigation System Error Models," TR-03-73, Intermetrics, Inc., Cambridge, Mass., May 1973.
5. Arshal, George, "Error Equations of Inertial Navigation," *Journal of Guidance, Control, and Dynamics*, Vol.14, No. 4, July-August 1987, pp. 351-358.
6. Friedland, B., "On the Calibration Problem," *IEEE Transactions on Automatic Control*, Vol. AC-22, No. 6, December, 1977, pp. 899-905.
7. Grewal, M.S., V. Henderson, and R. Miyasako, "Application of Kalman Filtering to the Calibration and Alignment of Inertial Navigation Systems," *IEEE Transactions on Automatic Control*, Vol. 36, No. 1, January 1991, pp. 4-13.
8. Nash, R.A., J. Kasper, B. Crawford, and S. Levine, "Application of Optimal Smoothing to the Testing and Evaluation of Inertial Navigation Systems and Components," *IEEE Transactions on Automatic Control*, Vol. AC-16, No.6, December 1971, pp. 806-816.
9. Widnall, W. S. and P. Grundy, "Inertial Navigation System Test Methods," TR-08-73, Intermetrics, Inc., Cambridge, Mass., August 1973.
10. Riegsecker, Darold G., "Accelerometer Size Effect Calibration Trajectory," C.S. Draper Laboratory, Inc., Memo No. EGE-91-120, 13 May 1991.
11. Morgan, A. A., "Anisonertia Calibration," Interoffice Correspondence, Honeywell, Inc., 25 February 1993.
12. Thorvaldsen, T. and Musoff, H., "Optimum Selection of Test Table Positions for Strapdown System Calibration," *Fifteenth Biennial Guidance Test Symposium*, Vol. 2, Holloman AFB, New Mexico, September 1991, pp. 25-43.
13. Riegsecker, Darold G., "Errors Produced by Accelerometer Pendulum Dynamics When There is RLG Dither Induced Platform Motion," C.S. Draper Laboratory, Inc., Memo No. BMD-10-83, 24 May 1983.
14. Ogden, G.S., "Delta-V Velocity Correction Equations," Lockheed Report No. TR1185, 10 August, 1977.
15. Riegsecker, Darold G., "Accelerometer Angular Motion Errors During Spinup and Coast," C.S. Draper Laboratory, Inc., Memo No. DGR-03-88, 10 March 1988.

16. Riegsecker, Darold G., C.S. Draper Laboratory, Inc., personal notes.
17. Gelb, Arthur (ed.), *Applied Optimal Estimation*, The M.I.T. Press, Cambridge, MA, 1974.
18. Brown, R. G. and Hwang, Y. C., *Introduction to Random Signals and Applied Kalman Filtering*, John Wiley and Sons, New York, 1992.
19. Potter, J.E., "New Statistical Formulas," Space Guidance Analysis Memo 40, April 1963, Instrumentation Lab, MIT, Cambridge, Mass.
20. Andrews, A., "A Square Root Formulation of the Kalman Covariance Equations," *AIAA Journal*, June 1968, pp. 1165,1166.
21. Carlson, N. A., "Fast Triangular Formulation of the Square Root Filter," *AIAA Journal*, Vol. 11, No. 5, pp. 1259-1265, September 1973.
22. *Acceptance Test Plan for the Model 53M-3C/30H Three Axis Test Stand, ATP-26944*. Prepared for The Charles Stark Draper Lab, Inc. of Cambridge, Mass. by the Contraves Goerz Corporation, Work Order #K87004, November, 1988.
23. "Contraves Model 53M-3C Three-Axis Motion Simulator Specifications," Contraves Goerz Corporation, Pittsburgh, PA, 1987.
24. Wertz, James R. (ed.), *Spacecraft Attitude Determination and Control*, Kluwer Academic Publishers, Boston, 1978.

5743-20